Dissertation
submitted to the
Combined Faculties for the Natural Sciences and for Mathematics
of the Ruperto-Carola University of Heidelberg, Germany
for the degree of
Doctor of Natural Sciences

Put forward by

Dipl. Phys. Christoph Kern
Born in Mount Kisco, NY, USA

Oral examination: June 10, 2009

Spectroscopic measurements of volcanic gas emissions in the ultra-violet wavelength region

Referees: Prof. Dr. Ulrich Platt

Prof. Dr. Thomas Wagner

Spektroskopische Messungen von Vulkangasemissionen im ultra-violetten Wellenlängenbereich

In dieser Dissertation wurden drei neue Fernerkundungsinstrumente gebaut und angewandt um Vulkangasemissionen zu charakterisieren: ein passiver abtastender differentieller optischer Absorptionsspektrometer (DOAS), ein aktives Langpfad DOAS Gerät, und eine SO_2-Kamera. Mit dem passiven DOAS wurden Schwefeldioxid (SO_2) Emissionsflüsse an 6 Vulkanen erfolgreich gemessen. Am Kilauea Vulkan (Hawaii) wurden z.B. im März 2008 erhöhte SO_2 Emissionsflüsse entdeckt, ein Anzeichen für einen möglicherweise bevorstehenden Vulkanausbruch. Dieser fand wenige Wochen später statt. Halogenchemie in Vulkanfahnen wurde auch untersucht. So wurde z.B. Brommonoxid (BrO) am Stromboli (Italien), Popocatépetl (Mexiko), und Masaya (Nicaragua) nachgewiesen. Durch die erstmalige Anwendung eines aktiven DOAS Geräts auf Vulkanfahnen konnte BrO am Masaya auch nachts quantifiziert werden. Ein deutlicher Tagesgang wurde gefunden in dem die höchsten Konzentrationen mittags auftraten, während sie nachts unterhalb der Nachweisgrenze lagen. Dieser Befund deutet auf eine photochemische Bildung von BrO in Vulkanfahnen hin. Schließlich wurde ein Strahlungstransportmodel benutzt um die Wege von Photonen in passiven Fernerkundungsmessungen zu simulieren. Die Ergebnisse zeigen, dass eine ungenaue Beurteilung von Photonenwegen in Vulkanfahnen zu großen Fehlern in den Messungen führen kann. Ein Korrekturalgorithmus wird vorgestellt, mit dem auch zum ersten Mal Aerosolbedingungen in Vulkanfahnen durch DOAS Messungen bestimmt werden können.

Spectroscopic measurements of volcanic gas emissions in the ultra-violet wavelength region

In this thesis, three new remote sensing instruments were designed and applied to characterize volcanic gas plumes: a passive scanning differential optical absorption spectrometer (DOAS), an active Long-Path DOAS, and an SO_2-camera. Using the passive DOAS, sulfur dioxide (SO_2) emission fluxes were successfully quantified at 6 volcanoes. At Kilauea (Hawaii), e.g., elevated fluxes were measured in March 2008, an indication of an upcoming eruption which occurred just weeks later. Halogen chemistry in volcanic plumes was also studied. Bromine monoxide (BrO) was positively detected at Stromboli (Italy), Popocatépetl (Mexico) and Masaya (Nicaragua) volcanoes. By applying an active DOAS system to volcanoes for the first time, BrO measurements were conducted at night at Masaya. A distinct diurnal cycle was found in which the highest concentrations were present around local noon while they were below the detection limit at night, a strong indication that BrO is photochemically formed in volcanic plumes. Finally, radiative transfer modeling was used to simulate the optical paths of photons during passive remote sensing measurements. The results show that an inaccurate assessment of radiative transfer can induce large errors in these measurements. A correction algorithm is presented that for the first time allows the retrieval of aerosol conditions in volcanic plumes from DOAS measurements.

Table of Contents

1 Introduction

Humans have always been fascinated by volcanoes, but the importance of volcanism for the Earth as it exists today extends far beyond human history. After the Earth was formed some 4.6 billion years ago, its glowing surface consisted of molten rock extending hundreds of kilometers down. The Earth's atmosphere is thought to have formed as a result of the release of trapped volatile compounds from this layer. Therefore, the early atmosphere of the Earth was likely a mixture of CO_2, nitrogen, and water vapor, with trace amounts of hydrogen, a mixture similar to that emitted by present day volcanoes (*Seinfeld and Pandis 2006*). The composition of the present atmosphere is very different. A large part of the water vapor has since condensed out of the atmosphere to form the oceans. After being dissolved in the ocean, most of the emitted CO_2 formed sedimentary carbonate rocks. Only nitrogen, which is chemically inert, non-soluble in water, and non-condensable, remained to form the modern atmosphere's most abundant constituent.

Oxygen in the earth's atmosphere is almost exclusively a product of photosynthesis. Before 2.5 billion years ago, the Earth's atmosphere lacked oxygen. As oxygen-producing cyanobacteria evolved, oxygen levels slowly increased (e.g. *Lyons 2007*). Interestingly, a temporal discrepancy between the first noticeable trace of persistent atmospheric oxygen (approximately 2.5 billion years ago, *Bekker et al. 2004*) and the oldest molecular fossils indicating the presence of cyanobacteria (approximately 2.7 billion years old, *Brocks et al. 1999*) exists. To sustain vanishingly low oxygen levels despite near-modern rates of oxygen production for about 200 million years requires that oxygen sinks must have been much larger during this period than they are now. *Kump and Barley 2007* suggest that reduced gases emitted from volcanoes on the sea floor (especially H_2 and H_2S) formed this sink. The authors show that the abundance of submarine volcanoes abruptly diminished 2.5 billion years ago while at the same time eruptions on land became more common as the continents became larger and more stable. Volcanism occurring on land is dominated by oxidized gases such as CO_2, which are much less able to consume atmospheric oxygen.

Volcanism was likely also a driving factor in the historical evolution of the Earth's climate. A link between a major volcanic event and a period of global warming was recently reported by *Storey et al. 2007*, who show that abrupt rise in sea surface temperature, ocean acidification

and deep-sea warming associated with the Paleocene-Eocene thermal maximum 55 million years ago (*Kennett and Stott 1991*) were likely caused by a period of massive volcanic eruptions along the east coast of Greenland and in the western British Isles. During this period of intense volcanism, large amounts of the greenhouse gases carbon dioxide and methane were emitted into the atmosphere from degassing lava flows (about 10 million cubic kilometers of magma were brought to the surface) and the heating of sediments rich in organic compounds.

Carbon dioxide is released from the solid earth to the atmosphere and ocean by volcanoes and metamorphism at a rate estimated by *Holland 1978* to be $3.3 \pm 1.1 \times 10^{14}$ g(CO_2)/a. This flux is large enough to double the amount of carbon in the atmosphere and ocean in only approximately 400,000 years in the absence of a sink. However, CO_2 is returned to the solid earth at an approximately equal rate over geologically significant periods through the chemical weathering of silicate minerals followed by the deposition of carbonate minerals in sedimentary rocks. The general process can be summarized as the reaction of silicate mineral with carbon dioxide and water to yield a carbonate mineral and silica. However, it remains unresolved how an equilibrium between CO_2 fluxes in and out of the atmosphere was maintained over millions of years. As one possible explanation, *Walker et al. 1981* suggest that the atmospheric CO_2 abundance is buffered by a negative feedback mechanism in which the rate of weathering of silicate minerals depends on surface temperature which in turn depends on atmospheric CO_2 abundance through the greenhouse effect. However, *Raymo et al. 1988* suggest that the silicate weathering rate and therefore the atmospheric CO_2 abundance depends mainly on orographic effects. Because fresh materials are exposed to weather during periods of orogeny and runoff is generally higher in mountainous areas, the authors postulate that the rate of silicate weathering is higher during periods of rapid uplift. While a negative feedback mechanism is missing in this hypothesis, *Edmond and Huh 2003* argue that pre-industrial atmospheric CO_2 was not in equilibrium with the solid earth, but instead at a 'kinetic minimum'. The authors suggest that at present, the Himalayan-Tethyan mountain range has an almost infinite capacity to absorb any CO_2 released from the mantle or by organic carbon oxidation over geological timescales. Besides chemical weathering and orographic effects, recent studies have emphasized the roles of vegetation (e.g. *Berner 1991*) and lithological changes (e.g. *Dessert et al. 2001*) to the historical evolution of atmospheric CO_2.

These studies show how important volcanoes have been in the past during the formation of the Earth's atmosphere and climate system. Aside from these long-term repercussions, however, volcanoes also have noticeable influence on the modern day atmosphere and climate. Examples include tropospheric cooling caused by volcanic sulfate aerosol from major eruptions (e.g. *Robock 2000*) or the destruction of ozone by halogen emissions of volcanic origin (e.g. *von Glasow et al. 2008*). These and other implications of volcanic gas emissions for the global atmosphere are discussed in chapter 2 of this thesis.

In human history, volcanism has always been a fascinating but dangerous phenomenon. The violence, duration and far-reaching effects of very large Plinian volcanic eruptions (named

after Pliny the Younger, a philosopher of ancient Rome who described the A.D. 79 eruption of Vesuvius in which his uncle, Pliny the Elder perished) have had long-lasting consequences for human communities, decimating populations in proximal areas and driving large-scale migrations of survivors (e.g. *Oliver-Smith 1996*). Due to the awesome and often terrifying nature of volcanic disasters, historical volcanic eruptions have in the past raised existential questions that altered religious beliefs, symbols and rituals, and have provoked extreme ritual reactions (see e.g. *Cashman and Giordano 2008*). A tragic example was the summer of prayer held by the Sanpoil and Nespelem Indians of northeast Washington and Idaho, USA, in response to large-scale volcanic ash fall in the early 19th century, likely a product of an eruption of Mt. St. Helens (*Cashman and Cronin 2008*). Unfortunately, the affected tribes failed to perform normal food-gathering tasks and therefore triggered a high mortality rate the following winter.

In fact, extreme ritualistic responses to volcanic eruptions were not unusual. While the local populations around the ~ 900 BP Sunset Crater eruption in the American Southwest made offerings of maize cob (*Ort et al. 2008*), the aboriginal people of Nicaragua believed that the persistent lava lake within Masaya Volcano's crater provided evidence that Masaya was a god who needed to be placated by human offerings (*Viramonte and Incer-Barquero 2008*). Similarly, when western people of Christian religion first observed this lava lake, they interpreted it as the "mouth of Hell", a belief that contributed to the justification of the religious conquest of America by the Europeans (*Viramonte and Incer-Barquero 2008*).

Of fundamental importance in all historical human responses evoked by confrontation with volcanic activity is the need for individuals and societies to make sense of the event (*Oliver-Smith 1996*). In this respect, this thesis can be considered the continuation of a search for answers to questions that have existed in the minds of human beings for millennia. Thankfully, technology has evolved rapidly in the last decades, and we now have a multitude of techniques available for characterizing volcanic activity in addition to visual observation.

The inherent challenge that the field of volcanology brings with it is that it is almost always impossible to measure a volcanic process directly. This is because volcanism is a phenomenon of superlatives – taking place over geological timescales at extreme temperatures kilometers below the Earth's surface, volcanic processes are not easily accessible to the interested observer. Instead, the products of volcanic activity are measured, be they certain types of seismic activity, ground deformation, or gases emitted at the surface. Finding the links between volcanic processes of geological nature and measureable products can be considered the main mission of experimental volcanology. Several such known links related to the field of volcanic gas emissions measurements are summarized in chapter 2.

The extreme conditions and high risk associated with making measurements at volcanoes greatly limits the measurement techniques suited for application to such environments. One breakthrough in the field of gas emissions quantification and characterization was the adaptation of the Differential Optical Absorption Spectroscopy (DOAS) technique (*Perner and Platt 1979*) to volcanoes. This contact-free remote sensing technique allows the detection and quantification of trace gases with characteristic absorption cross-sections in the ultra-

violet, visible, and near infra-red wavelength ranges without the need to take samples from inside the medium of interest (in this case the volcanic plume). Today, DOAS instruments (see *Platt and Stutz 2008* for a general overview) are used to measure volcanic emissions from the ground, from the air, and from space. The theory, instrumentation and measurement concepts applied during DOAS measurements at volcanoes are described in the first part of chapter 3.

The immediate success and extensive implications of the first DOAS measurements at volcanoes (see e.g. *Galle et al. 2003*, *Bobrowski et al. 2003*) led to the concept of installing a volcanic emissions monitoring network based on the DOAS technology at volcanoes all over the world. Named the Network for Observation of Volcanic and Atmospheric Change (NOVAC) this EU-funded project was begun in 2005 with the main goal of using volcanic gas emissions data provided by permanently installed DOAS sites for volcanic risk assessment and eruption prediction. Although the project is still ongoing and is funded until 2010, it has already been a great success with numerous achievements in many different fields, the most important of which are described in a short summary of the project given in chapter 5.

As this thesis was conducted within the scope of the NOVAC project, many of the performed tasks are directly linked to technological and scientific challenges posed by the work plan. For example, a highly versatile passive scanning DOAS instrument was designed and built specifically for the long-term monitoring of volcanic gas emissions. Secondly, measurement geometries were developed for the quantification of a number of different parameters such as gas emission flux, chemical plume composition, wind speed, and even aerosol conditions. Also, novel data retrieval concepts were developed and old ones were improved upon to enable the accurate evaluation of these measurements. All of these technical aspects are described in chapter 3 of this thesis with the exception of the aerosol retrievals. These are presented in the scope of a separate study on radiative transfer in volcanic environments in chapter 8.

Besides the DOAS technique, several other spectroscopic measurement methods can be used to characterize volcanic emissions. The application of Fourier Transform Infra-Red (FTIR) spectrometers to volcanic environments has e.g. greatly furthered our knowledge of plume composition and chemistry (see e.g. *Oppenheimer et al. 1998a, Horrocks et al. 2001*). More recently, the ability to measure the large SO_2 abundances present in many volcanic plumes with a simple UV band-pass filter and a two-dimensional CCD has been demonstrated (*Mori and Burton 2006, Bluth et al. 2007*). In chapter 4, a theoretical description of the functionality of the so-called SO_2-camera is given. Several potential problems are pointed out and quantitatively examined after which the design of a new SO_2-camera is presented. This camera was built and applied for SO_2 measurements at Mt. Etna in 2007 and 2008 (also see *Kick 2008* and *Wöhrbach 2008*).

To date, instrumentation developed in the scope of the NOVAC project has been installed at 19 volcanoes around the world. The installation sites are listed in the first part of chapter 5. Of these, five volcanoes were selected for comprehensive measurements using the advanced

NOVAC mark II instruments designed and built in the scope of this thesis: Stromboli (Italy), Popocatépetl (Mexico), Mt. Etna (Italy), Piton de la Fournaise (Réunion Island, France) and Tungurahua (Ecuador). The four installations carried out within this thesis in cooperation with the respective local volcano observatories are each described in the ensuing sections of chapter 5. Also, several example measurements are given to illustrate the potential of these instruments.

A unique opportunity presented itself in March of 2008, when degassing activity at Kilauea Volcano (Hawaii, USA) was unusually high during the attendance of a conference in Honolulu. Although time was limited, a short stopover on the Big Island of Hawaii allowed a snapshot of gas emissions to be taken. Only two weeks after the measurements were made, an explosive eruption occurred at Halema'uma'u crater, the first since 1924. Therefore, although few in number, the performed gas measurements are presented in detail in chapter 6 to possibly allow insights into processes leading up to the eruption.

The passive DOAS instruments that are today widely applied to measure volcanic gas emissions use solar radiation scattered in the atmosphere as a light source. While the measurement geometries of these instruments are extremely versatile during the day, one obvious disadvantage of the technique is the inability to measure at night. As a number of important chemical processes in volcanic emission plumes are driven by photolysis, the chemical characteristics of these plumes are different at night than during the day. To overcome this obstacle, a mobile active Long Path DOAS suitable for operation in remote volcanic environments was designed and built in the scope of this thesis. Its instrumental setup and technical specifications are described in chapter 3. Using an artificial light source (either a xenon arc lamp or UV-LED) it was then applied at Masaya Volcano (Nicaragua) and Mt. Etna (Italy) to measure the abundance of the halogen oxides BrO, ClO and OClO both at day and, in the case of Masaya, also at night with a higher sensitivity than previously achieved. A number of novel insights into the heterogeneous formation process of halogen oxides were obtained, and are presented in chapter 7.

As the NOVAC project progressed and more and more volcanoes were equipped with DOAS instrumentation, the great importance of an accurate measurement error budget assessment was recognized. Several error sources were identified including errors in spectroscopy, wind speed determination, measurement geometry, and possibly most importantly the influence of unknown radiative transfer on the measurement results. To date, all passive DOAS measurements of volcanic emission fluxes have been evaluated under the assumption that radiation was scattered in the atmosphere behind the plume and has traveled through it in a straight line. While valid for cases in which the instrument is close to the volcanic plume and aerosols both in and around the plume are negligible, this assumption certainly does not hold true for condensing plumes or measurements conducted at large distances from the plume. In the final stages of this thesis, a study of the radiative transfer in and around volcanic plumes was conducted using the three-dimensional radiative transfer model TRACY-II (*Deutschmann 2008*). Based on the strong absorption of SO_2, a method was established with which the measured column densities could be corrected for errors induced by unknown radiative

transfer. In fact, the first case studies presented in chapter 8 show that the method is not only useful for accurate trace gas measurements. It can also be applied to retrieve the aerosol abundance in volcanic plumes from DOAS spectra and therefore represents a breakthrough in volcanic emissions measurement technology.

Due to the extensive nature of this manuscript and the fact that a number of fairly independent studies were conducted, this thesis is written in a modular fashion in which each chapter is fairly self-contained and speaks for itself. At the same time, the interested reader is of course referred to other chapters for more comprehensive discussion where appropriate. In chapter 9, the most important results obtained in the scope of the thesis are summarized once more, and a short outlook is given into future perspectives in the field.

2 The importance of volcanic gas emissions in atmospheric chemistry and volcanology

In this thesis, the measurement of volcanic gas emissions using UV-spectroscopic techniques is discussed in detail. After covering instrumental aspects such as the technical implementation of new instrumentation (section 3.5 and chapter 4), measurement concepts using a variety of different techniques (sections 3.2 and 3.3), and data evaluation procedures (sections 3.1 and 3.4), the results of various volcanic emissions measurements are shown (chapters 5 - 8). The characterization of volcanic gas emissions is motivated by two main issues. For one, volcanic degassing has a potentially considerable impact on atmospheric chemistry, both in the troposphere (quiescent degassing) as well as in the stratosphere (major eruptions). On the other hand, both the absolute magnitude and relative speciation of gas emissions can give insights into volcanic processes occurring at depth, and therefore represent parameters useful for volcanic hazard assessment and eruption prediction. Both of these aspects are briefly described in this chapter.

2.1 The importance of volcanic gas emissions for atmospheric chemistry

Large explosive volcanic eruptions can cause major climatic perturbations when considerable amounts of ash and sulfate are transported to high altitudes, as was e.g. the case after the eruption of Mt. Pinatubo (Philippines) in 1991 (e.g. *McCormick et al. 1995*). The responsible processes are relatively well understood (see e.g. *Robock 2000*). However, the impact of quiescent degassing, which is similar to explosive eruptions in total flux when averaged over time (e.g. *Halmer et al. 2002*) on the chemistry of the troposphere has only recently become the topic of ongoing research. Especially since the detection of highly reactive halogen species in volcanic plumes both in the in troposphere (*Bobrowski et al. 2003*) and in the

stratosphere (*Theys et al. 2009*), the long-held assumption that volcanic plumes are relatively chemically inert has been disproven. The potential impact that these plumes could have on the chemistry of the atmosphere is described in the following.

2.1.1 Atmospheric chemistry and transport

One key distinction between the ambient atmosphere and the chemistry occurring in volcanic conduits is that the atmosphere is an oxidizing environment, while volcanic conduits generally exhibit very low oxygen levels (e.g. *Sigurdsson et al. 2000*). Once emitted into the atmosphere, volcanic sulfur emissions are therefore eventually oxidized to sulfate and carbonaceous compounds are oxidized to CO_2 unless these species are removed from the atmosphere via deposition processes first. Here, both wet and dry deposition on the ground as well as scavenging by aerosols and water droplets play an important role. The most important atmospheric oxidant is the hydroxyl radical (OH). OH is predominantly formed via the photolysis of ozone (O_3) and subsequent reaction of the excited oxygen atom with water vapor.

$$O_3 + h\,v \rightarrow O_2 + O(^1D) \qquad \textbf{R. 2.1}$$

$$O(^1D) + H_2O \rightarrow 2\ OH \qquad \textbf{R. 2.2}$$

The OH radical is sometimes referred to as the "detergent of the atmosphere" (*Crutzen 1996*), as it removes virtually all gases of natural and anthropogenic origin from the atmosphere. Aside from being a precursor for OH (R. 2.1, R. 2.2), the role of O_3 in atmospheric chemistry is manifold, with both positive and negative effects. On the one hand, the O_3 layer in the stratosphere acts as a shield for harmful UV-radiation, thus making non-maritime life on earth possible. On the other hand, O_3 in the troposphere is harmful to human health and vegetation. In the free troposphere, O_3 acts as a greenhouse gas. No significant direct sources of O_3 are known. The stratospheric O_3 layer is formed by photolysis of oxygen molecules O_2 by deep UV radiation ($\lambda < 240$ nm). In the troposphere, the photolysis of NO_2 is held largely responsible for the production of O_3.

$$NO_2 + h\,v \rightarrow NO + O(^3P) \qquad \textbf{R. 2.3}$$

$$O(^3P) + O_2 \rightarrow O_3 \qquad \textbf{R. 2.4}$$

Due to the role of nitrogen oxides as O_3 precursors, there is strong scientific interest in the understanding of NO_x chemistry in the atmosphere ($NO_x = NO + NO_2$). In Fig. 2.1, a schematic depicting the various reaction cycles responsible for O_3 production in the troposphere is shown. Again, photolysis plays an important role, as is the case for many of the reactions determining the state of the atmosphere at any given time. At night, chemical conditions in the atmosphere can be quite different. In the presence of NO_x, the NO_3 radical, which is rapidly photolyzed during the day, can take the place of OH as the major oxidative species in the troposphere at night (see e.g. *Geyer 2000*). A drastic difference between

daytime and nighttime chemistry was also observed for halogen chemistry in volcanic plumes (see chapter 7).

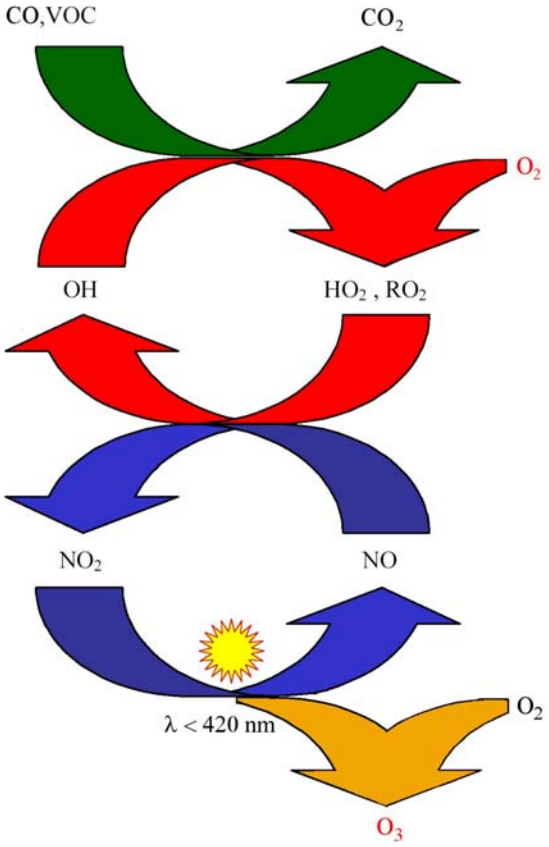

Fig. 2.1 – Simplified schematic of the ozone production cycle in the troposphere. OH radicals oxidize carbonaceous compounds and form HO_2 (Hydroperoxyl) or equivalent radicals. These in turn oxidize NO to NO_2, which is photolyzed at wavelengths below 420 nm (R. 2.3). The resulting free oxygen atom quickly recombines, often with an oxygen molecule, in which case O_3 is formed (R. 2.4).

As mentioned above, volcanic emissions can influence the lowest two layers of the atmosphere: the troposphere and the stratosphere. The troposphere spans the lowest approximately 10 km of the atmosphere. It is capped by the so-called tropopause, a strong and therefore very stable temperature inversion. All weather takes place in the troposphere. The lowermost kilometer or so of the troposphere is well-mixed, a result of the heating of the earth's surface by incident solar radiation. It is called the planetary boundary layer (PBL). Above the tropopause, the stratosphere is characterized by a positive vertical temperature gradient and therefore a strong stratification. It spans from the tropopause to about 50 km altitude. Only large explosive volcanic eruptions can emit gas and ash into the stratosphere.

Aside from chemical reactions, both horizontal and vertical transport affects the distribution of individual species in the atmosphere. Depending on which layer of the atmosphere is considered, typical transport times are very different. In the PBL, vertical transport and

mixing occurs on time scales around one hour. Above the PBL, vertical transport in the free troposphere is generally slower, with the exception of transport associated with convective systems such as thunderstorms, or associated with frontal systems. Horizontal transport times in the troposphere are about two months for transport from mid latitudes to the tropics, approximately 4 weeks for meridional transport around the globe, and on the order of one year from transport from one hemisphere to the other (e.g. *von Glasow et al. 2008*). If typical wind speeds of 10 to 20 m/s are assumed in the free troposphere, a rough estimate immediately shows that volcanic emissions can travel as much as 900 to 1800 km per day, and deposition of volcanic compounds (e.g. acids) can therefore occur at great distances from the source.

The mixing of volcanic plumes with background air is an important phenomenon when discussing plume chemistry, as species of volcanic origin can only react with (typically oxidizing) atmospheric compounds after sufficient mixing has taken place. In large explosive eruptions that reach the stratosphere, the volcanic gas and ash can be dispersed around a latitude band on time scales on the order of weeks. While the dispersion of plumes from eruptions at high latitudes is contained in a relatively narrow latitudinal band, plumes emitted into the stratosphere near the equator can quickly be dispersed over a large latitude range. Recent satellite measurements of the eruption of Kasatochi volcano in August of 2008, which was ranked 4 on the non-linear Volcanic Explosivity Index (*Newhall and Self 1982*), nicely demonstrate dispersion of a stratospheric plume at high latitudes (see Fig. 2.2 and *Richter 2008*). The massive amount of SO_2 injected into the stratosphere (*Carn 2008* estimated a total burden of approximately 1.5 Tg) makes the plume visible to satellite instrumentation for weeks.

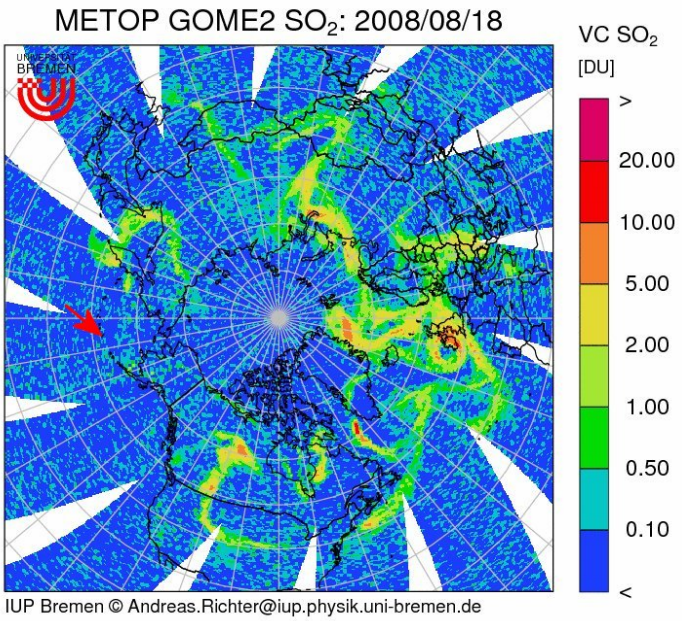

Fig. 2.2 – Vertical column of SO_2 over the north pole as measured by the GOME2 instrument on board the METOP satellite on August 18, 2008, ten days after the eruption of Kasatochi Volcano (position indicated by a red arrow). (Adapted from *Richter 2008*)

For plumes from quiescently degassing volcanoes that are emitted into the PBL or free troposphere, turbulent dispersion is responsible for the mixing with ambient air in the vicinity of the active vent. Here, dispersion is dominated by local wind fields and atmospheric stability. However, once a plume has entered the unperturbed free troposphere, dispersion becomes much slower and is dominated by vertical and horizontal wind shear which often leads to vertically thin horizontal filaments. These thin layers can survive in the atmosphere for days or even weeks (see Fig. 2.3 and *Zerefos et al. 2006*), but will eventually become indistinguishable through ever stronger filamentation or even molecular diffusion (unless mixed by a convective system).

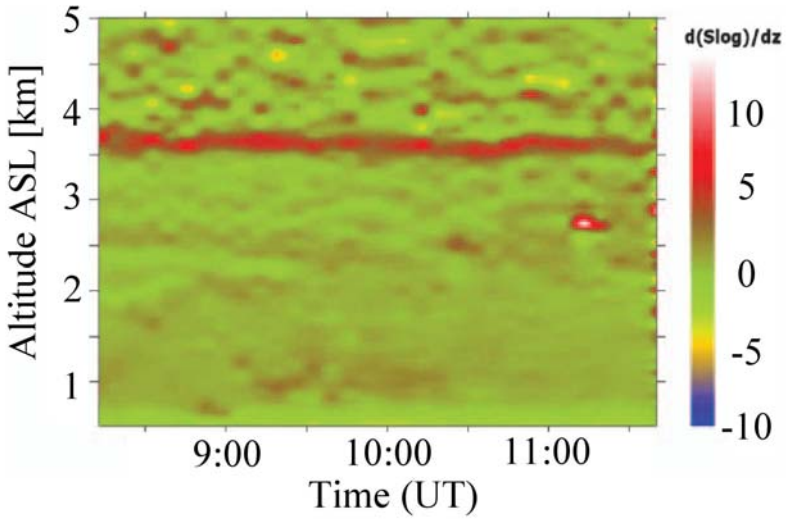

Fig. 2.3 – Backscattered LIDAR radiation as a function of altitude and time during measurements by *Zerefos et al. 2006* in Athens on July 26, 2001. The plume of Mt. Etna passed over the instrument on this day, and it is clearly visible as a thin layer of enhanced aerosol load spanning only about 200 m in height with a base at 3.5 km. (Adapted from *Zerefos et al. 2006*)

2.1.2 Volcanic gas composition

Volcanic emissions played a key role in forming the early atmosphere of the Earth. The main emitted compounds are, in order of descending magnitude, water vapor, CO_2, SO_2, H_2S, HCl, HF, H_2, CO and HBr (see Tab. 2.1), but a number of other compounds are also emitted in lower abundances. The volcanic input of CO_2 into the atmosphere (approximately 2.4×10^{13} g(C)/a as estimated by *Kerrick 2001*) is orders of magnitude below the current anthropogenic input of about 7×10^{15} g(C)/a (*IPCC 2007*). Furthermore, although water vapor is the most abundant gas species emitted by volcanoes, the global emissions are again negligible when compared to the global evaporation from oceans and lakes. A more detailed description of the composition of volcanic plumes is e.g. given in *Gerlach 2004, Textor et al. 2004, Pyle and Mather 2009*.

Species	H_2O	CO_2	SO_2	H_2S	HCl	HF	HBr	COS	CS_2
Composition [%/vol]	50-90	1-40	1-25	1-10	1-10	$<10^{-3}$	?	10^{-4}-10^{-2}	10^{-4}-10^{-2}
Global Flux [Tg/a]	?	75	1.5-50	1-2.8	0.4-11	0.06-6	0.0078-0.1	0.006-0.1	0.007-0.096

Tab. 2.1 – Typical composition of volcanic gases at the emission vent and estimated global source strengths according to *Textor et al. 2004*.

Once emitted into the atmosphere, volcanic volatiles are very rapidly diluted to about 1:1,000 or 1:10,000 by mixing with ambient air. This can e.g. be observed in SO_2 measurements. In the case of quiescent degassing, strong dilution has often already occurred at the crater rim. From an atmospheric chemistry perspective, two different types of measurements are of interest: For one, determining the total flux of individual volcanic compounds into the atmosphere allows insights into the global impact of volcanoes on atmospheric chemistry. However, the measurement of the relative plume composition is also important, as inferences about the ongoing chemistry inside the respective plume can be made on the basis of such measurements (see chapter 7). Of course, the relative plume composition also depends on magma composition and volcanic processes occurring at depth, and this fact can sometimes be used in volcanic risk assessment (see section 2.2 and e.g. *Aiuppa et al. 2007b*). For the characterization of the relative plume composition, it is useful to relate the abundances of individual species to that of a relatively stable species, which is thereby used as a tracer. SO_2 is often used to this extent, as its stable on the order of many hours in non-condensing volcanic plumes (*McGonigle et al. 2004*).

2.1.3 The effects of volcanic eruptions on stratospheric chemistry and climate

Large-scale explosive volcanic eruptions that that emit gas into the stratosphere have a direct (albeit short-term) impact on climate. When large amounts of ash and sulfur (particulate and SO_2, which is later oxidized to sulfate) are injected into the stratosphere, they effectively reflect solar radiation which directly leads to a cooling of the lower atmosphere. After the Mt. Pinatubo eruption in June of 1991, in which about 20 Tg of SO_2 where emitted into the stratosphere (*Bluth et al. 1992*), the Earth's global surface temperature was e.g. reduced by about 0.4°C for the year after the eruption, and 0.25°C for the following year. At the same time, absorption on aerosols and ash heated the lower stratosphere by about 1.5 °C the year after the eruption (*Parker et al. 1996*).

Together with other compounds of non-volcanic origin, volcanic aerosols (especially sulfur) are the basis for formation of the so-called Junge layer (*Junge et al. 1961*), an aerosol layer that spans the entire globe at an altitude of about 20 km. Aside from reflecting sunlight,

aerosols in this layer also provide a surface for heterogeneous chemical reactions to occur on, many of which are involved in catalytic ozone destruction (see e.g. *Brasseur et al. 1999*). According to model studies by *Brasseur and Granier 1992*, the injection of aerosols from the Mt. Pinatubo eruption might have led to a depletion in ozone concentrations by up to 50% at 20 km altitude, an effect that lasted for more than a year at high latitudes.

The magnitude of the volcanic input of halogens (mainly HCl) into the stratosphere is widely debated and uncertain. *Tabazadeh and Turco 1993* suggest that less than 1% of the HCl emitted from volcanoes has a chance to reach the stratosphere, as it is very efficiently removed by precipitation. This finding is consistent with the limited or unobservable changes in stratospheric HCl after the 1991 Mt. Pinatubo eruption reported by *Mankin et al. 1992, Wallace and Livingston 1992*. On the other hand, model simulations by *Textor et al. 2003* suggest that more than 25% of the total HCl emitted by volcanoes could indeed reach the stratosphere. However, the authors state that more than 90% of the HCl is scavenged by ice particles in the eruptive column during ascent. While these particles do reach the stratosphere, their fate depends on the volcanic and environmental conditions, and effective sedimentation could quickly remove the dissolved gases again.

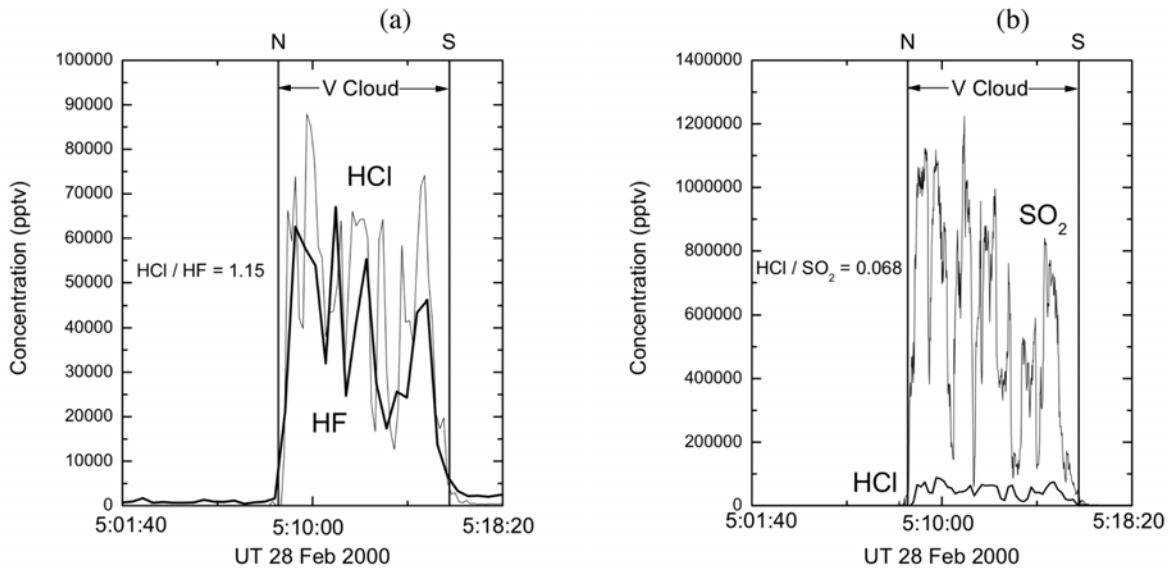

Fig. 2.4 – (a) Mixing ratios of HCl and HF measured by a chemical ionization mass spectrometer during an aircraft transect of the plume of Hekla Volcano (Iceland) on February 28, 2000. Up to 87 ppb of HCl were observed. (b) Mixing ratios of SO_2 and HCl for the same transect. (Adapted from *Rose et al. 2006*)

The only direct observations of enhanced halogen concentrations in the lower stratosphere as a result of volcanic degassing were made in the plume of Hekla Volcano (Iceland) in February of 2000 (*Rose et al. 2006*). In this case, SO_2, HCl and HF as well as particle concentrations were strongly enhanced compared to background values (Fig. 2.4). Furthermore, chemical

modeling suggests that volcanic water vapor and nitric acid promoted the formation of polar stratospheric clouds (PSCs). The authors state that these PSCs are likelt to have activated volcanic halogens and produced more than 2 ppb of ClO_x, which in turn destroyed ozone at a previous point in time (very low ozone levels were measured). It has to be stressed, however, that the current levels of halogens in the stratosphere are mainly caused by the decomposition of anthropogenic chlorofluorocarbons (CFCs), halons, and other gases of non-volcanic origin. While large-scale, explosive volcanic eruptions could lead to short-term, local ozone destruction, the "ozone hole" phenomenon, as it is observed in the Antarctic spring, is mainly a result of anthropogenic chlorine and bromine emissions (*WMO 2007*).

2.1.4 The effects of volcanic eruptions on tropospheric chemistry

Sulfur compounds

Volcanoes are strong emitters of sulfur compounds. The importance of these species lies in their conversion to acids which are later deposited downwind of the volcano, as well as in the radiative effects of sulfate aerosol. As mentioned in section 2.1.3, sulfate aerosol has a direct effect on climate, as sulfate aerosol in the stratosphere scatters solar radiation back to space, thus cooling the Earth's surface. However, indirect aerosol effects are also known. The number and size of cloud condensation nuclei (CCN) present in a cloud determine its radiative parameters, especially the single scattering albedo (SSA). Also, the precipitation rate and lifetime of a cloud are influenced by the size of the individual droplets. Sulfate aerosol provides additional CCN, thus reducing the average particle size, and enhancing the average lifetime of a cloud. At the same time, the SSA is enhanced, thus the cloud is "whiter" and radiation is more effectively backscattered (e.g. *Twomey 1974*). A perfect example of these effects was recently observed for interactions of a volcanic plume with clouds in the marine boundary layer at Mt. Michaels on Saunders Island in the South Atlantic Ocean by *Gasso 2008* (see Fig. 2.5).

Sulfur is emitted in a variety of species from volcanic vents. The most important sulfurous gases are SO_2, hydrogen sulfide H_2S, carbonyl sulfide COS and carbon disulfide CS_2 (see Tab. 2.1). In addition to these gaseous species, sulfate aerosol SO_4^{2-} is also prominent in many very young plumes (e.g. *Allen et al. 2002, Allen et al. 2006*) and is therefore either a primary volcanic emission compound, or is formed very quickly in volcanic plumes. The presence of this highly acidic aerosol is responsible for a possible release of reactive halogen compounds to the gas phase, as is described farther down.

As the atmosphere is oxidizing, all emitted sulfur species will eventually be oxidized to sulfate unless previously deposited on the ground. The oxidization of SO_2 to H_2SO_4 via the reaction with OH is slow in the gaseous phase, however, occurring only on timescales of several weeks (*Blitz et al. 2003*). Once formed, H_2SO_4 is very efficiently taken up by aerosol and cloud particles, and can also lead to the formation of new particles and CCN. If taken up to particles such as these, SO_2 can be oxidized much more efficiently than in the gas phase by reactions with O_3, H_2O_2, HOC, HOBr, and by oxygen if iron and manganese are available as

catalysts (see e.g. *Vogt et al. 1996, Seinfeld and Pandis 2006*). This reduces the atmospheric lifetime of SO_2 from weeks to days. The lifetime of H_2S with regard to oxidization by OH is about 70 h (*Cox and Sheppard 1980*), but can be shorter in the presence of halogens (see *Aiuppa et al. 2007a*). After passing several intermediate stages, it is eventually oxidized to SO_2. The atmospheric lifetime of CS_2 in regard to oxidization by OH is about 120 h (*Murrells et al. 1990*), with oxidation leading either to COS or SO_2. As COS is very stable in the troposphere but is rapidly photolyzed by deep UV radiation in the stratosphere, it is one of the main sources of sulfur for the stratospheric Junge layer (see section 2.1.2). The direct emissions strengths of COS and CS_2 from volcanoes are relatively poorly constrained, as shown in Tab. 2.1 and further discussed by *Halmer et al. 2002*.

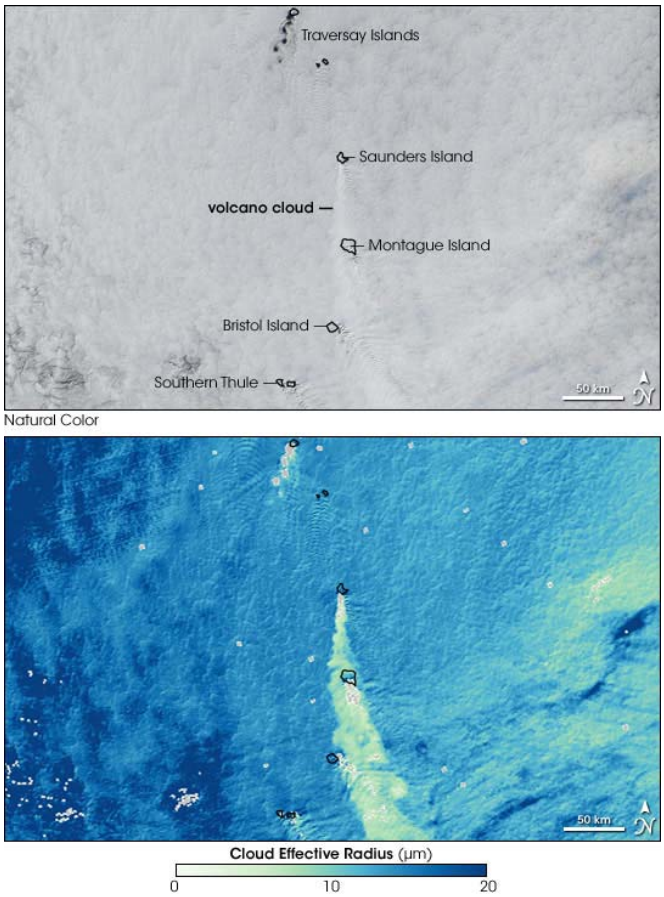

Fig. 2.5 – Natural color satellite image of a volcanic plume emitted into the marine boundary layer on April 27, 2006 (top). The plume originates from Mt. Michael on Saunders Island, located in the South Atlantic Ocean. It is clearly whiter (and therefore has a higher albedo) than the surrounding cloud cover. The bottom image shows the cloud effective radius calculated from data recorded by the MODIS instrument on board NASA's Aqua satellite. A significant decrease in cloud droplet size can be observed in the volcanic plume, as sulfate aerosols act as cloud condensation nuclei, thus forming a larger number of smaller dropplets than is the case for the background load of mainly marine aerosols surrounding the plume. (Adapted from *Gasso et al. 2008*)

Globally, most sulfur of volcanic origin is thought to be emitted as SO_2 (see Tab. 2.1). Volcanoes are believed to be responsible for approximately 10% of the global SO_2 flux into the atmosphere (*Brasseur et al. 1999*) and about 20% of the natural SO_2 emissions. The oceans are arguably the largest natural source of sulfur to the atmosphere, emitting both dimethylsulfide (DMS) and COS, which can subsequently be oxidized to SO_2 and SO_4^{2-}), The large variability in source strength from volcano to volcano as well as changes in over time as a result of different levels of volcanic activity lead to a large fluctuation of annual sulfur fluxes (*Andres and Kasgnoc 1998* reported between 1.5 and 50 Tg(SO_2)/a). *Halmer et al. 2002* estimate an average total sulfur flux of between 7.5 and 10.5 Tg(S)/a, with 60% of this flux originating from explosive eruptions and 40% the result of quiescent degassing. While only responsible for a fraction of the total sulfur flux, *Graf et al. 1997* argue that the contribution of volcanic SO_2 to the atmospheric burden of sulfate aerosol and its radiative effects (described earlier in this section) could be much higher than the comparison of total source strength to that of anthropogenic sources suggests. As most volcanoes effectively emit into the free troposphere where atmospheric lifetimes of the sulfur species are much longer than in the PBL, where the anthropogenic emissions take place, the volcanic gas emissions likely have longer atmospheric residence times and a stronger influence on climate.

The second most abundant sulfur compound is H_2S. On global average, the SO_2/H_2S ratio is thought to be around 10 (*Berresheim et al. 1995*), but ratios at individual volcanoes can vary considerably between about 1 and 125 (*Gerlach 2004*). Due to instrumental restrictions, it is difficult to measure H_2S and SO_2 simultaneously in the same air mass. *Aiuppa et al. 2007a* used diffusions tubes to measure the two compounds as a function of distance from the crater of Mt. Etna and found a more or less constant ratio between the two species indicating similar atmospheric loss rates due to deposition and chemical processing. This is surprising, as model results by the authors predicted a much stronger H_2S loss due to halogen chemistry, and points to open questions regarding the interaction of H_2S with halogens.

Acid deposition

In the vicinity of actively degassing volcanoes, a portion of the emitted acidic compounds are deposited to the ground. This is a cause of immediate health risks to humans and animals, and is detrimental for vegetation (see e.g. *Delmelle et al. 2002*). In fact, *Delmelle et al. 2001* found that 10% of the total SO_2 and HCl emitted from Masaya Volcano (Nicaragua) were deposited within a 44 km radius of the active vent. At Mt. Etna (Italy), *Aiuppa et al. 2004a* found dry deposition rates of 2.5-75 t/d for SO_2, 0.6-17 t/d for HCl, and 0.02-0.6 t/d for HBr.

Acid rain is also a widespread phenomenon in areas influenced by volcanic gas emissions. *Harding and Miller 1982* measured a very low pH of 3 in rainwater 800 meters downwind of the passively degassing Kilauea Volcano (Hawaii) summit vent. At 11 km distance, an average pH of 4.2 was measured, which was the normal value measured on the island in precipitation uninfluenced by volcanic emissions. Model calculations by *Kajino et al. 2004* suggest that the annual mean pH in precipitation in Japan decreased by between 0.3 and 1.0 due to volcanic sulfate from the eruption of Miyakejima Volcano (Japan) during its 2001 and

2002 eruptions. A review of environmental effects caused by the deposition of acids in the vicinity of volcanoes is given by *Delmelle 2003*.

Halogen species

Compared to other known sources, the volcanic fluxes of HCl, HF and HBr are very large (see *Pyle and Mather 2009*). While it has been known for some time that these gases are important for the acidity budget of the atmosphere, they were assumed more or less chemically inert until *Bobrowski et al. 2003* detected BrO in the plume of Soufrière Hills Volcano (Montserrat). The estimated mixing ratios of 1 ppb are the highest ever detected in the atmosphere. Since this detection, BrO has been measured in the plume of a number of volcanoes around the world including Ambrym, Vanuatu (*Oppenheimer et al. 2006a*), Kasatochi, USA (*Theys et al. 2009*), Masaya, Nicaragua (*Bobrowski and Platt 2007, Kern et al. 2008a*), Mt. Etna, Italy (*Bobrowski 2005, Oppenheimer et al. 2006b, Bobrowski and Platt 2007*), Nyiragongo, D.R. Congo (*Galle et al. 2005*), Sakurajima, Japan (*Lee et al. 2005*), Stromboli, Italy (*Bobrowski and Platt 2007*) and Villarica, Chile (*Bobrowski and Platt 2007*). Measured BrO/SO_2 ratios were typically between 10^{-3} and several 10^{-5}, as is e.g. shown in Fig. 2.6.

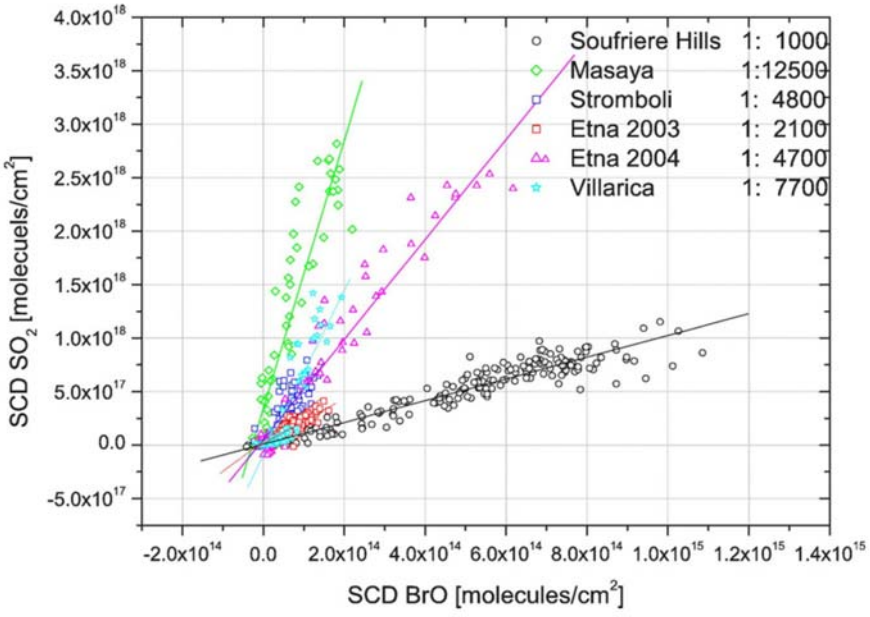

Fig. 2.6 – BrO/SO_2 ratios measured by *Bobrowski and Platt 2007* at five different volcanoes. The highest BrO/SO_2 ratio (10^{-3}) was seen at Soufrière Hills volcano (Montserrat), and corresponds to a BrO mixing ratio on the order of 1 ppb. (Adapted from *Bobrowski and Platt 2007*)

It has been suspected for some time that BrO is not a primary product emitted from volcanoes, but rather that it is mainly formed by the reaction of magmatic gases with atmospheric components mixed into the plume (*Bobrowski et al. 2003, Gerlach 2004, Martin et al. 2006,*

Oppenheimer et al. 2006b). Here the oxidation of HBr in the plume, which in turn leads to enhanced levels of reactive Br radicals as well as the photochemically active precursors Br_2 and BrCl seems to play a prominent role. Recent model results (*Bobrowski et al. 2007*) suggest that the peak in the BrO/SO_2 ratio may occur 2 to 3 hours after emission from the crater (see Fig. 2.7). The exact timing of BrO formation in the plume, however, is likely influenced by bromine speciation at the vent and by the abundance of additional species such as HO_x, NO_x and ClO_x (*Roberts et al. 2008*).

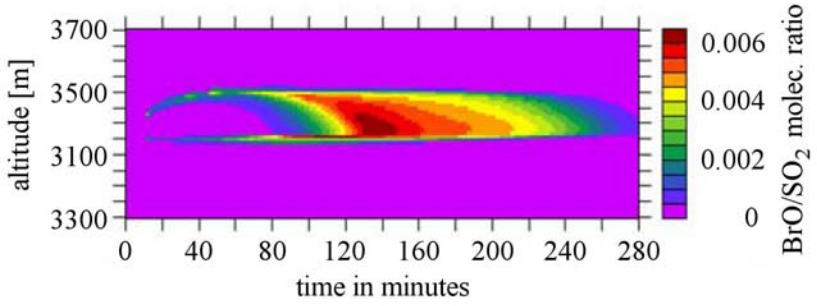

Fig. 2.7 – MISTRA Model simulation of the BrO/SO_2 ratio in the plume of Mt. Etna (Italy) by *Bobrowski et al. 2007*. The plume is emitted 11 minutes after the model start at 3340 m. The model is initiated with an effective source region gas composition of 60% volcanic gas and 40% ambient air at a temperature of 600°C. This model run best matched observations at Mt. Etna. A peak in the BrO/SO_2 ratio can be observed approximately 2 hours after emission. (Adapted from *Bobrowski et al. 2007*).

The postulated formation mechanism for BrO is similar to the so-called "bromine explosion" that has been suggested to explain high abundances (up to several ppt) of BrO in polar regions (see e.g. *Platt and Lehrer 1997, Wennberg 1999, Platt and Hönninger 2003, Bobrowski et al. 2007, Kaleschke et al. 2007, Simpson et al. 2007, von Glasow and Crutzen 2007*). In this mechanism, bromine is deposited to airborne aerosol particles in the form of HOBr and HBr. Here, an acid catalyzed reaction takes place in the aqueous phase, and Br_2 is released back to the gaseous phase where it is quickly photolyzed (during the day). Single Br atoms then react with ozone to form BrO. If BrO is photolyzed, the free oxygen atom recombines with O_2 to form O_3. However, the self reactions (R. 2.10 and R. 2.11) convert BrO back to Br or Br_2 without forming O_3. The net effect is a catalytic O_3 destruction. The reaction mechanism is shown in detail below and in Fig. 2.8. It is picked up again is slightly simplified form in chapter 7.

$HOBr_{(gas)} \rightarrow HOBr_{(aq)}$ **R. 2.5**

$HBr_{(gas)} \rightarrow Br^-_{(aq)} + H^+_{(aq)}$ **R. 2.6**

$HOBr_{(aq)} + Br^-_{(aq)} + H^+_{(aq)} \rightarrow Br_{2(gas)} + H_2O$ **R. 2.7**

$Br_2 + h\nu \rightarrow 2\ Br$ **R. 2.8**

$Br + O_3 \rightarrow BrO + O_2$ **R. 2.9**

$BrO + BrO \rightarrow 2\ Br + O_2$ **R. 2.10**

$BrO + BrO \rightarrow Br_2 + O_2$ **R. 2.11**

$BrO + HO_2 \rightarrow HOBr + O_2$ **R. 2.12**

It is important to note that both O_3 and HO_x must be present for BrO to be produced efficiently. As volcanic plumes are thought to contain very little if any O_3 at the point of emission, this is one reason why BrO/SO_2 ratios should increase as ambient air containing O_3 is mixed into the plume (see *Oppenheimer et al. 2006b, Bobrowski et al. 2007*). In recent measurements of the 2D distribution of the BrO/SO_2 ratio in the plume of Mt. Etna applying the Imaging DOAS technique (*Bobrowski et al. 2007, Louban et al. 2009a*), the authors report an apparent enhancement of the ratio towards the plume edges. This is interpreted as an effect caused by a higher availability of O_3 in these regions of the plume.

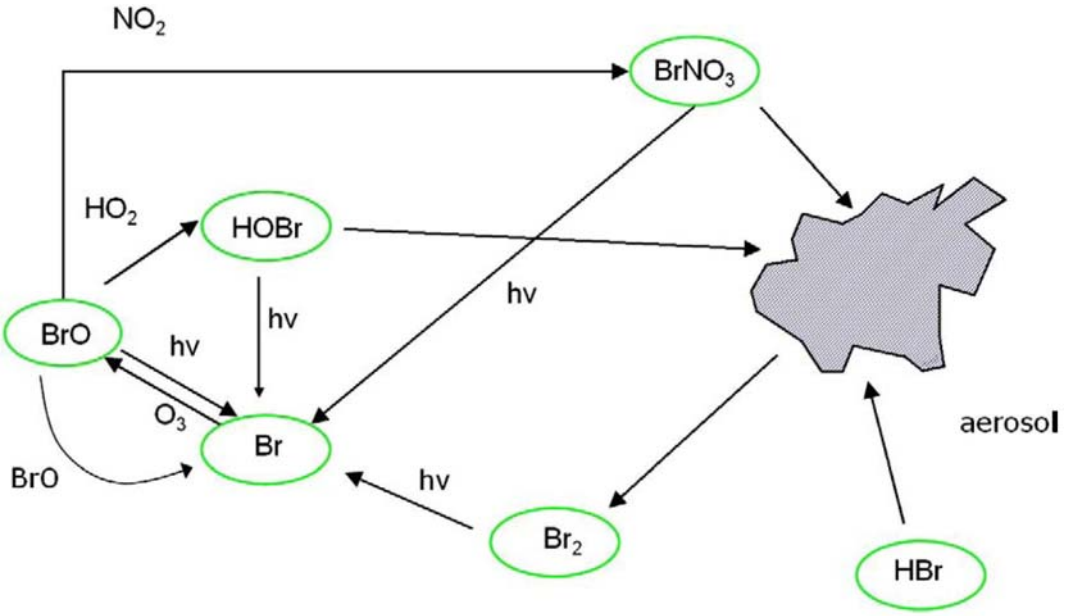

Fig. 2.8 – Schematic of the reactions involved in the conversion of HBr to BrO and the destruction of O_3 in the gaseous phase. (Adapted from *von Glasow et al. 2008*)

Aside from O_3, HO_x is also a necessary compound for the recycling of BrO to HOBr (R. 2.12) and back into the aerosol phase (R. 2.5), where it can release additional HBr (R. 2.7). As HO_x is a product of photolysis, it is only available in significant amounts during the daytime. The photolysis of Br_2 in R. 2.8 also requires incident solar radiation. Therefore, the BrO formation mechanism, as it is described here, will only work during the day, not at night. In the scope of this study (also see *Kern et al. 2008a*), the application of an active DOAS system at volcanoes for the first time enabled the quantification of BrO both at day and during the night. The results, which are described in detail in chapter 7, showed that BrO concentrations clearly follow the diurnal variation of incident solar irradiance, thus confirming this formation mechanism.

Also, the role of the chlorine oxides ClO and OClO in volcanic plume chemistry is not well understood to date. While recent passive DOAS measurements have detected ClO and OClO at various volcanoes (*Bobrowski 2005, Lee et al. 2005, Bobrowski et al. 2007*), model predictions by *Bobrowski et al. 2007* could not reproduce these measurements. By again applying the active DOAS technique and moving to wavelengths below those available in the spectrum of incident solar radiation, the detection limit for ClO could be reduced by more than an order of magnitude as compared to previous, passive DOAS measurements. However, ClO could not be detected, possibly indicating a technical problem with previous ClO measurements and pointing towards the model results. Details are again given in chapter 7. In any case, it is clear that the chemistry of chlorine is very different from that of bromine, as HCl that is taken up by aerosols or cloud droplets is fairly unreactive and can not be released in the same way as bromine is released during the bromine explosion.

While iodine compounds are emitted from volcanoes, the source strength is much weaker than that of the other halogens (see e.g *Aiuppa et al. 2008*). For measurements at Mt. Etna, *Aiuppa et al. 2005* estimate that the total flux of iodine is less than 1% of the bromine flux. Iodine oxides have yet to be detected in a volcanic plume, but they are known to play an important role for the ozone budget in other regions of the atmosphere such coastal regions, salt lakes, and coastal Antarctica (see e.g. *von Glasow and Crutzen 2007* for a review).

Behind HCl, HF is the second most abundant hydrogen halide in volcanic gas emisssions (see Tab. 2.1). However, the chemical processing of HF in the atmosphere is very limited. HF is very effectively taken up onto aerosols and cloud droplets. It is therefore an important source of acidity in the liquid phase, and is a relevant contributor to the deposition of acids in the proximity of actively degassing volcanoes (see above). However, it does not play an important role in chemical reactions in the atmosphere.

However, the impact of the other halogen species on tropospheric chemistry is prominent. It has already been shown that BrO can effectively destroy O_3 in the presence of incident solar radiation (R. 2.8 - R. 2.11). While O_3 destruction in volcanic plumes is arguably a local or at most regional effect, model studies by *von Glasow 2008* suggest that volcanic plumes could be depleted in O_3 for several days after being emitted into the atmosphere. It is unclear whether halogens emitted from volcanoes could significantly contribute to a steady atmospheric background of between approximately 0.5 and 2 ppt BrO in the free troposphere

(*Van Roozendael et al. 2002*). While this background is relatively low and close to the detection limit of most instrumentation, model calculations by *von Glasow et al. 2004* indicate that it could lead to an average ozone reduction of up to 20% compared to a halogen-free scenario. Aside from destroying ozone, halogen chemistry is also responsible for a reduction in O_3 production, as it interferes with the NO_x cycle shown in Fig. 2.1. Also, the ratio of the radicals HO and HO_2 is perturbed, and hypohalic acids (HOBr, HOCl) contribute to the formation of sulfate in aqueous particles (see e.g. *von Glasow and Crutzen 2007* for more details).

Other compounds

It has already been mentioned in section 2.1.1 that nitrogen oxides are very important in atmospheric chemistry. Usually associated with anthropogenic combustion processes, NO_x emissions have also been observed at volcanoes. Based on DOAS measurements of NO_2, *Oppenheimer et al. 2005* estimate that Mt. Erebus Volcano (Antarctica) could represent a NO_x source with a total flux of at least 600 t(N)/a, making it by far the largest source on the Antarctic continent. During earlier measurements performed by *Hobbs et al. 1982*, the authors found NO_2 mixing ratios of up to 280 ppb in the plume of Mt. St. Helens during its 1980-1981 eruptions. This was elevated by far above the measured background of less than 10 ppb. Extrapolation yielded an estimated momentary flux of about 70 t(N)/a, although this value was only sustained during the period of strong volcanic activity. Nitric acid (HNO_3) , the oxidation product of NO_2, was measured at Masaya Volcano (Nicaragua) by *Mather et al. 2004* using impregnated filters. They estimate a global source of HNO_3 from quiescently degassing volcanoes of around 20-60 Gg(N)/a.

However, the origin of NO_x in volcanic plumes is still uncertain. Studies by *Huebert et al. 1999* and *Mather et al. 2004* suggest the Zeldovich mechanism, which is responsible for NO_x formation in combustion processes, as a likely source of NO_x in volcanic emissions. In this mechanism, however, the NO_x formation rate is primarily a function of temperature and the residence time of nitrogen at that temperature (see e.g. *Annamalai and Puri 2006*). More recent model calculations by *Kaschka et al. 2009* indicate that a mix of volcanic volatiles and ambient air would need to be kept at magmatic temperatures for an extended period of time (many minutes) to explain several hundred ppt of NO_2. This is unlikely in volcanic systems, as even in the presence of a lava lake, ambient air is typically only heated to high temperatures for very short times (order of seconds).

Mercury is a toxic compound that has a number of different natural and anthropogenic sources. Gaseous elemental mercury is its most prevalent chemical state in the atmosphere. In this state, Hg is fairly unreactive with an atmospheric lifetime of about 1 year (*Ariya and Peterson 2005*). If oxidized, however, it becomes readily bio-available and is toxic for humans and biota (see e.g. *Schroeder and Munthe 1998*). Total mercury emissions from volcanoes are believed to be in the range of about 1-800 t(Hg)/a (see e.g. *Niragu and Becker 2003, Pyle and Mather 2003*). In a study conducted at Mt. Enta (Italy) by *Bagnato et al. 2007*, only about 1% (by mass) of emitted mercury was found to be in particulate form, and elemental mercury was by far the most abundant species. The authors estimate that emissions

from Mt. Etna make up about 5% of the total mercury emissions in the Mediterranean. However, studies in polar regions have shown that bromine explosion events were often correlated with mercury depletion in the atmosphere (*Schroeder et al. 1998*). This correlation is likely the result of the oxidation of Hg by Br atoms and BrO radicals in a process similar to the ozone destruction described by R. 2.8 - R. 2.11 (see *Steffen et al. 2008* for a review). As volcanic gases often include much higher amounts of BrO than is found in the Arctic, it is unclear whether volcanoes truly represent a net source of Hg, or whether the net effect is that of a scrubber, removing Hg from the atmosphere (see *von Glasow et al. 2008*).

In conclusion, volcanic emissions obviously have a considerable impact on various aspects of atmospheric chemistry and climate. The spatial and temporal variability of source strengths makes extrapolating global emissions from measurements at a handful of volcanoes very difficult, as is evident in the large uncertainties associated with global flux estimates for the individual species. This was one motivation for setting up a global network of volcanic gas emission measurements, as performed in the scope of the Network for Observation of Volcanic and Atmospheric Change (NOVAC, see section 5.1). Also, the improvement of satellite technology (especially in regard to spatial resolution) in recent years is helping to better constrain global source strengths for compounds such as SO_2, BrO, and volcanic ash (e.g. *Carn et al. 2005, Khokhar et al. 2005, Prata et al. 2009, Theys et al. 2009*). Aside from total fluxes, many of the chemical processes occurring in and around volcanic plumes are also not yet well constrained, and further measurements are needed to fully understand the total impact of volcanic emissions on the atmosphere.

2.2 The importance of gas emissions in volcanology and volcanic risk assessment

Aside from the importance for atmospheric chemistry, the assessment of volcanic gas composition and total source strength has become a tool used to gain insights into volcanic processes. Both the emission flux and the composition of volcanic emissions can be seen as a "telegraph from the deep", at times allowing inferences about processes occurring many kilometers below the surface of the earth. In this section, a short introduction will be given into the importance of SO_2 emission flux measurements and relative halogen abundance for the field of volcanology will be given. The introduction is limited to SO_2 and halogens in volcanic plumes, as these gases can be measured with the UV-spectroscopic techniques applied in the scope of this thesis (see chapters 3 and 4). However, other species also are of great importance to volcanologists in understanding the chemistry, geology and hazards associated with volcanoes. For a detailed treatise on this subject, see e.g. *Oppenheimer et al. 2003*.

2.2.1 SO_2 emission fluxes

Behind water vapor and CO_2, SO_2 is typically the third most abundant species in volcanic emission plumes (see Tab. 2.1). In contrast to the other two components, the atmospheric background of SO_2 is negligible compared to the concentrations found in the plumes of actively degassing volcanoes. As chemical conversion and deposition processes are fairly slow, SO_2 can usually be regarded as a passive tracer for the first few hours after emission into the atmosphere (see section 2.1.1 and e.g. *McGonigle et al. 2004*). These properties along with its detectability by spectroscopic remote sensing instruments in both the UV and IR wavelength ranges make it a perfect proxy for assessing the momentary gas emission strength of a volcano.

Various techniques exist to measure total SO_2 flux with remote sensing instruments. Typically, a cross-section of the plume is integrated perpendicular to the wind direction using either a traverse or scanning geometry. The thus integrated SO_2 amount is then multiplied by the wind speed to obtain the emission flux. These methods are described in detail in chapter 3.3. Emission fluxes of other compounds are often obtained by measuring both SO_2 and the species of interest with an in-situ instrument, and subsequently extrapolating the flux based on the ratio of this species to SO_2 (see e.g. *Gerlach et al. 2002, Niragu and Becker 2003*).

Through measurements of gas fluxes from volcanoes, insights can be gained into magmatic-hydrothermal systems below the surface. For open-vent volcanoes, the emission rates of volatile species are closely related to magma supply and transport to regions near the surface, and to the dynamical processes responsible for degassing (e.g. *Stevenson and Blake 1998*). Therefore, gas fluxes vary over time. Low frequency variations on the order of months to years are often related to magma intrusion and volatile depletion by degassing (e.g. *Ripepe et al. 2002, Badalamenti et al. 2004*), while high frequency fluctuations are typically related to shallow processes occurring near the surface of the conduit system (e.g. *Lautze et al. 2004*). In some cases, SO_2 emissions can be indicative of lava effusion rates (e.g. *Delgado Granados et al. 2001, Sutton et al. 2001*).

However, magma does not necessarily have to reach the surface for degassing to occur. Volatiles can be released whenever the concentration of a species in magma exceeds its solubility. Volatile solubility is a function of confining pressure and therefore depth. Therefore, a species can be degassed whenever magma reaches a depth shallow enough for degassing of that species to occur. This can e.g. lead to convection in volcanic conduits, in which gas-rich magma rises in the conduit, degasses, and the denser gas-depleted magma sinks back down to deeper regions (see Fig. 2.9 and e.g. *Kazahaya et al. 1994, Kazahaya et al. 2004*). Convection typically leads to steady, quiescent degassing without a need for any amount of lava to be erupted.

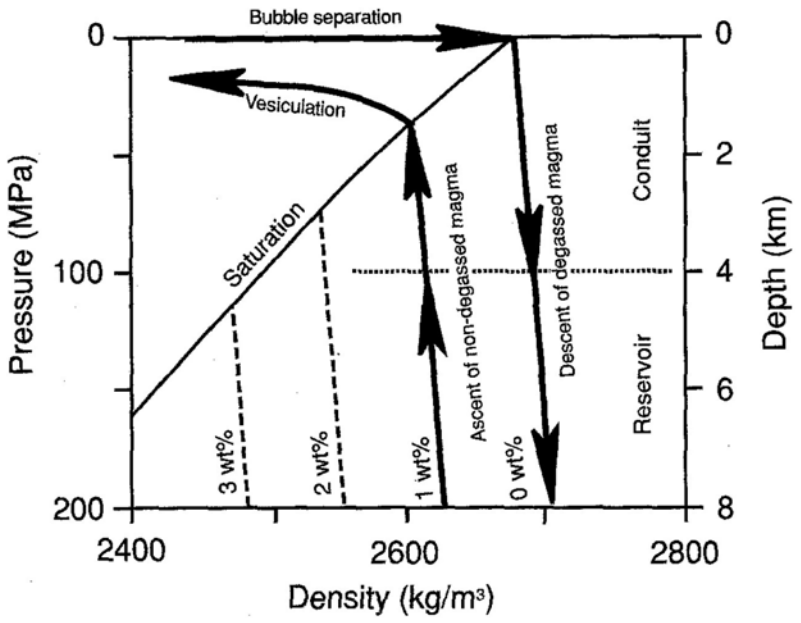

Fig. 2.9 – Density of ascending, non-degassed magma and descending, degassed magma as a function of depth in an exemplary convective volcanic conduit system. Arrows show the path of magma in the convective system. Theo dotted lines depict the water content of magma in weight %. (Figure from *Kazahaya et al. 1994*).

In some cases, volcanic degassing can show a certain degree of periodicity (e.g. *Watson et al. 2000, Fischer et al. 2002, Sweeney et al. 2008*), thus opening the possibility of implementing predictive approaches. From a standpoint of volcanic hazard assessment, one of the most important applications of measured SO_2 emission fluxes is the attempt to forecast possible eruptions, or at least to assess the general risk emanating from a volcano at a certain point in time. First success in this direction was made in predicting activity that followed the catastrophic eruption of Mount St. Helens in May of 1980 (*Casadevall et al. 1983*), after *Malinconico 1979* had reported an apparent increase in SO_2 prior to eruptions of Mt. Etna in July/August of 1977. A similar example was the eruption of Santa Anna volcano in El Salvador, where SO_2 fluxes increased by an order of magnitude from several hundred to several thousand tons per day shortly before and during the volcanic crisis of 2005 (*Olmos et al. 2007*, see Fig. 2.10). Helping to predict this eruption was the first significant output of the NOVAC project (see section 5.1).

Often, however, the simple relationship between an increase in SO_2 flux and eruption of a volcano does not hold true. Ideal open vent volcanic systems which contain magma-air interfaces through which gas can pass undisturbed to the atmosphere are rare. Most volcanic systems are more complex, with gas passing through a more or less fractured volcanic edifice from which numerous reactions can result (e.g. *Andres et al. 1993*). In such systems, an increase in SO_2 emission rates can indicate that SO_2 is rising to lower confining pressures, and that cracks have formed in the carapace covering the magma chamber (*Stoiber et al. 1983*), or an increasing magma supply from depth (*Edmonds et al. 2003b*). On the other hand,

chemistry occurring in magmas at depth can also influence the emission rate, especially when interaction with a hydrothermal system occurs (e.g. *Edmonds et al. 2003a, Edmonds et al. 2003b, Rodríguez et al. 2004*).

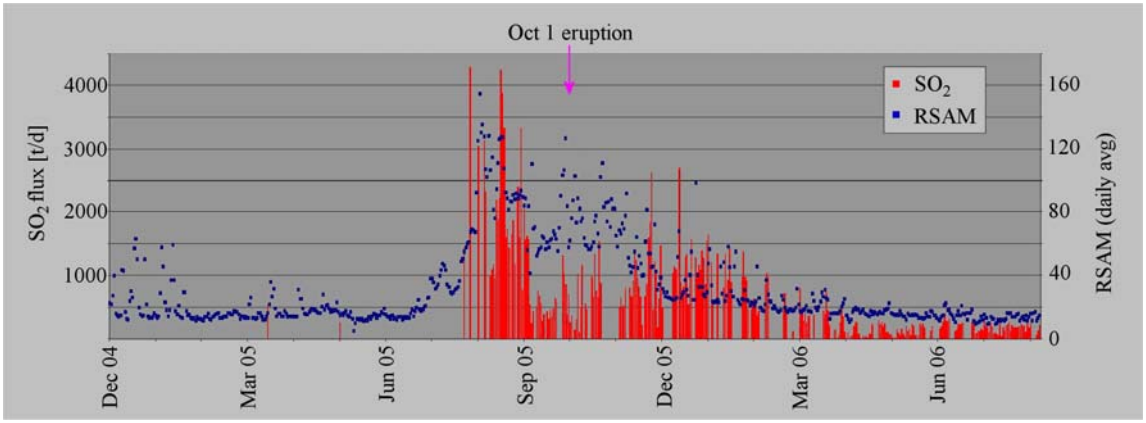

Fig. 2.10 – Real-time seismic amplitude (RSAM, see e.g. *Endo and Murray 1991*) (blue dots) and SO_2 emission fluxes (red bars) from Santa Ana Volcano (El Salvador) between December 2004 and August 2006. Both RSAM and SO_2 flux showed a considerable increase 2 months before the October 1, 2005 eruption. The measurements enabled a timely evacuation of thousands of inhabitants of nearby communities (Adapted from *NOVAC 2006*, also see *Olmos et al. 2007*).

As volcanic systems are generally complex, it is often impossible to constrain inferences made from a single monitoring technique. Therefore, a multi-parameter monitoring approach is necessary, coupled with the implementation of numerical models attempting to link observations with volcanic processes occurring at depth. Seismicity and degassing are often correlated as enhanced seismicity can e.g. indicate magma intrusion and lead to a higher gas permeability in the conduit area (see Fig. 2.10 and e.g. *Williams-Jones et al. 2001, Arciniega-Ceballos et al. 2008*). Deformation and tilt measurements (e.g. from space born interferometers or ground based GPS networks) can add information as to the nature of gas emissions (e.g. *Watson et al. 2000, Werner et al. 2008*), as can thermal monitoring of volcanoes (e.g. *Harris et al. 2005, Johnson et al. 2005*). Finally, looking at not only the magnitude of volcanic gas emissions but also the speciation and its evolution over time can give insights into the responsible volcanic processes occurring at depth. A brief overview is given in the next section.

2.2.2 Relative halogen abundances

From the standpoint of atmospheric chemistry, halogens in volcanic plumes are of special interest because highly reactive halogen species have a large impact on the oxidative capacity of the air (see section 2.1). However, halogen degassing also allows insights into volcanic processes and in some cases can also be useful for risk assessment and eruption prediction.

The halogens F, Cl, Br, and I have all been detected in volcanic gas plumes in the past (see Tab. 2.1 and e.g. *Aiuppa et al. 2005*). Halogens are mostly emitted in the form of hydrohalic acids HX (where X represents the halogen atom). The relative abundances of the individual compounds can vary strongly from volcano to volcano and over time, but while HF and HCl are typically emitted in similar concentrations, the abundance of HBr is about 2 orders of magnitude lower, and HI is approximately 4 orders of magnitude less common (*Textor et al. 2004, Aiuppa et al. 2005*).

While the total halogen flux is important for the acidity budget in a volcanic environment, variations in relative ratios of the individual halogens to one another and especially to SO_2, which is often used as a tracer for the total gas output (see section 2.1), can be indicative of certain types of volcanic activity (e.g. *Edmonds et al. 2001*). Based on previous findings by *Tazieff and Sabroux 1983* and *Pennisi and Le Cloarec 1998*, it has recently been shown that the halogen / sulfur ratio of volcanic gas can allow inferences about the depth at which degassing occurs. *Allard et al. 2005* measured the molecular ratios of CO_2/S and S/Cl using a Fourier Transform Infrared Spectrometer (FTIR). Their measurements show a significantly enhanced S/Cl ratio during episodes of violent lava fountaining from the south east crater of Mt. Etna (Italy) when compared to ratios in other etnean gas emissions. During magma ascent from depth, sulfur exsolves earlier and more extensively than chlorine (*Métrich et al. 2004*). A coexisting bulk gas phase thus evolves from very high S/Cl ratios at high pressure down to lower ratios (about 3 at Mt. Etna) during ascent to atmospheric pressure. As the observed lava fountaining was associated with enhanced S/Cl ratios, the authors argue that it must be driven by the gas exsolved (and possibly stored for some time) at depth rising through the magma column.

Burton et al. 2007a observed a similar behavior for slug-driven explosive activity at Stromboli Volcano (Italy) in 2002. Again, the SO_2/HCl ratio in gas slugs measured by FTIR spectroscopy was found considerably enriched compared to the typical Strombolian gas composition, thus indicating gas exsolution at depth. The authors followed up their measurements with model calculations in which the pressure-related evolution of H_2O, and CO_2 in the melt and in the gas phase was modeled for an assumed closed-system ascent from 280 MPa to the surface. Also inferred (with the help of melt inclusion data) were the amounts of S and Cl degassed during this process. The results (shown in Fig. 2.12) not only confirm the increase in S/Cl with increasing pressure and depth, but also allow an estimate of the depth at which the observed slugs originated. The observed SO_2/HCl ratios of between 4.5 for the most energetic slugs and 2.5 for slugs causing smaller explosions indicate gas exsolution is occuring between about 3 (violent explosions) and 0.8 km (smaller explosions) below the surface, or between the volcano-crust interface and the Tyrrhenian Sea level.

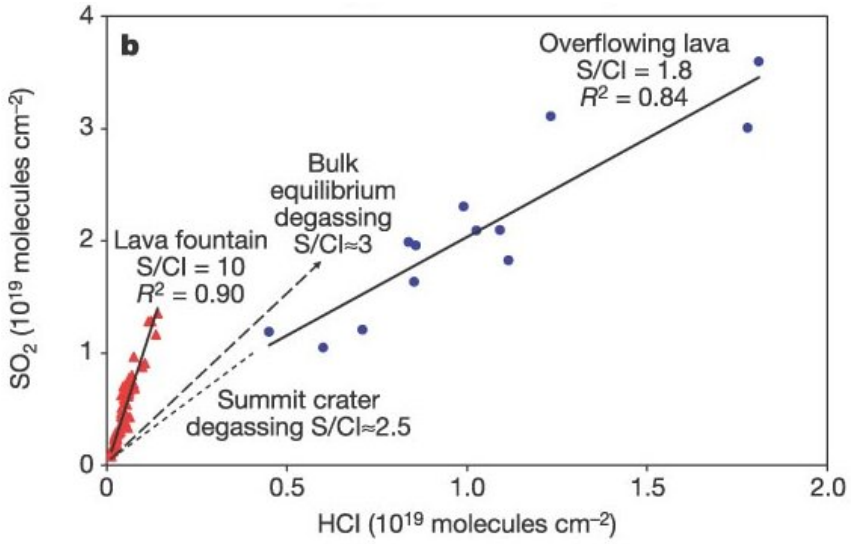

Fig. 2.11 – SO_2/HCl ratios measured at Mt. Etna's South East crater on June 14, 2000 by *Allard et al. 2005*. Typical equilibrium degassing has SO_2/HCl ratios of approx. 3 at Mt. Etna. However, the observed violent lava fountaining episodes exhibited a greatly enhanced ratio. This indicates these fountains are driven by gases exsolved at depth (aprox. 1.5 km), where Cl solubility in magma is higher than at low pressure near the surface. In comparison, fumes from overflowing lava in direct contact with the atmosphere are relatively depleted in SO_2 and enhanced in HCl.

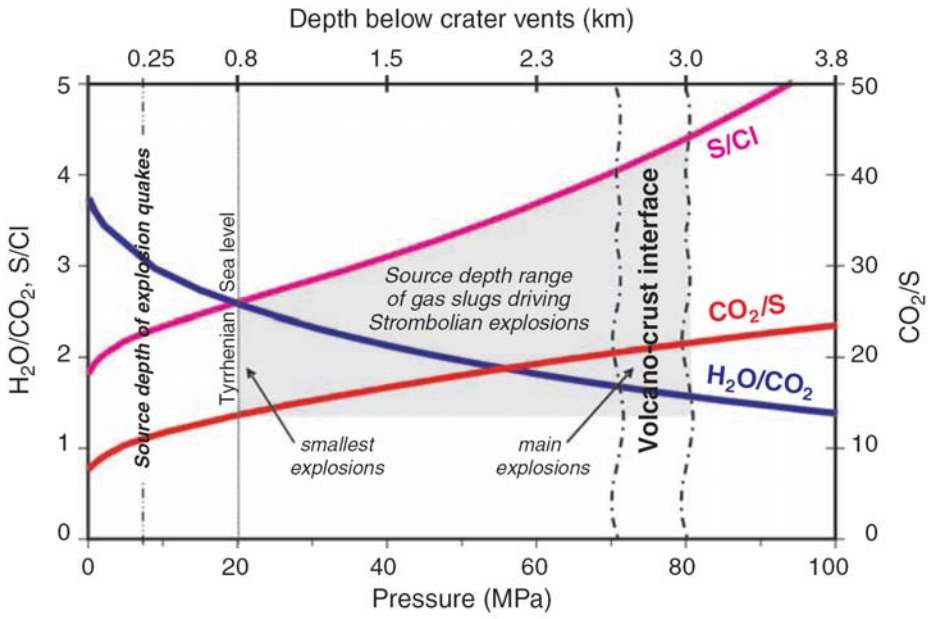

Fig. 2.12 - Pressure-related modeled evolution of H_2O/CO_2, CO_2/S, and S/Cl molar ratios in the magmatic gas phase during closed system ascent, differentiation, and degassing of Stromboli HK-basalt and inferred source depths of gas slugs driving Strombolian explosions. The measured CO_2/S and S/Cl ratios of gas slugs require their separate ascent from pressures of ~80 to 70 MPa to 20 MPa, or ~3 to 0.8 km depth below the vents. (from *Burton et al. 2007a*)

The results of these studies show that confining pressure and therefore depth significantly affect halogen sulfur ratios. However, it should be noted that other causes for variation in such ratios are also known and include the degree of degassing of shallow magma compared to degassing from depth (*Edmonds et al. 2001*) and the possible interaction with a hydrothermal system (e.g. *Villemant et al. 2005*).

In the above mentioned studies, the authors usually refer to Cl. This is due to the fact that, of the halogens, Cl is emitted in high abundance (in the form of HCl, see Tab. 2.1), and can be measured by multiple techniques (FTIR, volatile trap, filter pack). The second most abundant and most studied species is HF. *Edmonds et al. 2008* e.g. used the ratio of HCl/HF to gain insights into degassing depth of volatiles at Kilauea Volcano (Hawaii). Bromine, on the other hand, is less abundant and more difficult to measure. However, BrO is the halogen compound most accessible to the DOAS technique, which this study is centered around. BrO is not directly emitted from volcanoes in significant amounts, as described in section 2.1 and chapter 7. Instead HBr is the most common bromine species detected in volcanic plumes. *Gerlach 2004* measured HBr and HCl condensates at a range of volcanoes around the world. They report a mean HBr/HCl ratio of 0.0022, with a standard deviation 0.002.

Br and Cl are thought to behave similarly during most magmatic processes (*Villemant and Boudon 1999*), and likely degass more or less simultaneously under identical conditions (e.g. *Balcone-Boissard et al. 2009*), although the verification of this fact remains a bit uncertain, especially since Cl and F were found to behave somewhat differently (*Edmonds et al. 2008*). Even though the measured BrO abundance at a specific position in the plume depends significantly on environmental factors such as incident solar irradiance and ambient ozone concentration, the hope is that the BrO/SO_2 ratio in a volcanic plume can also be used as an indicator for volcanic processes at depth if the plume chemistry is well understood and accounted for. Significant progress in this direction was achieved by the DOAS measurements described in chapter 7 in combination with recent model studies by *Bobrowski et al. 2007, Roberts et al. 2008*. For a detailed review on the current state of knowledge regarding halogen degassing from volcanoes, see the upcoming special issue of Chemical Geology entitled "Halogens in Volcanic Systems" (introduction by *Aiuppa et al. 2008*).

3 Differential optical absorption spectroscopy

3.1 Principles

3.1.1 Atmospheric absorption spectroscopy

Absorption spectroscopy is based on the principle that molecules can enter excited states when irradiated by electromagnetic radiation. Electronic, vibrational, and rotational excited states exist, and molecules absorb radiation energy when entering them. As the energy levels of these states depend on the molecule type, every molecule absorbs light at distinct wavelengths. The absorption process is described by the Beer-Lambert Law of absorption:

$$I(\lambda) = I_0(\lambda)\cdot\exp\left(-\int_0^L\left(\varepsilon_R(\lambda,l)+\varepsilon_M(\lambda,l)+\sum_i\sigma_i(\lambda,p,T)\cdot c_i(l)\right)dl\right) \qquad \textbf{Eq. 3.1}$$

with
- $I(\lambda)$: light intensity after passing through the atmosphere
- $I_0(\lambda)$: intensity of the light source
- λ: wavelength
- $\varepsilon_R(\lambda,l)$: Rayleigh scattering coefficient
- $\varepsilon_M(\lambda,l)$: Mie scattering coefficient
- $\sigma_i(\lambda,p,T)$: absorption cross-section of the absorber i
- $c_i(l)$: concentration of the absorber i
- p: pressure
- T: temperature
- L: total light path length

The light intensity at a certain wavelength after passing through the atmosphere is determined by several factors. For one, two main types of broadband scattering occur. Rayleigh scattering describes the scattering of light on particles smaller than the wavelength. These are mostly air molecules and some small aerosol particles with spatial dimensions of less than about 0.1µm. The Rayleigh scattering coefficient ε_R is proportional to λ^{-4} in good approximation (*Hulst 1957*). The other scattering process is Mie scattering, which is the scattering on particles with spatial dimensions at or above the wavelength of the light. Such as aerosol particles, and cloud droplets. The Mie scattering coefficient ε_M is approximately proportional to $\lambda^{-1,3}$ (*Hulst 1957*).

Besides these two scattering processes, the radiative absorption by the individual atmospheric components determines the light intensity. As each molecule type *i* is characterized by the composition and configuration of its constituents, electronic and ro-vibronic states create a characteristic absorption cross-section σ_i. The measured absorption spectrum is composed of a unique linear combination of the individual trace gas absorption cross-sections, and therefore the concentrations of all absorbing compounds can be measured simultaneously.

However, this basic form of the Beer-Lambert Law cannot be applied to trace gas measurements in the atmosphere for several reasons. For one, it is nearly impossible to distinguish between the contributions of the different scattering processes in the atmosphere and broadband absorption of continuum bands of the absorbers. In fact, as the continuum bands of the individual absorbers feature no characteristic structures, distinguishing between them is impossible, as is the quantification of the individual contributions towards the measured total absorption. Also, applying the Beer-Lambert Law in its absolute form is made very difficult by the fact that a perfect spectral response is needed from the spectrometer and detector. The measurement results can easily be falsified if the detection sensitivity is wavelength dependant, and one does not correct for this effect.

All in all, these problems make absolute spectroscopy impossible in the atmosphere. However, Differential Optical Absorption Spectroscopy (DOAS) presents a solution to these difficulties.

3.1.2 Differential spectroscopy

Since broadband absorption caused by scattering processes in the atmosphere cannot easily be quantified, the DOAS technique divides the trace gas absorption cross-sections into two parts.

$$\sigma(\lambda) = \sigma_b(\lambda) + \sigma'(\lambda) \qquad \textbf{Eq. 3.2}$$

Here, σ_b characterizes the broadband scattering and absorption, while σ', often referred to as the differential absorption cross-section, describes the characteristic narrow band absorption structures of the individual trace gases. Using this principle, the exponent in the Beer-Lambert Law is split into two parts; one varying “slowly” with the wavelength and incorporating

broadband absorption and scattering, and one featuring a strong dependency on the wavelength due to narrow-band trace gas absorption. The Beer-Lambert Law can now be written as

$$I(\lambda) = I_0(\lambda)\cdot\exp\left(-\int_0^L\left(\varepsilon_R(\lambda,l)+\varepsilon_M(\lambda,l)+\sum_i\sigma_{b,i}(\lambda)\cdot c_i(l)\right)dl\right)$$

$$\cdot\exp\left(-\int_0^L\left(\sum_i\sigma_i'(\lambda)\cdot c_i(l)\right)dl\right) \qquad \textbf{Eq. 3.3}$$

For the sake of simplicity, the temperature and pressure dependency of the absorption cross-sections has been omitted, as they play a subordinate role for most absorbers in the lower parts of the atmosphere.

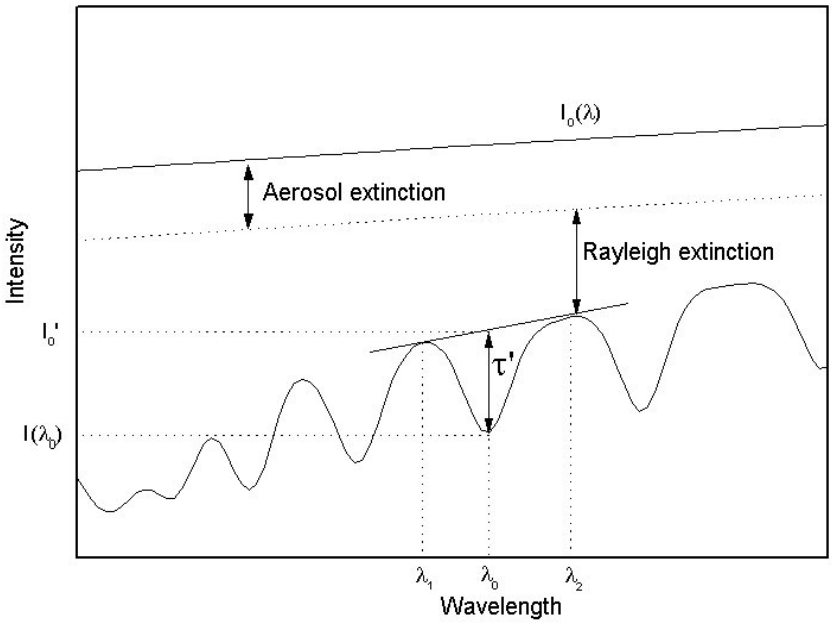

Fig. 3.1 – Contributions to the attenuation of radiation in the atmosphere. Aerosol scattering and Rayleigh scattering show broadband extinction only, while trace gas absorption causes narrow and broadband extinction.

The broadband part of Eq. 3.3 is then merged with the initial light intensity I_0 to form the differential baseline intensity I_0'.

$$I_0' = I_0(\lambda)\cdot\exp\left(-\int_0^L\left(\varepsilon_R(\lambda,l)+\varepsilon_M(\lambda,l)+\sum_i\sigma_{b,i}(\lambda)\cdot c_i(l)\right)dl\right) \qquad \textbf{Eq. 3.4}$$

Now, the Beer-Lambert Law can be formulated in the differential form applied by the DOAS technique.

$$\tau'(\lambda) = \ln\left(\frac{I_0'(\lambda)}{I(\lambda)}\right) = \int_0^L \left(\sum_i \sigma_i'(\lambda)\cdot c_i(l)\right) dl \qquad \textbf{Eq. 3.5}$$

$\tau'(\lambda)$ is referred to as the differential optical density, and can be considered the result of a DOAS measurement. $I_0'(\lambda)$ can be obtained in several different ways. For active Long-Path DOAS, $I_0(\lambda)$ is simply used in most cases, as it doesn't differ from $I_0'(\lambda)$ in narrow band structure. The differences are all of broadband nature, thus changing the absolute value of the quotient but leaving the relative depth of narrow band absorption structures unchanged. For light sources without narrow-band features (e.g. halogen lamps and some LEDs), $I_0'(\lambda)$ can alternatively be derived from the measured spectrum $I(\lambda)$ by applying a low-pass filter (typically triangular or Savitzky-Golay smoothing, see e.g. *Gonzalez and Woods 2001, Jähne 2002*), or by interpolating across the tops of the narrow band structures in the spectrum, as is indicated in Fig. 3.1.

For passive DOAS measurements using scattered sunlight as a light source, this is not possible because of the strong Fraunhofer lines superimposed on possible absorption features. Here, one option is to use a solar spectrum measured outside the atmosphere or a high resolution solar spectrum computed theoretically (*Kurucz et al. 1984*). This works well for satellites, as they can measure the reference spectrum directly. However, for ground-based measurements, this has the disadvantage that the reference spectrum is not measured with the same instrument as the atmospheric measurement, and optical resolution, instrument line shape, wavelength calibration, and spectral sensitivity of the spectrometer are different (also see section 3.1.4).

The second option is to measure the Fraunhofer reference spectrum with the instrument by looking in a direction in which the absorber of interest is either not present at all or present in lower abundances than in the area of interest. Alternatively, the reference spectrum can be measured under conditions in which the light path through the area of interest is particularly short. Such techniques can cause a non-zero baseline in the measurements, and results may only be interpreted relative to this baseline. Examples include measuring the Fraunhofer reference at noontime for stratospheric ozone measurements, measuring the reference looking towards the zenith for homogeneous tropospheric absorbers, or in the case of volcanic emissions, measuring the reference looking away from the plume.

From the measured differential optical density (Eq. 3.5), the column density S of the individual absorbers can be calculated, if the differential absorption cross-section is known for each.

$$S_i = \frac{\tau_i'}{\sigma_i'} = \int_0^L c_i(l)\, dl \qquad \textbf{Eq. 3.6}$$

The column density is the integral of the concentration of a species *i* over the entire optical path. Often, one distinguishes between vertical column density (VCD, the column density in a vertical column above the instrument) and slant column density (SCD, the column density along some diagonal optical path). However, all spectroscopic absorption techniques measure the column density, not the concentration. While some techniques fold the optical path into very small areas and can be considered nearly point measurements (e.g. Broadband Cavity Enhanced DOAS, see *Platt et al. 2008b*), this still holds true. The retrieval of the average concentration requires knowledge of the optical path. While this is fairly straightforward for active instruments with well-defined light paths, it can be more difficult for passive instruments using scattered sunlight. Chapter 8 deals with this topic.

3.1.3 Mathematical description of the instrumental spectral processing

The evaluation of the spectral data measured with a DOAS instrument must take two different types of phenomena into account. For one, atmospheric phenomena (e.g. scattering and absorption of radiation) influence the measurement spectrum. This is used to gain information on the sought trace gases, as was described in the previous section. However, the DOAS instrument itself also influences the measurement results. For example, all spectrometers have a limited optical resolution and a specific optical transfer function. This section deals with the instrumental aspects that must be considered in a DOAS data retrieval.

Fig. 3.2 displays the schematic of an atmospheric measurement with a DOAS instrument. As radiation emitted by the light source passes through the air, scattering and absorption processes reduce the intensity as described in the preceding section. At the end of the optical path, a collimating optical system focuses the transmitted radiation into a spectrometer.

In the example of Fig. 3.2, inset (a) represents the spectrum before the radiation enters the spectrometer. At this point, the spectrum is described by Eq. 3.1, with the addition of noise $N(\lambda)$, the magnitude of which is proportional to the square root of $I(\lambda)$ if dominated by photon noise.

$$I(\lambda,L)=I_0(\lambda)\cdot\exp\left(-\int_0^L\left(\varepsilon_R(\lambda,l)+\varepsilon_M(\lambda,l)+\sum_i\sigma_i(\lambda)\cdot c_i(l)\right)\cdot dl\right)+N(\lambda) \qquad \textbf{Eq. 3.7}$$

The optical resolution $\Delta\lambda$ / λ of a grating spectrometer as is typically used for DOAS is defined by the optical resolution of the grating as well as the line spread function (LSF) given by the spectrometer optics and especially the entrance slit. The optical resolution of the grating at a particular wavelength λ is given by its number of lines *n* and the spectral order *z* imaged onto the detector.

$$\frac{\Delta\lambda}{\lambda}\geq\frac{1}{nz} \qquad \textbf{Eq. 3.8}$$

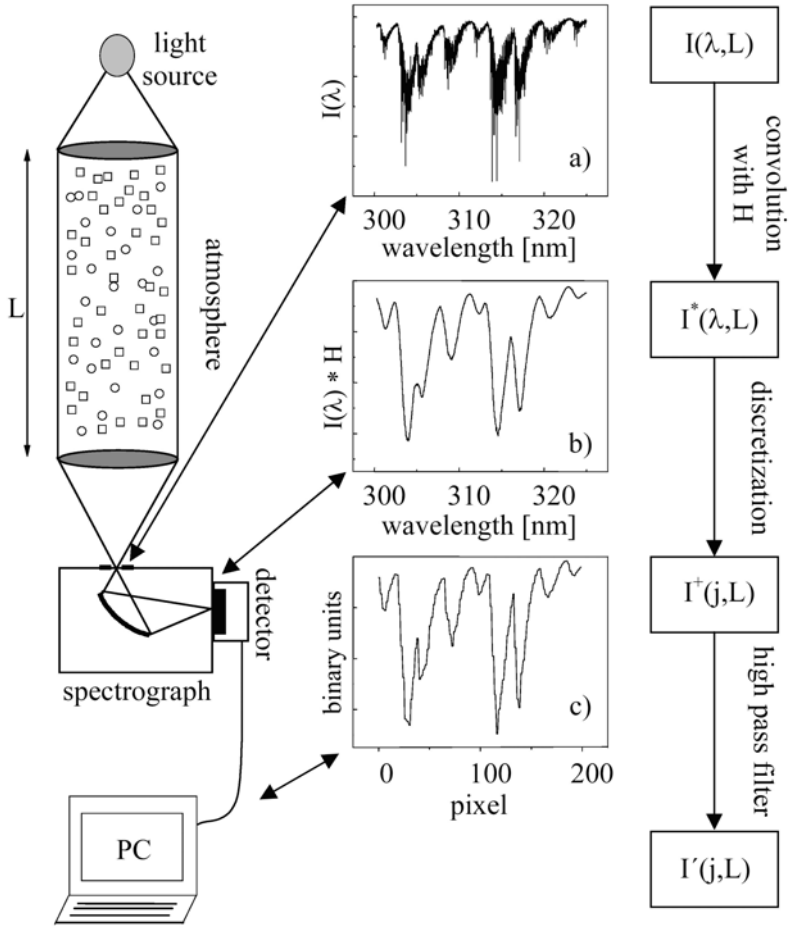

Fig. 3.2 – Schematic of the basic components of a DOAS system and the spectral processing steps involved. (adapted from *Stutz and Platt 1996*)

Interestingly, only the number of lines is decisive, and the lattice constant g (the distance between lines on the grating) does not affect the optical resolution of the grating. However, the optical resolution of the spectrometer can be limited by the lattice constant, because the smaller g is, the larger the spread of the spectrum on the detector. Even if an ideal spectrometer with an infinitely small entrance slit is assumed, the limited optical resolution of the grating leads to an imperfect imaging of the incident radiation onto the detector. Instead of all falling onto one position x^* on the detector (corresponding to one measured wavelength λ^*), monochromatic radiation will illuminate a certain area of the detector. Mathematically, the spectrum reaching the detector $I^*(\lambda)$ can be described as the convolution of the incident spectrum $I(\lambda)$ with a Gaussian distribution $K(\lambda)$ with a FWHM of $\Delta\lambda$ (taken from Eq. 3.8).

$$I^*(\lambda^*) \quad = \quad (I * K)(\lambda) \quad = \quad \int I(\lambda - \lambda') \cdot K(\lambda') \cdot d\lambda' \qquad \textbf{Eq. 3.9}$$

A graphical representation of this convolution is given in the top row of Fig. 3.3. In contrast to this scenario, however, real spectrometers have a finite entrance slit width. This slit is

imaged onto the detector by the spectrometer optics. Ideal optics and a grating with infinitely high spectral resolution would generate a perfectly sharp image of the slit on the detector if illuminated by monochromatic radiation. In a real spectrometer, the optics will cause a slight blurring of the image. This blurring is again mathematically described by a convolution of the spatial intensity distribution at the entrance slit $I(x)$ with the spectrometer's line spread function $H(x)$ (see *Jähne 2002* for details).

$$I^*(x^*) \;=\; (I * H)(x) \;=\; \int I(x - x') \cdot H(x', x^*) \cdot dx' \qquad \textbf{Eq. 3.10}$$

The second row of Fig. 3.3 shows this convolution. A high-quality optical system will have a line spread function (LSF) that is symmetrical and independent of the detector position x^*. Unfortunately, this was generally not the case for the miniature spectrometers used in the scanning DOAS systems in this thesis (see section 3.4.5). This fact is generally ignored, but it can cause problems during the preparation of literature absorption cross-sections, and future efforts will be made to correct for the effect (*Lehmann et al. 2009*)

Because the convolution is an associative process, the two operations described above can be written as

$$I^*(\lambda^*) \;=\; I(\lambda, x) * \big(K(\lambda) * H(x)\big) \qquad \textbf{Eq. 3.11}$$

In order to conduct the convolution of $K(\lambda)$ and $H(x)$, the wavelength calibration of the instrument must be known. Using this calibration, the detector position x^* can be converted to measured wavelength λ^*. The last row in Fig. 3.3 shows this complete operation for a monochromatic signal. The result is the so-called instrument line shape $L(\lambda)$. It can e.g. be measured in the laboratory using gas discharge lamps with characteristic atomic emission lines (e.g. Hg or Ne).

The instrument line shape (ILS) plays an important role in DOAS evaluations. In a typical DOAS evaluation, high-resolution trace gas absorption cross-sections are used as reference spectra and are fit to the measured optical density. These cross-sections are measured in a high resolution under controlled laboratory conditions. In order to use these references in the evaluation process, they must also be convoluted with the ILS $L(\lambda)$, as their resolution must be reduced to that of the DOAS spectrometer.

$$\overline{\sigma}_i \;=\; \sigma_i * L \;=\; \int \sigma_i(\lambda - \lambda') \cdot L(\lambda', \lambda) \cdot d\lambda' \qquad \textbf{Eq. 3.12}$$

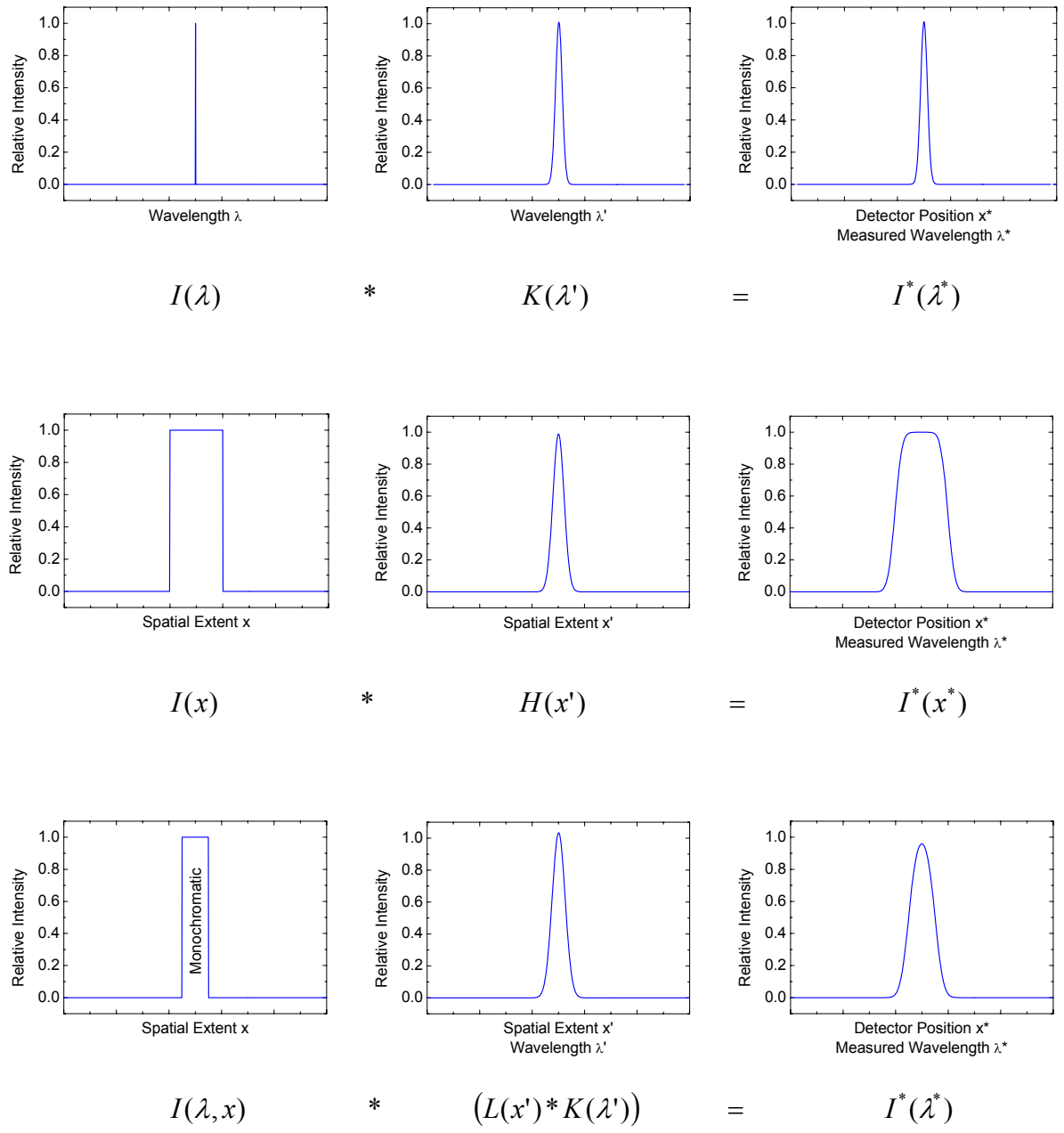

Fig. 3.3 – The instrument line shape (ILS) of a spectrometer is limited by both spectral and optical resolution. In the top row, the influence of the limited spectral resolution is shown. The limited spectral resolution of the grating will lead to a blurring of a monochromatic signal, even if a spectrometer with ideal optics and an infinitely small entrance is assumed. Mathematically, this is described by a convolution with a Gaussian *K*(*λ*). The second row shows the effect of the finite slit and imperfect optics. Here, the rectangular function originating from the entrance slit is convoluted with the line spread function *H*(*x*). In the bottom row, both effects are combined to model the real instrument response to a monochromatic signal, the ILS.

Inset (b) of Fig. 3.2 represents the spectrum $I^*(\lambda)$ as it arrives at the detector unit of the spectrometer. Next, the detector in the spectrometer performs a discretization of the spectrum. Typically, a spectrum with a width of around 100 nanometers is scanned by a detector with either 1024 or 2048 discrete pixels numbered j, each integrating the light in the wavelength interval from $\lambda(j\text{-}1/2)$ to $\lambda(j\text{+}1/2)$. This discretization is represented by the equation

$$I^+(j) = \int_{\lambda(j-1/2)}^{\lambda(j+1/2)} I^*(\lambda') \cdot d\lambda' \qquad \textbf{Eq. 3.13}$$

Inset (c) in Fig. 3.2 represents the spectrum after it has been discretely recorded by the detector unit, and as it is sent to the computer after having been digitized. In first order approximation, the wavelength to pixel mapping function Γ_I is a linear function assigning each wavelength to a specific pixel. However, upon closer examination, other orders also contribute. For this reason, the dispersion function is most accurately described by a polynomial of the order q.

$$\Gamma_I : \quad \lambda(j) \;=\; \sum_{k=0}^{q} \gamma_k \cdot j^k \qquad \textbf{Eq. 3.14}$$

The parameter vector γ_k determines the assignment of the pixel j to the wavelength $\lambda(j)$. γ_0 characterizes the placement of the spectrum on the detector. A change in this parameter corresponds to a shift of the spectrum, which can be caused by a temperature drift in the spectrometer. γ_1 characterizes the linear correlation of pixels to wavelength, and a change in this parameter, as can also be caused by temperature instability, causes a stretch or squeeze with respect to the original dispersion. Changes in higher orders of the parameter vector can also be caused by changes in environmental conditions e.g. temperature and pressure, and usually a 2nd order polynomial is used to describe the wavelength pixel mapping. The spectrometers used in this thesis were typically thermally isolated and temperature stabilized as well as possible to avoid temperature drift effects, but the effect must still be taken into account in the retrieval process, where a slight shift and squeeze of the references is usually allowed. Ongoing work aimed at implementing a calibration algorithm based on known wavelengths of Fraunhofer lines will allow the automatic calibration of each individual measured spectrum, thus possibly eliminating the need for a shift and squeeze in the DOAS retrieval (*Lehmann et al. 2009*).

The electronics that detect, amplify, and digitize the measured intensity signal also affect the spectrum that is later analyzed. The spectrometer has a varying spectral transmissivity, and the photo diode array is not completely homogenous in quantum yield. Also, a variable gain of the detector can lead to a multiplicative component of the electronic noise. A discrete multiplicative function $A^+(j)$ is used to describe these effects. Also, the following variables are introduced.

$$E \;=\; \int_0^L \varepsilon_R(\lambda, l)\, dl \;+\; \int_0^L \varepsilon_M(\lambda, l)\, dl \qquad \textbf{Eq. 3.15}$$

$$B = \int_0^L \sum_i \sigma_i^b(\lambda) \cdot c_i(l)\, dl \qquad \text{Eq. 3.16}$$

Thus, the Rayleigh and Mie scattering processes along the entire light path are described by E and the broadband absorption by atmospheric components is characterized by B. Using the definition of the column density given in Eq. 3.6, all influences on the measurement spectrum can now be merged into one equation.

$$I^+(j) = \left(I_0^+(j) \cdot \exp\left(-E^+(j) - B^+(j) - \sum_i \overline{\sigma}_i^+(j) \cdot S_i \right) + N^+(j) \right) \cdot A^+(j) \qquad \text{Eq. 3.17}$$

This fundamental equation describes the spectra as they are recorded by the computer and later evaluated. $I_0^+(j)$ is the discrete initial spectrum before atmospheric absorption and scattering. The narrow band absorption of the different absorbing gases, on which the DOAS principle is based, is described by the product of the individual differential absorption structures $\overline{\sigma}_i^+(j)$ and the column densities S_i of the absorbing gases. The term $N^+(j)$ added to the Beer-Lambert equation accounts for detector noise, photon noise, dark current, and electronic offset. The varying spectral transmissivity of the spectrometer and quantum yield of the detector makes the multiplicative function $A^+(j)$ at the end of the equation necessary.

3.1.4 Evaluation procedure

Before the analysis procedure can be used to derive the actual trace gas column densities from the measured data described by the previous equation, a few corrections must be taken into account (also see *Stutz and Platt 1996, Platt and Stutz 2008*). Since $A(j)$ is multiplied to the equation last, this spectral sensitivity function must first be divided out by the retrieval algorithm. However, this step can be omitted if the initial spectrum $I_0(j)$ is also measured by the same spectrometer, as the multiplicative function $A(j)$ is identical in this measurement and cancels out. If this is not possible and the spectral sensitivity is of a narrow-band nature, it must either be measured, the manufacturer's specifications must be used (although these are often not sufficiently accurate).

Next, the term $N(j)$ which is added to the equation and is not present in the exponent, is handled. The detector's dark current and electronic offset can be characterized by recording spectra with no light entering the spectrometer. Recording n spectra at the smallest possible exposure time yields n times the detector offset, while recording one spectrum at a long integration time yields the dark current for that time. For active DOAS, subtracting a background spectrum in which the light source is switched off or blocked can be used to correct for solar radiation scattered into the light path. The detector noise and photon statistics cannot be corrected for. They play an important role in determining the detection limit of the individual trace gases and estimating the measurement error (see chapter 3.1.5), but will be neglected here as they are not involved in the analysis procedure itself.

Once these corrections have been performed, the optical density can be calculated as described by Eq. 3.5.

$$\tau^+(j) \quad = \quad \ln\left(\frac{I_0^+(j)}{I^+(j)}\right) \quad = \quad E^+(j) + B^+(j) + \sum_i \overline{\sigma}_i^+(j) \cdot S_i \qquad \textbf{Eq. 3.18}$$

At this point, the individual trace gas column densities can be retrieved. The basic principle of a standard DOAS retrieval is to fit a model function $F(j)$ to the measured data described by Eq. 3.18. In this model, a polynomial $P_r(j)$ is used to describe the broadband structure of the spectrum ($E^+(j)$ and $B^+(j)$), and the column densities S_i of the individual absorbers can be calculated from the differential optical density that remains.

$$F(j) \quad = \quad P_\gamma(j) + \sum_i \overline{\sigma}_i'(j) \cdot a_i \qquad \textbf{Eq. 3.19}$$

The differential trace gas absorption cross-sections are represented by $\overline{\sigma}_i'$, and must be input by the user. They can either be measured in the laboratory, or, as was done in this thesis, high resolution literature cross-sections can be used (also see section 3.1.3). In this case, the absorption cross-sections must first be convoluted with the instrument line shape, thus smoothing them to the resolution of the spectrometer (see Eq. 3.12). Only then can they be fit to spectra recorded with this instrument. Although only the differential structures in the absorption cross-sections are used in the DOAS retrieval, the complete absorption cross-section σ_i can also be used in the fit, as the polynomial $P_\gamma(j)$ can be used to describe the broadband part of the cross-sections.

As the absorption cross-sections are usually not measured using the DOAS instrument, but with a high resolution spectrometer in the laboratory, they do not carry its wavelength to pixel mapping function. Because of this, there can be a slight difference in wavelength calibration. In order to correct for this effect, and the possibility of a varying of the mapping function due to environmental effects, standard DOAS algorithms often allow for a linear shift and squeeze/stretch of the references before fitting them to the measured differential optical density (see section 3.1.3).

All DOAS evaluations performed in the scope of this thesis were conducted using the DOASIS software developed at the Institute of Environmental Physics, University of Heidelberg (*Kraus 2004*). The fitting routine itself is comprised of a combination of the non-linear Levenberg-Marquardt Method (*Levenberg 1944, Marquardt 1963*) and a standard linear least-squares fit (*Albritton et al. 1976, Bevington and Robinson 2002*). Both methods minimize the variance χ^2 between $\tau^+(j)$ (Eq. 3.18) and $F(j)$ (Eq. 3.19) for all n channels of the retrieval range, where χ^2 is defined as

$$\chi^2 \quad = \quad \sum_{j=0}^{n} \left(\tau^+(j) - F(j)\right)^2 \qquad \textbf{Eq. 3.20}$$

During the fit, the parameters a_i (Eq. 3.19) as well as the coefficients of the polynomial P_γ (Eq. 3.19) are varied until χ^2 is minimized. Typically, a slight shift and squeeze in wavelength of the reference cross-section is also allowed. When the minimum is found, the fit coefficients a_i represent the difference in column density of each individual absorber between the measurement spectrum and the Fraunhofer reference, wherever this was recorded (see section 3.1.2).

In a real measurement, χ^2 can never be reduced to null. Even if all significant absorbers in the wavelength range of the retrieval where included in the DOAS model, the detector and photon noise will remain. The residual spectrum $\psi(j)$ of a DOAS fit is defined as the difference between the DOAS model $F(j)$ and the measured optical density $\tau^+(j)$.

$$\Psi(j) = \tau^+(j) - F(j) \qquad \textbf{Eq. 3.21}$$

In an ideal fit, $\psi(j)$ will consist purely of noise. The residual $\psi(j)$ is often used to assess the quality of a fit as well as the detection limit and error of a particular measurement (see sections 3.1.5 and 3.1.6.).

After the fitting process is complete, the average number densities or concentrations $\bar{c}$ of the individual absorbers along the light path can be calculated from the retrieved column densities S_i.

$$\sigma_i \cdot S_i \quad = \quad \tau_i \quad = \quad \sigma_i \cdot \int_0^L c_i(l)\, dl \qquad \textbf{Eq. 3.22}$$

and therefore

$$\bar{c}_i \quad = \quad \frac{S_i}{L} \qquad \textbf{Eq. 3.23}$$

Unfortunately, no information about the distributions of the individual trace gases along the light path can be extracted without additional information. By using multiple instruments to measure the same air mass simultaneously, however, a tomographic approach can allow the retrieval of 2 or even 3 dimensional trace gas concentration distributions. (see *Johansson et al. 2005, Pundt and Mettendorf 2005, Pundt et al. 2005, Hartl et al. 2006, Mettendorf et al. 2006, Hartl 2007, Platt et al. 2008a, Wright et al. 2008*). Alternatively, the light path of one instrument can be varied such that the total optical path length in a particular air mass is varied, thereby allowing inferences about the trace gas distribution in this air mass (see e.g. *Veitel 2002, Frins et al. 2006, Kazahaya et al. 2008, Louban et al. 2009b*).

3.1.5 Error estimation

The implemented least-squares fit algorithm returns the fit errors after completing the DOAS fit for each spectrum. However, these errors are only accurate if the pixel intensity errors have

a finite variance and are independent of one another, and the systematic pixel intensity errors are zero.

As the error in the measured differential optical density is dominated by photon noise, the variation is Poisson-distributed. However, at the high number of counts collected, the Poisson distribution can be approximated by a Gaussian distribution with a fixed standard deviation. Thus, the errors do have a finite variance.

Unfortunately, the photo diode arrays (PDA) and CCD detectors used in DOAS spectrometers often show a cross dependency of several percent between neighboring pixels. Also, doping errors in the diodes and CCDs cause systematic structures superimposed on the measurements. These can be corrected for if known, but these corrections are problematic, as the structures can change over time. Therefore, these structures do represent a systematic error. Also, if an unknown species is present in the measured air mass with absorption bands in the employed fit window, a systematic deviation from pure noise can be observed. In general, structures other than noise in the fit residual (see Eq. 3.21) can indicate an unknown absorber in the evaluated wavelength range, can originate from a faulty reference absorption cross-section, or can be caused by the instrument itself, in which case they normally occur randomly. Systematic residual structures cause systematic errors in the evaluation which cannot be described by statistical methods.

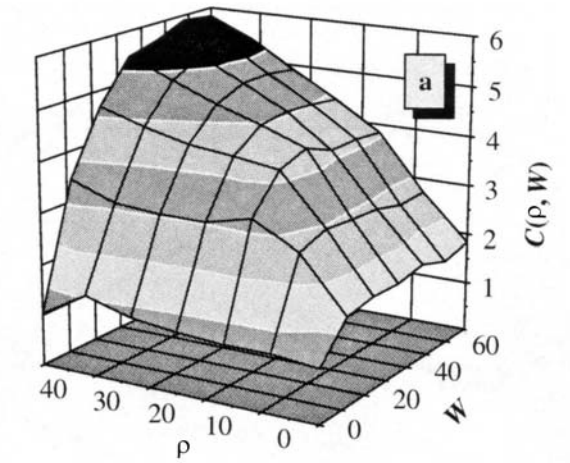

Fig. 3.4 – Correction factor *C*(*ρ,W*) as a function of the half width ρ of absorption bands and the width W of a running mean filter applied to a random noise spectrum in the Monte Carlo experiments conducted by *Stutz and Platt 1996*. The correction factor *C*(*ρ,W*) can be used to calculate the error of a measurement from the fit error. (adapted from *Stutz and Platt 1996*)

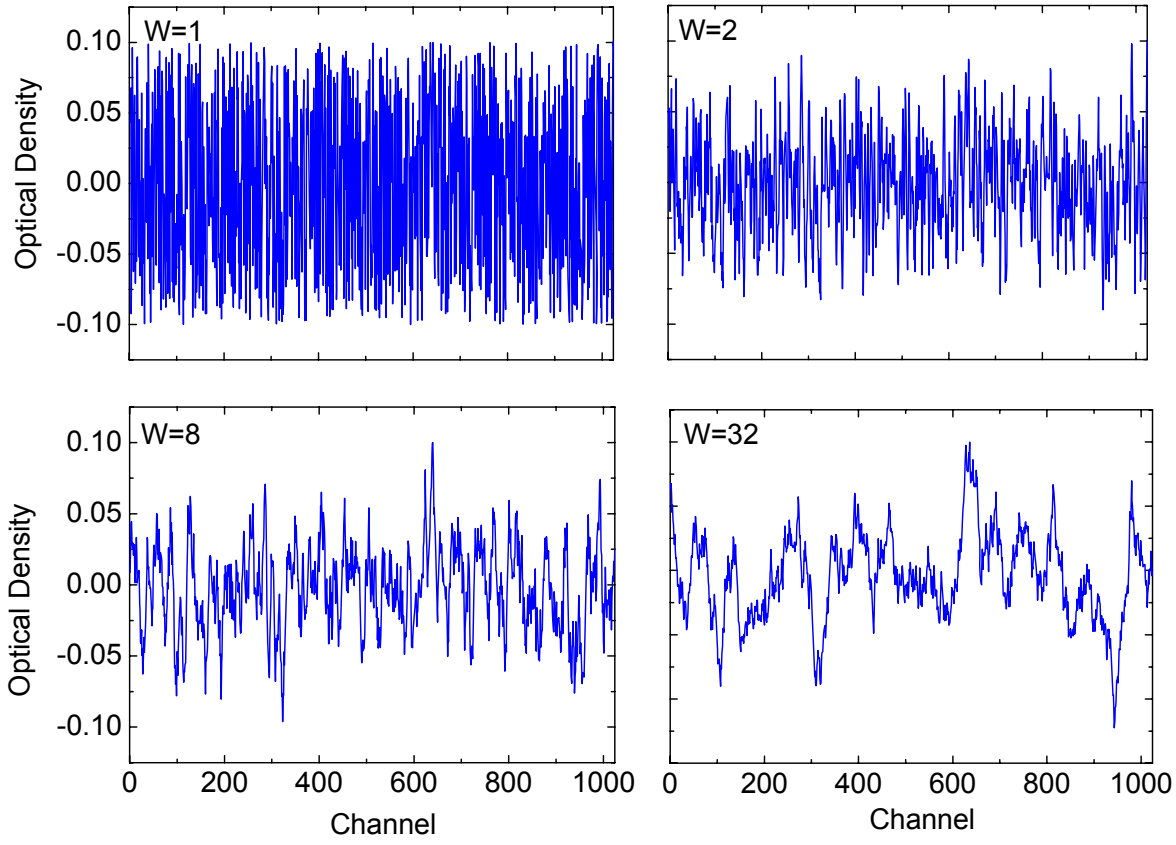

Fig. 3.5 – Influence of a running mean filter of various widths *W* on a random noise spectrum. Note the remaining structures become increasingly broad and begin to resemble possible trace gas absorption structures (assumed to be several channels wide). Therefore, the correction factor *C(ρ,W)* increases with increasing width *W*.

As a result of these problems, the measurement error is greater than the purely statistical fit error. *Stutz and Platt 1996* performed simulations with artificial absorption spectra containing five identical, Gaussian-shaped absorption lines with FWHM ρ. These absorption spectra were added to random noise spectra filtered by running mean filters with filter width W and normalized to a standard deviation of 1%. A DOAS fit was then applied to the spectra, and the mathematical error obtained from the fit σ_{fit} was compared to the known measurement error of the simulated experiment σ_{meas} for various values of ρ and W. A correction factor $C(\rho,W)$ was defined as

$$C(\rho,W) = \frac{\sigma_{meas}}{\sigma_{fit}} \qquad \textbf{Eq. 3.24}$$

Fig. 3.4 depicts the results of the simulations. The correction factor $C(\rho,W)$ increases when the width of the running mean filter W approaches the half-width ρ of the measured absorption lines. In this case, the measurement error σ_{meas} can be up to 6 times larger than the fit error σ_{fit}. In other words, the measurement error becomes large when the noise in the

spectrum has a similar frequency as the structures which are being retrieved. This is demonstrated in Fig. 3.5. Here, the influence of a running mean filter with width W applied to a random noise spectrum is shown. For increasing values of W, the noise increasingly begins to resemble possible absorption bands of an absorbing trace gas, which are assumed to be several channels wide in this case.

Usually, the noise is of a more high frequency nature than the absorption structures. For the measurements conducted in the scope of this thesis, a correction factor $C(\rho,W)$ of 2 was established as the best approximation for the ratio of measurement error σ_{meas} and fit error σ_{fit} (see *Stutz and Platt 1996, Platt and Stutz 2008* for more details on the calculation of errors in DOAS measurements).

3.1.6 Detection limit

The detection limit of a measurement is defined as the measurement value above which the detection of a species is considered significantly above the background noise level of the measurement. Two methods of estimating the detection limit of a DOAS measurement exist, and both will shortly be described in the following.

Detection limit from measurement error

One method of obtaining the detection limit of a DOAS measurement is by a statistical consideration. Assuming the measurement is subject to Gaussian error statistics, the retrieved measurement result only must be considered the most likely value. The measurement error calculated from the statistical fit error (see section 3.1.5) gives the 1σ range (see Fig. 3.6). The true measurement value lies in this range with a probability of 68 %. The 2σ confidence interval is obtained by multiplying the error by 2, and gives a range in which the probability of finding the true value is 95 %. If the 2σ confidence interval is located above null in its entirety, the measurement has a probability of more than 95 % of being above null. This is usually considered sufficient, and the measurement is therefore considered a significant detection of a certain species. However, other limits can also be used, e.g. the 3σ confidence interval gives a detection certainty of 99.7 %.

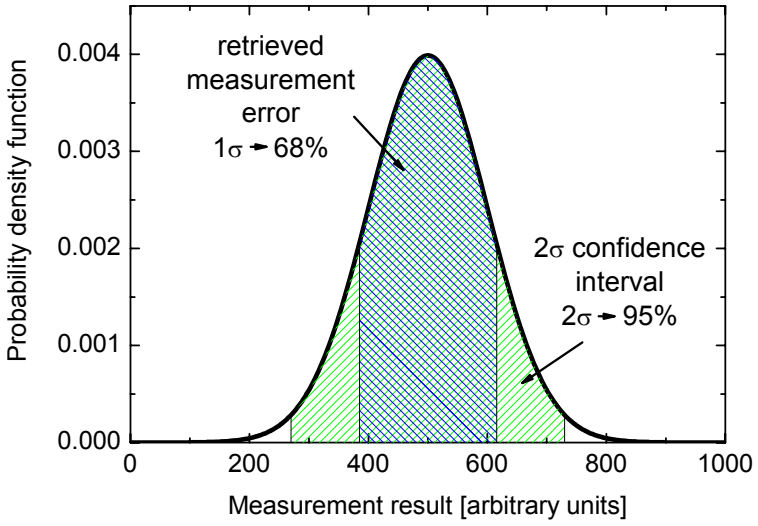

Fig. 3.6 – Gaussian probability density function symbolizing the confidence of a fictitious measurement. The retrieval of the measurement error (described in section 3.1.5) yields the 1σ error range. Multiplication by a factor of 2 yields the 2σ confidence interval. If this entire interval is located above 0 (as is the case in this example), the measurement is different from 0 with a probability of at least 95 % and is considered significant.

Detection limit from fit residual

Another method of retrieving the detection limit of a DOAS measurement is by analyzing the residual spectrum of the DOAS fit (see Eq. 3.21). The ability of a DOAS measurement to detect a certain species is limited by the fact that noise is superimposed on the measured spectra. The residual spectrum of the DOAS fit contains all structures that could not be explained by the DOAS model (Eq. 3.19) during the fit. In an ideal fit, the residual spectrum only contains electronic and photon noise. If, however, a species with relevant absorption bands in the fit window was omitted from the fit, this species absorption structures will also be visible in the residual spectrum. If absorption structures of a certain species have a lower differential optical density τ than that of the noise (or structures of other origin in the fit residual, see section 3.1.5), the species can not be identified. Therefore, the magnitude of the residual can be used as a measure for the detection limit of a specific DOAS retrieval.

According to the Beer-Lambert Law (Eq. 3.1), the differential optical density τ' of an absorber can be expressed as the product of the column density S and differential absorption cross-section σ' (see Eq. 3.6). The minimum differential optical density detectable in a retrieval must be larger than the differential optical density of the fit residual $\Delta\Psi$. This is easily calculated by taking twice the average deviation from the mean value in the wavelength interval of the considered trace gas absorption band.

$$\tau' \geq \Delta\Psi \qquad \text{Eq. 3.25}$$

The minimum detectable column density is therefore

$$S_{\min} = \frac{\Delta\Psi}{\sigma'} \qquad \text{Eq. 3.26}$$

This technique for deriving the detection limit of a DOAS measurement was e.g. applied in chapter 6.3.2. In Fig. 3.7, the differential absorption cross-sections σ' of some trace gases that can be measured with the DOAS technique are shown. The list is incomprehensive, as DOAS can detect many more species. Also, new trace gases are still being found to which DOAS is sensitive, such as the recent detection of glyoxal (*Volkamer et al. 2005a, Volkamer et al. 2005b, Sinreich et al. 2007*). Along the right margin of Fig. 3.7, the typical detection limit of each gas is given assuming a deviation of the fit residual $\Delta\Psi$ of 3×10^{-3}, a typical value achieved in measurements.

3.2 Measurement concepts – Active DOAS

The term Active DOAS refers to differential optical absorption measurements conducted with artificial light sources. Several different instrumental setups exist for active DOAS measurements. The most common configuration is that of the Active Long Path DOAS. Here, a telescope sends a beam of light through the atmosphere. This is received either by the same telescope or separate receiving optics, and is then analyzed in regard to atmospheric absorption structures (see e.g. *Platt et al. 1979, Edner et al. 1986, Axelsson et al. 1990b* and Fig. 3.2). *Pundt and Mettendorf 2005* used a long path DOAS setup with multiple light paths for tomographic trace gas measurments. Other active DOAS setups include multi-reflection systems such as the White cell (*White 1942, White 1976*) and, more recently, cavity based systems (Cavity Enhanced DOAS, see *Platt et al. 2008b*).

While passive DOAS measurements have become standard for monitoring volcanic emissions (see section 3.3), active DOAS systems were first applied to measure volcanic plume composition in the scope of this thesis (*Kern et al. 2008a*). In the following section, measurement concepts for Active Long Path DOAS setups at volcanoes are discussed. The technical instrument design is later explained in section 3.5.2, and the measurement results are presented in chapter 7.

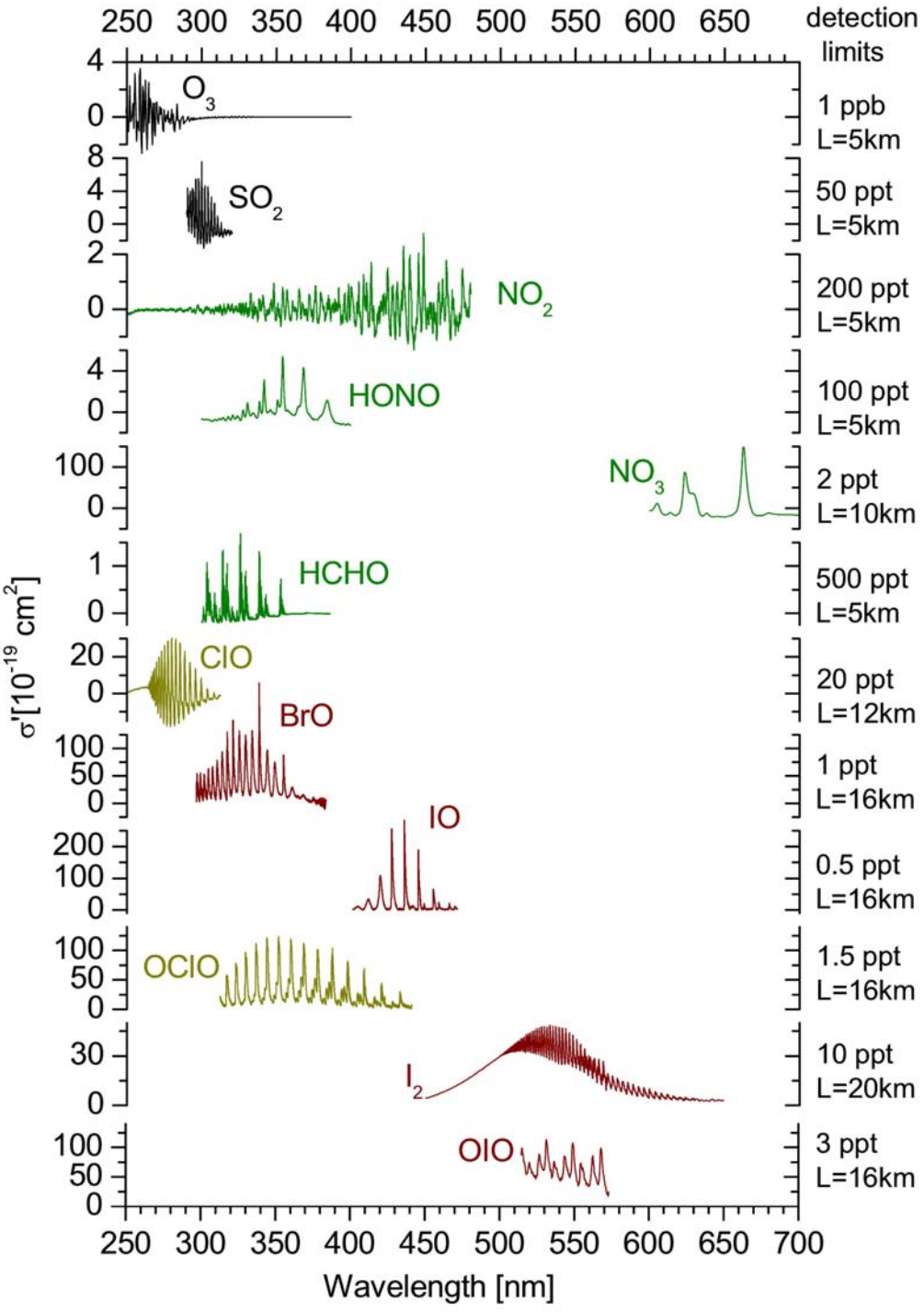

Fig. 3.7 – Incomprehensive list of species that can be measured with the DOAS technique. The differential absorption cross-section σ' is shown as a function of wavelength. Also given is the approximate detection limit of the individual species assuming a fit residual deviation ΔΨ of 1×10^{-3} (see Eq. 3.26).

3.2.1 Active Long Path DOAS

The Active Long Path DOAS (LP-DOAS) configuration is possibly the most straightforward DOAS approach. A beam of light is sent through the atmosphere. After having passed through the air, this radiation is then analyzed for differential absorption structures of trace gases in the optical path. As the optical path is well-defined, the average concentration of an absorber along the light path can directly be obtained from Eq. 3.23. This is not as straightforward for scattered light measurements, as the optical path of incident light is not inherently known and is different for each detected photon (see chapter 8).

The use of artificial light sources also has two obvious advantages. For one, uninterrupted measurements can be conducted at night as well during the day, thus allowing insights into night-time chemistry (see chapter 7). Also, artificial light sources can extend the available spectral range to wavelengths not found in the spectrum of scattered solar radiation (especially UV wavelengths below 300 nm, see e.g. *Axelsson et al. 1990a, Volkamer et al. 1998, Kern et al. 2008a, Merten 2008, Platt and Stutz 2008*).

Since the first measurements by *Platt et al. 1979*, LP-DOAS has become a standard method for the quantitative measurement of atmospheric trace gases. Applications include halogen measurements in the marine boundary layer (e.g. *Alicke et al. 1999, Allan et al. 2001, Saiz-Lopez and Plane 2004, Saiz-Lopez et al. 2004, Peters et al. 2005*), in the vicinity of salt lakes (e.g. *Hebestreit et al. 1999, Stutz et al. 2002*) and in polar regions (e.g. *Hausmann and Platt 1994, Tuckermann et al. 1997, Hönninger et al. 2004b, Saiz-Lopez et al. 2007*), as well as quantification of the oxidative capacity and chemical cycling of urban air (e.g. *Platt et al. 1979, Platt et al. 1980b, Platt et al. 1980a, Axelsson et al. 1990a, Geyer et al. 2003a, Geyer et al. 2003b, Trick 2004, Volkamer et al. 2005a, Acker et al. 2006, Merten 2008*).

3.2.2 Optical path length requirements in volcanic plumes

For all DOAS instruments, the measured optical density τ of a particular trace gas is determined by its differential absorption cross-section σ and its column density S (see Eq. 3.6). The detection limit S_{min} is determined by the absorption cross-section (see Eq. 3.26). However, when expressed in terms of average concentration $\bar{c}$ along the light path, the detection limit can be expressed as

$$\bar{c}_{\min} = \frac{\Delta\Psi}{\sigma' \cdot L} \qquad \textbf{Eq. 3.27}$$

Here, $\Delta\Psi$ is the magnitude of the fit residual (see section 3.1.6), and L is the length of the optical path. Therefore, the sensitivity of an LP-DOAS instrument can be increased to a

certain degree by increasing the light path length[1]. However, this assumes a well-mixed air mass filling the entire light path. While this assumption holds true for many LP-DOAS applications, it is not fulfilled for most measurements at volcanic plumes. Here, the average concentration $\bar{c}$ is in many cases not a valuable parameter. Typically, the spatial extent of plume inhomogeneities is much smaller than the length of the light path, and the retrieved average concentration $\bar{c}$ is therefore not very meaningful. Also, in many cases the plume only fills part of the path. As a result, the gas concentrations here are much larger than the average concentration $\bar{c}$.

Therefore, the instrument sensitivity can often not be increased by choosing longer optical paths, as these are typically only partially filled by volcanic emissions. In this case, longer paths only increase the impact of ambient absorbers on the measurement results. Also, the concentrations of certain species (especially SO_2) in volcanic plumes is so high that long path lengths often lead to the virtually complete absorption of emitted radiation at certain wavelengths, rendering the retrieval of other species impossible. Therefore, the path lengths of LP-DOAS measurements at volcanoes must be carefully selected and depend on the plume composition of the respective volcano. Studies conducted in the scope of this thesis used path lengths between about 1 km at Masaya volcano and 40 meters at Mt. Etna (see Fig. 3.8).

Fig. 3.8 – Active Long Path DOAS measurements conducted at Mt. Etna on July 15 of 2008. Here, a light path of only 2 × 20 m was used (site 5 in Fig. 7.15), as SO_2 mixing ratios in the order of 100 ppb regularly caused virtually complete absorption of radiation between 290 and 310 nm (see Fig. 3.23).

[1] The light path cannot be increased unlimitedly, as scattering on air molecules and aerosols decreases the light throughput, which in turn decreases the signal-to-noise ratio and reduces sensitivity. Therefore, an optimal light path length exists, as discussed by *Platt and Stutz 2008*.

3.2.3 Plume composition ratios

Passive scanning DOAS instruments can measure the emission flux of volcanic gases by scanning the cross-section of a plume and multiplying the total integrated amount of a certain species by the plume transport speed. This technique is described in section 3.3.2. As the optical path of an LP-DOAS measurement is determined by the configuration of the telescope and reflectors, both ends of the optical path must be located at ground level. Therefore, a similar approach to measuring volcanic emission fluxes is not easily implemented. Instead, LP-DOAS measurements were used to gain insights into the chemical composition of volcanic plumes.

The most common application for LP-DOAS measurements is the retrieval of concentration time series of various species. However, due to the degree of spatial and temporal inhomogeneity found at volcanic vents, such time series are typically of little value in volcanic applications. Fig. 3.9 shows a sequence of LP-DOAS measurements conducted at Masaya volcano (Nicaragua) in April of 2007. The spectral data is shown on the right side of the figure. A blue line indicates the measured SO_2 optical density, the red line represents the DOAS fit of SO_2. The retrieved column densities are shown above each spectrum. In the first spectrum, an SO_2 column density of 2.4×10^{18} molec/cm^2 was retrieved. The second spectrum, taken 45 seconds later, yielded only 2.8×10^{17} molec/cm^2. Taken 90 seconds after the initial spectrum, the retrieval of the third spectrum yielded only 3.4×10^{16} molec/cm^2. Thus, the SO_2 column density measured along the instrument optical path decreased by two orders of magnitude within 90 seconds.

Fluctuations such as these are typical for LP-DOAS measurements in volcanic plumes. As an example, Fig. 3.10 shows a longer SO_2 time series measured by the LP-DOAS at Masaya volcano in April of 2007. The SO_2 column densities fluctuate strongly on very short time scales. A webcam was installed at the telescope position and used to record an image of the Masaya crater area simultaneously with each recorded spectrum. The images corresponding to the three subsequently recorded spectra given in Fig. 3.9 are shown on the left side of the figure. It is evident from these images that the extreme decrease in measured SO_2 column density was caused by a shifting of the plume position from right to left and therefore out of optical path of the measurement.

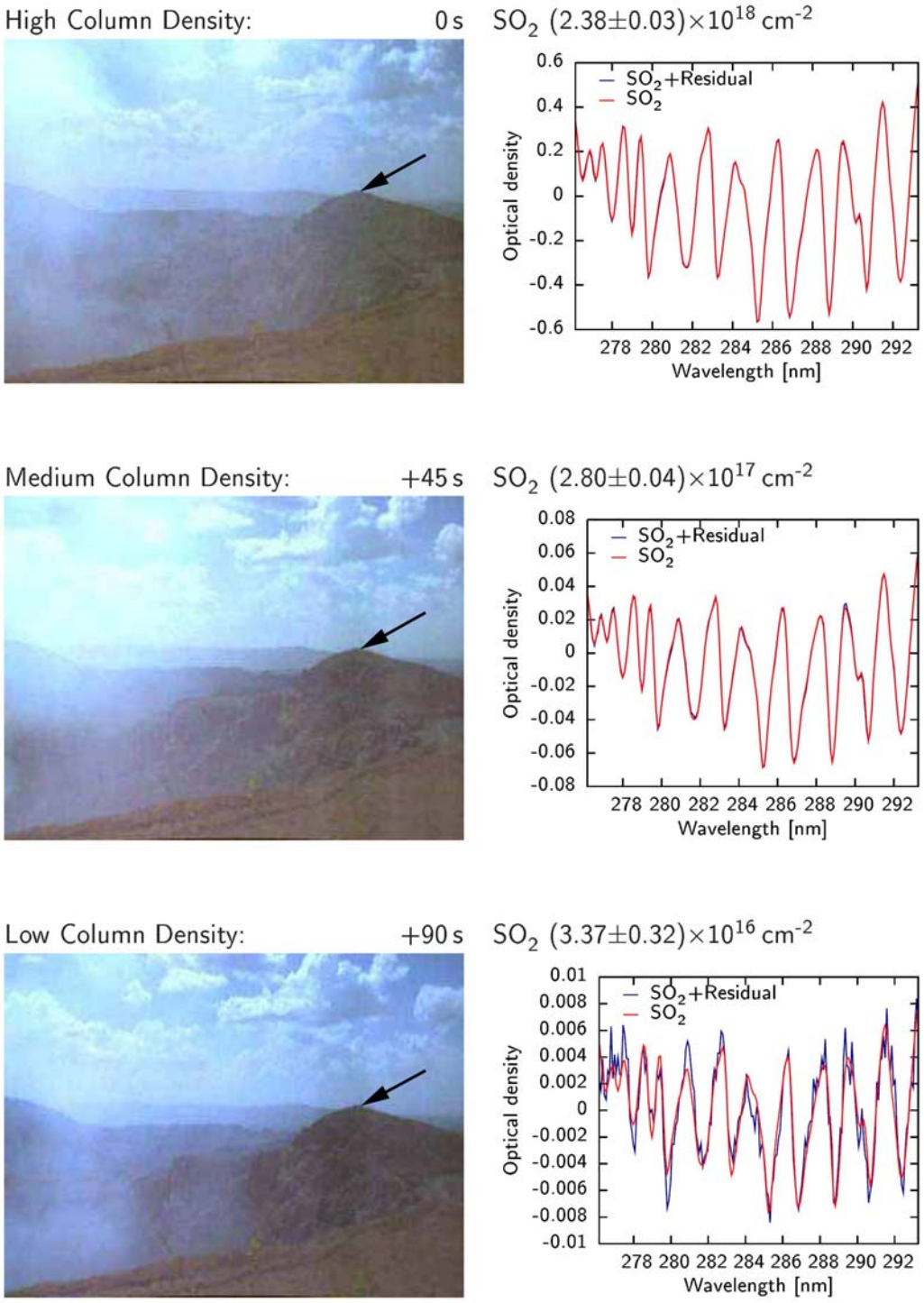

Fig. 3.9 – Three subsequent SO_2 measurements conducted with an LP-DOAS system at Masaya volcano (Nicaragua). During the acquisition of absorption spectra (shown at right) a webcam was used to simultaneously record visual images of the crater area (shown at left). The images were taken from the telescope position. The arrow indicates the reflector position. In the first spectrum of the series (top row) a column density of 2.4×10^{18} molec/cm^2 was retrieved. Only 45 seconds later, the column density had decreased by about 1 order of magnitude. 90 seconds after the initial measurement, 2 orders of magnitude less SO_2 were registered. The camera images show that this decrease is caused by a shift of the plume position. (adapted from *Sihler 2007*)

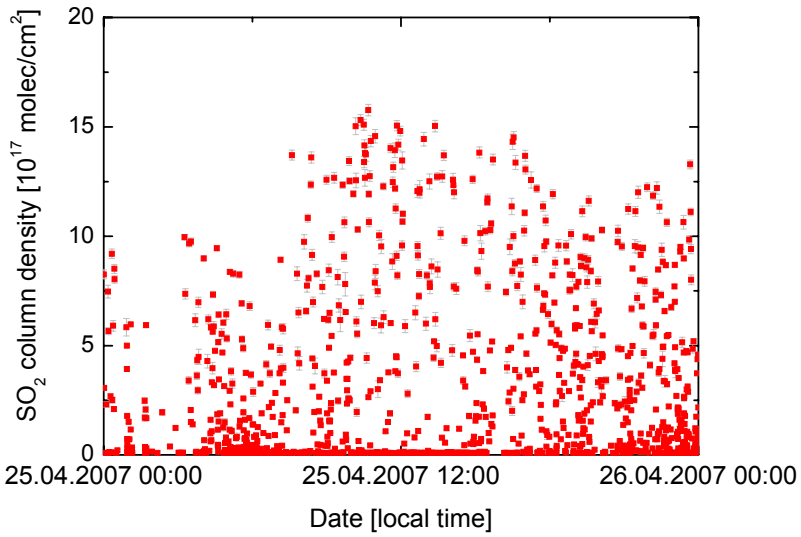

Fig. 3.10 – Time series of SO_2 column densities measured at Masaya volcano (Nicaragua) on April 25, 2007. The column densities fluctuate seemingly randomly on very short time scales. These fluctuations are caused by plume inhomogeneities and a shifting of the plume position in and out of the instrument optical path.

Due to the high spatial and temporal plume variability described above, it is difficult to interpret the measured time series of a single species in a meaningful manner. Therefore, in the measurements described in this thesis (see chapter 7), only the concentration ratios between different species are discussed. As SO_2 has a tropospheric lifetime in the order of several days (*McGonigle et al. 2004, von Glasow et al. 2008*), depletion of this species in non-condensing volcanic plumes is usually negligible in the first hours after emission.[2] Therefore, SO_2 is used as a tracer for the amount of volcanic gas in the optical path of the LP-DOAS system during a given measurement. The retrieved column densities (or detection limits) of other species (i.e. BrO, ClO, OClO) are related to those of SO_2 for each measurement. The ratio of X/SO_2 then gives a relative abundance of the indicated species X. As the halogen oxides BrO, ClO and OClO are secondary emission products that are formed by the reaction of volcanic gases with gases located in the ambient air (see chapter 7), the ratio X/SO_2 must be regarded as a function of several parameters governing the chemical processes (e.g. incident solar irradiance, ambient ozone concentration, ambient OH concentration, relative humidity, concentration of volcanic precursor gases, time since emission, etc.).

[2] This issue is still a topic of some debate. SO_2 loss rates in volcanic plumes reported in the past range between 10^{-3} s^{-1} and 10^{-7} s^{-1}, corresponding to e-folding times of between about 30 minutes and 115 days (*Martin et al. 1986, Oppenheimer et al. 1998b, Rodríguez et al. 2008*). However, past measurements are somewhat uncertain as several factors have not been accounted for. *Nadeau and Williams-Jones 2009* e.g. attribute a large part of the measured apparent SO_2 loss at Masaya Volcano to an increased wind speed downwind of the volcano. Also, the radiative transfer dilution effect (described in chapter 8 is likely to cause underestimation of downwind measurements under typical measurement geometries. As most measurements take place within the first few minutes after emission into the atmosphere, SO_2 depletion can usually be neglected.

3.3 Measurement concepts – Passive DOAS

Passive DOAS instruments use natural light sources such as the sun, moon, or stars to measure the absorption of trace gases along the optical path between the light source and the instrument. Such instruments can either be aligned so that they record unscattered photons directly traveling on a straight line from the light source to the instrument, or they can measure scattered radiation. Several different measurement geometries were used in the compilation of data for this thesis, and this section gives a brief description of the individual passive DOAS measurement concepts.

3.3.1 Direct sun / solar occultation geometry

The direct sun geometry (also called solar occultation geometry) is perhaps the most straightforward passive DOAS measurement geometry. A solar tracker is used to keep the instrument's field of view aimed directly at the sun. This has several advantages: for one, the intensity of the incident light is much greater than when measuring scattered radiation with a similar field of view on a cloud-free day (see e.g. *Sommer 2008*). Considering the fact that photon noise scales with the square root of the collected intensity, the theoretical signal to noise ratio of a direct light measurement is much better than for a scattered light measurement conducted at the same time resolution. Perhaps even more importantly, the optical path of unscattered radiation between the sun and the instrument is a well-defined straight line. For clear days and weak absorbers (see section 3.4.1), the total radiation scattered into the optical path can be ignored, as it is typically at least 4 orders of magnitude weaker than the direct sunlight (see e.g. *Garrat 1994, Wild et al. 1995, Philipona 2002*). As Rayleigh scattering in the atmosphere is proportional to λ^{-4} (where λ is the radiation wavelength), the ratio of direct to scattered light is smaller for shorter wavelengths, but recent measurements around 350 nm indicated a ratio of at least 500:1 under clear sky conditions (*Sommer 2008*). Therefore, under these conditions, the path length in a particular air mass can usually be simply calculated using geometrical considerations. However, in the case of clouds or aerosol-laden and condensing plumes, or for strong absorbers, these approximations may fail and radiative transfer becomes more complicated (see chapter 8).

The direct sun geometry, however, also has many disadvantages. First and foremost, the geometry is very inflexible, as the viewing direction is prescribed by the instrument position and the time of day. Therefore, it may be difficult or impossible to measure a certain air mass of interest without constantly moving the instrument. This is especially problematic when monitoring volcanic emissions, as the volcanic plume needs to be held between the instrument and the sun, which is not always possible. In the case of stationary measurements, a large portion of the theoretical measurement time is lost due to inappropriate measurement geometries.

The second complication involved in conducting direct light measurements is the fact that the ultra-violet part of the solar spectrum, as it is seen from the earth's surface, is highly variable.

It contains narrow band structures the depth of which depends on the instrument line of sight and the solar zenith angle as well as the stratospheric ozone load. The dependency of the Fraunhofer spectrum on the instrument line of sight is caused by the so-called center-to-limb-darkening effect (see e.g. *Greve and Neckel 1996, Bösch 2002, Bösch et al. 2003*).

The spectrum of radiation being emitted from the solar disk is dependent on the distance from the center of the disk. One reason for this is the temperature difference between the center of the sun and higher layers. According to the Stefan-Boltzmann Law, the emitted radiant flux of a thermal emitter is proportional to the fourth power of the emitter temperature. Also, according to Wien's Displacement Law, the maximum of the solar emission spectrum shifts toward shorter wavelengths with increasing temperature towards the center of the solar disk.

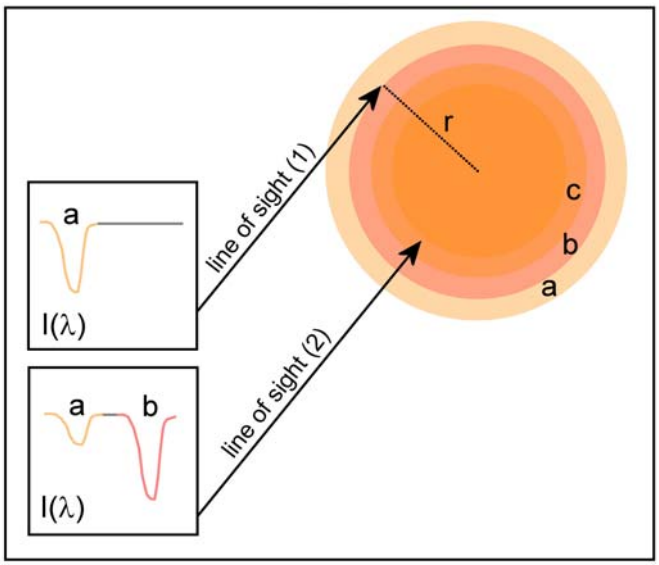

Fig. 3.11 – Schematic of the variability of narrow-band Fraunhofer absorption lines observed across the solar disk. In this example, both the outermost and the second layer of the solar disk (labeled a and b) each contain absorbers, so any line of sight intersecting them will result in a respective absorption signal in the measured spectrum I(λ). The relative absorption strengths of the two, however, depend on the exact position of the line of sight in regard to the solar disk.

While a shift in the thermal emission curve represents a fairly broad-band change in the solar spectrum, narrow-band structures i.e. Fraunhofer absorption lines also change across the solar disk. This phenomenon is depicted in Fig. 3.11. A line of sight penetrating only the outermost layers of the sun (marked (1) in Fig. 3.11) will only result in absorption lines of absorbers in this layer (marked (a) in Fig. 3.11) in the measured spectrum I(λ). A line of sight aimed at the center of the solar disk (marked (2)) will result in absorption signals from deeper layers (marked (b),(c)) of the sun in the measured spectrum I(λ). At the same time, the optical path through the outer layers will typically be shorter, so the relative optical density of the absorption lines from these layers will be smaller than for the outer line of sight.

A spectroscopic instrument using a solar occultation geometry will have a finite field of view, not an infinitely thin line of sight. Therefore, the measured spectrum will be an intensity weighted average of various spectral shapes. During a DOAS retrieval, however, it is of great importance that the narrow-band spectral features are identical in the atmospheric measurement and the Fraunhofer reference. Otherwise, changes in these features will be interpreted as atmospheric absorption features. Two approaches can be pursued to this extent. If the aperture of the instrument is smaller than that required to measure the entire solar disk (approx. 0.53°), the solar tracker of the instrument must be precise enough to ensure that the same position of the solar disk is always recorded. If, on the other hand, the instrument aperture is larger than 0.53°, the entire solar disk is recorded. In this case, the solar tracker must not be as precise, but the instrument sensitivity to the individual angles of incidence across the field of view must be constant.

For the solar occultation measurement mode of the NOVAC mark II instrument (see section 3.5.1), a diffuser plate was placed into the optical path of the telescope. The diffuser plate had a dual functionality: for one, the incident radiation was attenuated to a level safe for the following optical system. In addition, however, the diffuser plate mixed the entire incident solar radiation. In this way, the measured radiation represented a diffuse average of the total incident solar radiation, and the 0.1° precision of the solar tracker (*Sommer 2008*) was sufficient to keep the entire solar disk in the field of view.

3.3.2 Scanning DOAS measurements of localized plumes using scattered solar radiation

Using sunlight scattered in the atmosphere as a light source for spectroscopic measurements has the enormous advantage that the choice of measurement geometry is much less restricted than for solar occultation geometries. During daylight hours, the instrument line of sight can be aimed at any position in the sky (except for the sun itself), thus allowing the adaptation of the measurement geometry to the volcanic plume position.

In fact, the flexible measurement geometry of scattered light DOAS has been used for a large variety of applications aside from volcanic emissions measurements. *Solomon et al. 1987* e.g. used zenith sky measurements to retrieve dependable stratospheric O_3 column densities. By adding multiple elevation angles (especially those close to the horizon), information about the troposphere is gained using the so-called Mult-Axis geometry (MAX-DOAS) (see *Hönninger et al. 2004a* and references therein). Past applications include studies on urban pollution (e.g. *Gobiet et al. 2004, Heckel et al. 2005, von Friedeburg et al. 2005, Leigh et al. 2007*), chemical transport (e.g. *Sinreich et al. 2007*), polar air chemistry (e.g. *Hönninger et al. 2004b, Wittrock et al. 2004*), trace species in the marine boundary layer (e.g. *Leser et al. 2003, Pikelnaya et al. 2007*), and of course volcanic emissions measurements (e.g. *McGonigle et al. 2002, Bobrowski et al. 2003, Edmonds et al. 2003a, Galle et al. 2003, Bobrowski 2005*). Recently, the ability of these MAX-DOAS instruments to measure vertical aerosol profiles

based on the absorption on the oxygen dimmer O_4 has also been proven (e.g. *Wagner et al. 2004, Friess et al. 2006, Irie et al. 2008, Li et al. 2008*).

The remote sensing techniques discussed in this thesis measure the column density S of an absorber along the average optical path from the sun to the instrument (see section 3.1). When localized trace gas distributions such as plumes are measured from short distances, the optical path through the region of interest can oftentimes be assumed as a straight line in the instrument line of sight direction. While not always applicable, this simple geometric approach is assumed for the sake of simplicity in this chapter. Chapter 8 deals with correcting radiative transfer effects causing deviations from this assumption.

One main goal of spectroscopic volcanic emissions measurements is to quantify the emission flux Φ of a species, as this can e.g. be used for volcanic risk assessment and to study the impact on atmospheric chemistry (see sections 2.1 and 0). In order to calculate the volcanic emission flux using individual column density measurements, integrated plume slices are first determined from a set of column densities. One geometry used to obtain such information is the stationary scanning DOAS setup (see e.g. chapters 5 and 6 as well as *Bobrowski et al. 2003, Edmonds et al. 2003a, Galle et al. 2003, Bobrowski 2005, Fickel 2008*). Here, an instrument is placed in a fixed position from which it scans the area of interest in a number of steps. Ideally, the scanning plane is chosen perpendicular to the plume propagation direction (see below). Two approaches can then be applied to retrieve volcanic emission fluxes from the column density scans: The trace gas columns are integrated either in lateral or radial direction.

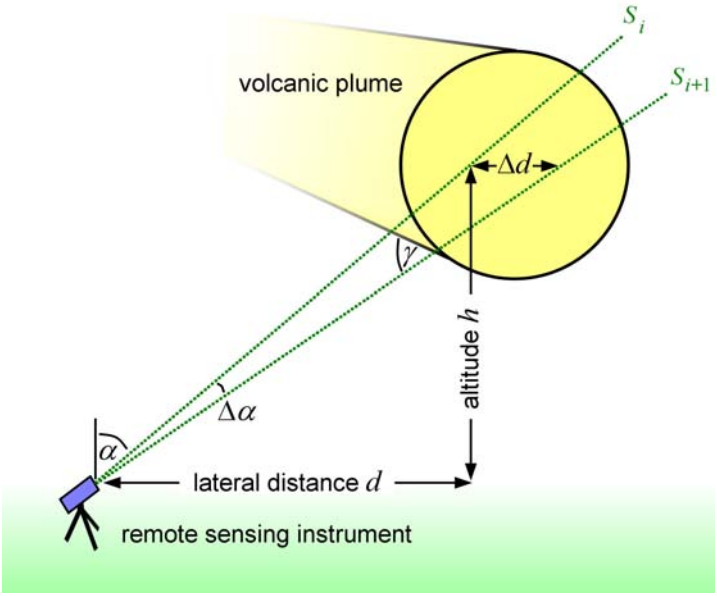

Fig. 3.12 – Schematic of the essential parameters for the lateral integration of the SO_2 amount in a volcanic plume slice. The plume is assumed circular in cross-section and moving nearly perpendicular to the scanning plane of the instrument.

Lateral plume integration

The lateral integration is e.g. used in the NOVAC real-time evaluation software (*Johansson et al. 2008*), and is conceptually closely linked to the established definition of the plume vertical column density V (see section 3.1.2).[3] The remote sensing instrument ideally scans the plume in a perpendicular direction, as shown in Fig. 3.12. The plume is detected by the instrument in a certain range of measurement zenith angles α. In addition to the angle, knowledge about the plume position is necessary. Sometimes the lateral distance d between the plume and instrument is known, e.g. from another scanning DOAS instrument (see e.g. section 5.2), from a DOAS traverse measurement (see e.g. section 8) or from the volcanic vent position combined with the wind direction (see *Fickel 2008*). At times the plume height h may be known instead, e.g. from visual observations or another scanning DOAS instrument. Together with the measurement zenith angle α_i of a specific measurement, either of these parameters will yield the other by means of the following relation.

$$\tan(\alpha_i) = \frac{d_i}{h} \qquad \textbf{Eq. 3.28}$$

Assuming that the next measurement is performed at the zenith angle $\alpha_{i+1} = \alpha_i + \Delta\alpha$ yields

$$\tan(\alpha_i + \Delta\alpha) = \frac{d_i + \Delta d}{h} \qquad \textbf{Eq. 3.29}$$

and therefore

$$\Delta d_i = h \cdot \tan(\alpha_i + \Delta\alpha) - d_i \qquad \textbf{Eq. 3.30}$$

By calculating Δa_i, the distance between the two points where the instrument's viewing direction intercepts the plume altitude is now known. The next step is to calculate the vertical column density V inside the volcanic plume along this segment. For each individual measurement zenith angle α, the straight column density S can be converted to the vertical column density V using the following relation.

$$V = S \cdot \cos(\alpha) \qquad \textbf{Eq. 3.31}$$

The average vertical column density between the two viewing directions is therefore given by

$$V_i = \frac{1}{2}\left(S_i \cdot \cos(\alpha_i) + S_{i+1} \cdot \cos(\alpha_i + \Delta\alpha)\right) \qquad \textbf{Eq. 3.32}$$

The integrated amount X of a certain absorber inside a slice of the volcanic plume can then be calculated by adding the individual vertical columns V_i measured inside the plume scaled by

[3] The vertical column density is usually defined as the column density of an absorber along a vertical path through the entire atmosphere. Here, only the path in the volcanic plume is considered. This works well for trace gases that do not have a significant atmospheric background (e.g. SO_2), but more extensive radiative transfer considerations must be taken into account for gases that are abundant in the ambient atmosphere.

their respective lateral widths a_i. Multiplication with $\sin(\gamma)$ corrects for a possible non-perpendicular intersection of the scanning plane with the plume.

$$X = \sum_{i \in Plume} \left(V_i \cdot \Delta d_i\right) \cdot \sin(\gamma) \qquad \textbf{Eq. 3.33}$$

After calculating the integrated amount X of an absorber in a volcanic plume slice, the instantaneous flux through this slice ϕ can be obtained by multiplying with the wind speed v at plume height.

$$\phi = X \cdot v \qquad \textbf{Eq. 3.34}$$

If the measured species is stable on the transport time scales between vent and measurement position as is e.g. the case for SO_2 (see e.g. *McGonigle et al. 2004, Rodríguez et al. 2008*), the average of the flux through the measured plume slice ϕ is equal to the average of the volcanic emission flux Φ.

$$\overline{\phi} = \overline{\Phi} \qquad \textbf{Eq. 3.35}$$

Note that the instantaneous fluxes are not equal, because time elapses between emission from the vent and detection downwind, and because turbulence and diffusion in the atmosphere causes the measured time series to differ from the time series of emission flux.

The lateral integration method has the advantage that the vertical column density is calculated, which in itself is an interesting parameter, especially in respect to possible comparison with other measurements. Also, it directly uses the plume altitude h and lateral distance d, both of which can be measured or estimated by numerous methods. However, the results of the lateral integration method easily become skewed if the measurement zenith angle is large, i.e. the plume is close to the horizon. This is because the method assumes that the average vertical column density V_i is present along the entire segment Δd_i. As these segments become increasingly large for measurement zenith angles α_i approaching ±90°, this assumption is not always correct.

Radial plume integration

The radial integration method is less sensitive to such errors. In contrast to the lateral integration method, it does not assume a constant plume height, but rather assumes a constant distance between instrument and the center of the volcanic plume, labeled r in Fig. 3.13. While this distance typically is not directly measured, it can be obtained from the lateral distance d, the plume altitude h, and the measurement zenith angle α using one of the following relations.

$$r = \frac{d}{\sin(\alpha)} = \frac{h}{\cos(\alpha)} = \sqrt{d^2 + h^2} \qquad \textbf{Eq. 3.36}$$

The length of the segment Δy is then directly given by the increment in measurement zenith angle α between two measurement positions.

$$\Delta y = r \cdot \sin(\Delta\alpha) \qquad \textbf{Eq. 3.37}$$

In this case, the integration is carried out analogous to Eq. 3.33, but instead of calculating vertical columns (Eq. 3.32), the average straight column densities along the segment Δy are added.

$$X = \sum_{i \in Plume} \left(\tfrac{1}{2}(S_i + S_{i+1})\Delta y_i \right) \cdot \sin(\gamma) \qquad \textbf{Eq. 3.38}$$

If the scanning measurements are performed at regular angular increments Δα, Eq. 3.38 becomes

$$X = \sum_{i \in Plume} (S_i) \cdot \Delta y \cdot \sin(\gamma) \qquad \textbf{Eq. 3.39}$$

where N is the number of measurement positions inside the plume. The remaining flux calculation is performed according to Eq. 3.34 and Eq. 3.35.

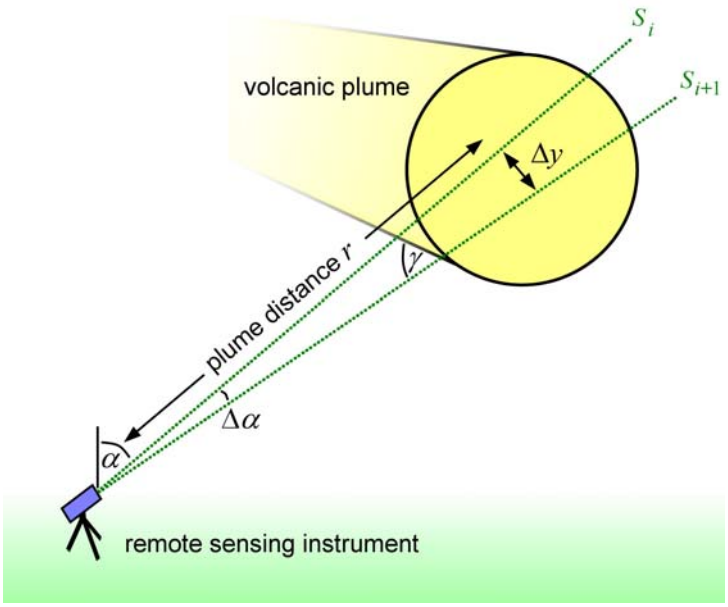

Fig. 3.13 – Schematic of the essential parameters for the radial integration of a volcanic plume slice. The plume is assumed circular in cross-section and moving nearly perpendicular to the scanning plane of the instrument.

The radial integration method is considerably more stable than lateral integration at high measurement elevation angles. Only in situations where the plume is directly overhead does the lateral integration method have slight advantages in accuracy. However, the percentage of measurements where this is the case is small. Therefore, the radial integration technique was

chosen for the volcanic emission flux calculations performed in this study. Numerous examples of this technique are given in chapters 5 and 6.

3.3.3 Mobile DOAS traverse method

The mobile DOAS traverse method has proven an excellent geometry for measuring volcanic emission fluxes. Measurements are conducted from a mobile platform traversing either under the plume (for foot, vehicle, or ship traverses, see *McGonigle et al. 2002, Galle et al. 2003, Kantzas and McGonigle 2008*) or over the plume (for aircraft or unmanned aerial vehicle (UAV) traverses, see *Heue et al. 2008, Kantzas and McGonigle 2008, Kazahaya et al. 2008, McGonigle et al. 2008*). The goal of the technique is to integrate the total SO_2 amount in a cross-section of the volcanic plume. In this case, integration along the viewing direction is performed automatically by the DOAS approach as column densities are retrieved (see Eq. 3.6), and along the second spatial dimension by moving the instrument perpendicular to the plume direction.

Fig. 3.14 shows a schematic of the parameters essential for the mobile DOAS traverse geometry. In the simplest form of the traverse method, the remote sensing instrument is pointed straight to the zenith (or nadir for airborne measurements above the plume). During the recording of a measurement i, the mobile platform is moved by the step distance z_i. Assuming a constant vehicle velocity w_i during the acquisition, the distance covered is given by

$$\Delta z_i = w_i \cdot \Delta t_i \qquad \textbf{Eq. 3.40}$$

where Δt_i is the acquisition time of the individual measurement. The column density S_i retrieved from the recorded spectrum represents the average column density along the step distance Δz_i. If the instrument is aligned vertically (S^Z in Fig. 3.14) and neglecting radiative transfer effects possibly complicating the situation (see chapter 8), the measured column density S^Z is equal to the average plume vertical column density V_i along the step distance Δz_i. If the instrument is moved from one side of the plume to the other, the total amount of an absorber X in the cross-section (or "slice") of the plume is given by

$$X = \sum_{i \in Plume} \left(V_i \cdot \Delta z_i \cdot \sin(\gamma_i) \right) \qquad \textbf{Eq. 3.41}$$

The volcanic emission flux Φ can subsequently be calculated according to Eq. 3.34 and Eq. 3.35. The main advantage of the DOAS traverse technique is that no additional information about the plume geometry is necessary, as is the case for the scanning geometries described in section 3.3.2. Neither the plume height nor the distance to the plume is needed to calculate the volcanic emission flux Φ.

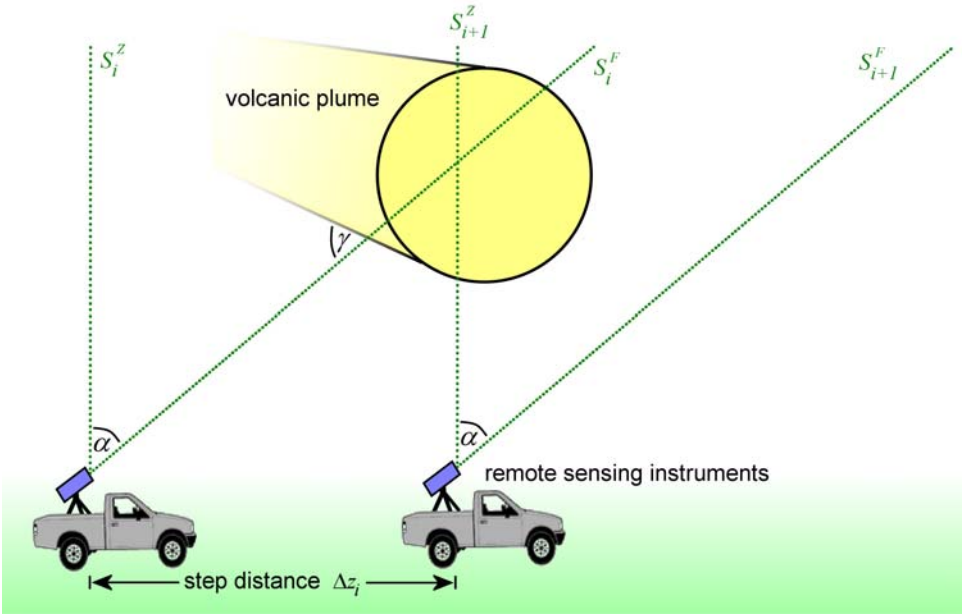

Fig. 3.14 – Schematic of the essential parameters for the mobile DOAS traverse geometry. One or more instruments are pointed in constant directions and moved across the plume, thus integrating the total amount of the measured species along a cross-section of the plume under various elevation angles.

However, additional information can be gained in DOAS traverse measurements by adding additional lines of sight to the measurement. In the example shown in Fig. 3.14, a second instrument was added with a field of view tilted by an angle α in forward-looking direction. This instrument therefore registers the absorption signal of air masses in front of the instrument. One application of such a measurement is to calculate the plume altitude h of a localized plume. If, e.g., the distance between the point of first detection of the plume by the forward-looking instrument and the point of first detection by the zenith-looking instrument is ΔZ, simple trigonometry yields

$$h = \frac{\Delta Z}{\tan(\alpha)} \qquad \textbf{Eq. 3.42}$$

For the special case of $\alpha = 45\ °$, the plume altitude h equals the distance ΔZ. While not yet applied to volcanic emission measurements in the scope of this thesis, forward looking geometries were tested in collaboration with *Volk 2008*.

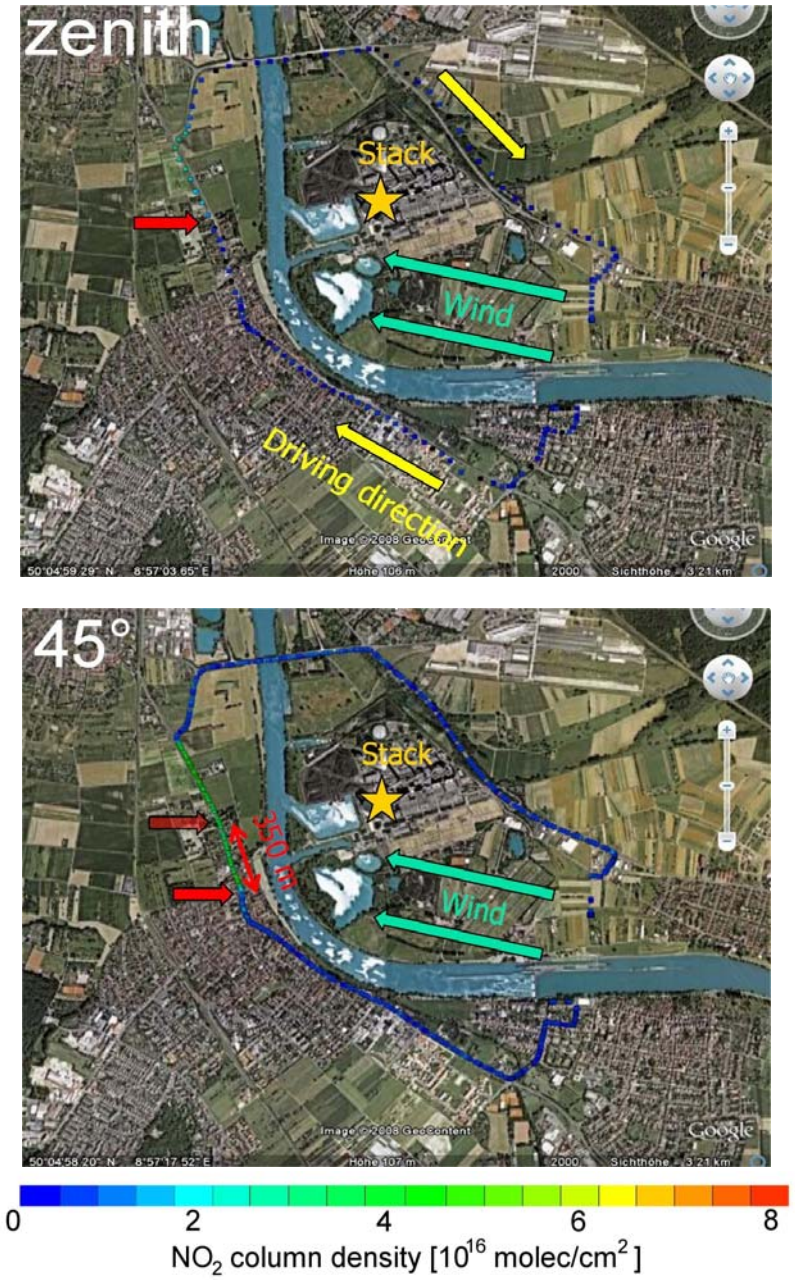

Fig. 3.15 – NO_2 column densities measured during a Multi-Axis DOAS traverse conducted on September 17, 2008 at the Staudinger power plant near Frankfurt, Germany. The top image shows the column densities measured above the vehicle (zenith), the bottom image shows the values measured in a 45° forward-looking geometry. Red arrows mark the respective first detection of the plume. A distance of ΔZ = 350 m was calculated, indicating an identical plume altitude of h = 350 m. (images adapted from *Volk 2008*)

As an example, Fig. 3.15 shows NO_2 column densities measured during a Multi-Axis DOAS traverse at Staudinger power plant near Frankfurt, Germany on September 17, 2008. The left image shows the column densities measured overhead (zenith), the right image depicts the results of a 45° forward-looking DOAS instrument. The forward looking instrument exhibited a higher quantum efficiency, than the zenith instrument, so the acquisition time Δt_i was

shorter resulting in a higher spatial resolution. The measured NO_2 was emitted (partially as NO) from the stack indicated by a yellow star in the images. The wind direction was east-south-east, blowing the emissions towards the north-west. A flux of approximately 30 g/s NO_2 was calculated assuming a wind speed of 3 m/s (*Volk 2008*). The power plant was circled in a clockwise direction, and the red arrows indicate the respective positions at which the first detection of the plume occurred for each instrument. The two positions are separated by a distance of 350 m, thus indicating an identical plume altitude of 350 m. This is a realistic value, as the stack height of this power plant is approximately 250 m. Additional details of this measurement as well as further examples can be found in *Volk 2008*.

3.3.4 Wind speed determination

When retrieving volcanic emission fluxes Φ, the plume-integrated SO_2 amount X is multiplied by the wind speed v at plume height. While this approach is straightforward, the question remains how to obtain an accurate assessment of the wind speed at the altitude of the plume. In the past, different approaches to this problem have been attempted. *Edmonds et al. 2003a* used wind speed data collected by a meteorological station positioned on a hill neighboring Soufriere Hills Volcano (Montserrat). However, as is often the case, the station was located at a considerable distance (more than 4 km from the volcano's summit) and a different elevation than the volcano (350 m, 1/3 of that of the volcano). As the authors themselves state, such measurements are limited in their validity when used as plume speeds, especially since the wind fields around volcanoes can be considerably perturbed by the local, mountainous topography.

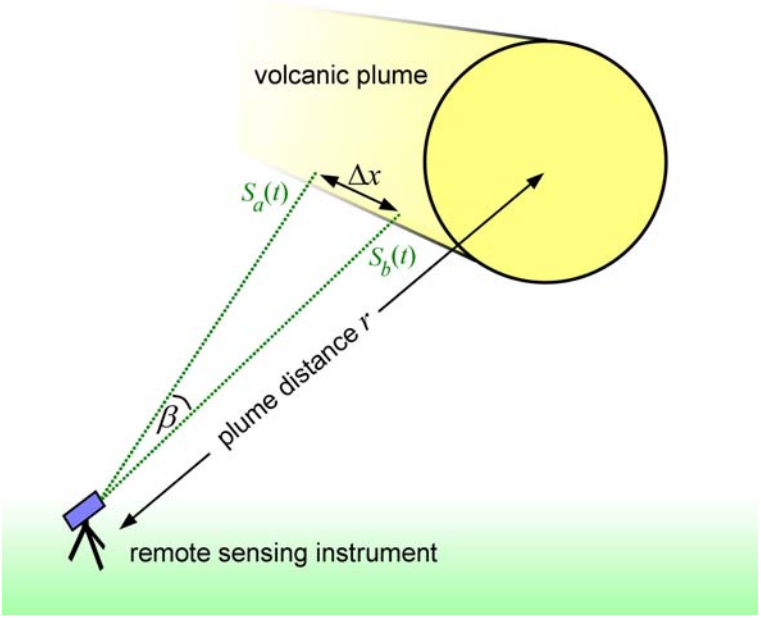

Fig. 3.16 – Schematic of the measurement geometry used for wind speed determination. The two viewing directions intersect the plume at different downwind distances from the emission source.

A better approach was recently introduced (*McGonigle et al. 2005a, McGonigle et al. 2005b, Williams-Jones et al. 2006, Fickel 2008, Johansson 2009a, Johansson et al. 2009b*) in which the wind speed is measured with one or more passive DOAS instruments. The technique uses the fact that volcanic emission plumes are typically inhomogeneous. If the plume SO_2 column density is e.g. measured over an extended period of time at a fixed position, the time series will usually exhibit considerable fluctuations originating in variable instantaneous emission fluxes Φ and turbulence in the atmosphere. For the determination of wind speed, such time series are obtained in two viewing directions intersecting the volcanic plume in two positions with different distances x_a and x_b from the vent and separated by a known distance Δx. This geometry can either be implemented with two remote sensing instruments or, as is shown in Fig. 3.16., with one instrument aimed in two downwind directions either simultaneously (*Johansson et al. 2009b*) or in rapid alternation (implemented in the NOVAC mark II instrument, see section 3.5.1). If only one instrument is used, the distance r between instrument and plume must be known. The transport distance Δx can then be calculated as

$$\Delta x = 2r \cdot \tan\left(\frac{\beta}{2}\right) \qquad \textbf{Eq. 3.43}$$

where β is the angle between the two viewing directions. The optimal value for β depends on the distance to the plume and the typical spatial dimension of plume inhomogeneities. For the measurements performed at Mt. Etna, an ideal transport distance Δx of around 1 km was found. However, for separation angles larger than 20° (this can occur if the plume distance r becomes small), the difference viewing geometry between the two viewing directions leads to a limited comparability. Typically, a separation angle β of about 10° was utilized (see *Fickel 2008* for details).

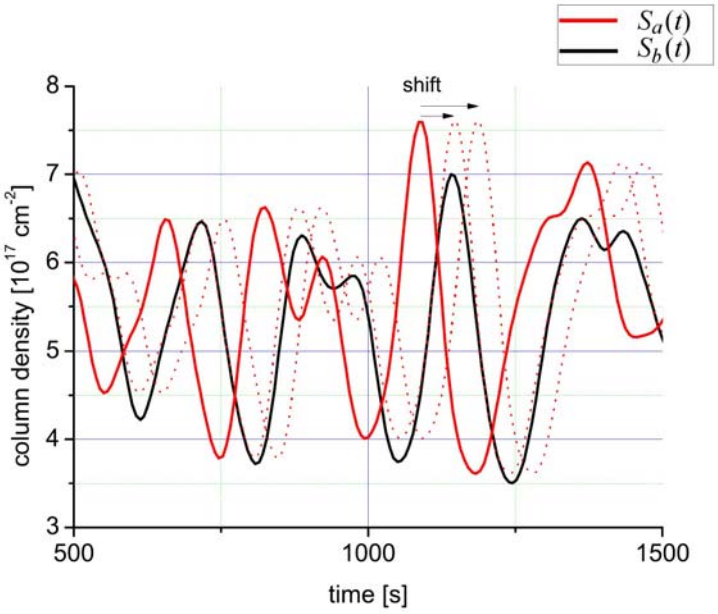

Fig. 3.17 – Example of two SO_2 column density time series $S(t)$ measured by passive DOAS in two different positions downwind of Mt. Etna, Sicily on July 9, 2008 at 15:00. In this example, $S_a(t)$ was measured 900 m closer to the source vent than $S_b(t)$. (adapted from *Fickel 2008*)

As the two measured SO_2 column density time series $S(t)$ are recorded in relative proximity to one another, they are typically similar in their progression, but shifted relative to one another by the plume transfer time ΔT which the plume takes to move from one position to the other. An example measurement is shown in Fig. 3.17. For the plume speed retrieval, the correlation coefficient $c_{a,b}$ between the two time series $S_a(t)$ and $S_b(t)$ is now calculated for different time shifts Δt between the two time series $S(t)$. The correlation coefficient $c_{a,b}$ is defined as

$$c_{a,b}(\Delta t) = \frac{1}{k} \cdot \int S_a(t) \cdot S_b(t + \Delta t) \cdot dt \qquad \textbf{Eq. 3.44}$$

where k is a normalization coefficient. If the measured time series consist of N discrete individual measurements $S(i)$ of equal integration time as is typically the case, the normalized correlation coefficient can be calculated as

$$c_{a,b}(n) = \frac{\sum_{i=1}^{N} \left(\left(S_a(i) - \overline{S}_a \right) \cdot \left(S_b(i+n) - \overline{S}_b \right) \right)}{N \cdot \sigma_a \cdot \sigma_b} \qquad \textbf{Eq. 3.45}$$

where n represents the shift (in units of measurement integration time), $\overline{S}_{a,b}$ is the respective average column density, and $\sigma_{a,b}$ denotes the standard deviation of the respective the time series (see *Fickel 2008* for details). Fig. 3.18 shows the correlation coefficient $c_{a,b}$ of the time series $S_a(t)$ and $S_b(t)$ as a function of the time shift Δt. The displayed points represent the correlation coefficient calculated for different values of Δt corresponding to n integer multiples of the integration time. As the highest correlation coefficient could be obtained between two discrete measurements, a Gaussian is fit to the highest peak in correlation, and the peak of this interpolation is subsequently used to determine the exact plume transfer time ΔT. The error of the thus determined transfer time depends on the measurement integration time and the quality of the fit, as described by *Fickel 2008*.

In the example shown in Fig. 3.18, a plume transfer time of ΔT = 59 s was obtained. During the measurements, the plume was located at a distance r of 5.5 km from the instrument (obtained by means of simultaneous traverse measurements). As a separation angle β of 9.4° was employed, the transport distance Δx amounted to 900 m. Therefore, a wind speed of 15 m/s was obtained according to the following relation.

$$v = \frac{\Delta x}{\Delta T} \qquad \textbf{Eq. 3.46}$$

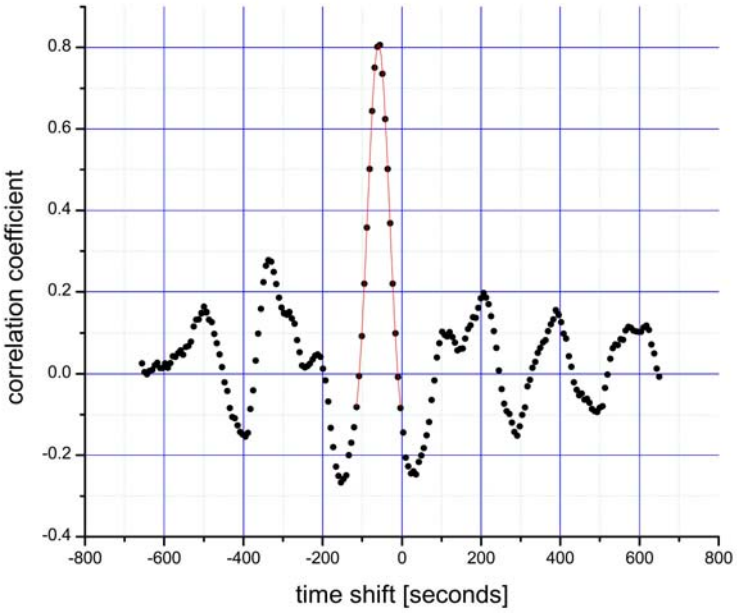

Fig. 3.18 – Correlation coefficient *c* as a function of the time shift Δ*t* of $S_b(t)$ relative to $S_a(t)$. Several peaks in correlation are found, but the peak at -59 s has by far the highest correlation coefficient *c* indicating that this time shift is representative of the plume transfer time from one viewing direction to the other. (adapted from *Fickel 2008*)

3.3.5 Longitudinal diffusion along plume axis

When calculating the volcanic emission flux ϕ by multiplying the integrated SO_2 amount X by the wind speed v (Eq. 3.34), the assumption is made that advective transport by winds represents the only significant form of transport in the plume propagation direction. To this extent, the question could be raised whether or not longitudinal diffusion along the plume axis can be neglected. A recent study by *Platt 2007* showed that this is indeed the case under most conditions.

While being transported downwind, the plume emitted from a point source widens. This widening is a result of turbulent diffusion occurring perpendicular to the propagation direction. If the cross-section of the plume is assumed to be circular in shape (see Fig. 3.19), the radius σ of the plume cross-section can be parameterized using the diffusion coefficient D and the time t since emission into the atmosphere.

$$\sigma = \sqrt{2Dt} \qquad \textbf{Eq. 3.47}$$

Assuming that the concentrations of the emitted gases are constant across the circular cross-section[4] at a given time t, the concentration $c(t)$ scales with the inverse of the cross-sectional area of the plume.

$$c(t) = c_0 \cdot \frac{A_0}{A(t)} = c_0 \cdot \frac{A_0}{\pi \sigma^2} = c_0 \cdot \frac{A_0}{2 \pi D t} \propto \frac{1}{t} \qquad \textbf{Eq. 3.48}$$

If a constant wind speed $v = x/t$ is assumed, the concentration c can be expressed as a function of the distance x from the emission source.

$$c(x) = c_0 \frac{v A_0}{2 \pi D x} \propto \frac{1}{x} \qquad \textbf{Eq. 3.49}$$

Now, the longitudinal concentration gradient along the axis of the plume can be calculated.

$$\frac{dc}{dx} = -c_0 \cdot \frac{v A_0}{2 \pi D x^2} \qquad \textbf{Eq. 3.50}$$

While this formula neglects the effect that longitudinal diffusion would have on the gradient itself, it represents an estimate of the upper limit as longitudinal diffusion would decrease the gradient slightly.

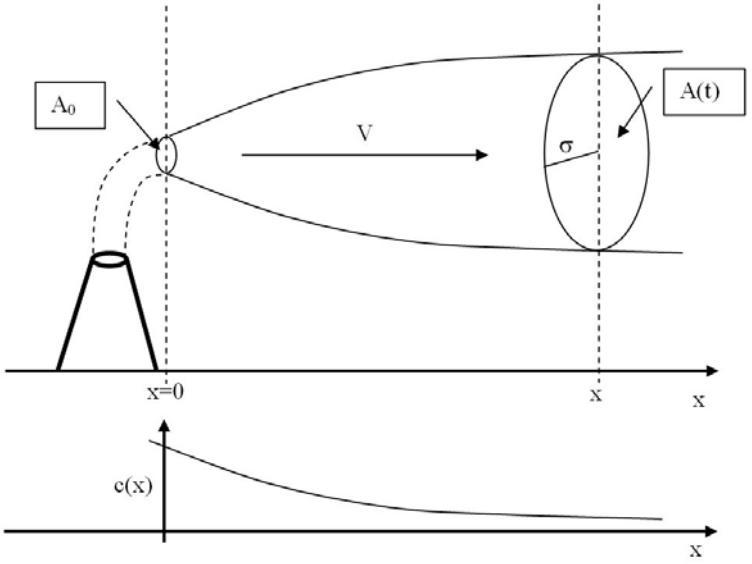

Fig. 3.19 – Schematic of the propagation of a volcanic plume. The plume is assumed to be circular in cross-section with a radius of *σ* and an area *A*. The concentration of an emitted gas *c*(*x*) is assumed to be constant across the circular cross-section, but depends on the distance *x* from the emission point (and therefore on time *t*). (Adapted from *Platt 2007*)

[4] While typical volcanic plume cross-sections can usually be better described by Gaussian distributions, this fact does not fundamentally alter the following calculation. The Gaussian FWHM replaces the diameter 2σ as a measure for the width of the plume.

According to Fick's first law, the diffusive trace gas flux density along the gradient calculated in Eq. 3.50 can be written as

$$J_T = -\frac{dc}{dx} \cdot D_T \qquad \text{Eq. 3.51}$$

Since the horizontal and vertical diffusion coefficients are similar in magnitude in the turbulently mixed troposphere (a fact that can be observed in the similar horizontal and vertical extent of typical plumes perpendicular to their propagation direction), the diffusion coefficient D introduced in Eq. 3.47 can be equated with D_T, and the turbulent diffusive flux density J_T along the plume axis can be calculated.

$$J_T = c_0 \cdot \frac{v\, A_0}{2\, \pi\, x^2} \qquad \text{Eq. 3.52}$$

It is interesting to note that the diffusion coefficient D_T actually cancels. Aside from a number of constants, the turbulent diffusive flux is only dependent on the wind speed v and the inverse of the squared distance from the emission source $1/x^2$.

The diffusive flux density J_T can now be compared to the advective flux density J_A, which is simply given by the product of the wind speed v and the concentration $c(x)$ (as given by Eq. 3.49).

$$\frac{J_T}{J_A} = \frac{D_T}{x \cdot v} \qquad \text{Eq. 3.53}$$

In the free troposphere, the turbulent diffusion coefficient D_T is on the order of 10 m^2/s (*Fiedler 1982*). Therefore, at a distance of 1 km from the vent and a wind speed of 5 m/s, the ratio of diffusive flux to advective flux is only about 0.2%. While these numbers will vary somewhat in actual measurements, the diffusive flux appears to be negligible in the calculation of volcanic emission fluxes, and Eq. 3.34 remains valid.

3.3.6 Error sources in emission flux measurements

The errors directly associated with DOAS retrievals are discussed in section 3.1.5, but this general treatise pertains only to ideal DOAS measurements in which the optical path of the measured radiation is known and instrumental issues such as spectrometer stray light (see section 3.4.4) and temperature effects (section 3.4.5) are neglected. When calculating a volcanic emission flux according to Eq. 3.34, a number of other factors such as the wind speed error and errors in the geometry of the measurement additionally contribute to the total measurement error. For the example of the radial integration technique described in section 3.3.2, the total flux error $\Delta\phi/\phi$ can be expressed using Gaussian error propagation.

$$\left(\frac{\Delta\phi}{\phi}\right)^2 = \left(\frac{\Delta\left(\sum S_i\right)}{\sum S_i}\right)^2 + \left(\frac{\Delta r}{r}\right)^2 + \left(\frac{\Delta(d\alpha)}{d\alpha}\frac{d\alpha}{\tan(d\alpha)}\right)^2 + \left(\frac{\Delta\gamma}{\gamma}\frac{\gamma}{\tan\gamma}\right)^2 + \left(\frac{\Delta v}{v}\right)^2 \qquad \text{Eq. 3.54}$$

(1) (2) (3) (4) (5)

A short examination of each of the terms in Eq. 3.54 is given in the following. The first term describes the error of the measured column densities in a scan or a traverse measurement. For the flux, the relative error of the sum of the column densities is decisive. This can be calculated from the errors of the individual column densities by taking the square root of the quadratic sum of the individual absolute errors ΔS_i. This first term is influenced by errors in the DOAS retrieval (described in section 3.1.5), errors in the spectroscopy e.g. caused by spectrometer stray light (section 3.4.4), temperature effects (section 3.4.5), and errors in assumed optical path in the volcanic plume. While the errors of the DOAS retrieval and those caused by instrumental issues are typically small (< 10%), uncertainties in the optical path inside the plume can be very large (> 70%), and under certain conditions dominate the error of the flux measurement. Because the importance of uncertainties in the optical path for volcanic emission flux measurements was identified, a detailed study on the radiative transfer in and around volcanic plumes was conducted in the scope of this thesis, and the results are given in chapter 8.

The second term in Eq. 3.54 denotes the relative error of the distance r between instrument and volcanic plume. For the lateral integration technique, this term is replaced by the error of the plume height h. When flux is calculated from traverse measurements, this term is omitted. The relative error of the distance r or the plume height h is decisively determined by the available measurements. In some cases, visual observation may be enough to judge the plume height to a high degree of accuracy. Other times, multiple instruments are available, and the plume height or distance can be triangulated (see e.g. section 5.2). In yet other cases, the distance between instrument and plume is retrieved from the wind direction and the measurement zenith angle α. *Johansson 2009a* examined the propagation of errors in measurement geometry for several scenarios and found that while errors can be very large near the horizon, values of below 35% are typically obtained if the plume is located between -50° and 50° measurement zenith angle. Additional calculations on this topic can be found in *Fickel 2008*.

The third term in Eq. 3.54 describes the error of the scan step width $d\alpha$ (in previous sections referred to as $\Delta\alpha$, this notation is not used here to avoid confusion with the error of the measurement zenith angle α). For small steps $d\alpha$, this term can be approximated by the relative error of the step width $\Delta d\alpha/d\alpha$. As tests of the NOVAC mark II instrument by *Sommer 2008* showed that the total positioning error is better than about 0.05°, this term is typically on the order of 1% and can usually be neglected. For traverse measurements, the term is replaced by the relative error in the distance between two subsequent measurement points. As these are determined by GPS, the relative error is usually also small.

The fourth term in Eq. 3.54 describes the influence of the error in the plume propagation direction relative to the scanning plane. Again, the relative error of the intersection angle γ (see Fig. 3.14) is weighted by $\gamma/\tan(\gamma)$. For nearly perpendicular intersection ($\gamma \approx 90°$), the contribution of this term is negligible, as the weighting factor approaches null. Only if the relative intersection angle becomes smaller than about 20° does the weighting factor approach 1. Then, the relative error of the plume propagation direction (or wind direction), which can be considerable, becomes a dominant error source.

The final term in Eq. 3.54 is simply the relative error of the wind speed. As is to be expected, an overestimation or underestimation in wind speed by a certain amount directly translates to the same error in the flux. Therefore, the determination of the wind speed at plume height remains one of the most important aspects of accurate volcanic emission flux measurements (see section 3.3.4).

Error Source	Associated Term in Eq. 3.54	Typical Value	Maximum Value	See sections
DOAS retrieval	1	5%	15%	3.1.5
Spectroscopy	1	10%	20%	3.4.1, 3.4.2, 3.4.4, 3.4.5
Scanner positioning	3	3%	10%	3.5.1
Plume height / distance[5]	2	15%	40%	3.3.2
Relative wind direction[6]	4	20%	40%	3.3.2
Wind speed in plume	5	20%	50%	3.3.4
Radiative transfer	1	30%	70% or more	Chapter 8
Total error in flux $\Delta\phi/\phi$		Approx. 40%	90% or more	

Tab. 3.1 – Overview of the error sources that influence volcanic emission flux measurements. For each contribution, a typical and maximum value is given, and the corresponding total flux error $\Delta\phi/\phi$ was calculated according to Eq. 3.54. In the last column, references to other sections in this thesis are given where the individual effects are described in more detail.

[5] Does not need to be considered in traverse measurements

[6] Here, 90° error in wind direction correspond to 100% error

A summary of the effects that contribute to the total flux error $\Delta\phi/\phi$ is given in Tab. 3.1. Also given are typical and assumed maximum values for each contribution. Using these values, the typical error in volcanic emission flux measurements was calculated to about ± 40%. While this value is rather high and future efforts are required to reduce the uncertainty (see e.g. the radiative transfer retrievals discussed in chapter 8), volcanic emission fluxes often fluctuate over several orders of magnitude between different phases of activity. Therefore, the DOAS measurements conducted in this thesis and in the scope of the NOVAC project (see chapter 5) are valuable for volcanic monitoring and risk assessment, even if the uncertainties are high. Also, as many of the errors are of stochastic nature, the uncertainty of average fluxes retrieved from long-term monitoring measurements can be assumed lower.

3.4 Advanced concepts for data retrieval

In the previous sections of this chapter, the DOAS technique has been described both in principle and application. Additional information can be found in *Platt and Stutz 2008*. The described methods are valid for the differential spectroscopy of any trace gas in the atmosphere. During the course of this study, however, a number of issues specifically related to the measurement of volcanic emissions (especially SO_2) with miniature passive DOAS instruments were examined. This section gives an overview of a number of the encountered issues and summarizes the potential problems along with some possible solutions.

3.4.1 Wavelength dependent optical paths

Like most other remote sensing techniques, the DOAS technique does not directly yield the concentration of a certain species, but rather the column density S, which is defined by the integral of the concentration over the optical path of the measured incident radiation. In principle, the column density is obtained by measuring the differential optical density $\tau(\lambda)$ of an absorber and dividing by the known differential absorption cross-section $\sigma(\lambda)$ (compare Eq. 3.6).

$$S = \int_L c \cdot dl = \frac{\tau'(\lambda)}{\sigma'(\lambda)} \qquad \text{Eq. 3.55}$$

However, this approach assumes that the length of the light path L in the atmospheric area of interest is identical for all wavelengths λ. Unfortunately, this assumption is not always valid. When scattered solar radiation is used as a light source for remote sensing measurements, the optical path length L is not well defined. Each photon that reaches the detector of the instrument has taken a different path through the atmosphere. Both scattering and absorption can cause the optical path length L in the area of interest to become dependent on wavelength. In this case, the column density also becomes dependent on wavelength.

$$S(\lambda) = \int_{L(\lambda)} c \cdot dl \qquad \text{Eq. 3.56}$$

If absorption occurs at a specific wavelength, less photons of this wavelength make it from the sun to the instrument. However, the average optical path length L of the photons that do arrive at the instrument (these are the ones that were measured, not the absorbed ones) may differ from the path length of those at an adjacent, non-absorbing wavelength. The wavelength dependency of the column density must be taken into account according to Eq. 3.56 whenever the optical density of an absorbing species is large enough to significantly influence the average optical path length L. In the following, this is referred to as "strong absorption". If the path length is not significantly influenced by the absorbing trace gases, the "weak absorption" approximation is valid and the standard DOAS approach is applicable (Eq. 3.5).

The influence of strong absorption was first observed for measurements of stratospheric ozone (*Solomon et al. 1987, Perliski and Solomon 1993, Marquard et al. 2000*). In the scope of this study, strong absorption was found to complicate the retrieval of SO_2 column densities in volcanic plumes (*Kern et al. 2009*). The SO_2 mixing ratios typical for such plumes (ppm range) are high enough to considerably influence the radiative transfer of scattered solar radiation on (and sometimes even between) the strong absorption bands of SO_2 near 300 nm. Two approaches were developed for dealing with this issue.

Both the absolute magnitude and the differential depth of the SO_2 absorption cross-section decrease by two orders of magnitude between 300 and 325 nm (see e.g. Fig. 3.23). This fact can be used to maintain a constant, low optical density in DOAS evaluations of SO_2. This is achieved by using a variable wavelength window for the DOAS fit. In an iterative algorithm, the wavelength range is shifted from wavelengths around 309 nm where the instrument sensitivity is typically highest (see section 3.4.3) towards longer wavelengths until the retrieved SO_2 differential optical density is below a predefined threshold for the maximum allowed optical density. This method is referred to as the weak absorption DOAS retrieval technique in the following.

Radiative transfer modeling results indicated that the optical path of scattered radiation could be assumed approximately independent of wavelength for SO_2 optical densities below 5%, if the distance between instrument and volcanic plume is shorter than about 2 km (see chapter 8). Therefore, this value was defined as the weak absorption threshold, and was used as a condition indicating wavelength independent optical paths. Tab. 3.2 shows the spectral positions of the fit windows used in the iterative evaluation process. For each window, the respective maximum allowed SO_2 column density was calculated from the respective maximum differential SO_2 cross-section and the above mentioned weak absorption threshold. The weak absorption retrieval technique starts with the first fit window, calculates the SO_2 column density, and moves to the next window if the threshold is exceeded. This process is repeated until the weak absorption condition is met. Examples of evaluations conducted with this technique are given in chapter 5.5.

Fit window	Spectral fit window [nm]	Max. differential SO_2 cross-section [cm^2]	Max. SO_2 column density [molec/cm^2]
1	305.6 – 327.0	4.47×10^{-19}	1.12×10^{17}
2	307.8 – 327.0	3.29×10^{-19}	1.52×10^{17}
3	309.8 – 327.0	1.93×10^{-19}	2.59×10^{17}
4	314.3 – 327.0	5.53×10^{-20}	9.04×10^{17}
5	319.1 – 327.0	2.10×10^{-20}	2.38×10^{18}
6	320.7 – 327.0	1.30×10^{-20}	3.85×10^{18}
7	324.9 – 331.9	3.20×10^{-21}	1.56×10^{19}

Tab. 3.2 – Fit windows used in the weak absorption SO_2 evaluation technique. The maximum of the differential SO_2 absorption cross-section (according to *Bogumil et al. 2003*) is given for each window. Also shown is the respective maximum SO_2 column density that fulfills the requirement for weak absorption i.e. that results in a differential SO_2 optical density of < 5%.

While the weak absorption technique can be used to ensure that the standard DOAS approach is applicable and yields a correct column density S in the retrieved wavelength window, in-depth analysis of the radiative transfer occurring in and around volcanic plumes showed that the average optical path length L of measured scattered solar radiation in these plumes is greatly influenced by certain measurement parameters. These include the distance between instrument and plume, the aerosol extinction coefficient in the plume, the SO_2 load in the plume, and the aerosol conditions in the ambient air surrounding the plume. Without knowledge of the optical path length L, the column density measured with the DOAS technique can not be dependably converted to average concentration or mixing ratio.

Furthermore, the subsequent retrieval of volcanic emission flux can be skewed by inaccurate assumptions of L. Problems arise when the aerosol loads inside and around the plume increase, or when measuring high SO_2 columns at long distances from the plume. However, an algorithm was developed in the scope of this thesis for the first time allowing the retrieval of optical path lengths L by using additional information inherent in spectroscopic measurements capable of resolving individual SO_2 absorption bands combined with radiative transfer modeling. The allowance for wavelength dependent optical paths (Eq. 3.56) is the key to this retrieval. Chapter 8 is dedicated to the description of this technique.

3.4.2 Non-commutative convolution

When reference absorption cross-sections are fit to the measured optical density during the DOAS retrieval, the limited resolution of the spectrometer must be taken into account. This can either be done experimentally by recording the reference cross-sections with the same spectrometer with which the measurements are performed, or mathematically by convoluting high resolution literature reference cross-sections with the instrument line shape (ILS), as described in section 3.1.3 (Eq. 3.12). The ILS describes the response of the spectrometer to a monochromatic light source (also see e.g. *Jähne 2002*).

Both techniques work well for weak absorbers (see section 3.4.1), but strong absorbers can complicate the DOAS retrieval, because the limited resolution of the spectrometer can cause a non-linear relationship between the measured optical density τ_{meas} and the column density S compare Eq. 3.6). As mentioned in section 3.1.3, a DOAS instrument does not directly measure the optical density τ (see Eq. 3.5), but instead records the incident spectral intensity $I_{inc}(\lambda)$ convoluted with the ILS. In the following equations, the convolution with H will be represented by a set of brackets (<>).

$$I_{meas}(\lambda) = < I_{inc}(\lambda) > \qquad \textbf{Eq. 3.57}$$

Therefore, the measured optical density τ is given by

$$\tau = \ln\left(\frac{I_0}{I_{meas}}\right) = \ln\left(< \exp(\sigma \cdot S) >\right) \qquad \textbf{Eq. 3.58}$$

For small optical densities ($\sigma \cdot S << 1$), the exponential function can be expanded and the convolution can then be performed directly on the absorption cross-section.

$$\tau = \ln\left(< 1 + (\sigma \cdot S) >\right) = \ln\left(1 + S \cdot < \sigma >\right) = S \cdot < \sigma > \qquad \textbf{Eq. 3.59}$$

Standard DOAS retrieval algorithms using literature absorption cross-sections rely on this approximation (compare to Eq. 3.6). However, this approach is only valid for weak absorbers. For large optical densities, the convolution and the exponential function are not commutative.

$$\tau = \ln\left(< \exp(\sigma \cdot S) >\right) \neq S \cdot < \sigma > \qquad \textbf{Eq. 3.60}$$

Therefore, convolving literature cross-sections σ with the ILS is not a valid approach if the optical density τ is not small compared to unity. Instead, the cross-section σ must first be multiplied with the column density S, the exponential must be taken followed by the convolution with the instrument line shape, and lastly the logarithm must be taken. In practice, however, this approach can only be implemented in an iterative manner, as it requires a priori information about the column density *S. Frankenberg et al. 2005* describe such an iterative retrieval algorithm for strong absorbers called Iterative Maximum A Posteriori DOAS (IMAP-DOAS).

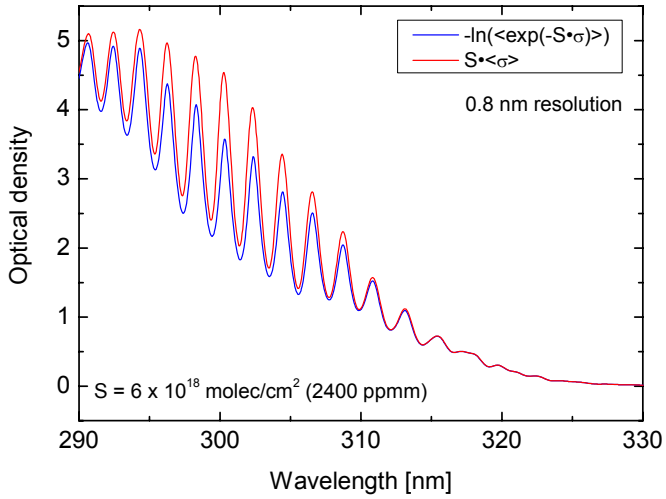

Fig. 3.20 – Comparison of the standard DOAS convolution approximation (red) and the mathematically correct convolution (blue) for a strong absorption scenario (S = 2400 ppmm). Discrepancies can be observed for the strong SO_2 absorption bands.

Because of the added complexity of an iterative retrieval, the magnitude of the non-commutative convolution effect was quantified for DOAS retrievals of SO_2. This was achieved by comparing the direct convolution of a reference SO_2 absorption cross-section (right side of Eq. 3.60) with the comprehensive preparation of the cross-section (left side of Eq. 3.60) for a variety of SO_2 column densities S. An example is shown in Fig. 3.20. The blue line represents the SO_2 optical density according to the exact model, as it would be measured in the radiation entering the spectrometer assuming an SO_2 column density of $6 \cdot 10^{18}$ molec/cm^2 (2400 ppmm), a value which is large, but not unrealistic for volcanic emission measurements. The red line, however, describes the column density calculated according to the simplified model (right side of Eq. 3.60) assuming a DOAS instrument with an 0.8 nm FWHM Gaussian ILS (typical for Ocean Optics USB2000 or similar spectrometers). The differential absorption line depths are significantly larger in this approximation, indicating that the DOAS retrieval of the measured (blue) spectrum would result in a considerably lower column density S (more than 30% lower at 300 nm). Towards higher wavelengths where the SO_2 optical densities decrease, the discrepancy between the two approaches decreases as well and practically identical results are obtained for wavelengths above 320 nm.

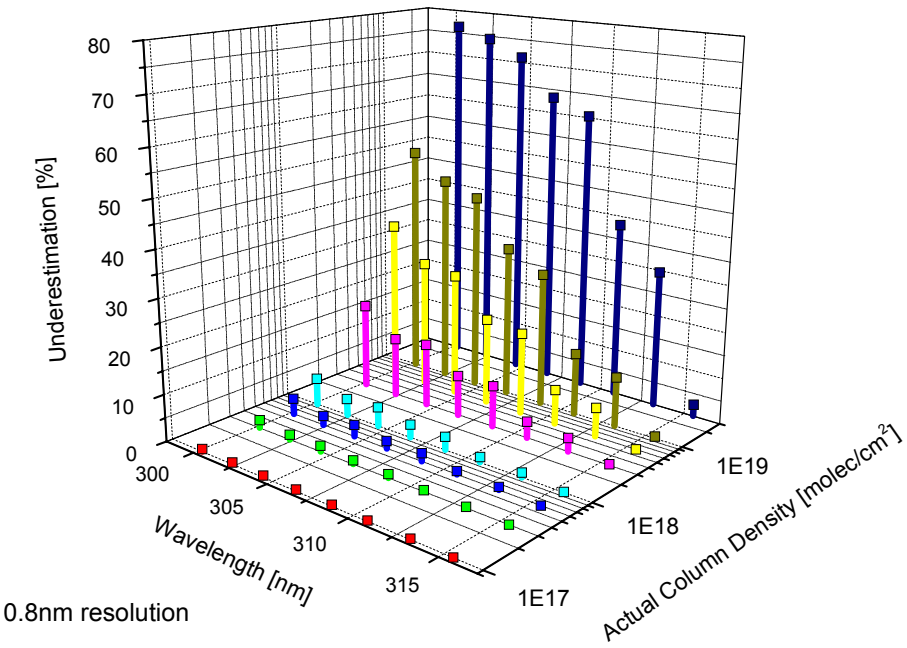

Fig. 3.21 - Magnitude of underestimation in standard DOAS measurements conducted at 0.8 nm optical resolution caused by a non-commutative cross-section convolution. The largest errors occur for high column densities *S* and short wavelengths *λ*, where the differential absorption bands of SO_2 are strongest.

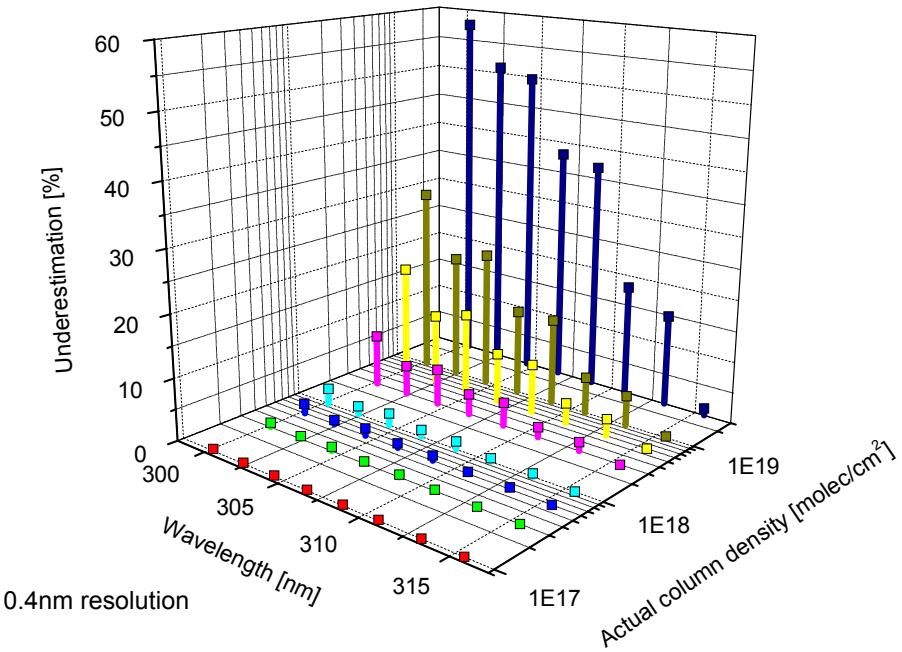

Fig. 3.22 – Magnitude of underestimation in standard DOAS measurements conducted at 0.4 nm optical resolution caused by a non-commutative cross-section convolution. Errors are slightly smaller than for 0.8 nm optical resolution (Fig. 3.21) and again occur for high column densities *S* and short wavelengths *λ*.

These calculations were repeated for several different SO_2 column densities typical for volcanic emissions measurements. The results are displayed in Fig. 3.21. It is evident that the underestimation is significant for wavelengths around 300nm and for extreme column densities. To ensure an underestimation of less than 5% for column densities below 10^{19} molec/cm^2 (4000 ppmm), it is necessary to move the retrieval range to wavelengths above 315 nm. The same study was conducted for a spectrometer with an 0.4 nm FWHM Gaussian ILS, as was used for the NOVAC mark II instruments described in section 3.5.1. While typically reduced by about 1/3, the underestimation was still considerable for high column densities and short wavelengths, as is shown in Fig. 3.22. An underestimation of below 5% for column densities below 10^{19} molec/cm^2 (4000 ppmm) was achieved for wavelengths above the 313 nm absorption band.

While the results of the study on the non-commutative convolution effect described above may be alarming at first, it is fairly easy to compensate for the errors. Either the weak absorption method described in section 3.4.1 should be applied, or an iterative algorithm must be used (e.g. *Frankenberg et al. 2005*). However, modelling results showed that the radiative transfer errors mentioned in section 3.4.1 and described in detail in chapter 8 are significantly higher in magnitude and therefore the decisive source of the total measurement error.

3.4.3 Instrument sensitivity

As the first and foremost goal of the NOVAC project (see section 5.1) was to quantitatively measure the volcanic emission flux of SO_2 at numerous volcanoes around the world, maximizing the sensitivity (i.e. minimizing the detection limit) of the developed DOAS instruments in regard to this species was of great importance. In section 3.1.6, it was shown that the detection limit of a DOAS instrument S_{min} is proportional to the deviation of the DOAS fit residual $\Delta\Psi$ and inversely proportional to the differential absorption cross-section σ' of a particular trace gas (see Eq. 3.26). The sensitivity s of an instrument to a certain species can now be defined as the inverse of the instrument's detection limit regarding this species.

$$s = \frac{1}{S_{\min}} = \frac{\overline{\sigma}'}{\Delta\Psi} \qquad \textbf{Eq. 3.61}$$

In all spectroscopic techniques, the effective differential absorption cross-section $\overline{\sigma}'$ is dependent on the high resolution absorption cross-section of the particular absorber as well as the instrument's optical resolution (see **Eq. 3.12**).

Optical resolution

In the case of SO_2, literature absorption cross-sections measured at an optical resolution of 0.2 nm are known (*Vandaele et al. 1994, Bogumil et al. 2003*). However, volcanic emissions measurements of SO_2 are typically conducted at lower resolutions (between 0.4 nm and 1.2 nm). The reason for this is of technical nature. As the spectral resolution of a spectrometer is

decisively influenced by the width of its entrance slit (see section 3.1.3), a tradeoff between optical resolution and light throughput must be considered when designing a spectroscopic instrument. The smaller the entrance slit is, the higher the optical resolution will be, but the lower the light throughput (which approximately scales with the slit width) will be at the same time. A lower light throughput will increase noise in the measurement. Therefore, the ideal spectrometer will not necessarily be the one with the highest resolution.

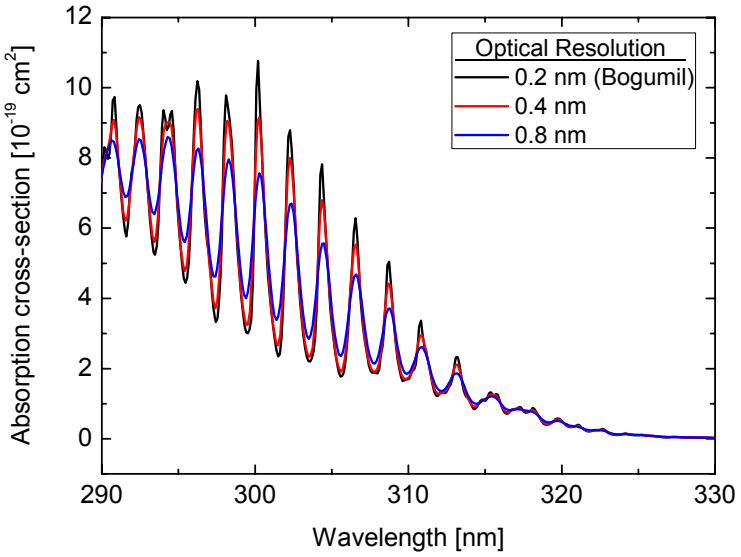

Fig. 3.23 – Influence of the instrument optical resolution on the observed differential absorption cross-section $\overline{\sigma}'$ of SO_2. Instruments with higher optical resolution can better resolve the narrow absorption structures. (0.2 nm resolution data taken from *Bogumil et al. 2003*, 293K)

The influence of optical resolution on the magnitude of the effective differential absorption cross-section $\overline{\sigma}'$ of SO_2 is depicted in Fig. 3.23. Here, the reference cross-section measured at 0.2 nm resolution by *Bogumil et al. 2003* was convoluted with Gaussian ILS representing optical resolutions of 0.4 nm (red) and 0.8 nm (blue). The results show that the differential SO_2 absorption cross-section effective at 0.4 nm optical resolution is approximately 15 % lower than in the 0.2 nm literature spectrum for the absorption bands around 300 nm. An optical resolution of 0.8 nm leads to an effective differential absorption cross-section that is 50 % lower than the original literature spectrum, and about 40 % lower than for 0.4 nm optical resolution.

Since the doubling of the entrance slit width increases the light throughput of an instrument by approximately a factor of 2, the signal-to-noise ratio (SNR*)* is increased by approximately 40% (see below). Therefore, moving from 0.2 nm to 0.4 nm increases the sensitivity by about 25%. Doubling the slit width again (moving from 0.4 to 0.8 nm optical resolution) however,

does not improve the instrument sensitivity, as the increase in SNR is approximately compensated by the decrease in effective differential absorption cross-section $\overline{\sigma}'$.

Noise

Aside from the effective differential absorption cross-section $\overline{\sigma}'$, the deviation of the DOAS fit residual $\Delta\Psi$ determines the instrument sensitivity. In an ideal spectroscopic measurement (in which the electronic readout noise is negligible), the magnitude of the fit residual $\Delta\Psi$ is determined by the photon noise (or shot noise). The standard deviation of a measured radiation intensity is susceptible to statistical fluctuations whenever a finite number of photons are measured (known as photon statistics). The standard deviation σ of this photon noise is equal to the square root of the average number of photons detected *N*.

$$\sigma = \sqrt{N} \qquad \textbf{Eq. 3.62}$$

As the measured intensity *I* is itself proportional to the number of measured photons *N*, the SNR I/σ_I of a spectroscopic measurement is given by

$$\frac{I}{\sigma_I} = \frac{k \cdot N}{k \cdot \sigma_N} = \frac{N}{\sqrt{N}} = \sqrt{N} \qquad \textbf{Eq. 3.63}$$

In the DOAS retrieval, the measured intensities are converted to optical densities according to Eq. 3.5. Thereby, the logarithm of the ratio of intensities $\ln(I_0/I)$ is obtained. If *R* denotes the ratio of intensities I/I_0, the SNR of this ratio can be calculated according to the standard statistical propagation of uncertainty.

$$\frac{R}{\sigma_R} = \left(\left(\frac{\sigma_I}{I} \right)^2 + \left(\frac{\sigma_{I0}}{I_0} \right)^2 \right)^{-1/2} \qquad \textbf{Eq. 3.64}$$

If both intensities *I* and I_0 are recorded with the same instrument, the SNR of the two will typically be similar. Under this assumption, the SNR of the ratio R becomes

$$\frac{R}{\sigma_R} = \frac{1}{\sqrt{2}} \cdot \frac{I}{\sigma_I} = \frac{1}{\sqrt{2}} \sqrt{N} \qquad \textbf{Eq. 3.65}$$

According to statistical error propagation, the noise of the logarithm of intensities (or optical density, see Eq. 3.5) $\ln(I_0/I)$ can be calculated as

$$\sigma_\tau = \frac{\sigma_R}{R} = \sqrt{2} \cdot \frac{1}{\sqrt{N}} \qquad \textbf{Eq. 3.66}$$

Considering that the measured intensity *I* is proportional to the number of detected photons *N* yields

$$\sigma_\tau = \sqrt{2k} \cdot \frac{1}{\sqrt{I}} \qquad \textbf{Eq. 3.67}$$

According to this relation, the noise superimposed on the measured optical density τ is proportional to the inverse of the square root of the measured intensity *I*. This noise can not be taken into account by the DOAS fit and will remain in the fit residual. In an ideal fit, the fit residual will be solely composed of noise, and the deviation of the fit residual $\Delta\Psi$ will be proportional to the standard deviation σ_τ of the noise (see *Stutz and Platt 1996* for a detailed analysis). This yields the proportionality

$$\Delta\Psi \propto \frac{1}{\sqrt{I}} \qquad \textbf{Eq. 3.68}$$

Simply put, the magnitude of the DOAS fit residual will decrease by about 30% for every doubling in measured intensity. This can be achieved either by increasing the light throughput of an instrument, or by increasing the total integration time of a measurement. However, the relation is limited to the regime in which photon statistics dominate the measurement noise, so both techniques will only improve the measurement to the point where the electronic readout noise becomes dominant.

Spectral sensitivity

The sensitivity of a DOAS instrument (as defined by Eq. 3.61) is dependent on the spectral position of the retrieval. The above considerations can be used to calculate the relative spectral sensitivity. Fig. 3.24 displays the inverse of the noise $1/\sigma_\tau$ superimposed on the measured optical density τ for a typical DOAS measurement relative to its value at 322 nm (blue line, calculated according to Eq. 3.67). The noise level decreases towards higher wavelengths, as the incident spectral intensity *I* increases (see Eq. 3.67). Therefore the inverse of the noise increases. Also shown (red) is the effective SO_2 differential absorption cross-section $\overline{\sigma}'$, which decreases towards higher wavelengths (see Fig. 3.23).

From these two curves, the relative spectral sensitivity *s* can be calculated according to Eq. 3.61. The results of this study are presented in Fig. 3.25. For an instrument with an optical resolution of 0.4 nm, the spectral sensitivity to SO_2 was found to peak on the absorption band located at 309 nm. At lower wavelengths, the limited intensity of incident scattered solar radiation increases the noise level and thereby lowers the sensitivity. Towards higher wavelengths, the sensitivity decreases due to the decrease in the depth of the differential SO_2 absorption structures (see Fig. 3.23). When the study was repeated for an instrument with an optical resolution of 0.8 nm, a very similar spectral sensitivity was obtained, again peaking at 309 nm.

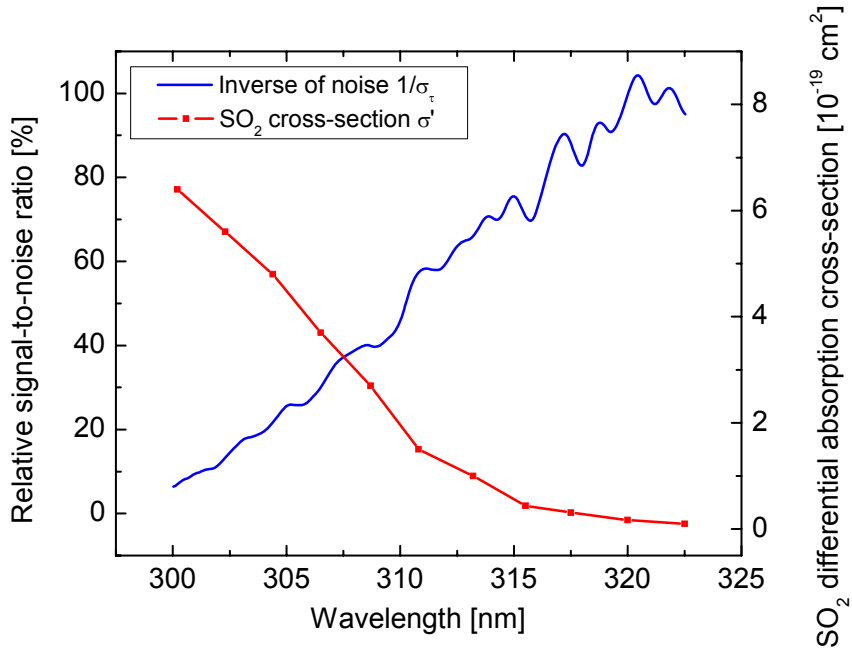

Fig. 3.24 – Inverse of the noise level $1/\sigma_\tau$ inherent in a DOAS retrieval of SO_2 relative its value at 322 nm (blue line). The noise level was obtained from a typical DOAS measurement of scattered solar radiation (59° solar zenith angle). Also shown (red) is the differential depth of the measured SO_2 absorption bands between 300 and 325 nm assuming an instrument optical resolution of 0.4 nm.

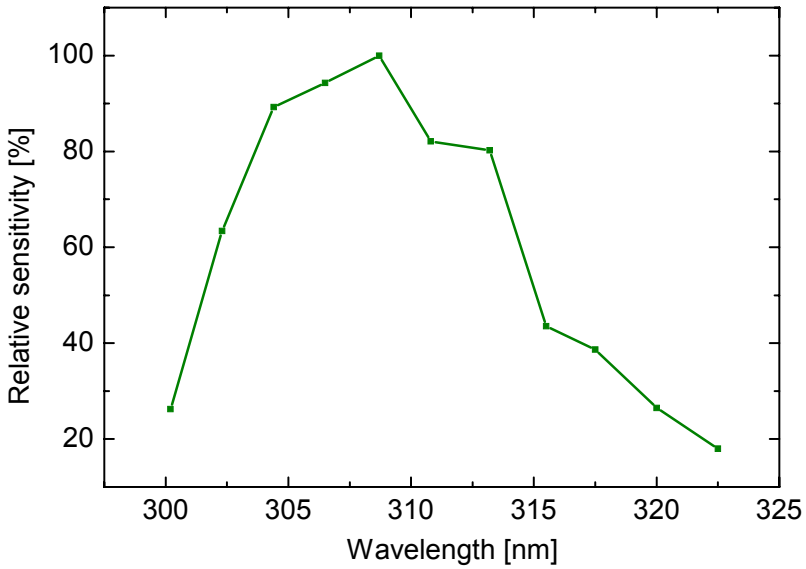

Fig. 3.25 – Instrument spectral sensitivity as a function of wavelength for a DOAS spectrometer with 0.4 nm optical resolution calculated according to Eq. 3.61. The optimal sensitivity is attained for the SO_2 absorption band at 309 nm. Here, the ideal tradeoff between strong SO_2 absorption and sufficient incident radiation was found.

This study shows that a DOAS retrieval aimed at achieving the highest possible sensitivity (i.e. the lowest possible detection limit) in regard to SO_2 should be conducted in the wavelength range around 309 nm. For high SO_2 column densities, however, it was found that this wavelength range is not ideal, as strong absorption effects can cause wavelength-dependent optical paths in the volcanic plume, as described in section 3.4.1. Therefore, this evaluation range is only recommended for low SO_2 column densities.

3.4.4 Spectrometer stray light

In spectroscopy, the term stray light is used to describe radiation that falls onto an instrument's detector in an unwanted, often uncontrolled manner. If $\lambda(j)$ denotes the wavelength of radiation that is measured by pixel j of the spectrometer's detector according to the spectrometer's dispersion function (Eq. 3.14), radiation of all other wavelengths should be rejected from this pixel. However, this is never entirely the case for several reasons. For one, grating spectrometers have multiple orders, and light from other orders also reaches the detector. Also, the light reflected off baffles inside the spectrometer inherently illuminates the detector to some degree. Both of these effects contribute to spectrometer stray light.

The contribution of stray light to the measurement signal should be kept as low as possible, as it will falsify measured optical densities if it becomes significant. Hardware methods for reducing stray light include careful baffling inside the spectrometer and positioning a band-pass filter at the spectrometer entrance to avoid radiation of wavelengths not needed for the DOAS retrieval from entering the spectrometer. However, stray light will never be completely avoided. Because the effect of stray light on the DOAS retrievals of SO_2 was thought to be of similar magnitude as other error sources, a study was performed by *Van Roozendael et al. 2006* to characterize the stray light inside an Ocean Optics© USB2000 spectrometer. The authors measured the spectrometer response to a monochromatic light source (solar simulator with a Bentham© double monochromator) at approximately 30 different wavelengths in the spectral range of the spectrometer (275 to 425 nm). An example of such a measurement is given in Fig. 3.26.

The intensity of light measured outside of the range given by 3 times the FWHM of the spectral line is considered purely the result of stray light.[7] In this manner, the contribution of pixels outside the spectral peak itself towards the total spectrometer stray light was characterized.

[7] An accurate correction of electronic offset and detector dark current are fundamental in this approach. A temperature stabilization is therefore mandatory.

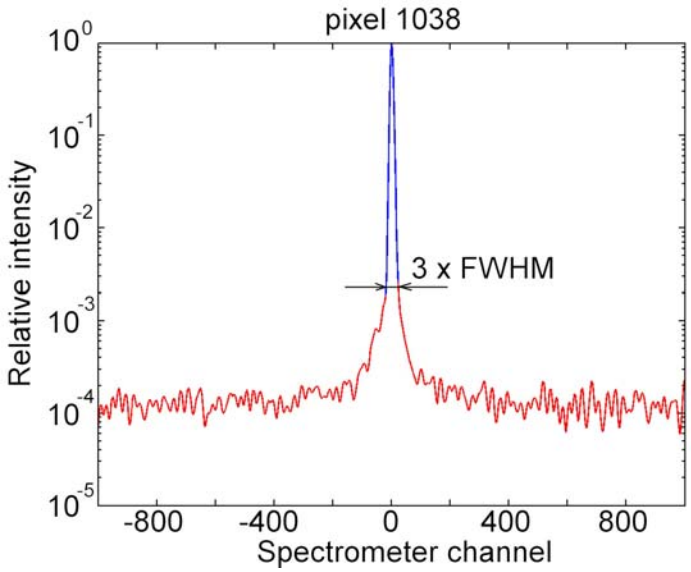

Fig. 3.26 – Spectrometer response to a monochromatic light source at 350 nm. Note the logarithmic intensity scale. Any signal measured outside the wavelength range given by 3 times the FWHM of the spectral line was considered stray light. (adapted from *Van Roozendael et al. 2006*)

Based on this approach, a method for correcting stray light in a spectrometer was introduced by *Zong et al. 2006*. Here, the "stray light distribution function" SDF is determined. It is set to null for values inside 3 times the FWHM of the spectral line (referred to as B(λ) in the following), and describes the pixel intensity I_i relative to the total stray light intensity for all other wavelengths. The SDF therefore represents the contribution of radiation of a particular wavelength λ (i.e. the respective pixel) to the total stray light. It is determined for a number of wavelengths λ_j across the detector, then interpolated for all other pixels, thereby yielding an $n \times n$ SDF matrix $\boldsymbol{D}$, where n is the number of pixels on the detector.

$$D_{i,j} = \frac{I_{i,j}}{\sum_{i \notin B(\lambda_j)} I_{i,j}} \qquad \text{for } i \in \mathrm{B}(\lambda_j) \qquad \textbf{Eq. 3.69}$$

$$D_{i,j} = 0 \qquad \text{for } i \in \mathrm{B}(\lambda_j) \qquad \textbf{Eq. 3.70}$$

In this approach, a measured spectrum vector $\boldsymbol{Y_{meas}}$ can now be divided into the contribution originating from the incident light $\boldsymbol{Y}_{\mathrm{inc}}$ and the contribution of the stray light $\boldsymbol{Y_{str}}$, which in turn can be formulated using the above defined SDF matrix $\boldsymbol{D}$. Note that this approach is only valid, if a band-pass filter is used blocking wavelengths outside the spectral range of the instrument from entering.

$$Y_{meas} = Y_{inc} + Y_{str} = (E + D) \cdot Y_{inc} \qquad \textbf{Eq. 3.71}$$

Here, $\boldsymbol{E}$ is the identity matrix. A new matrix $\boldsymbol{A}$ is then defined as

$$A = E + D \qquad \text{Eq. 3.72}$$

This matrix needs to be inverted to obtain the incident radiation vector $\boldsymbol{Y_{inc}}$.

$$Y_{inc} = A^{-1} \cdot Y_{meas} \qquad \text{Eq. 3.73}$$

Because $\boldsymbol{A^{-1}}$ is nearly an identity matrix (see Eq. 3.72), the inversion is reliable. Further details of this technique are given by *Zong et al. 2006*. Fig. 3.27 depicts the influence of a stray light correction performed in the above described manner on a typical measurement spectrum. The original spectrum (blue) is slightly affected by stray light, and the corrected spectrum (red) lies somewhat lower.

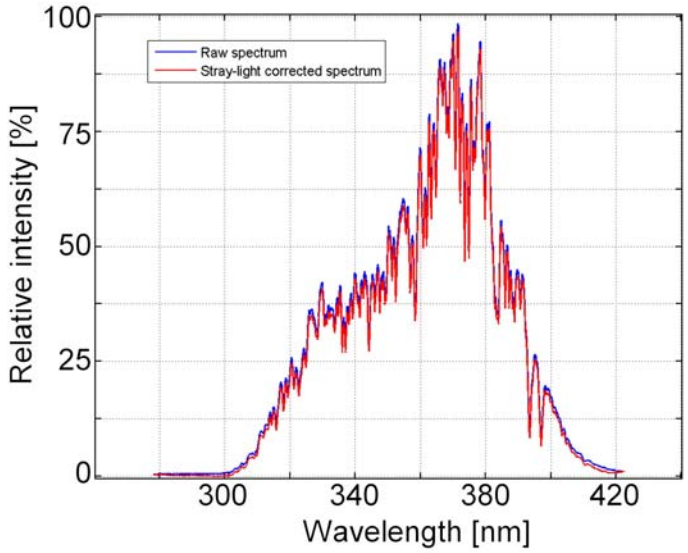

Fig. 3.27 – Influence of the stray light correction on a measurement spectrum. The raw spectrum (blue) was slightly lowered when the stray light correction was applied. The red spectrum depicts the corrected spectrum. (adapted from *Van Roozendael et al. 2006*)

In Fig. 3.28, the relative contribution of stray light to the total measured intensity at a particular wavelength in the SO_2 retrieval range is given. For the USB2000 spectrometer characterized in this study, the stray light level was below 5 % for wavelengths above 310 nm. Towards lower wavelengths where the incident scattered solar radiation becomes weak, the contribution of stray light rises, and reaches more than 20% for values below 304 nm. Therefore, a stray light correction must be applied if wavelengths below 310 nm are to be used in a DOAS retrieval.

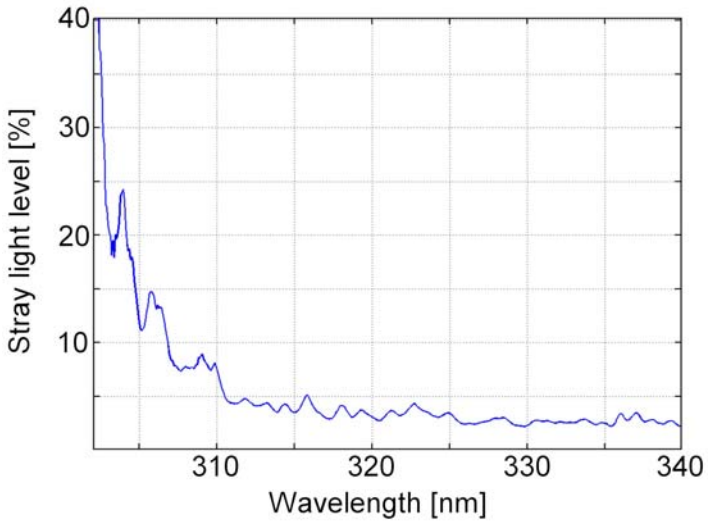

Fig. 3.28 – Contribution of stray light to the total measured intensity at a particular wavelength. The stray light level is below 5 % for wavelengths above 310 nm, but increases sharply below 310 nm. If these wavelengths are to be used in a DOAS retrieval, a stray light correction must be applied. (adapted from *Van Roozendael et al. 2006*)

Although *Van Roozendael et al. 2006* limited their study to a single USB2000 spectrometer, this instrument is thought to be representative of the performance regarding stray light rejection for the Ocean Optics© USB and HR product lines. The verification of this hypothesis could, however, be the goal of a future study. The finding that stray light is negligible for wavelengths above 310 nm led to the development of a simpler approach for cases in which a retrieval below 310 nm is desirable (e.g. in the radiative transfer retrievals described section 8).

Instead of measuring the stray light distribution matrix D for all spectrometers utilized in the NOVAC project, a baseline stray light intensity was obtained directly from each measurement spectrum. For this, the spectra were first corrected for offset and dark current. According to the data sheet of the SONY© ILX 511 detector (*SONY 2006*) used in both versions of the NOVAC scanning DOAS instrument, the first 18 pixels are optically black, meaning they should register null. If this is not the case, a slightly inaccurate offset correction was likely the cause. Therefore, the first 18 pixels in the spectrum were averaged, and the mean value was subtracted from the entire spectrum, thus compensating for the possibility of an imperfect offset correction.

Next, a stray light baseline is calculated from the mean of pixels 25 to 45. This assumes that these 20 pixels should always be completely dark, an assumption that is only valid if the spectrometer's spectral range begins below 300 nm. An example spectrum recorded with an HR2000 spectrometer at Mt. Etna in July of 2008 is shown in Fig. 3.29, along with the calculated offset correction and stray light baseline (in this case about 1.5 % of the intensity obtained at 312 nm was caused by the two effects).

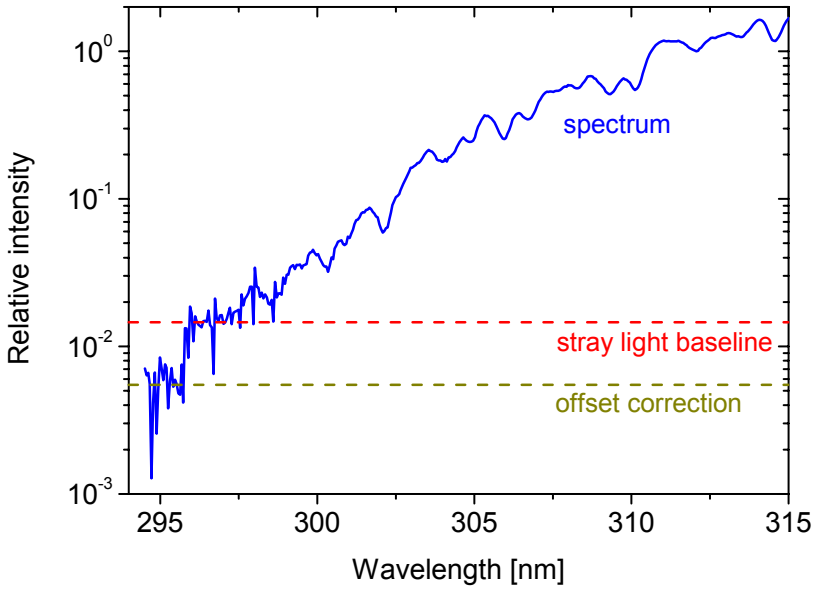

Fig. 3.29 – Example of the simple offset and stray light correction methods applied in the NOVAC data retrievals of SO_2, in this case shown for an HR2000 spectrometer. The offset correction is obtained by averaging the first 18 channels and subsequently subtracting the mean value from the entire spectrum. For the stray light baseline, the same technique is applied to channels 25 to 45, assuming that they should be completely dark.

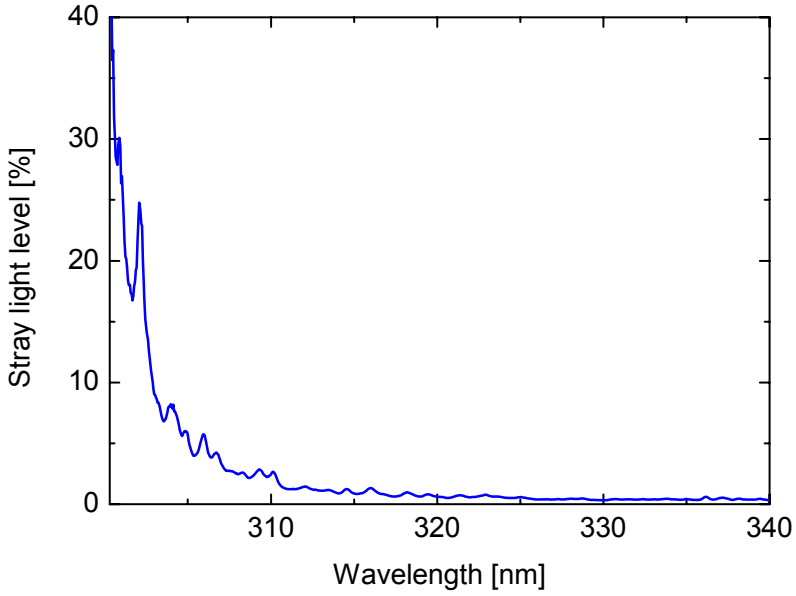

Fig. 3.30 – Relative contribution of spectrometer stray light (calculated by averaging channels 25 to 45 of the HR2000 spectrometer) to the total measured intensity. The stray light level obtained with this simple approximation is very similar to the level obtained using the stray light distribution matrix (compare to Fig. 3.28), especially for wavelengths below 310 nm.

The relative stray light level was also calculated as a function of wavelength by dividing the stray light baseline by the measured intensity. The results are shown in Fig. 3.30. Comparing Fig. 3.30 with Fig. 3.28 shows that the relative stray light contribution calculated with this simple approximation is very similar to the level obtained using the stray light distribution matrix (*Zong et al. 2006*), especially for wavelengths below 310 nm. Since the stray light contribution is below 5 % above 310 nm, this justifies the use of the simple stray light correction method for DOAS evaluations in general. Therefore, this approach was chosen for the SO_2 data retrievals conducted in the NOVAC project (also see *Johansson et al. 2008, Johansson 2009a*).

3.4.5 Temperature effects

Temperature plays an important role in multiple aspects of the SO_2 data retrieval. For one, the temperature of the spectrometer optical bench can influence the spectroscopy by slightly changing the alignment of optical components. The detector temperature governs the magnitude of the dark current, and the temperature of the readout electronics influences the electronic offset. Lastly, the temperature of the volcanic plume affects the SO_2 absorption cross-section. Each of these effects will briefly be described in this section.

Temperature of the spectrometer optical bench

Variations in the temperature of the spectrometer optical bench cause parts to contract or expand. This can cause a misalignment of the spectrometer. The effect of temperature variations on the instrument spectroscopy can best be characterized by measuring the monochromatic emission lines of a gas discharge lamp. In the initial phase of the NOVAC project (see section 5.1), *Pinardi et al. 2007* conducted a study in which incident radiation from a mercury emission lamp was measured for a range of temperatures expected at designated NOVAC installation sites. This study was repeated for 10 acquired Ocean Optics© S2000-type spectrometers which were later used for NOVAC mark I scanning DOAS instrumentation.

The measured spectra for one exemplary spectrometer are shown in Fig. 3.31. For the mercury emission line at 296 nm, both a change in FWHM of the measured peak as well as a shift in the wavelength position λ_c of the peak were registered. While the peak at 365 nm was relatively stable, the peak at 404 nm also changed shape and position. Unfortunately, the study showed that this behavior was not exemplary for all characterized spectrometers. Each spectrometer was different, although the general behavior was similar and will be discussed in the following. A separate test of several HR2000-type spectrometers conducted at the Institute of Environmental Physics in Heidelberg (*Kern 2006*) revealed an analog behavior.

Fig. 3.32 displays the FWHM of the 302 nm mercury emission line measured with a number of S2000 spectrometers. The official specifications of the individual spectrometers were identical, each stating an optical resolution of 0.7 nm. However, Fig. 3.32 shows that the true optical resolution was found to be significantly different for the individual spectrometers, and

variable for changing temperatures. A general trend towards higher optical resolution (i.e. smaller FWHM) was observed for increasing temperatures.

As was discussed in section 3.4.3, the effective differential SO_2 absorption cross-section $\overline{\sigma}'$ is known to depend on the optical resolution of the instrument. Therefore, a change in optical resolution corresponds to a change in the effective cross-section and therefore in the instrument sensitivity. The variation in the effective differential SO_2 absorption cross-section $\overline{\sigma}'$ relative to its value at 25°C is shown in Fig. 3.33. According to these results, the measured optical density of a constant SO_2 column density could change by up to about 10 % for a significant variation in spectrometer temperature. In the temperature range between 10 and 30°C, the average change in sensitivity is about 0.5 % per °C. For temperatures above 30°C, the optical resolution becomes relatively independent of temperature. However, these high temperatures are not advantageous in regard to detector dark current, which increases significantly with increasing detector temperature.

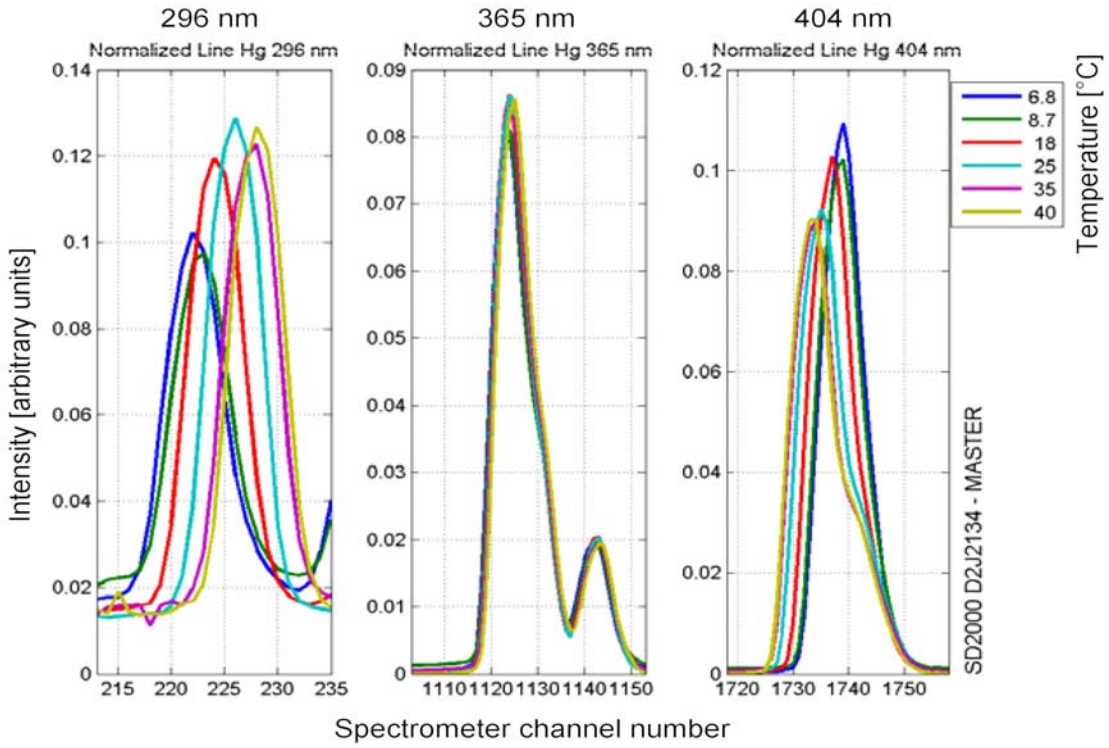

Fig. 3.31 – Effect of variability in temperature of the spectrometer optical bench on the instrument line shape ILS at three different wavelengths. In this example, the monochromatic mercury emission lines at 296, 365 and 404 nm were measured with an Ocean Optics© S2000 spectrometer (ser. nr. D2J2134). Both a change in the FWHM of the ILS and a shift in central position λ_c was observed. (adapted from *Pinardi et al. 2007*)

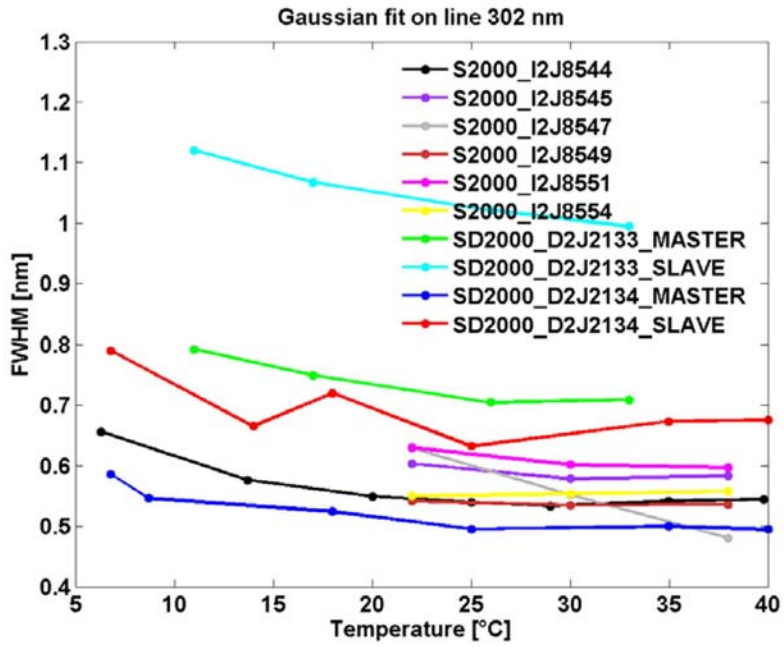

Fig. 3.32 – Measured FWHM of the mercury emission line at 302 nm as a function of the spectrometer temperature for 10 different Ocean Optics© S2000 spectrometers. In all cases, the FWHM increases towards lower temperatures. (adapted from *Pinardi et al. 2007*)

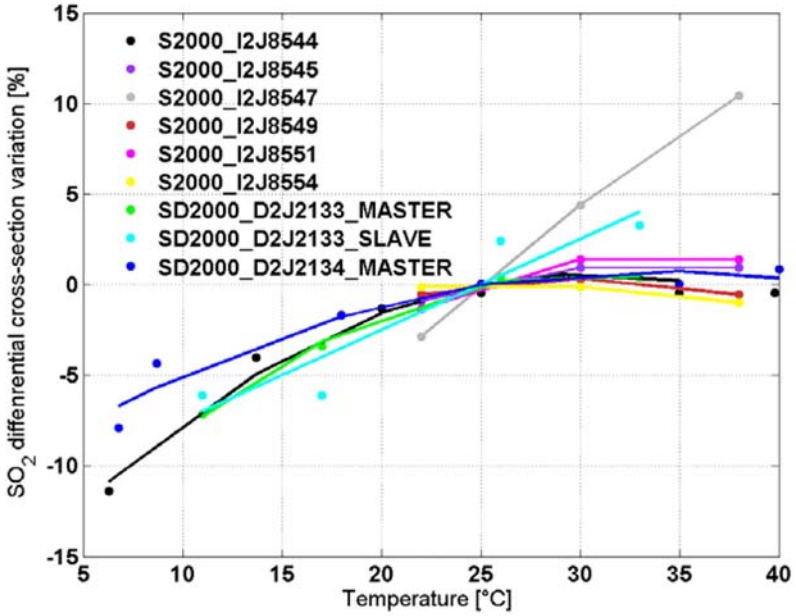

Fig. 3.33 – Influence of the measured changes in FWHM (Fig. 3.32) on the effective SO_2 differential absorption cross-section $\overline{\sigma}'$. A wider instrument line shape ILS is equivalent to a decrease in optical resolution, and therefore induces a lower effective differential absorption cross-section $\overline{\sigma}'$ (see section 3.4.3 for details). (adapted from *Pinardi et al. 2007*)

Aside from causing a change in optical resolution and therefore sensitivity towards SO_2, temperature variations of the optical bench typically lead to a shift in the wavelength calibration of a spectrometer. In Fig. 3.34, the measured spectral position of the 302 nm mercury emission line is shown relative to its position at 25°C optical bench temperature. While a general trend towards higher wavelengths (i.e. higher channel number of the peak wavelength λ_c) was observed, the behavior of the individual spectrometers was quite different. Temperature induced shifts ranged from about 0 to 0.21 nm/°C (*Pinardi et al. 2007*).

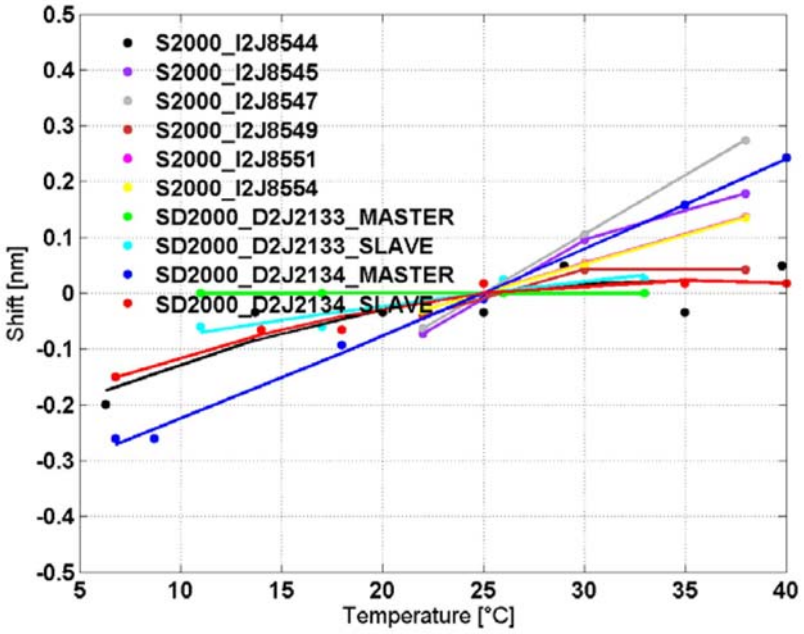

Fig. 3.34 – Measured spectral position of the 302 nm mercury emission line as a function of temperature relative to its position at 25°C. Temperature induced wavelength shifts range from 0 to 0.21 nm/°C for the different spectrometers characterized. (adapted from *Pinardi et al. 2007*)

The study by *Pinardi et al. 2007* clearly showed that the retrieval of SO_2 column densities could be significantly influenced by changes in the optical bench temperature. Several solutions to the problem exist. For the NOVAC mark II scanning DOAS instruments, a temperature stabilization system was implemented to keep the spectrometer temperature stable during the measurements (see section 3.5.1). The above described effects can thereby be avoided. However, this solution leads to a slightly enhanced power consumption of the instrument. For both NOVAC instrument types, the temperature of the spectrometer is measured by a thermocouple and saved with the acquired spectra. As this information is available, the spectrometer optical resolution can be calculated using the trends shown in Fig. 3.32 during the data evaluation process. Lastly, ongoing work by *Lehmann et al. 2009* is aimed at optimizing the instrument line shape ILS and wavelength calibration of each individual measurement spectrum in the DOAS fit itself. In this approach, the ILS is e.g. parameterized as a Gaussian curve with a variable FWHM (2 parameters allow an asymmetric

line shape). The wavelength calibration is represented by a simple polynomial with variable coefficients. The ILS parameters and calibration coefficients are then varied during the least squares DOAS fit (see Eq. 3.20). The ideal values are therefore found simultaneously with the absorber column densities.

Temperature of spectrometer readout electronics

The Ocean Optics© S and USB series spectrometers have a known issue with their electronic offset. This offset is added to each channel prior to digitization of the CCD signal to avoid negative values which cannot be properly processed by the analog-digital-converter. The electronic offset of the mentioned spectrometers is dependent on the spectrometer temperature, or more accurately put, on the temperature of the readout electronics.

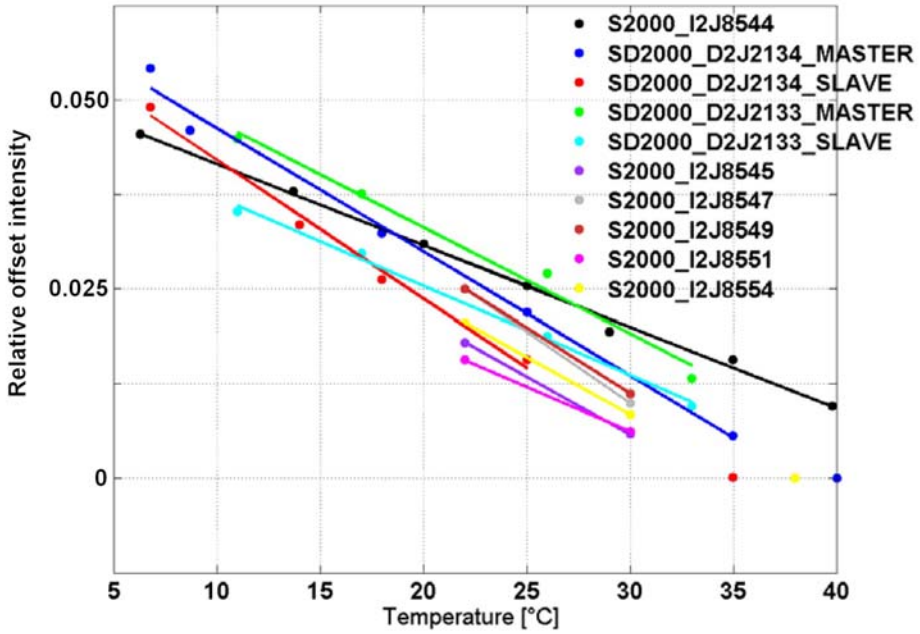

Fig. 3.35 – Average value of the electronic offset relative to the maximum detector saturation. A steep decrease in offset of approximately -0.15% detector saturation per °C was observed for increasing temperatures. (adapted from *Pinardi et al. 2007*)

Pinardi et al. 2007 also characterized this behavior for a number of S2000 spectrometers, and the results are shown in Fig. 3.35. The measurements indicate a decrease in the mean offset of about -0.15% detector saturation per °C temperature increase. This behavior complicates the correction of the offset somewhat for applications that do not use a temperature stabilized spectrometer. In this case, the offset must be measured in regular intervals to assure a similar temperature as is present during the measurements. The final offset correction can subsequently be trimmed according to the dark pixel method described in section 3.4.4 (see Fig. 3.30).

Detector temperature

The dark current of CCD detectors is defined as the offset-corrected measured signal under zero illumination. Even in the absence of incident light, CCD detectors still register a limited number of activation events. These are caused by thermally excited electrons reaching the activation energy ΔE of the semiconductor material. The magnitude of the dark current D typically follows the Arrhenius equation, which describes many thermally induced activation processes (also often referred to as Meyer-Neldel rule, see e.g. *Meyer and Neldel 1937, Widenhorn et al. 2002*).

$$D = D_0 \cdot \exp\left(\frac{\Delta E}{k \cdot T_D}\right) \qquad \text{Eq. 3.74}$$

Thus, the dark current signal is dependent on the detector temperature T_D. For higher temperatures and the associated higher thermal energy of the electrons, the probability for thermal activation increases. An accurate correction of the dark current again requires measuring the dark current signal at the same temperature as the measurement spectra. Therefore, the instrument must either be stabilized in temperature, or the dark current must be measured on a shorter time scale than possible temperature fluctuations.

Plume temperature

Aside from the temperature effects of the instrument itself, the temperature of the measured gas also influences the measurement results. The temperature of the volcanic plume will determine the shape of the SO_2 absorption cross-section due to temperature broadening of the absorption lines. The magnitude of this effect was examined in previous studies, and the results are shown in Fig. 3.36. It is evident, that the temperature of the measured sample (in this case the volcanic plume) is very critical in obtaining correct column densities. While this issue can theoretically be resolved by using a reference cross-section recorded at the plume temperature, it proves difficult to address in practice. Temperatures inside the plume can vary in space and time, and obtaining reliable temperature data is difficult. In this work, a mean temperature of 293K is always assumed, and the respective reference is used (*Bogumil et al. 2003*, 293K). In the event of measurements in close proximity to the volcanic vent or high temperature fumaroles, this approach should be reconsidered, and possibly a reference at a higher temperature selected.

However, even if a 293K reference is selected, the quality of the fit may be poor. Inconsistencies were found when comparing several different literature SO_2 absorption cross-sections recorded at or around 295K (see Fig. 3.37). Differences include discrepancies in the wavelength calibration, and depth of the differential absorption structures. While a slight shift in wavelength calibration can usually be corrected for during the DOAS retrieval (see section 3.1.4), a discrepancy in absorption depth directly translates to a difference in retrieved SO_2 column density. The absorption cross-sections shown in Fig. 3.37 exhibit discrepancies of up to 15%. Also, the shape of the absorption lines is not consistent between the different references, as can best be seen in the transmission band at 309.5 nm. Fitting references of

improper shape to measurements will result in residual structures in the DOAS retrievals that correlate to the cross-section and therefore cause difficulties in the evaluation of other chemical components in the same wavelength region. Such effects were e.g. observed for high column densities during the long-path DOAS measurements at Masaya volcano (see chapter 7).

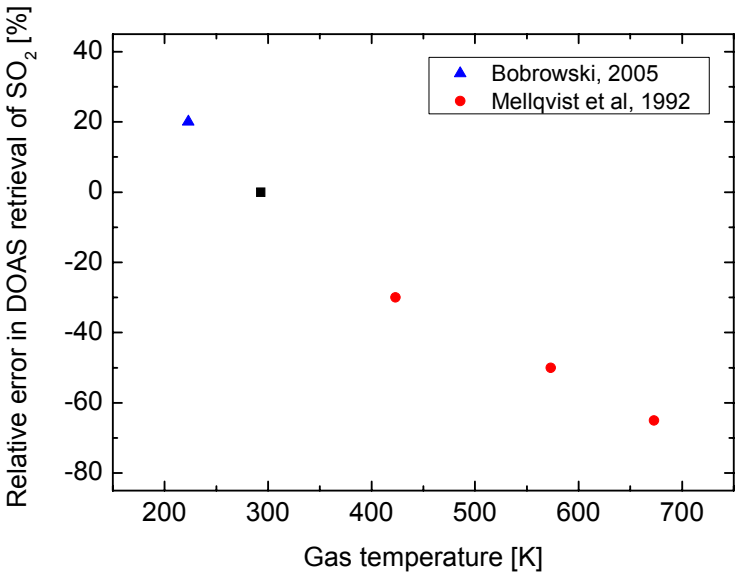

Fig. 3.36 – Errors in DOAS retrievals of SO_2 induced by the temperature dependency of the differential SO_2 absorption cross-section. Errors are calculated assuming a reference recorded at 293K (*Bogumil et al. 2003*) is applied in DOAS evaluations of measurements conducted at a variety of other gas temperatures. High gas temperatures lead to an underestimation of the SO_2 column density. The results are compiled from *Mellqvist et al. 1992* (experimental data) and *Bobrowski 2005* (theoretical retrieval using temperature dependent SO_2 cross-sections measured by *Bogumil et al. 2003*).

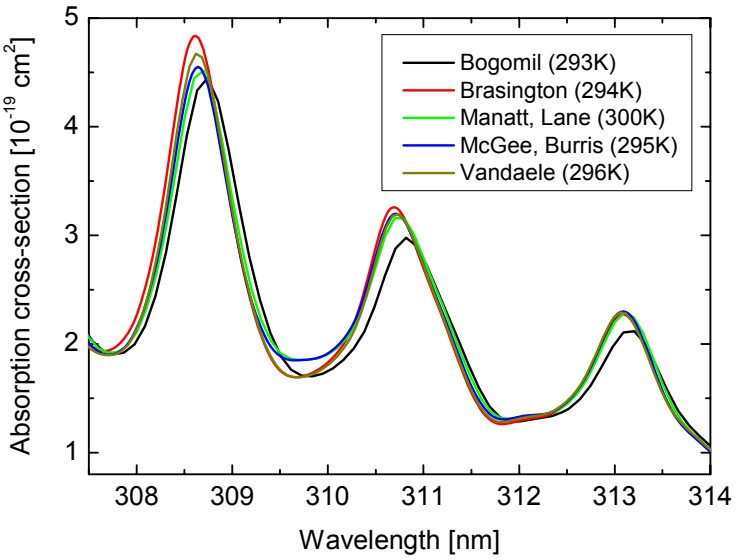

Fig. 3.37 – SO_2 absorption cross-section between 308 and 314 nm for temperatures at or around 295K according to 5 different studies (*Brassington 1981, McGee and Burris 1987, Manatt and Lane 1993, Vandaele et al. 1994, Bogumil et al. 2003*). Each reference was convoluted with an 0.4 nm FWHM Gaussian instrument line shape (ILS).

3.5 Development of DOAS instrumentation for volcanic gas emissions measurements

In the scope of this thesis, two novel DOAS instruments were conceived for the quantitative measurement of volcanic gas emissions. For one, a passive scanning DOAS instrument was designed for permanent installation and continuous measurement of volcanic emission fluxes and plume composition. In addition, a miniature, light-weight Active Long Path DOAS instrument was designed and built for application in remote environments such as those typically found around active volcanoes. Both instrument designs are presented in this section. A third instrument, the SO_2-camera, was also designed and built. However, as it is technically not a DOAS instrument, it is discussed separately in chapter 4.

3.5.1 NOVAC mark II gas emissions monitoring instrument

One of the initial tasks of the NOVAC project (Network for Observation of Volcanic and Atmospheric Change, see section 5.1) was to design a passive scanning DOAS instrument specifically long-term volcanic emissions monitoring applications. While the scanning DOAS technique was already established in earlier studies (*McGonigle et al. 2002, Edmonds et al. 2003a, Galle et al. 2003*) and in the predecessor project DORSIVA (Development of Remote Sensing Instruments for Volcanological Applications, see *DORSIVA 2005*), many questions

remained open as to the actual technical implementation of an instrument sufficiently robust for the long-term monitoring measurements proposed in NOVAC.

The task with the highest priority in the NOVAC project is the continuous measurement of SO_2 fluxes emitted from the partner volcanoes. First and foremost, the measured fluxes are to be used by the local observatories for volcanic hazard assessment. Also, possible correlations to other measurements of volcanic activity (e.g. seismicity and deformation) are being studied to possibly gain insights into actual volcanic processes. However, additional science questions are also being targeted. These include the measurement of additional species (especially the halogen compounds BrO, ClO and OClO) and the observation of background tropospheric and stratospheric chemistry in both remote and urban volcanic sites.

During preliminary discussion, it was found that the instrument requirements for the supplementary science questions deviate from the basic measurement of volcanic SO_2 fluxes. For one, a high time resolution is important for the correct assessment of fluxes, as the temporal variability of the flux can be high. However, for measuring additional trace gas species, a high optical resolution can be advantageous. This typically decreases light throughput and therefore negatively affects time resolution (see section 3.4.3). Energy consumption poses another conflict of interest. In many cases, power is extremely limited and supplied only by solar panels. There are some situations, however, in which additional power is available, either because a land line is accessible, or because a large monitoring station with accordingly dimensioned solar panels and batteries was chosen as the installation site for the NOVAC instrument. In such cases, it is possible to actively regulate the temperature of the NOVAC spectrometer, which has been found to greatly reduce calibration shifts and changes in the instrument line shape (ILS), thus enhancing the quality of the spectroscopy (see section 3.4.5). Lastly, while the cone geometry introduced by *Galle et al. 2009* is well-suited for measuring SO_2 fluxes for a large range of wind directions (also see *Johansson 2009a*), it is not ideal for tropospheric and stratospheric background measurements. For these, additional flexibility in regard to the instrument viewing direction is desirable. Due to these irreconcilable demands and the desire to maximize the scientific output of the deployed instruments, two separate optical configurations were designed and employed according to individual installation conditions and science goals. In the following, the NOVAC mark II scanning DOAS instrument, which was designed and built at the Institute of Environmental Physics, University of Heidelberg within the scope of this thesis, is presented. The optical configuration of the NOVAC mark I instrument (designed and built at Chalmers University of Technology in Gothenburg, Sweden)is explained in detail by *Galle et al. 2009, Johansson 2009a, Johansson et al. 2009b* and will not be presented here.

Scanner and optics

The NOVAC mark II instrument was designed to allow the best possible spectroscopy and enhanced flexibility in regard to measurement geometry. An improved optical resolution of 0.4 nm is achieved by using an Ocean Optics© HR2000 with a focal length of 101.6 mm at f/4, a 100 µm entrance slit, and a 2400 groove/mm grating yielding a wavelength range of 295 to 390 nm. The spectrometer optical bench temperature is controlled by a thermoelectric

Peltier module regulated using a SuperCool© PR-59 temperature controller with constant voltage pulse-width modulation. To keep power consumption to a minimum, the temperature is typically kept constant at the average daytime ambient temperature at the instrument's location, and the spectrometer is wrapped in Armaflex© insulating foam. Both heating and cooling are possible. Excess heat is dissipated by a heat sink located on the underside of the instrument, where it is shielded from the sun. The thermoelectric temperature regulator can consume up to 50 W in addition to the rest of the electronics (described in section 5.2), but typical values are much lower, as less than 1W/°C is consumed for a given temperature difference between spectrometer and ambient.

The NOVAC mark II optics feature a dual axis scanner that allows the instrument to point in any direction in the sky or, as is sometimes useful for tropospheric measurements, at the ground. One scanning element protrudes from the side of the instrument (see Fig. 3.38), while the entire instrument box is mounted on a vertical axis that allows the additional adjustment of the instrument's azimuth angle. Both axis are positioned using Faulhaber© brushless DC servomotors with position generators. The motors are controlled by Faulhaber© MCBL 3003 motor drivers, which in turn receive their instructions from an embedded PC running the measurement (described below). Both the elevation and the azimuth scanner motors use gear reductions of 9:1 and 246:1, respectively. The achieved relative position accuracy was found to be better than 0.05° (*Sommer 2008*).

Fig. 3.38 shows the optical paths inside the NOVAC mark II optics. Scattered light enters the scanner on the side of the instrument. It is deflected by 90° by a prism which replaces the mark I mirror to avoid variable sensitivity to different directions of polarization. After passing through a Hoya© U330 UV filter, the incident light is collimated with a 25 mm diameter spherical mirror and is focused onto a single 400 μm fused silica fiber positioned in the focal point 75 mm away and leading to the spectrometer. Between the mirror and the fiber entrance, a diffuser plate can be moved in and out of the light path with a rotary solenoid for solar occultation measurements. The diffuser plate is thus used to attenuate the incident radiation while at the same time mixing variations in the spectrum originating in different positions on the solar disk (see section 3.3.1).

The dimensions of the instrument box are 30 × 30 × 15 cm, and the instrument weighs approximately 7 kg. It can either be mounted on a fixed structure for permanent installation (see examples shown in chapter 5), or on a tripod for mobile measurements (shown in Fig. 3.40).

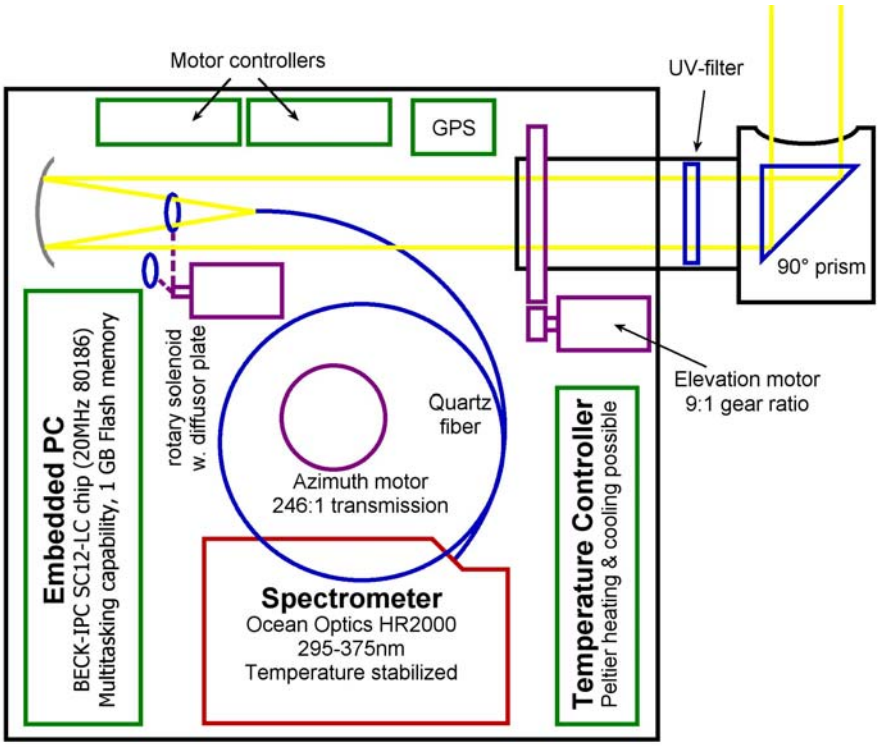

Fig. 3.38 - Schematic view of the NOVAC mark II instrument as seen from the top. Light enters the system through the elevation scanner protruding from the side of the instrument. After passing through a UV-filter, it is collimated by a spherical mirror and focused on the end of a fused silica fiber leading to the spectrometer. A diffuser plate can be moved into the light path for solar occultation measurements using a rotary solenoid.

Electronics

The NOVAC mark II scanning DOAS instruments are controlled by an embedded PC. Based on the Beck© SC12 "System-On-A-Chip" IPC, this computer features a 186 processor running at 20 MHz. It has 512 Kbytes of on-board RAM and another 512 Kbytes on a flash EEPROM. A 1 GB flash card is installed for the storage of measured spectral data. Two serial ports and a 10 Mbit Ethernet connection allow external interfacing. Software is processed by a multitasking operating system stored on the flash EEPROM. The entire PC can be run off between 10 and 24 V unregulated DC power.

The implementation of an on-board PC in the instruments was chosen to allow fully autonomous operation. Even in the event of an interrupted data link to the observatory (e.g. caused by a volcanic crisis), the instrument continues to collect data and save it to the 1 GB flash card. This is done according to a measurement configuration text file stored on the instrument EEPROM. Aside from general settings related to instrument performance (see *Kihlman 2007*), the exact sequence of measurement viewing directions, integration times and measurement repetitions is listed in this file.

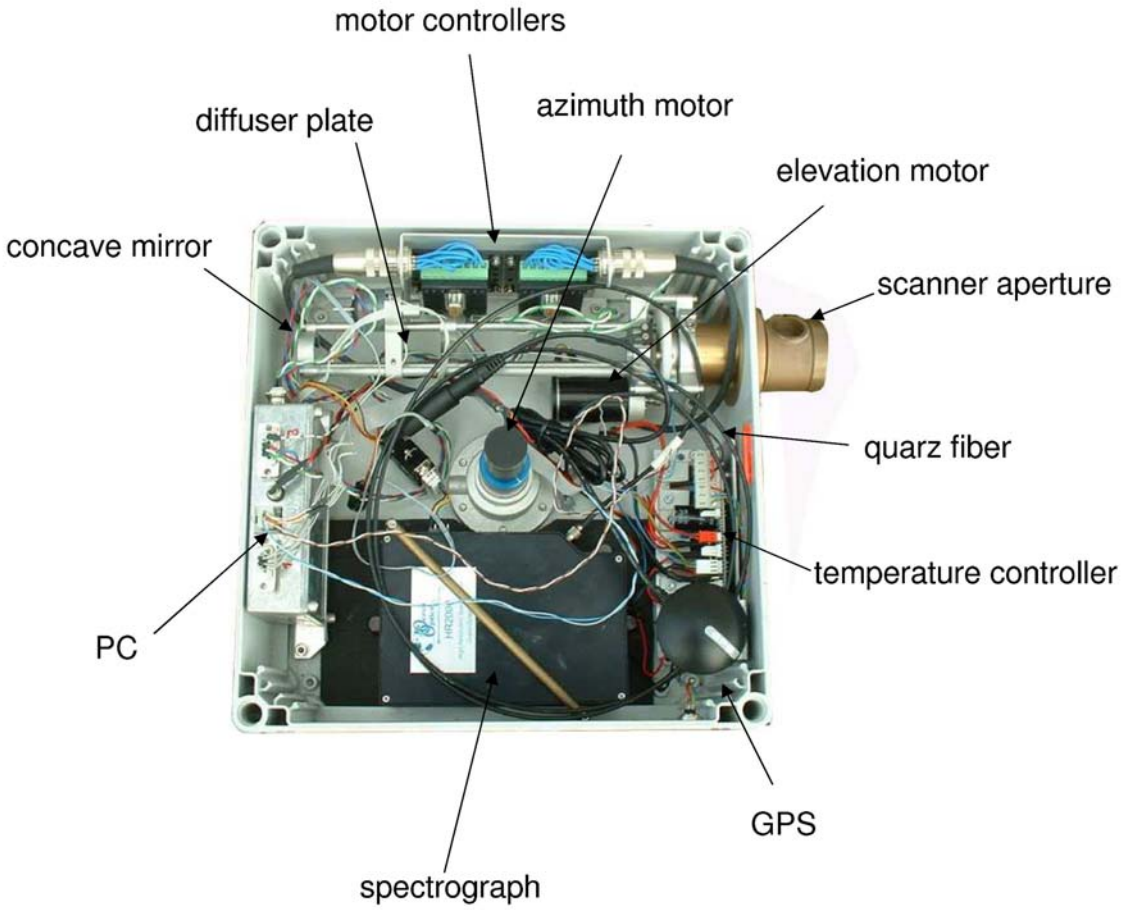

Fig. 3.39 – Top view of a NOVAC mark II instrument opened for demonstration purposes. The orientation of the instrument is identical to the schematic shown in Fig. 3.38. In this picture, the spectrometer insulation was removed for demonstration.

Measured spectral data is stored in a compressed format on the 1 GB flash memory. When scanning the plume, subsequent spectra recorded as part of one scan are binned and compressed in a single file to reduce storage space and minimize data transfer time. The same is true for subsequent spectra recorded in the wind speed, plume composition and solar occultation measurement modes. A typical scan of the volcanic plume has a file size of about 130 Kbytes. Assuming the instrument runs 12 hours per day at a measurement time resolution of 10 minutes, the 1 GB flash memory allows for a buffering of approximately 3 months of data.

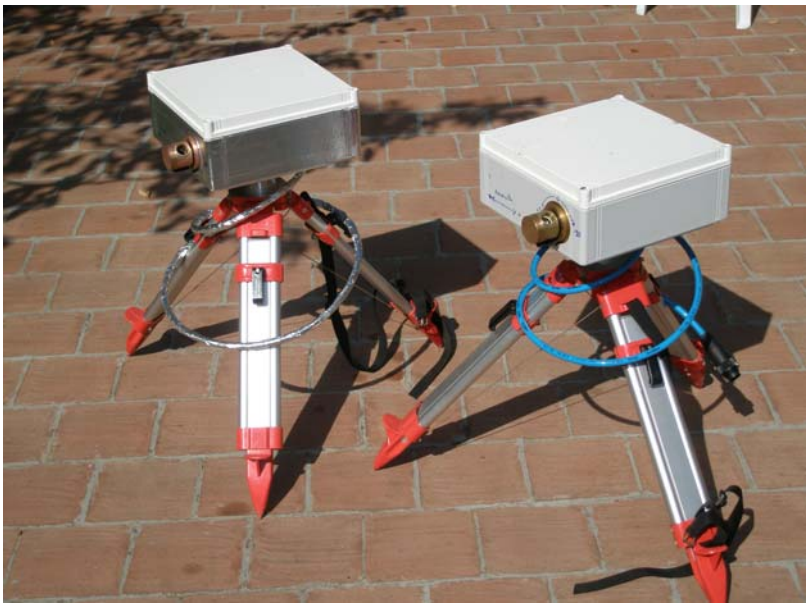

Fig. 3.40 – Two NOVAC mark II scanning DOAS instruments mounted on tripods for mobile, short-term deployment. The left instrument was coated with aluminum shielding to reduce interferences with local CB radio frequencies.

A GPS receiver is used to supply precise position and time tags to all measured spectra. An eight channel ADC is used to digitize spectrometer temperature and battery voltage signals, and these are also saved with each spectrum. The six currently unused ADC channels are free for future extension of the system.

The data interface to the instrument can be set up in several ways. For one, the operating system on the embedded PC has full network capabilities. Both a web server and an FTP server are automatically started when the system is booted. This allows full accessibility to the data stored on the compact flash via any standard FTP client software, or with the NOVAC data evaluation and display software (*Johansson 2009b*). Alternatively, the instrument offers a serial interface. This can be used either via a telnet of hyperlink connection, or again with the NOVAC software.

Power consumption

The NOVAC instruments can either be connected to a 12V DC power supply or a 12V battery. In many installation sites, power is supplied by solar panels in combination with a 12 V solar battery of typically 80Ah. As power is a limited resource at many of the installation sites, the instruments were designed to conserve power as much as possible. For one, a timer controls operation time. The entire instrument is switched off at night. Also, a sleep mode is available. In this mode, the power to the spectrometer and motors is turned off, while the electronics continue to function. This mode can be used to transmit buffered data to the observatory at night. Lastly, the temperature controller of the NOVAC mark II instrument is capable of both heating and cooling. Stabilization occurs on the average daytime temperature. In this manner, the difference between spectrometer and ambient temperature is minimized,

therefore also reducing power consumption. Careful insulation of the spectrometer resulted in a power consumption of below 1W per °C temperature difference to ambient. An overview of the power consumption of the individual instrument components is given in .

Instrument Component	Power Consumption
BECK© IPC and Faulhaber© motor controllers	2.7 W
Ocean Optics© HR2000 spectrometer	1.5 W
GPS receiver	0.6 W
Azimuth motor while moving	0.6 W
Elevation motor while moving	0.6 W
Temperature stabilization	~ 0.8 W/°C
Minimal power consumption	4.8 W
Typical power consumption	7 to15 W
Maximum power consumption	56 W

Tab. 3.3 – Power consumption of the NOVAC mark II scanning DOAS instrument split into individual components. Power needed for data communication is not included.

Data transmission

The establishment of a data link between the NOVAC mark II scanning DOAS instruments installed in the field and the volcanic observatories is often one of the main challenges in the system setup. Distances of several tens of kilometers often need to be bridged with wireless technology due to the extremely remote location of the measurement sites. Two different hardware systems were used (see detailed descriptions in chapter 5).

The fastest and most elegant data connection to the instrument is established via FTP. Therefore, Wi-Fi networks are desirable. At some installation sites, such networks either already exist (e.g. Mt. Etna) or will be set up in the foreseeable future (e.g. Stromboli). While the high data transfer rate (10 Mbit in this case) is a great advantage, network installation is complicated by the fact that Wi-Fi connections over distances of more than about 3 km can only be established using accurately aligned, directional antennas (see e.g. *Rappaport 2002*).

As two such antennas are needed for each link in a spaced out network, installations quickly become complex (see *Zhang 2005*).

As an alternative, Freewave© spread spectrum wireless data transceivers were used in many installations, especially at sites where such networks were already existent (e.g. Popocatepetl and Tungurahua) for other volcanic sensors. Operating either around 900 MHz or 2.4 GHz (*FREEWAVE 2009*), these radio modems establish a serial connection between two locations separated by up to 100 km. While directional antennas are required for long distance communication, the adjustment is less critical. Typically, an omni-directional antenna can be used at one end of the communications link, thereby greatly simplifying the network setup. The network installations of the NOVAC project were the subject of a masters thesis by *Zhang 2005*. Additional information regarding NOVAC hardware and software can be found in *Galle et al. 2009*.

3.5.2 Miniature Active Long Path DOAS

The Active Long Path DOAS (LP-DOAS) technique has a number of advantages over passive DOAS measurements of scattered solar radiation. For one, measurements can be conducted both night and day. Also, as an artificial light source is used, the instrument spectral range can be expanded to wavelengths not readily available in scattered solar radiation (see e.g. *Axelsson et al. 1990a, Volkamer et al. 1998, Kern et al. 2008a, Merten 2008, Platt and Stutz 2008*). Finally, while complex radiative transfer modelling must be used to retrieve average optical paths in the atmosphere when using scattered light DOAS, the optical path is well-defined in active DOAS applications. Therefore, the conversion from measured column density to average concentration along the light path is simple.

For all of these reasons, LP-DOAS has become a standard technique for measuring atmospheric trace gases. In the past, LP-DOAS instruments have e.g. been deployed for halogen measurements in the marine boundary layer (e.g. *Alicke et al. 1999, Allan et al. 2001, Saiz-Lopez and Plane 2004, Saiz-Lopez et al. 2004, Peters et al. 2005*), in the vicinity of salt lakes (e.g. *Hebestreit et al. 1999, Stutz et al. 2002*) and in polar regions (e.g. *Hausmann and Platt 1994, Tuckermann et al. 1997, Hönninger et al. 2004b, Saiz-Lopez et al. 2007*). The atmospheric chemistry in urban environments has been a second major focus of many LP-DOAS studies (e.g. *Platt et al. 1979, Platt et al. 1980b, Platt et al. 1980a, Axelsson et al. 1990a, Geyer et al. 2003a, Geyer et al. 2003b, Trick 2004, Volkamer et al. 2005a, Acker et al. 2006, Merten 2008*). For two reasons, however, the application of LP-DOAS in volcanic environments remained problematic. First, the instrument size, weight, and complexity (see e.g. *Edner et al. 1986, Axelsson et al. 1990b, Geyer 2000*) was such that transportation was limited to areas accessible by motor vehicle. Secondly, the xenon arc lamps usually used as LP-DOAS light sources are extremely power consuming (typically several hundred Watt), thus making battery operation only feasible for very short periods of time.

Fiber bundle coupling system

However, two recent technological advances have made possible the design of a portable LP-DOAS system. *Merten et al. 2009* for the first time used an optical fiber bundle to couple light into and out of the LP-DOAS telescope. In this approach, multiple optical fibers are configured in a Y-shaped bundle, as shown in Fig. 3.41. The joint end of the fiber bundle is then positioned in the focal point of the LP-DOAS telescope (see Fig. 3.42). One of the branches of the fiber bundle is used to couple the light source into the telescope, the other is used to receive radiation that has passed through the atmosphere and couple it into the spectrometer.

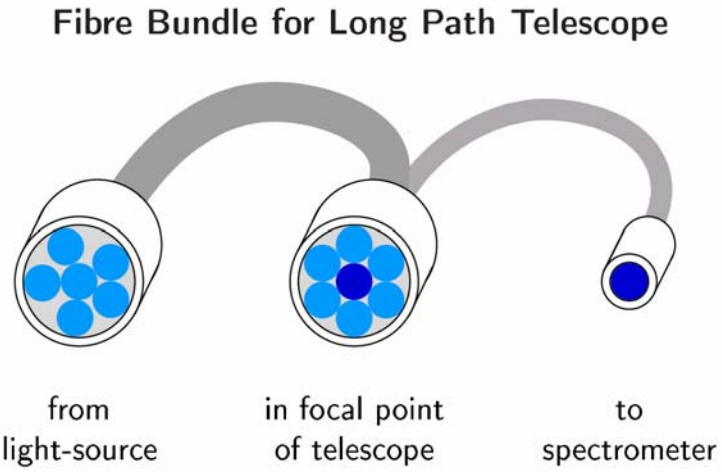

Fig. 3.41 – Configuration of the optical fiber bundle used to couple light into and out of the novel LP-DOAS systems introduced by *Merten et al. 2009*. (figure adapted from *Sihler 2007*)

The great advantage of this technique is that both the light source and the spectrometer can thus be completely mechanically decoupled from the telescope. Therefore, the telescope frame does not need to support any weight other than that of the optics themselves. This has enabled a considerable reduction of telescope weight.

In addition, the fiber system has significantly decreased the complexity of the LP-DOAS system. Previously, the coaxial mirror system used to couple light into and out of the main telescope was very sensitive to misalignment. A slight misalignment of one element often made it necessary to realign the entire system. In the fiber system, the position of the joint end of the bundle is the only crucial variable in the alignment. A slight misalignment in telescope pointing direction can easily be compensated by moving the fiber bundle in the focal plane of the telescope. As long as a single specific light path is aligned at a time, large motors for moving the telescope are no longer necessary. All in all, the weight of the optical system could be reduced from more than 100 kg to approximately 10 kg. A photograph of the light-weight telescope is shown in Fig. 3.46. Further details of the fiber technique can be found in *Sihler 2007, Tschritter 2007, Merten 2008, Merten et al. 2009*.

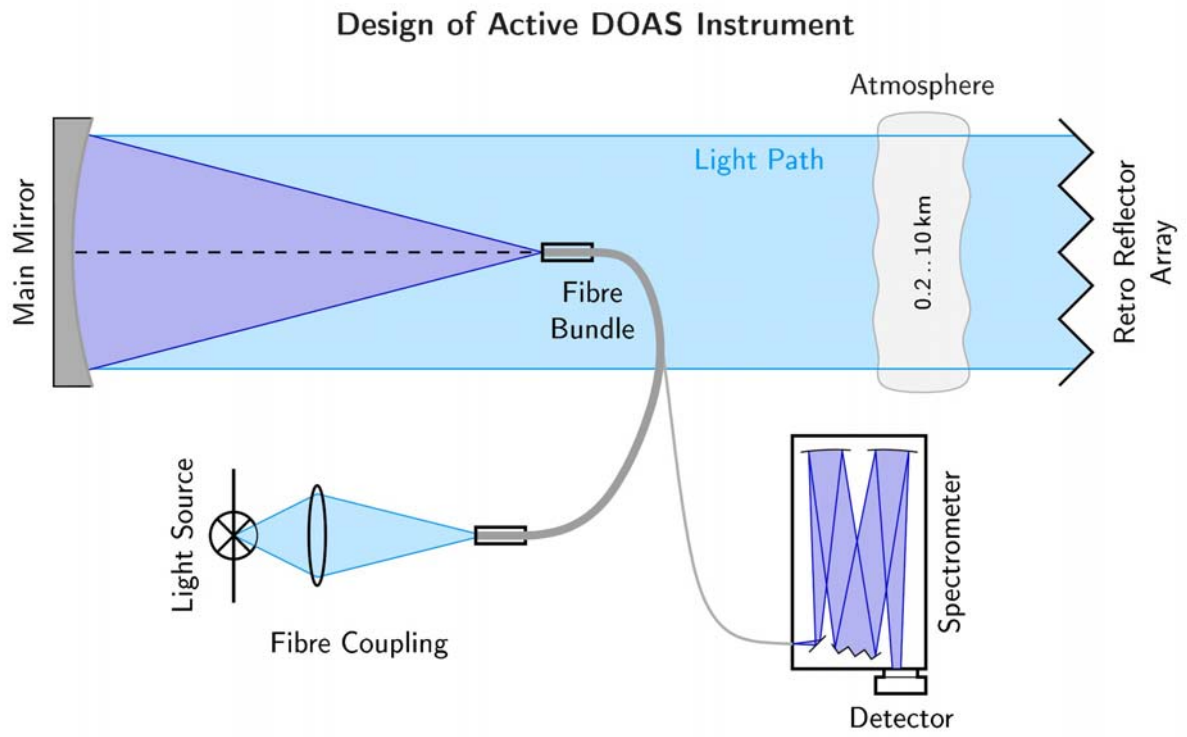

Fig. 3.42 – Schematic of the active LP-DOAS using a fiber bundle design (*Merten et al. 2009*). Light is coupled into one of the split branches of the bundle. The joint bundle end is positioned in the focal point of the telescope. This sends out a nearly parallel beam of light through the atmosphere. After being reflected back to the instrument by an array of retro reflectors, the light is coupled into the spectrometer by means of the second split branch of the fiber bundle (see Fig. 3.41). Here, the spectral analysis takes place. (figure adapted from *Sihler 2007*)

Light emitting diodes as LP-DOAS light sources

The second technological breakthrough enabling the construction of truly mobile LP-DOAS systems was the proven applicability of light-emitting diodes (LEDs) as light sources for active DOAS measurements (*Kern et al. 2006*). While LEDs have a much lower total emitted optical power than xenon arc lamps, the spectral radiance (power emitted per solid angle and emitter area at a specific wavelength) of modern LEDs is comparable (see Fig. 3.43 (a)). When normalized to the electrical power consumption, however, LEDs are far superior (Fig. 3.43 (b)). As the DOAS retrieval of a certain species is limited to a specific wavelength window anyway, the use of one or multiple LEDs emitting in this spectral range not only reduces power consumption by orders of magnitude, it also reduces radiation of wavelengths unnecessary for the retrieval from entering the spectrometer and causing stray light (see section 3.4.4).

Recent advances in the field of UV-LED technology have further improved the applicability of LEDs in LP-DOAS instruments (see *Sihler 2007*). LEDs are now available with wavelengths down to 250 nm (*SET 2009*), thus making possible the detection of a wide range

of atmospheric trace gases with LED-powered LP-DOAS systems. In particular, the species SO_2, BrO, ClO, OClO and O_3 can now be measured using UV-LEDs as active light sources.

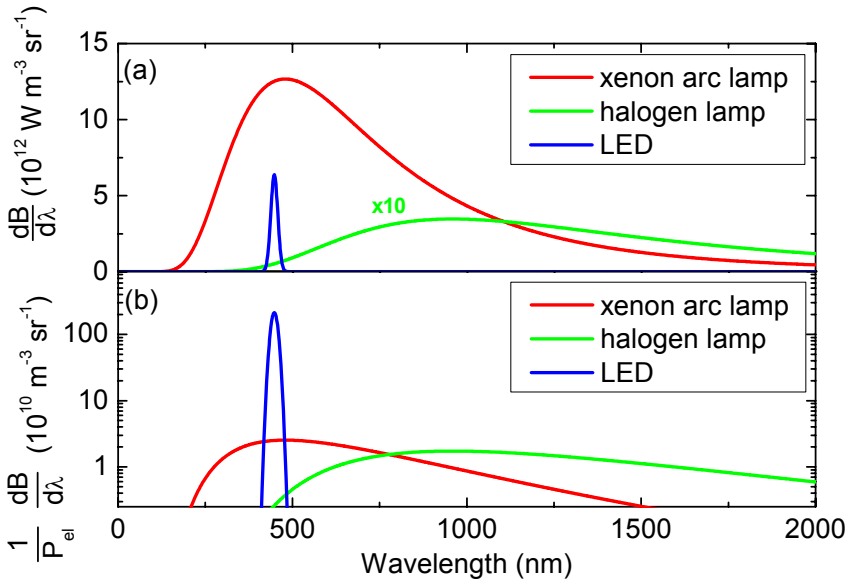

Fig. 3.43 – (a) Spectral radiance dB/dλ of a xenon arc lamp, an LED, and a halogen lamp (multiplied by 10 for the sake of perceptibility). While the LED has a much lower total radiance (integral of the spectral radiance over all emission wavelengths), the spectral radiance at the emission peak is comparable to that of the xenon arc lamp. If the curves are normalized to electrical power consumption (shown in (b)), the LED is two orders of magnitude more effective than the xenon arc lamp. Details are discussed in *Kern et al. 2006*.

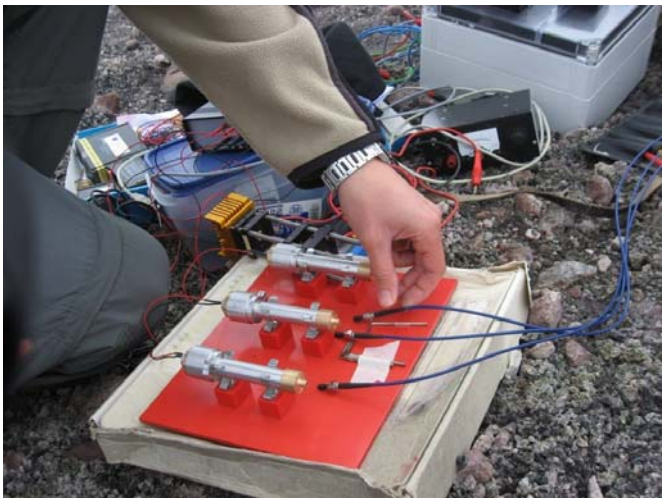

Fig. 3.44 – Multi-LED coupling setup. A different UV-LED is mounted on the left end of each of the three aluminum pipes. Inside the pipes, two plano-convex lenses are used to image the LED onto the end of the quartz fiber bundles. Each bundle contains two fibers, and the three bundles are merged into one which is then positioned in the focal point of the LP-DOAS telescope (see Fig. 3.42).

For measurements of volcanic gas emissions, a fiber coupling system was specifically designed to allow the use of multiple LED light sources. Instead of using a Y shaped fiber bundle as shown in Fig. 3.41, the light source bundle is itself split into three different bundles, each of which is used to couple light from a UV-LED into the telescope. A photograph of this setup is shown in Fig. 3.44. Here, three different UV-LEDs are mounted on the end of three aluminium pipes. The LED positions can be accurately adjusted in 3 dimensions with the help of a dual nested eccentric. Inside the aluminium pipes, two plano-convex lenses image the LED onto the end of three fused silica fiber bundles, each containing two individual fibers. The fiber bundles are merged together with a single fiber leading to the spectrometer (as shown in Fig. 3.41) and positioned in the focal point of the miniature LP-DOAS telescope. Hence, the radiation emitted by the three LEDs is sent through the atmosphere in a nearly parallel beam. Note that the coupled radiance is not significantly increased by using multiple light sources. Instead, radiation emitted into a smaller solid angle is used from each LED. By merging the fiber bundles from the three LEDs, the initial radiance is again obtained.

Fig. 3.45 shows the absorption cross-sections of SO_2, BrO, ClO, OClO, and O_3 along with the emission spectra three Sensor Electronic Technology© UVTOP LEDs (*SET 2009*) with central emission wavelengths of 280, 320 and 340 nm. As this spectrum was measured with the LP-DOAS system after the light had passed an approximately 40 m light path on the edge of the plume of Mt. Etna, close examination reveals periodic SO_2 absorption structures in the 280 nm LED spectrum. The measurements conducted with this system in July of 2008 at Mt. Etna (Italy) are discussed in chapter 7. For further details concerning the use of LEDs in LP-DOAS instruments, see *Kern 2004, Kern et al. 2006, Sihler 2007, Sihler et al. 2008*.

Mechanical setup

By combining both the fiber coupling and LED technology described above, a truly mobile LP-DOAS could for the first time be constructed. An image of the system is shown in Fig. 3.46. One or several LED light sources are coupled into a fiber bundle, the other end of which is positioned in the focal point of a 20 cm diameter spherical mirror using precision 3 dimensional optical positioning system. A nearly-parallel beam of light is sent to an array of retro reflectors located some tens to hundreds of meters away. After returning, light is collimated by the same telescope and some of the returning light enters the spectrometer through the central fiber of the fiber bundle (see Fig. 3.41 and Fig. 3.42).

For the measurements conducted in this thesis, an Ocean Optics QE65000 spectrometer with a back illuminated UV-sensitive CCD was used. Its spectral range was 275 to 360 nm. The spectrometer was placed in a 30 × 30 × 20 cm well-insulated plastic housing. A SuperCool thermoelectric temperature controlling system was used to stabilize the air temperature in the housing, thus stabilizing the temperature of the spectrometer optical bench (see section 3.4.5). The detector was cooled using a second Peltier stage mounted on the chip itself.

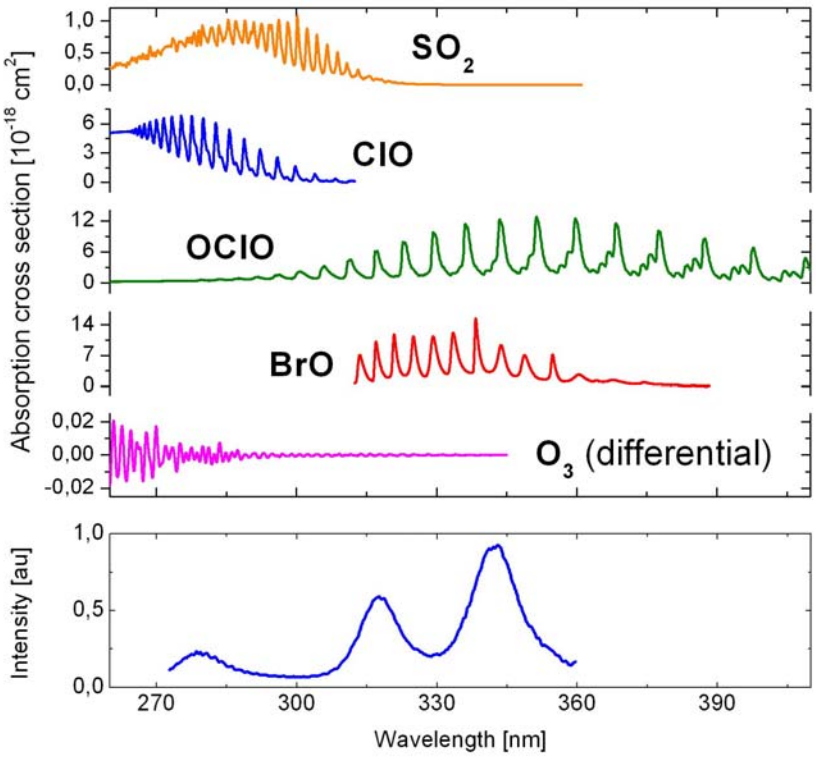

Fig. 3.45 – Absorption cross-sections of SO_2, ClO, OClO, BrO, and O_3, all of which are interesting species to measure in and around volcanic plumes. Also shown is the spectrum of the three Sensor Electronic Technology© UV-LEDs (*SET 2009*) after the radiation has passed a light path of 40 m on the edge of the Mt. Etna plume (recorded in July 2008, see chapter 7). Close examination reveals SO_2 absorption structures superimposed on the LED spectrum with the shortest wavelength.

In the focal point of the telescope, a solenoid can be used to move a metal shutter in front of the fiber bundle. If the LEDs are kept on, light is then reflected off the shutter and into the receiving fiber. In this manner, the LED emission spectra can be measured without atmospheric influence (often called shortcut spectrum). If the LEDs are turned off, dark current and offset can be recorded using the mechanical shutter.

Fig. 3.46 – Miniature Active Long Path DOAS designed for application in remote environments. The blue fiber bundle is positioned in the focal point of a 20 cm diameter spherical mirror, thus emitting nearly-parallel light. After being reflected back to the telescope by an array of retro reflectors, the central fiber in the bundle couples the incident radiation into the spectrometer. Here, an Ocean Optics QE65000 spectrometer was applied, located in a temperature stabilized housing (bottom left of the image). The measurements are controlled by a laptop computer.

Power consumption

Power is supplied to the entire system by a 12 V battery. The power consumption of the instrument in this setup is summarized in Tab. 3.4. When LEDs are employed as light sources, the total power consumption is determined by the laptop and the spectrometer temperature controller. Both can take up to 50 W for a short period of time. However, once the set point temperature is reached in the spectrometer housing (usually set close to ambient), the power consumption drops to below 3 W/°C temperature difference to ambient. As the laptop also has its own battery, it can be disconnected much of the time.

The power consumption of the QE65000 spectrometer depends on the set temperature of the CCD detector. In the measurements conducted in this thesis, the detector was typically cooled to -10°C to keep the dark current low (due to their design, back thinned detectors have higher dark currents than comparable front illuminated CCDs). Over longer periods of time, the average power consumption of the system was approximately 60W. Therefore, the instrument could be supplied for 2 hours off a 12 Ah motorcycle battery, or for 12 hours using a 60 Ah car battery.

Instrument Component	Power Consumption
Ocean Optics© QE65000 spectrometer	5 to 18 W
SuperCool© thermoelectric temperature stabilizer	0 to 50 W
Light-emitting diodes	< 1 W
Laptop computer	0 to 50 W
Minimal power consumption	6 W
Typical average power consumption	60 W
Maximum power consumption	120 W

Tab. 3.4 –Power consumption of the miniature LP-DOAS instrument. When using LEDs instead of xenon arc lamps, power consumption is no longer determined by the light sources. Instead, the thermoelectric temperature stabilization of the spectrometer and the laptop computer are the decisive components. On average, the total setup consumes about 60 W.

4 The SO_2-camera

4.1 Introduction

SO_2 is widely monitored at actively degassing volcanoes, as its emission flux can be used as a proxy for degassing magma volume, and its long atmospheric lifetime (order of days) makes it an ideal benchmark for studying other, less stable species (*Oppenheimer et al. 1998b, McGonigle et al. 2004, Rodríguez et al. 2008*). A number of measurement techniques exist, but ever since the first application of the correlation spectrometer (COSPEC) to volcanic emissions measurements (*Moffat and Millán 1971, Stoiber et al. 1983*), remote sensing techniques have become more and more established. More recently, the introduction of miniature ultra-violet spectrometers to the field (*Edmonds et al. 2003a, Galle et al. 2003*) has reduced both the cost and complexity of such measurements, and applying the well-established retrieval techniques of differential optical absorption spectroscopy (DOAS) is now standard practice (*Platt and Stutz 2008*). Aside from the obvious advantage of being able to measure volcanic emissions from a safe distance, it is also possible to implement measurement geometries that allow the retrieval of the total volcanic emission flux of a species, assuming lossless transport to the point of measurement (e.g. *Galle et al. 2003, McGonigle et al. 2005b*).

The relatively high spectral resolution (typically around 1 nm) of the DOAS instruments allows the simultaneous retrieval of different trace gas species. Aside from SO_2, both BrO and NO_2 have e.g. been detected in volcanic plumes in the past using scattered light DOAS observations (*Bobrowski et al. 2003, Oppenheimer et al. 2005*). Fourier transform infrared spectroscopy (FTIR) and active long-path DOAS can measure even more species in the IR and deep UV spectral ranges (*Oppenheimer et al. 1998a, Burton et al. 2007a, Kern et al. 2008b*), but they require more complex measurement geometries, as these wavelengths are not readily available in scattered sunlight.

The large amounts of SO_2 present in volcanic plumes and the fact that SO_2 is by far the strongest absorber around 300 nm, however, make high resolution measurements unnecessary for the quantification of SO_2 alone. *Mori and Burton 2006* and *Bluth et al. 2007* have demonstrated the ability to measure 2-dimensional SO_2 distributions in volcanic plumes using a simple UV-sensitive camera and band-pass filters only transmitting radiation at wavelengths significantly influenced by SO_2 absorption. Here, this concept is first dealt with in a theoretical approach. Certain problems are identified, and methods for improving both the accuracy and technical implementation of the technique are ascertained. According to these, a prototype of an improved SO_2-camera was then constructed, and test measurements were conducted at Mt. Etna (Italy).

4.2 Measurement principle

In its simplest form, an SO_2-camera is solely composed of a UV sensitive camera and a single spectral band-pass filter (referred to as filter *A* in the following) allowing only light of wavelengths in which significant SO_2 absorption takes place to enter the camera optics. Fig. 4.1 shows an example of the transmittance $T_A(\lambda)$ of such a band-pass filter along with the absorption cross-section $\sigma(\lambda)$ of SO_2. The intensity signal collected through this filter is compared to a background intensity either measured in a region in which no plume is present or interpolated from values acquired on either side of the plume. A schematic of the SO_2-camera measurement geometry is shown in Fig. 4.2.

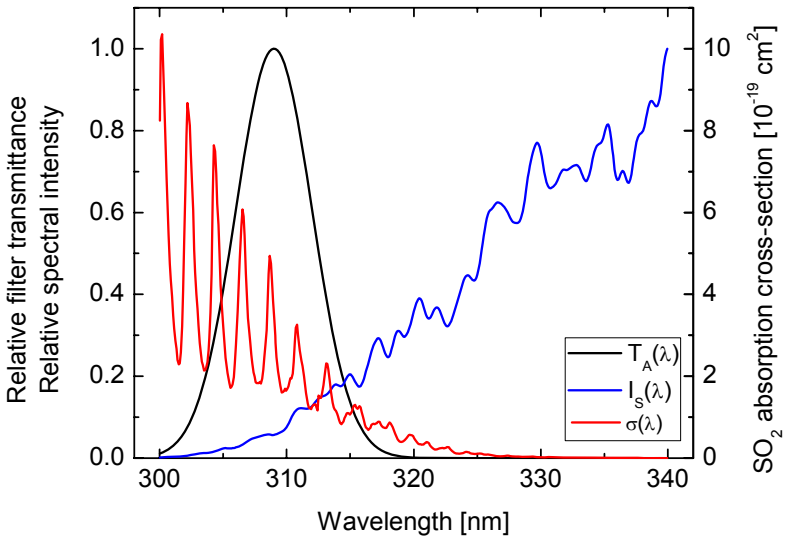

Fig. 4.1 – Example of the spectral transmittance *T*(*λ*) of a band-pass filter which could be used in an SO_2-camera setup. In this case, the maximum transmittance is centered at 309 nm, a region in which the SO_2 absorption-cross-section $\sigma(\lambda)$ is prominent (*Bogumil et al. 2003*). Also shown in blue is an example spectrum of incident scattered solar radiation $I_S(\lambda)$, in this case measured with an Ocean Optics© USB2000 spectrometer.

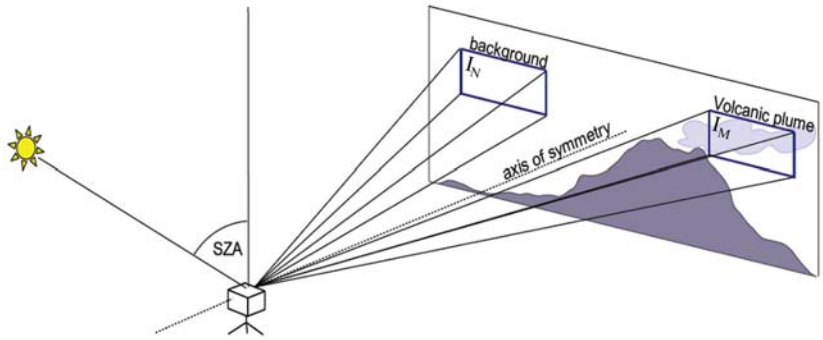

Fig. 4.2 – Geometry of an SO_2-camera measurement. The integrated intensity detected in the direction of the volcanic plume is compared to a background value. In the absence of inhomogeneous clouds, the background can be measured next to the plume. Because the Rayleigh scattering phase function is not spherically symmetric, it is, however, advantageous to use a similar relative solar azimuth and measurement elevation angle as in the measurement. (Adapted from *Kick 2008*)

In the absence of SO_2, the wavelength-dependent light intensity $I_{0,A}(\lambda)$ arriving at each pixel of the 2D camera CCD is given by the intensity of scattered radiation $I_S(\lambda)$ arriving at the instrument (see Fig. 4.1), the filter transmittance $T_A(\lambda)$, and the quantum efficiency $Q(\lambda)$ of the detector.

$$I_{0,A}(\lambda) = I_S(\lambda) \cdot T_A(\lambda) \cdot Q(\lambda) \qquad \textbf{Eq. 4.1}$$

If SO_2 is added to the optical path of the incident radiation, the spectral intensity is attenuated according to the Beer-Lambert equation (see chapter 3.1).

$$I_A(\lambda) = I_{0,A}(\lambda) \cdot \exp(-\sigma(\lambda) \cdot S) \qquad \textbf{Eq. 4.2}$$

Here, $\sigma(\lambda)$ is the absorption cross-section of SO_2 and S is its column density[8]. The negative logarithm of $I(\lambda)/I_0(\lambda)$ therefore gives the optical density $\tau(\lambda)$, which is directly proportional to the SO_2 column density S if SO_2 absorption is the only cause of light attenuation at the wavelength λ along the optical path.

$$\tau(\lambda) = -\ln\left(\frac{I_A(\lambda)}{I_{0,A}(\lambda)}\right) = \sigma(\lambda) \cdot S \qquad \textbf{Eq. 4.3}$$

A spectroscopic DOAS instrument with sufficient resolution would measure the optical density $\tau(\lambda)$ to retrieve the column density S, but the SO_2-camera takes a different approach.

[8] Note that in cases of very strong SO_2 absorption, the column density S will also be a function of wavelength $S(\lambda)$. This is discussed in chapter 8.

Instead of using a diffractive element (i.e. grating or prism) to image the spectral information on one dimension of the CCD, the SO_2-camera only employs the band-pass filter. For each pixel *i,j* of the 2-dimensional detector, the measured intensity $I_{M,A}$ is therefore described by the integral of the incident intensity $I_A(\lambda)$ over the transmission range of the filter.

$$I_{M,A} = \int_{\lambda} I_A(\lambda)\, d\lambda \qquad \textbf{Eq. 4.4}$$

The respective relation is valid for the background measurement $I_{N,A}$.

$$I_{N,A} = \int_{\lambda} I_{0,A}(\lambda)\, d\lambda \qquad \textbf{Eq. 4.5}$$

From these measured quantities, the weighted average optical density $\hat{\tau}_A$ is retrieved.

$$\hat{\tau}_A = -\ln\left(\frac{I_{M,A}}{I_{N,A}}\right) = \ln\left(I_{N,A}\right) - \ln\left(\int_{\lambda} I_{0,A}(\lambda)\cdot\exp\left(-\sigma(\lambda)\cdot S\right)\cdot d\lambda\right) \qquad \textbf{Eq. 4.6}$$

If the original notation is used, the weighted average optical density $\hat{\tau}_A$ is given by

$$\hat{\tau}_A = -\ln\left(\frac{\int_{\lambda} I_S(\lambda)\cdot T_A(\lambda)\cdot Q(\lambda)\cdot\exp\left(-\sigma(\lambda)\cdot S\right)\cdot d\lambda}{\int_{\lambda} I_S(\lambda)\cdot T_A(\lambda)\cdot Q(\lambda)\cdot d\lambda}\right) \qquad \textbf{Eq. 4.7}$$

While the weighted average optical density $\hat{\tau}_A$ is obviously a function of the SO_2 column density *S*, it is important to note that the dependency of $\hat{\tau}_A$ on *S* is generally non-linear. Only if the filter wavelength transmittance range is sufficiently narrow that the SO_2 cross-section σ can be regarded as independent of the wavelength λ in the measurement window, can the integrated optical density be written as

$$\hat{\tau}_A = -\ln\left(\frac{I_{N,A}\cdot\exp(-\sigma\cdot S)}{I_{N,A}}\right) = \sigma\cdot S = \tau \qquad \textbf{Eq. 4.8}$$

In this exceptional case, the weighted average optical density $\hat{\tau}_A$ is equal to the optical density τ of SO_2 at the measurement wavelength and is therefore proportional to the column density *S*. The instrument is in principle calibration free, as the relationship between the measured value $\hat{\tau}_A$ and the column density *S* is defined by Eq. 4.8 (where σ is known from laboratory measurements).

In all other cases, it is impossible to solve Eq. 4.7 for the column density *S*, because the incident scattered solar radiation spectrum $I_S(\lambda)$, the filter spectral transmittance $T_A(\lambda)$ and the quantum yield of the detector $Q(\lambda)$ are not analytical functions. They must either be accurately parameterized (especially difficult in the case of the scattered solar radiation spectrum, see Fig. 4.1) or an empirical instrument calibration must be conducted to determine the

relationship between the weighted average optical density $\hat{\tau}_A$ and the SO_2 column density S. This has been done with mixed success in the past (see *Mori and Burton 2006, Bluth et al. 2007, Kick 2008, Wöhrbach 2008*). The theoretical description given above now allows inferences to be made about where problems with calibration lie and how these can be solved (see section 4.4). First, however, the concept of normalized optical density is discussed.

4.3 Normalized optical density / apparent absorbance

In general, the relationship between the measured weighted average optical density $\hat{\tau}_A$ and the column density S of SO_2 is complex (see Eq. 4.7), but empirical calibration can greatly simplify the data evaluation process. However, one condition that must be fulfilled for the measurement principle described in section 4.2 to work is that SO_2 absorption is the only cause of light attenuation in the transmitting wavelength window of the applied filter *A*. While this condition may approximately be fulfilled in the case of cloudless skies and translucent, non-condensing, aerosol-free volcanic plumes (see *Bluth et al. 2007*), it will not generally be valid. In the presence of aerosols or water droplets in the volcanic plume, radiation entering the plume from behind will in part be scattered out of the instrument's field of view, thus causing a decrease in intensity. On the other hand, light entering the plume from other angles will in part be scattered towards the instrument, thereby causing an increase in intensity. Depending on the single scattering albedo of the plume aerosols, radiation will also be absorbed to some degree by the particles. Finally, a species other than SO_2 could be present in the plume and also absorb light in the measurement wavelength window. All of these processes compete with one another and can lead to attenuation or enhancement of radiation intensity being emitted from the plume towards the instrument as compared to the background sky intensity. If the measurement principle described in section 4.2 is simply applied, each of these influences will falsify the retrieved weighted average optical density $\hat{\tau}_A$ and therefore the SO_2 column density S.

Fortunately, aerosol scattering and absorption processes are of a broad-band nature, i.e. they are only weakly dependent on radiation wavelength. This stands in contrast to the SO_2 absorption, which only significantly affects the UV-wavelengths between about 250 and 320 nm (see Fig. 4.1 and *Bogumil et al. 2003*). Therefore, a second band-pass filter with a transmittance window above 320 nm (referred to as filter *B*) can be used to quantify the amount of light attenuation (or enhancement) not originating from SO_2 absorption. *Mori and Burton 2006* successfully applied this technique at Sakurakima volcano in 2005. In this approach, band-pass filter *A* on the SO_2-camera is at times replaced by filter *B*. Both background ($I_{N,B}$) and plume images ($I_{M,B}$) are recorded through filter *B*. Before the weighted average optical density $\hat{\tau}_A$ is calculated, the ratio of pixel intensities measured through filter *A* ($I_{M,A}/I_{N,A}$) is normalized by the ratio of pixel intensities measured through filter *B* ($I_{M,B}/I_{N,B}$). Alternatively, the weighted average optical density $\hat{\tau}_B$ can be calculated and subtracted from

the integrated optical density $\hat{\tau}_A$. The thus retrieved value is the normalized optical density $\hat{\tau}$, sometimes also referred to as the apparent absorbance *AA*.

$$\hat{\tau} = AA = -\ln\frac{\left(I_{M,A}/I_{N,A}\right)}{\left(I_{M,B}/I_{N,B}\right)} = \ln\frac{\left(I_{M,A}/I_{M,B}\right)}{\left(I_{N,A}/I_{N,B}\right)} = \hat{\tau}_A + \ln\left(I_{M,B}/I_{N,B}\right) = \hat{\tau}_A - \hat{\tau}_B \qquad \textbf{Eq. 4.9}$$

Because of its greatly improved robustness in regard to the influence of scattering and broadband absorption effects, normalizing the optical density is necessary whenever a significant aerosol load is present or water condensation occurs in a volcanic plume. The condition that SO_2 must be the dominant narrow-band absorber in the filter *A* wavelength window remains important. Only then can accurate SO_2 column densities *S* be retrieved.

4.4 Calibration issues

While the normalization of the integrated optical density is an important concept for the correction of broad-band light attenuation, the issue of how to calibrate the observed optical density remains. While it is in principle possible to construct a version of the SO_2-camera with inherent calibration by using very narrow band-pass filters (or possibly an interferometer), the transmittance window width would need to be on the order of 0.1 nm to ensure that the SO_2 absorption cross-section can be assumed constant in the transmittance window (see Eq. 4.8). However, such a design greatly reduces the instrument light throughput and therefore the measurement signal-to-noise ratio. For an optimal SO_2 sensitivity, the ideal filter transmittance is considerably wider, as is shown in section 4.5.2.

In the past, calibration has been conducted prior to or after measurements were made by inserting various SO_2 calibration cells with known SO_2 column densities *S* into the instrument's field of view and determining an empirical relationship between the weighted average optical density $\hat{\tau}$ (or apparent absorbance *AA*) and the SO_2 column density *S*. Because the weighted average optical density $\hat{\tau}$ depends on the incident scattered solar radiation spectrum $I_S(\lambda)$, the spectral transmittance of the band-pass filters $T(\lambda)$, and the quantum efficiency of the detector $Q(\lambda)$ (see Eq. 4.7), this simple approach will only function properly if all three parameters are constant in time. Unfortunately, this is usually not the case. While the quantum efficiency $Q(\lambda)$ can be assumed more or less constant in time and independent of wavelength in the region of interest, the other two parameters can vary depending on certain measurement conditions.

A model was set up to study the sensitivity of the SO_2-camera to variations in incident scattered solar radiation $I_S(\lambda)$ and filter transmittance $T(\lambda)$. The transmittance of the band-pass filter *A* was simulated using a Gaussian transmittance distribution centered around λ_C = 309 nm and with a standard deviation of 3 nm (shown in Fig. 4.1). This curve closely resembles

the transmittance curve of the filter later chosen for the construction of the SO_2-camera prototype (compare Fig. 4.11). For each wavelength between 300 and 340 nm, the measured incident scattered solar radiation spectrum $I_S(\lambda)$ was multiplied by the filter transmittance $T_A(\lambda)$. The quantum efficiency $Q(\lambda)$ was not taken into account further, as the quantum efficiency of the spectrometer's detector is intrinsically included in the measured solar spectrum $I_S(\lambda)$ and is thought to closely resemble that of a typical SO_2-camera. In this manner, the spectral intensity $I_{0,A}(\lambda)$ was calculated according to Eq. 4.1. The calculation was then repeated, this time including SO_2 absorption by multiplying with the exponent given in Eq. 4.2, assuming an SO_2 column density of 1×10^{18} molec/cm^2 or 400 ppmm. This is a typical value for volcanic emissions measurements.

4.4.1 Incident spectral intensity

The spectrum of scattered radiation arriving at the earth's surface depends on the solar zenith angle (SZA), especially in the UV wavelength region. For high solar zenith angles, the average optical path length through the stratospheric ozone layer is considerably longer than for lower SZAs.[9] As the ozone absorption cross-section increases dramatically towards deep UV wavelengths (see Fig. 4.3), the lower end of the scattered light spectrum is particularly influenced by these variations in optical path length.

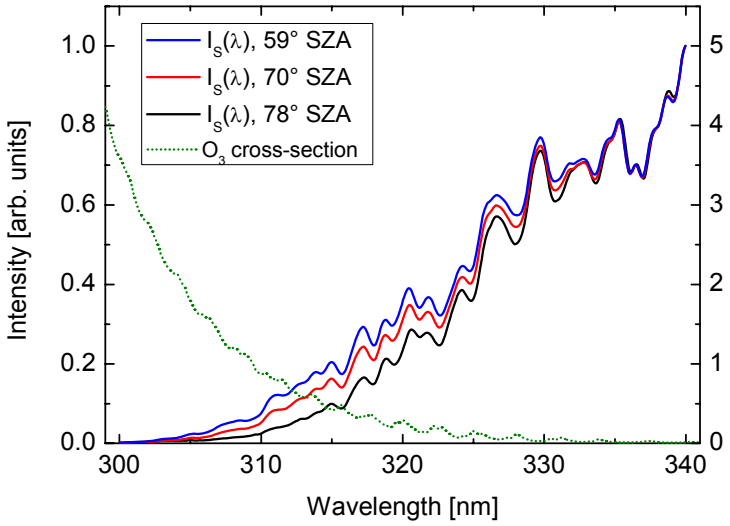

Fig. 4.3 – Measured spectrum of scattered solar radiation $I_S(\lambda)$ for three different solar zenith angles (SZA). While an absolute calibration was not undertaken (the quantum yield Q(λ) of the spectrometer is unknown), the intensity between 300 and 340 nm obviously increases relative to the intensity at 340 nm with decreasing solar zenith angle. This is caused by a decrease in

[9] There is one exception to this rule. For SZAs approaching 90° the average optical path through the ozone layer decreases. This so-called Umkehr-Effect (*Götz 1931, Götz et al. 1934*) is caused by an increase in the contribution of radiation scattered above the ozone layer to the total incident scattered light.

optical path length of the detected radiation in the ozone layer. The ozone absorption cross-section (shown dotted) increases sharply towards lower wavelengths (*Voigt et al. 2001*, 223K).

Fig. 4.3 depicts measurements of the incident scattered radiation spectrum $I_S(\lambda)$ made in Heidelberg, Germany on a cloudless day. Three spectra were recorded at 59, 70, and 78° SZA, respectively. Each spectrum was normalized to its intensity at 340 nm. While all spectra fall off to null at approximately 300 nm, their relative intensities vary across the wavelength range from 300 to 340 nm, a result of variations in ozone optical density.

Using these measured spectra and the described model, the effect of such variations on the weighted average SO_2 optical density $\hat{\tau}$ measured with an SO_2-camera can be discussed. In this first study, the spectral intensities $I_{0,A}(\lambda)$ and $I_A(\lambda)$ were calculated using the incident spectral intensities measured at the solar zenith angles 59° and 78°. The four curves calculated in this manner are shown in Fig. 4.4. It is immediately evident that both the background intensity $I_{0,A}(\lambda)$ and the measurement intensity $I_A(\lambda)$ are by no means smooth. The presence of Fraunhofer absorption lines and, in the case of $I_A(\lambda)$, superimposed SO_2 absorption lines makes for a rough distribution.

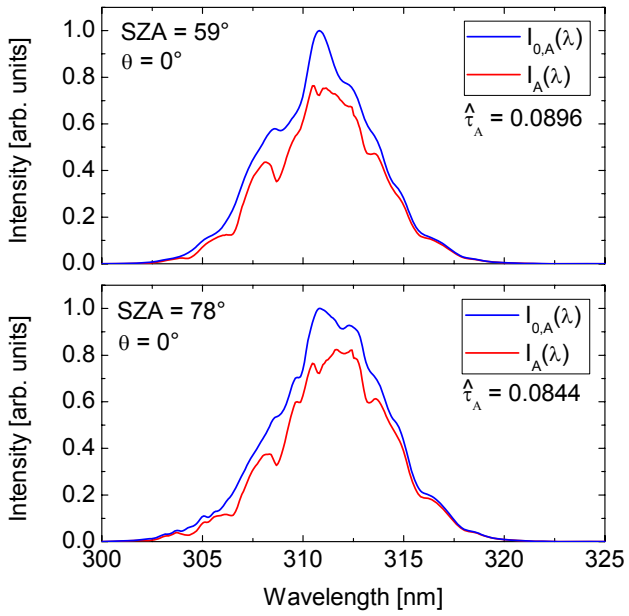

Fig. 4.4 – Modeled light intensity I_A passing filter *A* of the UV-camera as a function of wavelength *λ* for two different solar zenith angles (SZA). The blue curve ($I_{0,A}$) assumes no SO_2 in the optical path (background spectrum), while the red curve (I_A) represents an SO_2 column density *S* of 400 ppmm. In both cases, light passes the filter in a perpendicular direction (θ = 0). The ratio of integrated intensity under the background spectrum and under the measurement spectrum yields the indicated integrated optical density $\hat{\tau}_A$ according to Eq. 4.6. The two weighted average optical densities $\hat{\tau}_A$ are 6% different, even though the assumed SO_2 column density *S* was the same in both cases.

The SO_2 camera, however, does not measure the spectral intensities $I(\lambda)$, but only the integrated intensities $I_{M,A}$ and $I_{N,A}$ defined in Eq. 4.4 and Eq. 4.5. These can be extracted from the plots in Fig. 4.4 by integrating the spectral intensities $I(\lambda)$ over the transmittance range of the filter. Then, the integrated optical density ϑ_A can be calculated according to Eq. 4.6. The obtained values for the integrated optical density ϑ_A are given below the legends in Fig. 4.4. For the assumed measurement conditions, the two values exhibit a discrepancy of 6 %. This example therefore illustrates the fact that a correct calibration of the measured weighted average optical density $\hat{\tau}_A$ will depend on the solar zenith angle at the time of the measurement. In fact, a variation in the total stratospheric ozone column will have the same effect, as the total O_3 column density along the optical path determines the spectrum $I_S(\lambda)$. The use of a correction factor for this effect is non-trivial, however, as the magnitude of the correction will depend on other factors as well, including the SO_2 column density S itself.

4.4.2 Filter illumination angle

It is a well documented fact that the central wavelength of the transmittance window of a band-pass interference filter λ_c decreases if the filter is not illuminated perpendicularly (e.g. *Lissberger and Wilcock 1959*). For incidence angles θ below 20°, the central wavelength λ_c of the transmittance window can be approximated by the expression

$$\lambda_c(\theta) = \lambda_c(0°)\sqrt{1-\frac{\sin^2(\theta)}{n^2}} \qquad \textbf{Eq. 4.10}$$

In the case of the filter obtained for the construction of the SO_2-camera prototype, this relation was confirmed by a measurement. Fig. 4.5 shows the measured relative transmittance $T(\lambda)$ of the filter as a function of the illumination angle θ. The transmittance window shifts towards lower wavelengths as the illumination angle θ increases. Also, the maximum transmittance decreases, and the width of the window increases slightly.

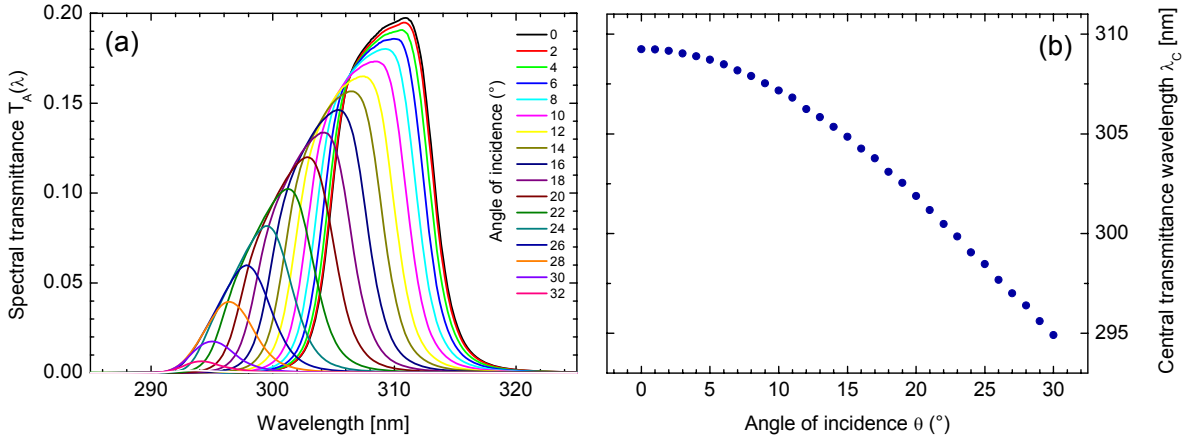

Fig. 4.5 – (a) Measured relative filter transmittance $T_A(\lambda)$ as a function of the illumination angle θ. (b) Central transmittance wavelength λ_c of the interference filter as a function of filter illumination angle θ (as given in Eq. 4.10). The filter transmittance window shifts towards lower wavelengths if the filter is illuminated in a non-perpendicular direction. (from *Kick 2008*)

The dependence of the filter transmittance $T(\lambda)$ on the illumination angle can therefore change the sensitivity of the SO_2-camera to a certain SO_2 load if the filter is not always illuminated perpendicularly (θ = 0). This effect was studied using the model described in the previous section. Fig. 4.6 depicts the modeled spectral light intensity passing filter A of the SO_2-camera under the incidence angles θ of 6° and 10°. These angles correspond to a shift in the filter transmittance window of approximately 1 and 2 nm, respectively, towards shorter wavelengths (see Fig. 4.5). The further the filter transmittance window shifts towards shorter wavelengths, the larger the influence of strong SO_2 absorption bands (located around 300 nm, see Fig. 4.1) becomes on the measured weighted average optical density $\hat{\tau}_A$. This leads to an increase in the sensitivity of the SO_2-camera on a given SO_2 column density (again kept constant at 400 ppmm in this case). Compared to the weighted average optical density $\hat{\tau}_A$ modeled for perpendicular illumination (Fig. 4.4, top), an increase of 9 % was obtained for an angle of incidence θ of 6° and an increase of 20 % was found for θ = 10°.

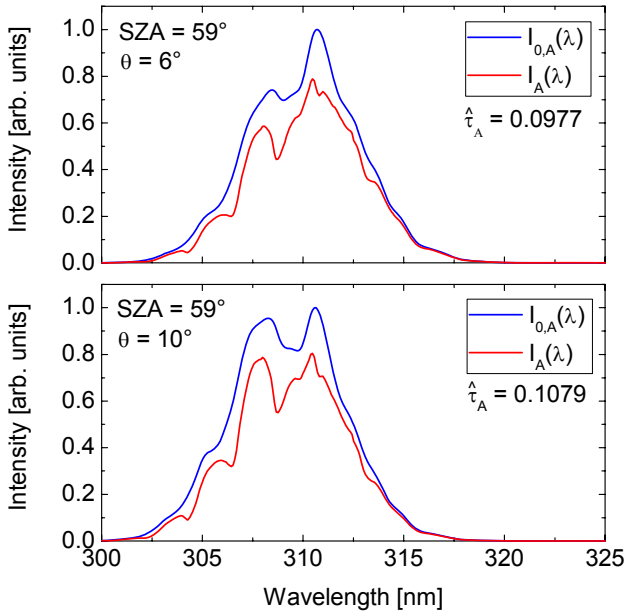

Fig. 4.6 - Modeled light intensity I_A passing filter *A* of the SO_2-camera as a function of wavelength λ for two different illumination angles θ. The blue curve ($I_{0,A}$) assumes no SO_2 in the optical path (background spectrum), while the red curve (I_A) represents an SO_2 column density *S* of 400 ppmm. In both cases, the solar zenith angle (SZA) was kept at 59°. The ratio of integrated intensity under the background spectrum and under the measurement spectrum yields the indicated integrated optical density $\hat{\tau}_A$ according to Eq. 4.6. The two integrated optical densities $\hat{\tau}_A$ are 9% and 20% higher than for perpendicular illumination (compare to Fig. 4.4 (top)).

This significant increase in sensitivity for non-perpendicular illumination can make a spatially inhomogeneous calibration necessary if the filter illumination is not equal for all measured radiation. In a simple setup of the SO_2-camera, for example, the band-pass filter is placed in front of the camera lens. In this configuration (shown in Fig. 4.7), however, light originating from different areas in the field of view will have a different angle of incidence through the band-pass filter. Therefore, the sensitivity (and the calibration) of the SO_2-camera in this setup will depend directly on the incidence angle θ. The maximum filter incidence angle θ_{max} is identical to half of the camera's total aperture angle α.

Fig. 4.8 shows the spatial sensitivity distribution of this setup obtained by modeling the integrated optical density for various illumination angles θ and assuming an SO_2 column density of 400 ppmm and a solar zenith angle of 59°. Towards the edge of the measured image, the camera exhibits a sensitivity to SO_2 that is more than 20 % greater than in the center of the image. This is caused by non-perpendicular illumination of the filter shifting its transmittance window towards lower wavelengths and stronger SO_2 absorption bands, as demonstrated in Fig. 4.6.

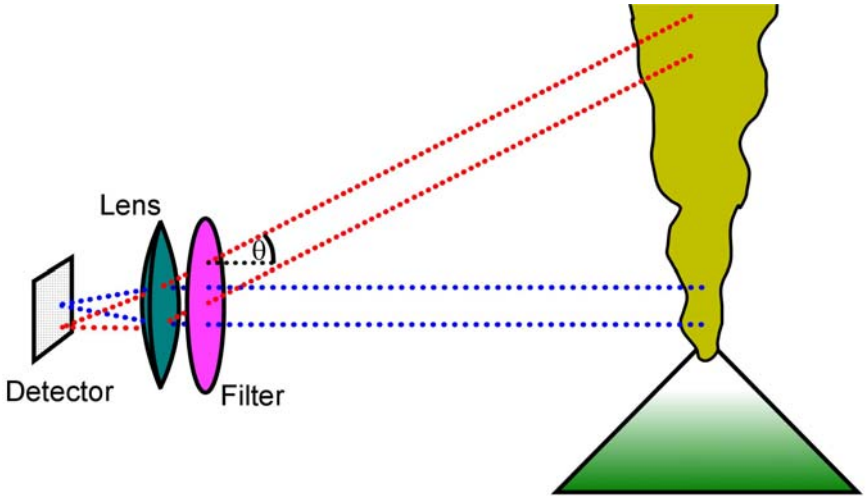

Fig. 4.7 – Schematic of a simple SO_2-camera setup. Parallel light that passes the band-pass interference filter is focused on the 2-dimensional UV-sensitive detector. Depending on the viewing direction, however, the light passes through the filter under different incidence angles θ and therefore different filter transmittance curves $T(\lambda)$ apply.

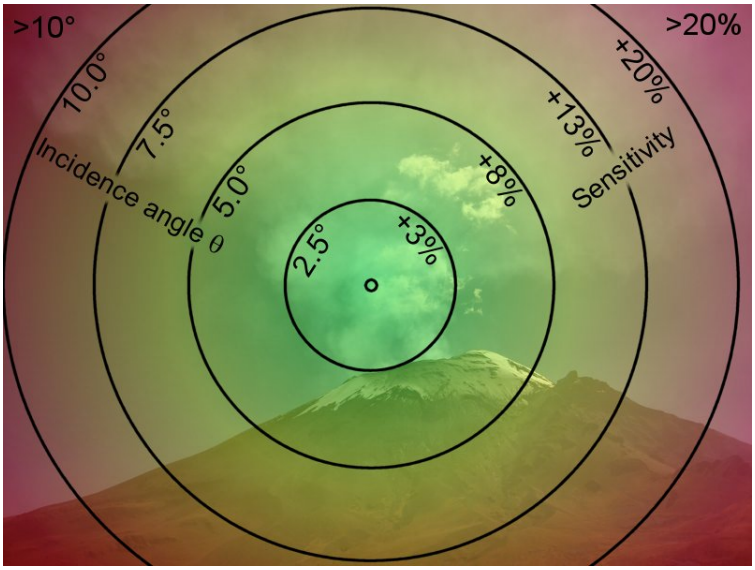

Fig. 4.8 – Modeled spatial sensitivity distribution of the simple SO_2-camera shown in Fig. 4.7. Given is the modeled sensitivity relative to the position in the center of the image assuming an SO_2 column density S of 400 ppmm and a solar zenith angle (SZA) of 59°. If left uncorrected, the SO_2 column density measured at the edge of the image would be overestimated by more than 20% even though the depicted camera aperture angle α is comparatively small (only 20°).

Correcting for the effects described above is not trivial, as a simple correction factor approach fails due to the non-linearity of Eq. 4.7. In order to solve the integral in the equation, all wavelength dependent parameters (incident solar spectrum $I_S(\lambda,\text{SZA})$, detector quantum efficiency $Q(\lambda)$, filter transmittance $T(\lambda,\theta)$) as well as the SO_2 column density S must be taken into account. The equation must subsequently be solved for each pixel i,j on the camera's detector, as each sees a different column density $S_{i,j}$. Due to the numerical costs of this calculation, one approach to the problem could be to generate 3 dimensional lookup tables containing typical correction factors based on the measurement parameters SZA, θ, and S. Since the column density S is unknown at first, an iterative approach would be necessary to later retrieve the correct value. In the first iteration, the uncorrected measured column density S_0 could be used to retrieve appropriate correction factors which yield an improved column density S_1. In subsequent iterations, the accuracy of the column density could be further improved.

4.5 Design of an SO_2-camera prototype

Keeping the theoretical principles described above in mind, an advanced prototype for an SO_2-camera was constructed. Several components (optics, filters, detector) were changed as compared to previous setups (*Mori and Burton 2006, Bluth et al. 2007*) to improve the performance of the novel prototype.

4.5.1 Advanced optical system

An advanced optical system was designed specifically for the SO_2-camera in an attempt to reduce the illumination angle dependent calibration issues described in section 4.4. A schematic of this design is shown in Fig. 4.9. The optical system is composed of two lenses or lens groups[10] between which the band-pass interference filter is located. An adjustable aperture is centered in the focal point of the first lens group (if the focus is assumed to be infinity). The total aperture angle of the camera is therefore given by the relation

$$\alpha = 2 \cdot \arctan\left(\frac{R_1}{f_1}\right) \qquad \textbf{Eq. 4.11}$$

where R_1 is the effective radius of the first lens and f_1 is its focal length. A virtual image of the viewed landscape is created in the opposite focal plane of the first lens group. The band-pass interference filter is positioned either in front of or behind this image, so that dust or inhomogeneities on the filter are not in focus. The maximum angle of incidence θ_{max} on the

[10] Lens errors can be reduced by using multiple lenses, as the respective refraction angles can be reduced.

filter is now no longer given by the aperture angle α of the camera, but rather by the aperture d and the focal length f_1.

$$\theta_{max} = \arctan\left(\frac{d}{2f_1}\right) \qquad \text{Eq. 4.12}$$

Behind the filter, a second group of lenses projects the virtual image onto the detector. In this setup, the maximum incidence angle θ_{max} can be greatly reduced compared to the aperture angle α. For the prototype, a lens group with effective focal length f_1 of 25 mm was used and the aperture d was typically 2.5 mm, resulting in a maximum illumination angle θ_{max} of less than 3°, while the camera's aperture angle α was approximately 20° (the effective radius R_1 of the first lens was 5 mm). Also, even though the filter was not illuminated exactly perpendicularly, the distribution of incidence angles was identical for each position on the image. This does not hold true for the simple construction shown in Fig. 4.7.

Next to the obvious advantage of a spatially homogeneous calibration, the optical system does have two disadvantages. For one, the relatively small aperture in the front of the optical system makes for a lower light throughput than in a conventional setup (Fig. 4.7). However, by using of a UV-sensitive back-illuminated CCD detector instead of a standard front-illuminated chip, the signal to noise ratio was sufficient to achieve a time resolution on the order of Hz (mainly limited by camera readout and filter exchange times). Secondly, the proximity of the band-pass filter to the focused intermediate virtual image can lead to artifacts in the final image if dust or other spatial inhomogeneities are present on the filter. Therefore, it should be positioned as far as possible from the focused intermediate image.

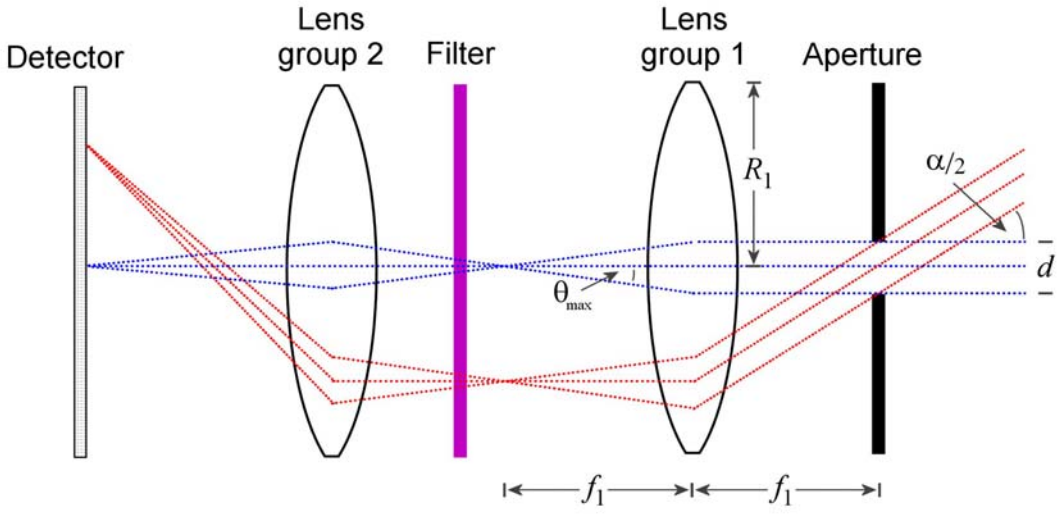

Fig. 4.9 – Schematic of the advanced optical system used in the SO_2-camera prototype. Two groups of lenses are used. The first group creates a virtual image of the landscape. Behind the band-pass filter, the virtual image is then imaged onto the CCD detector. In this design, the aperture angle of the camera α is no longer directly related to the illumination angle of the filter θ. The maximum illumination angle θ_{max} is instead controlled by the aperture *d*.

4.5.2 Ideal filter selection

When selecting the band-pass interference filters for use in the SO_2-camera, several aspects must be considered. Both the spectral position of the filter transmittance window as well as its width will determine the light throughput of the optical system. On the one hand, it can be advantageous to chose a very narrow-band transmittance window positioned directly on one of the strong SO_2 absorption lines, as the SO_2 sensitivity will be high and the calibration becomes simpler (see section 4.4). On the other hand, the light throughput of such a system will be extremely low, thus resulting in an increased relative noise level. In the following, an attempt is made to determine the ideal filter transmittance width and central wavelength λ_c for filter *A*. Filter *B* is less critical, as the incident solar radiation is much more intense above 320 nm. Therefore, the instrument signal-to-noise is decisively limited by filter *A*.

The model described in section 4.4 was used to calculate the relative signal-to-noise ratio for a variety of filter configurations. The spectral transmittance curve of filter *A* was again parameterized using a Gaussian distribution. For FWHM between 1 and 30 nm, the relative signal-to-noise ratio was calculated as a function of the central transmittance wavelength λ_c of the filter. For the sake of comparability, an identical maximum transmittance was assumed for all filters. This does not necessarily reflect reality, as very narrow band-pass interference filters tend to have lower maximum transmittances than wider filters, but actual transmittances vary. When comparing filters with known transmittances, further normalization of the results given in Fig. 4.10 by the individual maximum filter transmittances can easily be conducted. Also, a wavelength-independent detector quantum yield Q was assumed. If the quantum yield of a specific detector changes significantly over the considered wavelength interval (300 to 325 nm), the quantum efficiency curve $Q(\lambda)$ should be included in the model according to Eq. 4.7. Sensitivity studies showed that this can result in a slight shift in the ideal filter transmittance central wavelength λ_c (see *Wöhrbach 2008* for details).

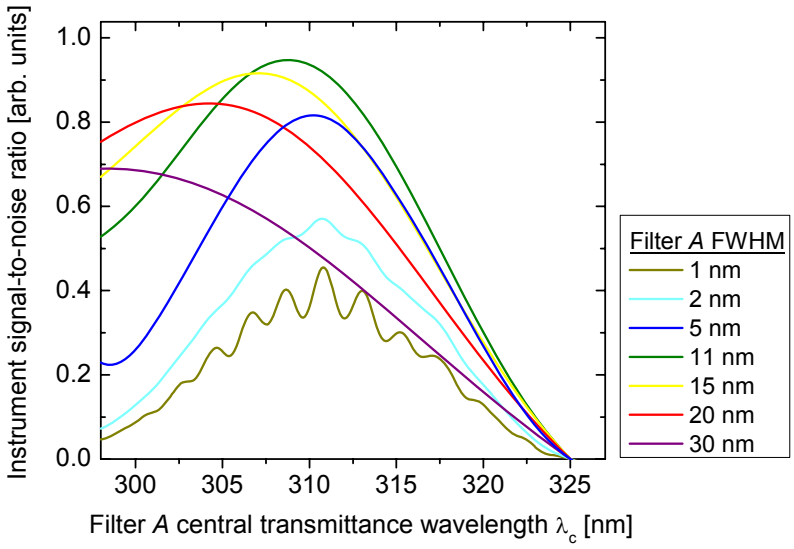

Fig. 4.10 – Modeled instrument signal to noise ratio as a function of the central wavelength of filter *A*. Different colors represent different transmittance window FWHM. A FWHM of less than about 2 nm is needed to resolve an individual SO_2 line. However, the signal-to-noise ratio increases for larger FWHM up to a width of 11 nm due to the increased light throughput. (adapted from *Wöhrbach 2008*)

For the calculation of instrument signal-to-noise ratio, a second filter (filter *B*) was simulated using a transmittance window centered at λ_c = 325 nm and an identical FWHM as filter *A*. The normalized weighted average SO_2 optical density $\hat{\tau}$ was then retrieved according to Eq. 4.7 and Eq. 4.9, assuming an SO_2 column density of 4×10^{18} molec/cm^2. Furthermore, as the noise of each measured integrated intensity is proportional to the square root of the intensity itself (photon statistics), the total noise of the weighted average optical density $\Delta\hat{\tau}$ could be quantified using Gaussian error propagation (see *Wöhrbach 2008* for details). Dividing $\hat{\tau}$ by $\Delta\hat{\tau}$ yields a value proportional to the signal-to-noise ratio.

The thus obtained ratios are shown (relative to one another) in Fig. 4.10. In general, the ideal central transmittance wavelength varies between 300 and 310 nm. Towards the shorter wavelengths, the incident scattered solar radiation $I_S(\lambda)$ decreases due to strong ozone absorption, and the relative signal-to-noise ratio $\hat{\tau}/\Delta\hat{\tau}$ drops. Towards longer wavelengths the incident intensity $I_S(\lambda)$ increases, but the SO_2 absorption cross-section becomes smaller (see Fig. 4.1), therefore decreasing the measured signal (see section 4.4).

Very narrow filters (less than 2 nm) are sensitive to individual SO_2 absorption bands. Therefore, the signal-to-noise ratio oscillates, depending on whether the transmittance window is on or between an SO_2 absorption line (compare to Fig. 4.1). If a very narrow filter is used, the results indicate that placing the central wavelength λ_c on the SO_2 absorption band at 311 nm will yield the ideal signal-to-noise ratio. Wider transmittance windows are no longer sensitive to individual lines, but rather to the integral over several bands. As the filter

transmittance width increases, the light throughput of the system increases thereby reducing the measurement noise and increasing the signal-to-noise ratio. However, if the transmittance window becomes too wide, parts of the scattered solar spectrum are included in which SO_2 absorption is less significant. Therefore, the measured signal no longer increases, and the signal-to-noise ratio decreases again.

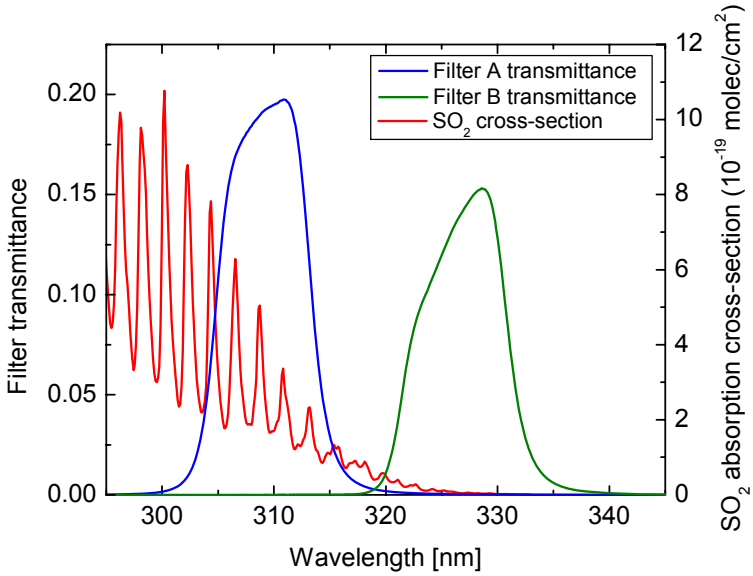

Fig. 4.11 – Measured transmittance of the two band-pass filters used for construction of the SO_2-camera prototype. Also shown (red) is the absorption cross-section of SO_2 (*Bogumil et al. 2003*). (Adapted from *Kick 2008*)

The ideal filter transmittance curve $T(\lambda)$ given by the model was centered at λ_c = 309 nm and had a FWHM of 11 nm. The filters used for the construction of the SO_2-camera prototype were chosen accordingly. Fig. 4.11 shows the transmittances of the two band-pass interference filters acquired for this purpose from BK Interferenzoptik,© Nabburg, Germany. Filter *A* was centered at 309 nm, filter *B* at 326 nm. The spectral transmittance curves $T(\lambda)$ are slightly asymmetric, with FWHM of about 10 nm.

4.5.3 Technical implementation

A schematic of the designed SO_2-camera prototype is shown in Fig. 4.12. An ANDOR© 420 BU back-thinned CCD camera was chosen for as a detector. This back thinned detector features a quantum efficiency *Q* that is about 5 times higher at 300 nm than that of a standard front illuminated CCD. It has a wide image area of 26.6 × 6.7 mm (only about 11 × 6.7 mm were used) split into 1024 × 256 pixels, each with an area of 26 µm^2 and a well depth of 400,000 electrons. The camera is controlled by a Jetway© J7F21GE Mini-ITX PC via a PCI interface. The PC has a 1 GHz VIA© Eden processor, 1 GB RAM, and an 80 GB hard drive. It

is powered off 12V DC input voltage by an M1-ATX power supply system. The entire setup can alternatively be run off a 12V DC power supply or a 12V battery.

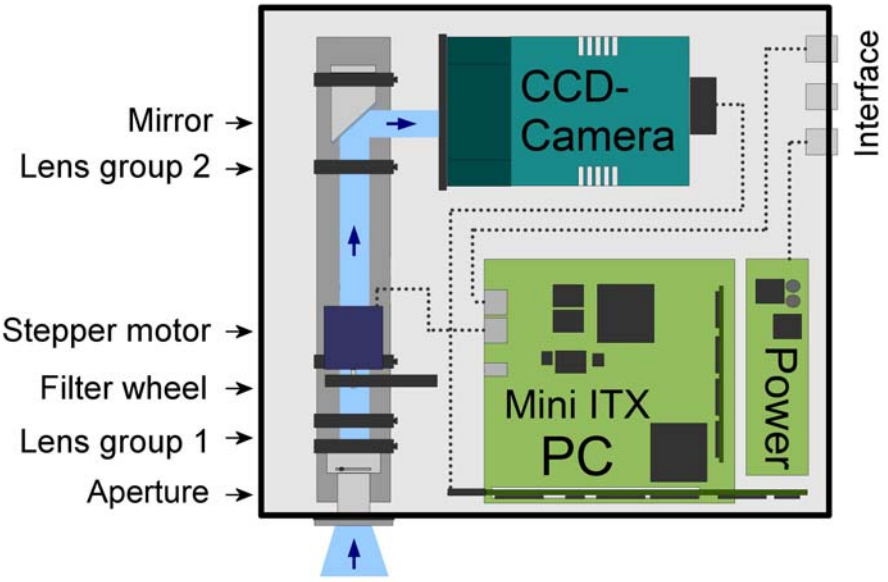

Fig. 4.12 – Schematic setup of the SO_2-camera prototype. Light enters the instrument through an aperture, passes through the band-pass filter and is focused on the CCD detector. The measurement is controlled by an internal ITX PC, and data is saved on an internal hard drive. The interface is used to configure the measurement and collect data, as well as supply 12V DC power. (adapted from *Wöhrbach 2008*)

The advanced optical system depicted in Fig. 4.9 was constructed using 1 inch quartz lenses mounted on an adjustable OWIS© optical bench. An adjustable iris aperture was installed at the optical entrance. The entire system has an effective focal length of 24 mm and a total aperture angle α of 26° (horizontal). The two filters *A* and *B* are alternatively placed in the optical path by a Trinamic Pandrive PD1-110-42-232 stepper motor driven by a motor controller connected to the serial port of the ITX PC.

4.6 Measurement examples

The designed SO_2-camera was tested twice at Mt. Etna, Italy. The first tests were conducted in October of 2007. Volcanic activity at Mt. Etna was elevated during the measurement period, with a new vent opening on the eastern flank of the active south-east crater. Periodically, explosions at this vent emitted short, ash-laden gas pulses. Fig. 4.13 shows a visible image of such an explosive event ejecting a dark ash plume.

In the first test of the instrument conducted on October 15, 2007, the SO_2-camera was used to measure the SO_2 distribution around the summit of Mt. Etna. Fig. 4.14 shows an example time series of SO_2 images recorded from the town of Milo located about 11 km east-south-east of the volcano's summit. The viewing direction of the SO_2 camera coincides with that shown in Fig. 4.13.

The first 9 images in Fig. 4.14 show the slightly variable distribution of SO_2 in the summit area of Mt. Etna. On this particular day, an easterly wind was blowing the volcanic plume away from the instrument. However, it is interesting to notice the elevated SO_2 column densities around both the north-east (typically the most active) and the south-east craters. This area of elevated SO_2 is not apparent in the visible image (compare Fig. 4.13).

In the 10^{th} image in Fig. 4.14, an area of apparently reduced SO_2 can be observed on the southern side of the image. This area expands in the subsequently recorded images, and corresponds to a dark, ash-laden plume being emitted from the active vent on the eastern flank of the south-east crater (compare Fig. 4.13). As UV-radiation cannot sufficiently penetrate this ash-rich plume, the enhanced signal from the volcanic plume behind the ash cloud is blocked. Therefore, the measured SO_2 column density drops to null for areas in which the ash cloud blocks the plume behind it. As the short pulse of ash-laden emissions dissipates, the original SO_2 column density can once again be measured. This example measurement illustrates the fact that radiative transfer effects can skew or even falsify a measured SO_2 column density if they are not taken into account. This topic is discussed in more detail in chapter 8.

Fig. 4.13 – Visible image of Mt. Etna taken on October 15, 2007 from the town of Milo. In this image, a dark, ash-laden plume is being emitted from the new vent on the eastern flank of the south-east crater. Plumes such as this one were intermittently emitted as a consequence of ongoing explosions at this vent. (adapted from *Kick 2008*)

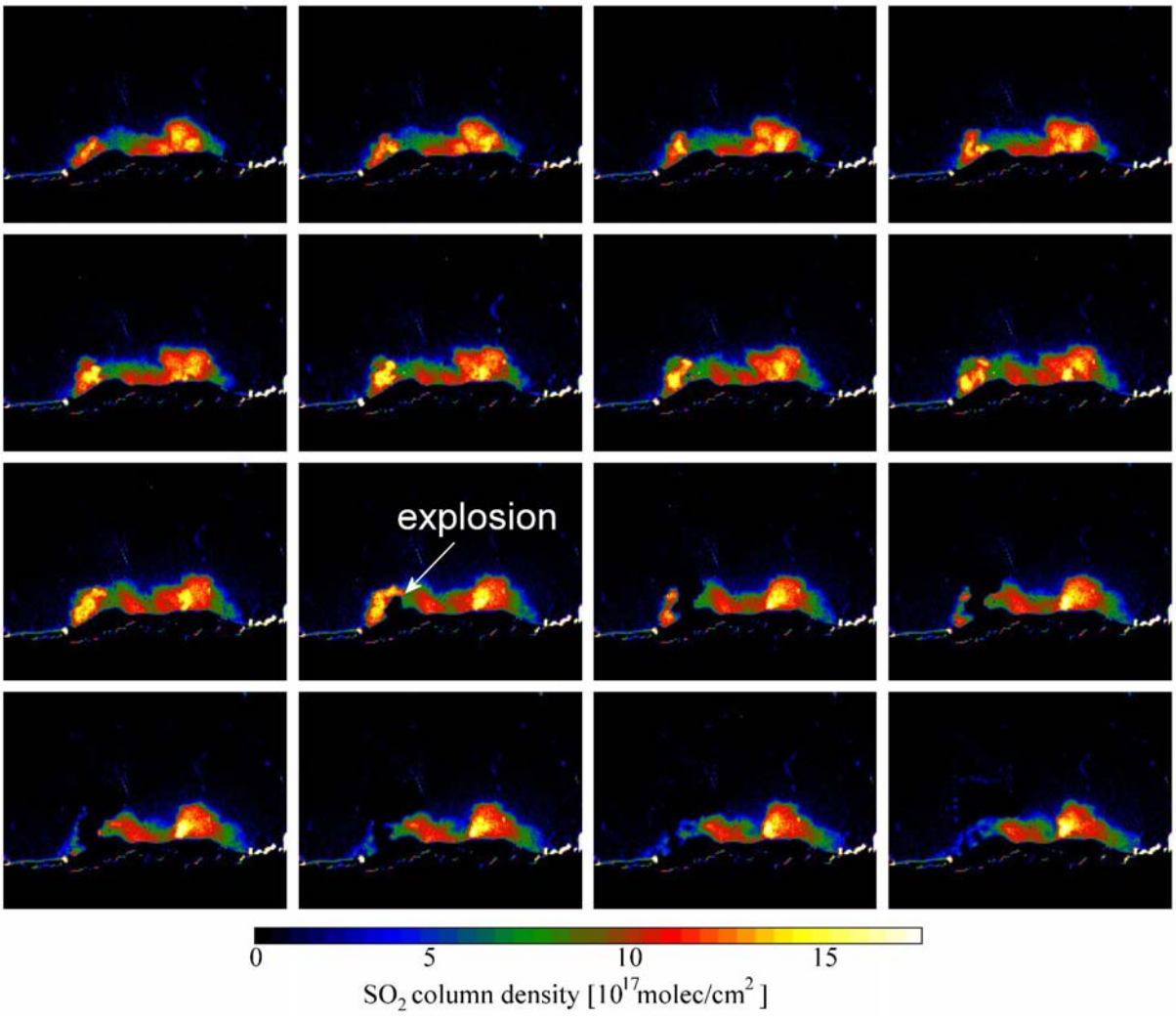

Fig. 4.14 – Time series of SO_2 images recorded at Mt Etna on October 15, 2007 beginning at 13:00 local time. The time gap between each of the depicted images is 21 seconds. In the 10th image, a dark cloud can be observed rising up from the vent on the eastern flank of the south-east crater. As UV-radiation cannot sufficiently penetrate this ash-rich plume, the signal from the volcanic plume behind the ash cloud is blocked, resulting in an area of decreased measured SO_2 column density. (adapted from *Kick 2008*)

As a second example, a measurement conducted on July 16, 2008 at the same site in Milo is shown. In this case, however, the SO_2 camera was not aimed at the volcano's summit but in a southerly direction instead. On this particular day, a westerly wind was blowing the volcanic emissions towards the east, such that they passed above and to the south of Milo. In the left side of Fig. 4.15, a visible image of the volcanic plume is shown. The plume can be identified by the slight white haze apparent in the center of the image. The plume was blown from right to left through the image. A large black rectangle represents the field of view of the SO_2-camera. On the right side of the image, an example SO_2 distribution measured at 12:30 local time with the SO_2-camera is shown. This image was smoothed slightly to remove artifacts caused by dust in the camera's optical system. SO_2 column densities of more than 1×10^{18} molec/cm^2 (400 ppmm) were detected in the center of the plume.

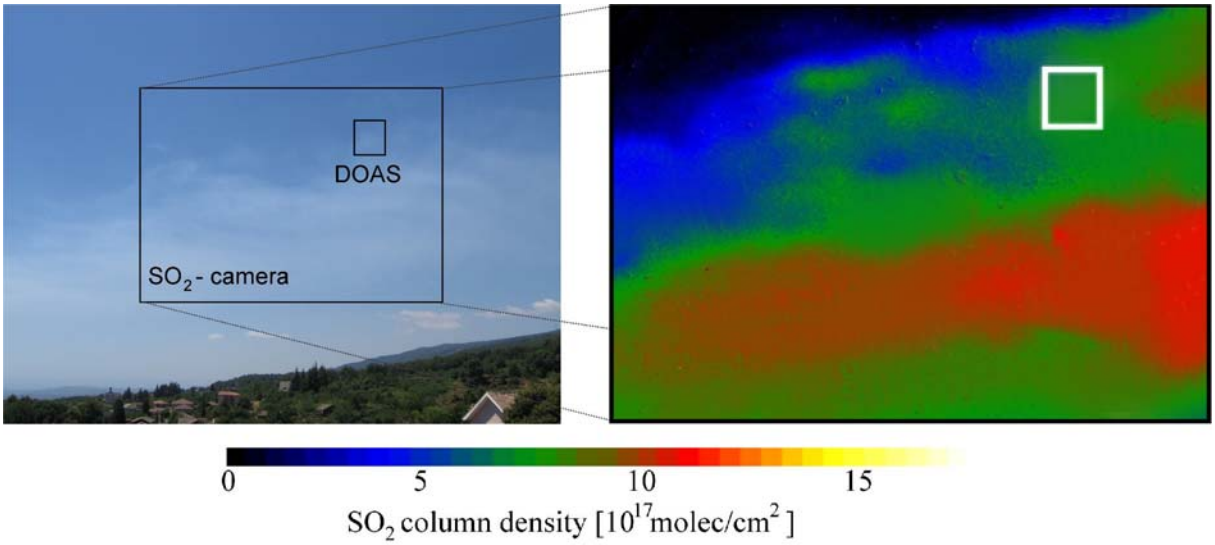

Fig. 4.15 – Visible and SO_2-camera images recorded over the town of Milo at the base of Mt. Etna on July 16, 2008. The images were taken in southerly direction, the plume was moving from right to left through the images. The SO_2 image was slightly smoothed to remove artifacts caused by dust in the optical system. A passive DOAS instrument was also aimed at the volcanic plume. Its approximate viewing direction is indicated by a small rectangle in both images. (adapted from *Wöhrbach 2008*)

Next to the SO_2 camera, a passive DOAS instrument (NOVAC mark II, see chapter 3.5.1) was located on the same rooftop in Milo on July 16, 2008. This instrument was set to use a single, fixed viewing direction. The approximate location of this direction is given by the small rectangle in Fig. 4.15. However, the DOAS instrument's field of view was 0.35° which corresponds to an area of only approximately 3×3 pixels on the SO_2 camera's image. In order to compare the DOAS results with those of the SO_2 camera, the relative location of the DOAS field of view on the SO_2-camera image is necessary. Instead of laboriously aligning the instruments in an exact manner in the field, this relative location can be extracted from the

measurement data. This is achieved by dividing the SO_2 camera image into small sectors. For each sector i, the average SO_2 column density S_i is computed by averaging over all pixels in the sector. This process is repeated for all images in the time series measured by the SO_2-camera (to reduce computation time, some images can be omitted if the time resolution of the SO_2-camera is higher than that of the DOAS, which is usually the case). In this manner, an SO_2 time series $S_i(t)$ is computed for each sector i on the SO_2 image. Fig. 4.16 shows several examples of such time series retrieved in different sectors of the SO_2-camera image. In total, 14 different sectors of 50×50 pixels were analyzed.

Next, the correlation coefficient c_i of each time series $S_i(t)$ with the time series retrieved from the DOAS data $S_D(t)$ is calculated.

$$c_i = \frac{1}{k} \cdot \int S_i(t) \cdot S_D(t) \cdot dt \qquad \textbf{Eq. 4.13}$$

k is a normalization constant. If the sector size is smaller than or equal to the typical inhomogeneities of the volcanic plume, the maximum correlation coefficient will be retrieved for the sector that best corresponds to the viewing direction of the DOAS instrument. This sector (sector 6 in Fig. 4.16) is indicated by the small rectangle in Fig. 4.15.

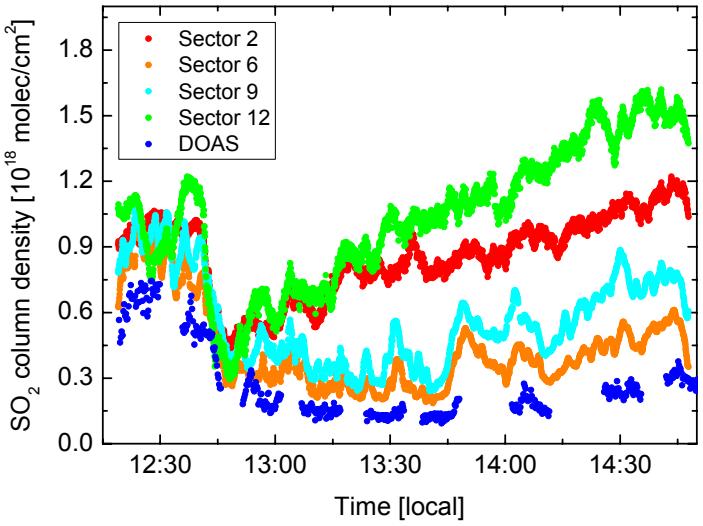

Fig. 4.16 – Example of several SO_2 column density time series retrieved in different sectors of the SO_2-camera image. Also shown (blue) is the time series obtained from the passive DOAS instrument. (adapted from *Wöhrbach 2008*)

If the field of view of the DOAS instrument is drastically smaller than that of the SO_2-camera (as is typically the case), an iterative approach should be implemented rather than initially dividing the SO_2 image into an extreme number of sectors. Here, the sector with the highest correlation coefficient (sector 6) was again divided into subsectors. After the correlation

coefficient c_i was calculated for each subsector, one was identified as the best match to the passive DOAS data (subsector 6/5).

The SO_2 time series calculated in this best match subsector is shown in Fig. 4.17 along with the passive DOAS data. The general trends of the time series match extremely well, indicating a successful operation of the SO_2-camera. However, the column densities measured with the SO_2-camera are an average of 24% higher than those retrieved with the DOAS. This is likely due to an imperfect calibration (see section 4.4, a simple linear relation between the measured weighted average optical density $\hat{\tau}$ and the SO_2 column density was assumed here). Details of this measurement can be found in *Wöhrbach 2008*.

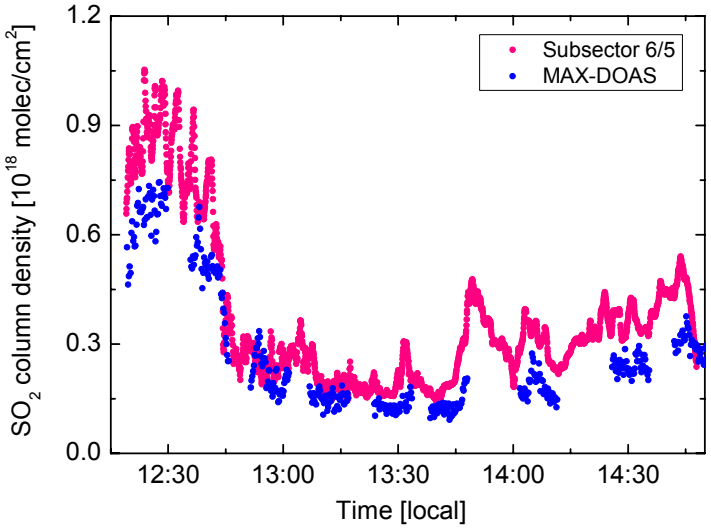

Fig. 4.17 – SO_2-column densities measured with the passive DOAS instrument compared to those obtained in a small subsector of the SO_2-camera's field of view. The time series of the subsector with the best correlation to the DOAS data is shown. (adapted from *Wöhrbach 2008*)

Perhaps the most impressive feature of the SO_2 camera is its ability to directly measure the flux of SO_2 through a certain area in the image. This is made possible by the high temporal and spatial distribution available in the SO_2-camera data which allows the tracking of inhomogeneities in the volcanic plume as they are transported downwind. Modern image processing algorithms can be set up to follow characteristic features in the volcanic plume over subsequent images, thereby giving a 2-dimensional wind field. Together with the measured SO_2 column densities, this wind field can be used to calculate the SO_2 flux through any area in the image. For calculating the volcanic emission flux, however, simpler approaches can also be applied (e.g. *Mori and Burton 2006, Bluth et al. 2007, Wöhrbach 2008*). These are analogous to the techniques used for passive DOAS measurements (described in section 3.3 and by *Galle et al. 2003, Fickel 2008, Johansson 2009a*) An example of an SO_2 flux measurement with an SO_2 camera is given in Chapter 8.

4.7 Conclusions and outlook

4.7.1 Features

The introduction of the SO_2-camera concept has brought with it a new dimension to volcanic emissions monitoring. The advantages of this method over other remote sensing techniques are obvious. For one, a 2-dimensional image of SO_2 column densities is obtained with each measurement. While such images have been compiled in the past using the imaging DOAS technique (*Bobrowski et al. 2006, Louban et al. 2009a*), the time needed to record a 2-dimensional image with this method is around 15 minutes. In presently available SO_2-cameras, one image is recorded about every second, and the time resolution could be further improved by using a back-illuminated detector.

Multiple, sequentially recorded DOAS measurements need to be interpolated and integrated when calculating the amount of SO_2 in the cross-section of a volcanic plume. For emission flux calculation, this value is subsequently multiplied by the wind speed at plume height, which itself is either retrieved from other DOAS measurements (see e.g. *McGonigle et al. 2005b, Fickel 2008, Johansson et al. 2009b*) or taken from an external source. This procedure is greatly simplified for the SO_2-camera. Here, the SO_2 column density can be integrated along any line of pixels in a single image, directly yielding the SO_2 amount along this line. By choosing a line perpendicular to the plume's movement direction, the SO_2 amount in the plume cross-section can thus be calculated from a single image. The plume speed can then be determined by observing the movement of characteristic plume inhomogeneities in subsequent images. Together, the volcanic emission flux is thus directly obtained from the SO_2-camera's data without the necessity of any additional information.

4.7.2 Limitations

Despite the major advantages of the technique over other remote sensing measurements (DOAS, FTIR), there are also several limitations. High resolution spectroscopic techniques are able to identify different absorbers by their characteristic absorption structures. Therefore, these instruments can measure multiple components simultaneously, even if their narrow-band absorption lines are located in the same wavelength range. For example, DOAS can distinguish between SO_2 and O_3 absorption, as well as separate BrO and NO_2 structures. The principle of the SO_2-camera, on the other hand, will only yield correct results if SO_2 is by far the strongest narrow-band absorber in the wavelength interval used for the measurement. This condition is usually fulfilled in volcanic plumes, but it disqualifies the technique for use in applications in which this is not the case. Also, while the design of similar instruments for the measurement of other species is generally possible, this condition is not fulfilled for any other volcanic emission product in the UV wavelength range. As helpful as it would be, the construction of a BrO-camera using the same techniques will fail in volcanic plume environments.

The second limitation of the SO_2 camera is its difficult calibration. The incident radiation intensity $I(\lambda)$ is not measured as a function of wavelength λ, but instead integrated over the entire transmittance window of the band-pass interference filter (I_M is obtained, see Eq. 4.4). Therefore, the optical density $\tau(\lambda)$, which is proportional to the SO_2 column density S (Eq. 4.3) can not be retrieved. Instead, a weighted average optical density $\hat{\tau}$ is obtained (Eq. 4.7). The relationship between $\hat{\tau}$ and S is not linear and the calculation of a calibration coefficient can be complex. As described in section 4.4, the calibration depends on the solar zenith angle (SZA), the total O_3 column, the filter illumination angle θ, and the SO_2 column density S itself.

Lastly, the column densities measured with the SO_2-camera (or any other remote sensing instrument that uses scattered solar radiation as a light source) can be largely influenced by radiative transfer effects. Two competing effects are known. For one, radiation scattered into the instrument's line of sight between the volcanic plume and the instrument itself can cause a "dilution" of the measured SO_2 signal. On the other hand, multiple scattering on aerosols and water droplets in the volcanic plume can extend the average optical path in the plume, thus enhancing the measured SO_2 column density. *Kern et al. 2009* have shown that these effects can greatly influence the retrieved column densities, possibly skewing them by more than a factor of 3 under certain conditions. Examples for these effects are given in chapter 8.

4.7.3 Solutions

The SO_2-camera is a novel technology that brings with it a vast variety of applications. However, both the technical implementation of the instrument as well as the data retrieval procedures are still in a premature stage. Several advances along both lines were made in the scope of this study. The optical system described in section 4.5.1 greatly reduces the dependence of the instrument sensitivity on the viewing direction. The use of a back-illuminated CCD detector and the associated increase in quantum efficiency (factor of 5) enhances the signal-to-noise ratio of a given incident radiation intensity by more than a factor of 2 compared to front-illuminated chips. Finally, the maximum possible sensitivity was achieved by selecting filters according to the theoretical considerations explained in section 4.5.2.

On the data retrieval side, a model was used to describe the difficulties involved in calibrating the SO_2 camera. This or similar models can be used to simulate the exact influence of the measurement parameters (solar zenith angle, stratospheric O_3 column, illumination angle and SO_2 column density) on the measured integrated optical density ϑ for a specific SO_2 camera design. Instead of using a fixed linear relationship between the integrated optical density ϑ and the column density S, a multi-dimensional lookup table can thus be computed from Eq. 4.7 giving much more accurate results.

Finally, the recent advances in retrieving the radiative transfer in and around volcanic plumes (*Kern et al. 2009*) can be applied to SO_2 camera measurements. Here, 3-dimensional radiative

transfer modeling is combined with high resolution spectral information to calculate the influence of dilution and multiple scattering on the measurement results (see chapter 8). However, the spectral data necessary for a correction of these effects cannot be attained from the SO_2 camera alone. In field measurements, a DOAS spectrometer should therefore be co-located with each SO_2 camera with its field of view inside that of the camera (as described in section 4.6). In this manner, the 2-dimensional SO_2 distributions measured with the camera can be normalized using the high resolution spectroscopic measurements conducted in one subsector of the camera's field of view.

4.7.4 Future work

Having implemented the solutions described above, the potential of the SO_2-camera for volcanic emissions research is enormous. The instrument gives 2-dimensional SO_2 distributions at time resolutions on the order of 1 Hz or better. The relatively low cost of the instrument (order of € 10,000) makes the SO_2-camera an ideal tool for the real-time monitoring of volcanic activity. Most volcano observatories already have visible and IR cameras permanently observing potentially active volcanoes. Adding an SO_2-camera instantly gives an overview of gas emissions, even to the untrained observer.

However, the possibilities go far beyond simple visible observation. Fundamental digital image processing algorithms can be applied to retrieve the SO_2 flux through any line in the image (see e.g. *Mori and Burton 2006, Bluth et al. 2007, Wöhrbach 2008*). But the information content of the measured series of images is much greater than is often realized. Modern motion correspondence algorithms (see e.g. *Cox 1993, Jähne 2002*) should even allow the calculation of a 2-dimensional projection of the 3-dimensional wind field in the wake of the volcano. Such data is interesting from a meteorological standpoint, as volcanoes often represent significant topographical perturbances in regional wind fields. Also, spatial variations in the wind speed and direction can influence the accuracy of volcanic emission fluxes measured downwind of the volcano by scanning or traverse remote sensing techniques (described in section 3.3).

Finally, the relatively low cost of the instrument makes the purchasing of multiple instruments possible. If several SO_2-cameras are used to view a volcanic plume from different locations simultaneously (or sequentially from a mobile platform), a tomographic reconstruction could help gain insights into the 3-dimensional plume distribution and its temporal evolution. Such inversions have already been performed for volcanic plumes in the past using passive DOAS instruments (*Kazahaya et al. 2008, Wright et al. 2008, Johansson et al. 2009a*), but they are inherently ill-constrained due to the very limited amount of measurement geometries available. As a single SO_2-camera image contains as many viewing directions as the sensor has pixels, the problem quickly becomes better constrained, and the influence of a-priori assumptions is reduced. For all of the above reasons, the SO_2-camera may well become the standard instrument most frequently applied worldwide for volcanic emissions measurements in the foreseeable future.

5 Installation of long-term gas monitoring instruments

The EU-funded project Network for Observation of Volcanic and Atmospheric Change (NOVAC) started appropriately on October 1, 2005 with the eruption of Santa Ana Volcano, El Salvador (see section 2.2.1). In the scope of this project, scanning DOAS instruments are to be installed on 24 volcanoes worldwide to monitor gas emissions, especially those of SO_2. The data is collected and evaluated in real-time to provide the partner observatories with an additional parameter for risk assessment, the main goal of the project.

This thesis was conducted in the scope of the NOVAC project. A large portion of the work done was aimed at tasks directly related to NOVAC. To this extent, a scanning DOAS instrument conceived specifically for volcanic emissions monitoring was designed and built. It is described in section 3.5.1. Also, advanced data retrieval concepts were developed to improve the DOAS data evaluation routines (described in section 3.4) applied in the automatic real-time and post-processing software used in the NOVAC project. In addition, an in-depth study of radiative transfer effects and their influence on volcanic SO_2 emission measurements was conducted, and the results are presented in chapter 8 (also see *Kern et al. 2009*). Finally, the designed NOVAC mark II DOAS instruments were installed for continuous monitoring at Stromboli (Italy), Popocatépetl (Mexico), Mt. Etna (Italy), and Tungurahua (Ecuador) volcanoes.

The NOVAC project is funded through March of 2010. In section 5.1, a brief summary of the goals and achieved milestones of the project is presented. In the subsequent sections, instrument installations performed in the scope of this thesis at the above mentioned volcanoes are described, along with example measurements at each location.

5.1 The Network for Observation of Volcanic and Atmospheric Change (NOVAC)

The potential for volcanic risk assessment using real-time gas emissions data and the recognized power of sharing data from multiple eruptive centers were the motivation for a European Union (EU) project entitled NOVAC: Network for Observation of Volcanic and Atmospheric Change. Starting in 2005, a worldwide network of permanent scanning DOAS instruments (described in section 3.5.1 and *Galle et al. 2009*) was installed at 19 volcanoes around the world. Installations conducted in the scope of this thesis are described in sections 5.2 to 5.5. Observatory personnel at each partner institution were trained on technical and scientific aspects, and a central database was created allowing the exchange of data and ideas between all partners.[11] A bilateral benefit for volcano observatories as well as scientific institutions (e.g. universities and research centers) resulted. Volcano observatories were provided with leading edge technology for measuring volcanic SO_2 emission fluxes, and now use this technology for real-time monitoring and risk assessment, while the involved universities and research centers are working on global studies and atmospheric impact of the observed gas emissions.

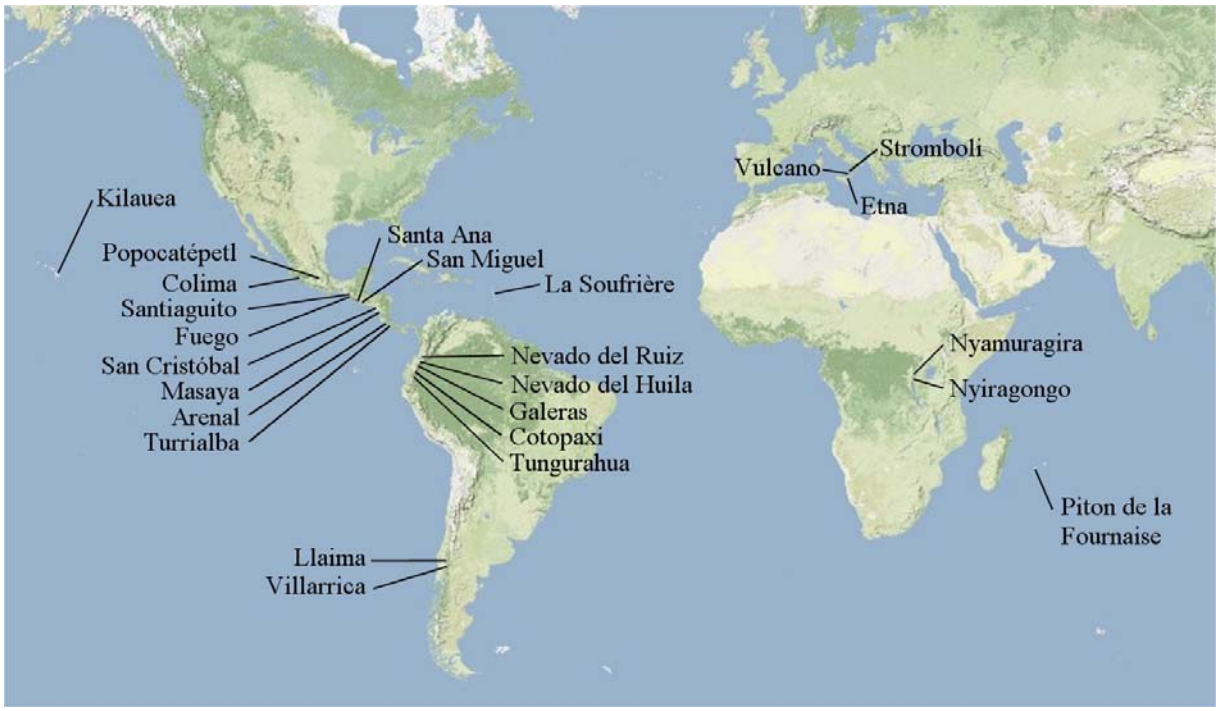

Fig. 5.1 – Geographical location of the volcanoes involved in the NOVAC project as of March 2009. The project is open to participation by any interested institution, so the network may be expanded in the future. Also see Tab. 5.1. (Map © 2009 Google & 2009 Europa Technologies)

[11] The NOVAC database is accessible at http://novac.iup.uni-heidelberg.de/

Volcano	Country	Latitude [° North]	Longitude [° East]	Summit Elevation [m]	Data Acquired Since	Instruments ver 1 / ver 2	
Arenal	Costa Rica	10.463	-84.703	1670	To be installed		
Cotopaxi	Ecuador	-0.677	-78.436	5911	Oct 2007	1	
Colima	Mexico	19.514	-103.62	3850	Dec 2007	2	
Fuego	Guatemala	14.473	-90.880	3763	Apr 2008	2	
Galeras	Colombia	1.22	-77.37	4276	Nov 2007	3	
Kilauea	USA	19.421	-155.287	1222	To be installed		
La Soufrière	Guadeloupe	16.05	-61.67	1467	To be installed		
Llaima	Chile	-38.692	-71.729	3125	To be installed		
Masaya	Nicaragua	11.984	-86.161	635	Apr 2007	2	
Mount Etna	Italy	37.734	15.004	3330	Jul 2008	2	2
Nevado del Huila	Colombia	2.93	-76.03	5364	Apr 2009	2	
Nevado del Ruiz	Colombia	4.895	-75.322	5321	To be installed		
Nyamuragira	D. R. Congo	-1.408	29.20	3058	To be installed		
Nyiragongo	D. R. Congo	-1.52	29.25	3470	Jun 2007	4	
Piton de la Fournaise	Reunion (F)	-21.231	55.713	2632	Aug 2007	3	1
Popocatépetl	Mexico	19.023	-98.622	5426	May 2007	3	1
San Cristóbal	Nicaragua	12.702	-87.004	1745	Nov 2006	3	
San Miguel	El Salvador	13.434	-88.269	2130	Apr 2008	2	
Santa Ana	El Salvador	13.853	-89.630	2381	Apr 2008	2	
Santiaguito	Guatemala	14.739	-91.568	2500	Apr 2008	2	
Stromboli	Italy	38.789	15.213	924	Mar 2007	0	2
Tungurahua	Ecuador	-1.467	-78.442	5023	Mar 2007	3	1
Turrialba	Costa Rica	10.025	-83.767	3340	Apr 2008	4	
Villarrica	Chile	-39.422	-72.929	2847	Apr 2009		
Vulcano	Italy	38.404	14.962	500	May 2008	1	

Tab. 5.1 – List of volcanoes involved in the NOVAC project as of April 2009.

The EU provided funding for instruments in European countries as well as some developing countries in Central and South America as well as Africa, in which funding for such technology was unavailable. The geographical location of the volcanoes involved in the NOVAC project as of March 2009 is shown in Fig. 5.1 and Tab. 5.1. Stromboli Volcano (Italy) is not officially part of the project, but was used for test installations (see section 5.2). As the project is open to participation by any interested institution, the network may be expanded in the near future (the USGS[12] has e.g. voiced interest in joining the NOVAC project with Kilauea Volcano, Hawaii).

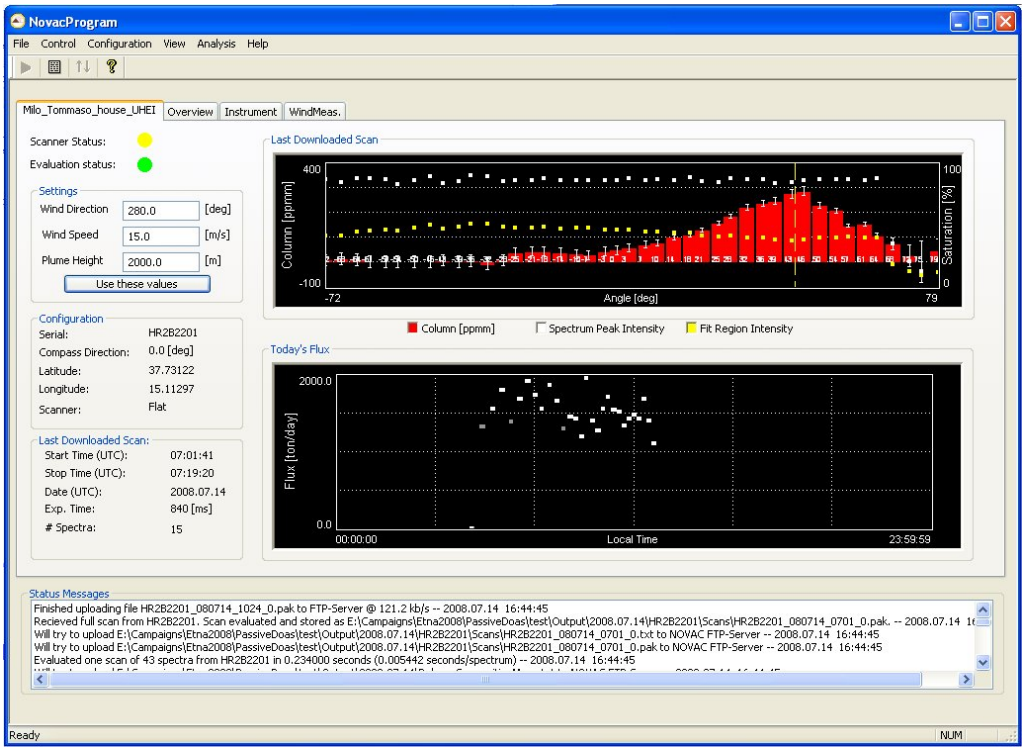

Fig. 5.2 – Screen shot of the NOVAC data evaluation and display software running at INGV Catania. The top plot shows the retrieved SO_2 column density as a function of the measurement zenith angle (from horizon to horizon). In this measurement, the center of the Mt. Etna plume was detected slightly north of the instrument in Milo (see section 5.4). The bottom graph shows the calculated SO_2 emission fluxes for July 14, 2008. On this day, the emission flux was fairly stable at around 1800 t(SO_2)/d.

Two types of scanning DOAS instruments were specifically designed for continuous, high time resolution volcanic monitoring applications. A simple scanner with minimal power consumption and cost was installed in most cases. However, at particularly high-profile volcanoes as well in locations whose topography posed special challenges, a more complex instrument with additional functionality was chosen. This instrument, called the NOVAC mark II scanning DOAS, was designed and built within the scope of this thesis. It is described in detail in section 3.5.1. In the meantime, NOVAC instruments have been installed at 19 volcanoes (see Tab. 5.1), and over 15

[12] United States Geological Survey

million spectra have been recorded, evaluated, and stored in the central database. The measurement principle of scanning DOAS instruments applied to volcanic gas emission measurements is described in section 3.3.

The project is funded through March of 2010, but it has already been a great success and many very interesting scientific findings have resulted. Technical aspects of continuous monitoring with scanning DOAS systems such as instrument design, station networking, and measurement geometries were analyzed (*Zhang 2005, Galle et al. 2009, Johansson 2009a*). Data analysis was significantly improved by identifying and considerably reducing the two main sources of error: wind speed at plume height and radiative transfer effects (*Johansson et al. 2009b, Kern et al. 2009*, also see section 3.3.4 and chapter 8). New software for data evaluation and display specifically implemented for the NOVAC network (*Johansson 2009b*) allows volcanologists at the partner observatories to take notice and react to exceptional conditions regarding SO_2 degassing in real-time, a prerequisite for hazard management (see Fig. 5.2).

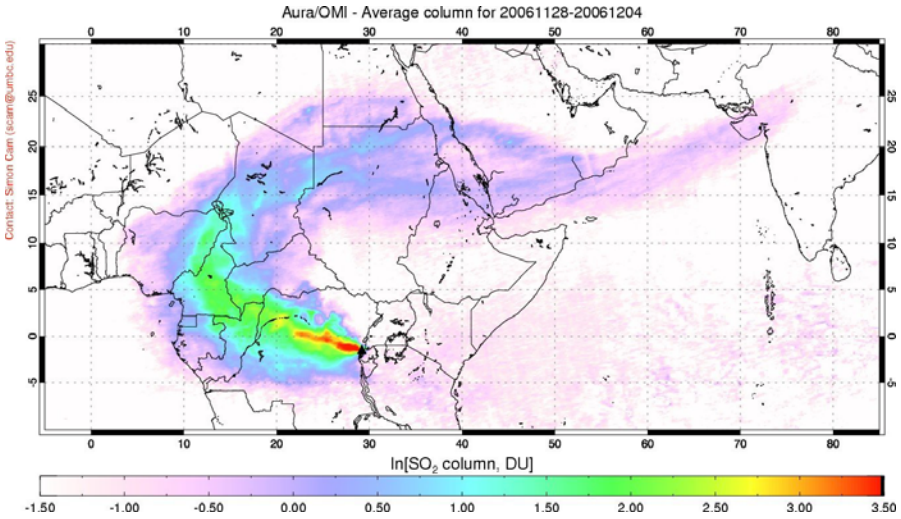

Fig. 5.3 – Nyamuragira Volcano is in a very remote location on the eastern border of the D.R. Congo. Recently, it has been inaccessible for ground-based measurements due to civil unrest in the region. However, the Ozone Monitoring Instrument (OMI) aboard NASA's Aura satellite captured this eruption between November 29 and December 4, 2006. During this major eruption, the SO_2 emissions can be traced all the way to northwest India (note the logarithmic color scale, 1 DU = 2.7×10^{16} molec/cm²). (Adapted from *Carn 2006*)

After the first instruments were installed, observatories are now beginning to publish results related to SO_2 emissions monitoring (e.g. *Arellano et al. 2008a, Delgado Granados et al. 2008, Staudacher et al. 2008*). Highlights include the continuous data from Tungurahua (also see *Arellano et al. 2008b*), in which a mean emission rate of 1458 t/d between 1999 and 2006 was detected. This requires SO_2 exsolution of an andesitic magma volume that is two orders of magnitude larger than that determined by the observed lava effusion rate. Possible explanations include SO_2 degassing from magma at depth or convection in the volcanic conduit (also see section 2.2). Another highlight was the eruption of Santa Anna volcano in El Salvador, where SO_2 fluxes increased by an order of magnitude from several hundred to several thousand

tons per day shortly before and during the volcanic crisis of 2005 (*Olmos et al. 2007*, see Fig. 2.10).

One of the great benefits of the NOVAC project is the ability to use the network data in a collective manner. Behind risk assessment, several additional scientific tasks are aimed at exploiting this global perspective of the project. For one, total global emission fluxes from volcanoes are still very poorly constrained (see chapter 2). As over 300 actively degassing volcanoes exist, it is impossible to incorporate all of them into a measurement network at this time. However, the ability to measure volcanic emissions from space has been demonstrated in the past for the compounds SO_2 and BrO (e.g. Fig. 5.3 and *Khokhar et al. 2005, Carn et al. 2008, Theys et al. 2009*). However, the radiative transfer conditions in the atmosphere during a particular measurement remain one of the major uncertainties in satellite retrievals of volcanic emissions. As the plumes of quiescently degassing volcanoes are typically located in the boundary layer or free troposphere, only a portion of the radiation detected by the satellite instrument has actually passed through the plume. The ground-based remote sensing measurements conducted in the scope of the NOVAC project are extremely well suited for validation of satellite measurements.[13] After validation, the satellite instruments can then be used to accurately quantify global emissions.

NOVAC data is also being used for comprehensive geological studies involving multiple volcanoes. In one example, *Hansteen et al. 2008* estimated magma flux rates through the Central American Volcanic Arc (CAVA) from regional SO_2 fluxes at quiescently degassing volcanoes. When compared to the erupted magma masses estimated from Pacific offshore records of ash sediments (*Kutterolf et al. 2008*), the authors found a remarkable agreement of current volcanic activity along the CAVA with the average Plinian activity in the last 200 ka.

In addition to volcanic monitoring, the NOVAC sites can be used for additional atmospheric studies. For example, instruments located in remote sites are well suited for background measurements in the free troposphere when the plume of the volcano is not in the instrument's field of view. Also, NOVAC instruments are being incorporated into the Network for Detection of Atmospheric Composition Change (NDACC)[14] with the goal of expanding the number of instruments monitoring long term changes in the upper troposphere and lower stratosphere.

The installation of NOVAC mark II instruments (see section 3.5.1 for a technical description) at four different volcanoes was one NOVAC task attended to in the scope of this thesis. In the following sections, a description of the installation at each volcano is given along with some example measurements. Long-term, continuous monitoring results will be the subject of future publications.

[13] While ground-based remote sensing measurements are also subject to errors caused by inaccurate assumptions about radiative transfer, the ground-based geometry has the advantage that the instrument is much closer to the volcanic plume. Also, as the source of radiation is behind the plume in this geometry, the radiative transfer is typically better constrained. A detailed description of the impact of radiative transfer effects on ground-based remote sensing measurements is given in chapter 8.

[14] http://www.ndsc.ncep.noaa.gov/

5.2 Stromboli (Italy)

The small, 924 m high island of Stromboli is the northeast most of the Aeolian Islands. With an unusually small area of only 12.6 km^2, the island juts steeply down from the summit to the ocean. Below the surface of the Mediterranean Sea, the cone of Stromboli Volcano rises up approximately 3 km from the ocean floor to the surface, bringing the total height to almost 4 km. Spectacular incandescent nighttime explosions have led to the nick name "Lighthouse of the Mediterranean". Frequent, mild explosive activity has been characteristic of Stromboli throughout much of historical time and has led to the common labeling of such activity as "Strombolian".

5.2.1 Instrument installation and configuration

Although Stromboli is not officially part of the NOVAC project, the volcano was chosen for a test installation of the NOVAC mark II instruments for a number of reasons. For one, the relative close proximity to Heidelberg and relatively easy accessibility of the island, which is a popular tourist location, is obviously an advantage. Secondly, the steep topography (see Fig. 5.4) is ideal for scanning DOAS measurements, as the instruments are located considerably below the plume (see section 3.3.2). Lastly, the exposure of the instruments to the corrosive marine air around the island can be regarded as a true test of the impermeability of the instrument's housing. Therefore, the first two NOVAC mark II instruments were installed on the island in the beginning of March 2007. The installations were conducted in cooperation with the Istituto Nazional di Geofisica e Vulcanologia (INGV) Palermo, who have also been servicing the instruments and collecting data since the installations were completed.

The two instruments were installed at sites in the northeast and southern tip of the island (see Fig. 5.4). The northwest site is called Pozzo Saibbo, and is referred to in the database as spectrometer serial number HR2B2199. Here, the instrument is installed in a fenced-off enclosure in which INGV Palermo maintains a well for ground water CO_2 and He isotope analysis (see e.g. *Carapezza et al. 2004, Inguaggiato and Rizzo 2004*) in the vicinity of the ferry landing in the town of Stromboli. As shown in Fig. 5.5, the instrument is mounted on an approx. 2m tower. Due to the other instrumentation located at this site, power is available from a 12V land line. Still, a battery was installed in the box mounted at the base of the tower as a buffer in case of short-term power failures or power spikes. A timer turns the instrument off at night to save power and reboot the system once per day. The temperature stabilization was set to 23°C, the approximate average daytime temperature in spring. The instrument was configured to perform a folded scan in two planes. Before each scan, one spectrum is taken in the zenith (later used as a reference for the evaluation). Afterwards, the dark current and offset are measured. The scan then begins at an azimuth of 215° relative to north, thereby pointing directly towards the other installation on the southern tip of the island. Once the zenith is reached, the instrument rotates and the scan continues in an azimuth direction of 335°. 15

exposures are taken in each viewing direction. This geometry enables the instrument at Pozzo Saibbo to measure the plume during wind directions between about 225° and 350°.

The second installation was performed on the southern tip of Stromboli Island. This site is called Punta Lena (HR2B2200) and is accessible either by boat or 3 km foot path from the town of Stromboli. The instrument is installed on the roof of a small one story building, as shown in Fig. 5.6. A small aluminum structure serves as a mounting and is weighed down to the roof of the building with rocks and sand bags. Here, no power is available, so a solar panel was installed to supply the instrument. A 100 Ah solar battery was used as a buffer, and the instrument is again turned off at night to conserve power. The scanner was configured in a similar manner as the other instrument. After recording a zenith reference and measuring the dark current and offset, the instrument performs a folded scan beginning (-90° measurement zenith angle MZA) in an azimuth direction of 270° relative to north. Once the zenith is reached, the azimuth is changed to 35°, thereby pointing in the direction of the instrument at Pozzo Saibbo (+90° MZA). Again, 15 exposures are taken in each viewing direction. The instrument covers a range of wind directions between about 45° and 260° relative to north.

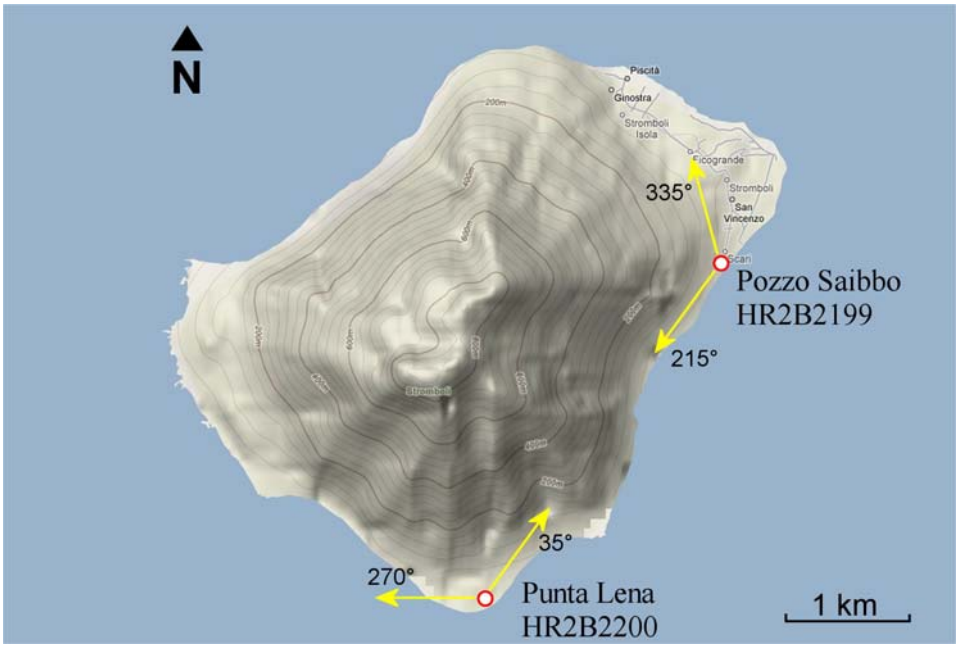

Fig. 5.4 – Geographical location of the 2 NVAC mark II installation sites on Stromboli Island, Italy. The yellow arrows indicate the scanning planes of the instruments. Between the two instruments, the same plane is scanned, thus allowing simple calculation of the plume height. (Map © 2009 Google & 2009 Tele Atlas)

This setup was chosen to enable the measurement of the volcanic plume from both sites as often as possible, as the predominant wind direction is from the northwest. For wind directions between 260° and 350°, the plume is blown between the instruments and is detectable by both. As both instruments scan the same plane in this area, simple triangulation can be performed to retrieve the geometry of the plume at a given time (see Fig. 5.11).

Fig. 5.5 – Both images show the NOVAC test installation at Pozzo Saibbo, Stromboli. The NOVAC mark II instrument is installed on an approx. 2 m aluminum tower on the beach just southwest of the ferry landing. Power is supplied by a 12 V land line. A 40 Ah battery in the electric installation box at the base of the tower is used as a buffer in case of short term power outages. A timer switches the instrument off at night. A data link has not yet been established, so measurement data needs to be downloaded using a laptop computer.

Fig. 5.6 – Installation at Punta Lena. The NOVAC mark II instrument is mounted on an aluminum structure on the roof of a small building. It is weighed down by stones. An additional housing contains the 100 Ah solar battery, which in turn is charged by a solar panel. The instrument is switched off at night with a 12V DC timer. The laptop computer is not part of the installation, but is only used to download data from the instrument.

5.2.2 Measurement examples

While frequent, mild "Strombolian" activity is typical of Stromboli Volcano, a period of increased activity began on February 27, 2007. During the following weeks, lava was erupted from a fissure on the northeastern flank of the northeast crater of the volcano. As is usually the case for such eruptions at Stromboli, the lava flowed down the Sciara del Fuoco, a prominent horseshoe-shaped scarp formed about 5000 years ago as a result of the most recent of a series of slope failures that extend to below sea level (*INGV 2007*). This scarp funnels pyroclastic ejecta and lava flows to the northwest. The lava flows formed two branches that reached the sea, resulting in steam plumes and a modified coastline (see Fig. 5.7).

Fig. 5.7 – Photograph of the eruption of Stromboli Volcano taken on March 6, 2007 from the northwest side of the island. Lava was erupted from a vent in the northwest flank of the mountain, flowed down the Sciara del Fuoco in two separate branches, and reached the ocean resulting in large steam plumes.

Due to the increased activity of the volcano at the time of the installations, the example measurements described in this section not only represent a proof of principle, but are also indicative of gas emissions during this phase of unusually high activity. Therefore, the measurements conducted during the installation campaign from March 3 through 8, 2007 are discussed in some detail in the following.

Volcanic SO_2 emission flux

In this study, data evaluation of the SO_2 fluxes was performed according to the NOVAC real-time evaluation procedure (see *Galle et al. 2009, Johansson 2009a*). Each measurement spectrum was divided by the zenith reference recorded at the beginning of each scan. The

optical density was then obtained by taking the logarithm. The subsequent DOAS fit was performed in the wavelength interval between 312 and 325 nm. Here, the absorption cross-sections of SO_2 (*Bogumil et al. 2003*) and O_3 (*Voigt et al. 2001*) were fit to the measured optical density, along with a Ring spectrum calculated from a measured Fraunhofer spectrum using the DOASIS software (*Kraus 2004*). Details of the DOAS evaluation can be found in chapter 3. After each spectrum in the scan was evaluated, the absolute values of the individual column densities were adjusted so that the smallest values were consistent with null. This is necessary whenever the zenith reference spectrum contains SO_2 absorption, as all measurements in a scan are evaluated relative to this spectrum.

After the individual spectra were each evaluated, the total SO_2 amount X in the scanned cross-section of the volcanic plume was retrieved according to the radial integration procedure described in section 3.3.2. Several examples of plume scans measured on March 5, 2007 at Pozzo Saibbo are shown in Fig. 5.8 and Fig. 5.9. The date, local time, and instrument location is marked in the top left corner of each figure. The indicated time corresponds to measurement time of the first spectrum in a particular scan. The scan time resolution (i.e. the time it takes to complete an entire scan) was around 10 minutes during midday. The red data points indicate the measured SO_2 column density at a particular measurement zenith angle (MZA). The grey shaded area represents the area taken into account during the integration of the SO_2 amount X, which is given in the top right corner of each diagram.

In section 3.3.2, it was however shown that information is needed about either the plume height or the distance between instrument and plume in order to correctly calculate the SO_2 amount X (see Eq. 3.36 - Eq. 3.39). The measurements conducted on March 5, 2007 at Stromboli represent a good example of how these parameters can be derived from multiple instruments. In Fig. 5.9, a scan started at 15:23 at the site Pozzo Saibbo is shown. From the data shown here, the plume seems to be directly overhead. The highest SO_2 column density (3.8×10^{18} molec/cm^2) was found at a MZA of -20° off to the southwest of the instrument site. From this measurement alone, the plume height cannot be retrieved. However, Fig. 5.10 shows the results of a scan conducted almost simultaneously at Punta Lena. Here, the plume is close to the northeastern horizon. The highest SO_2 column (2×10^{18} molec/cm^2) was detected at a MZA of +70°.

The fact that the respective maximum SO_2 column densities are different could be caused by the different viewing geometry of the two instruments. While the instrument at Pozzo Saibbo looks almost vertically through the plume, the instrument at Punta Lena sees the plume from the side. Another reason for the discrepancy could be the dilution of radiation in the signal from Punta Lena (see chapter 8), because this instrument is farther away from the plume than the one at Pozzo Saibbo (as is shown below).

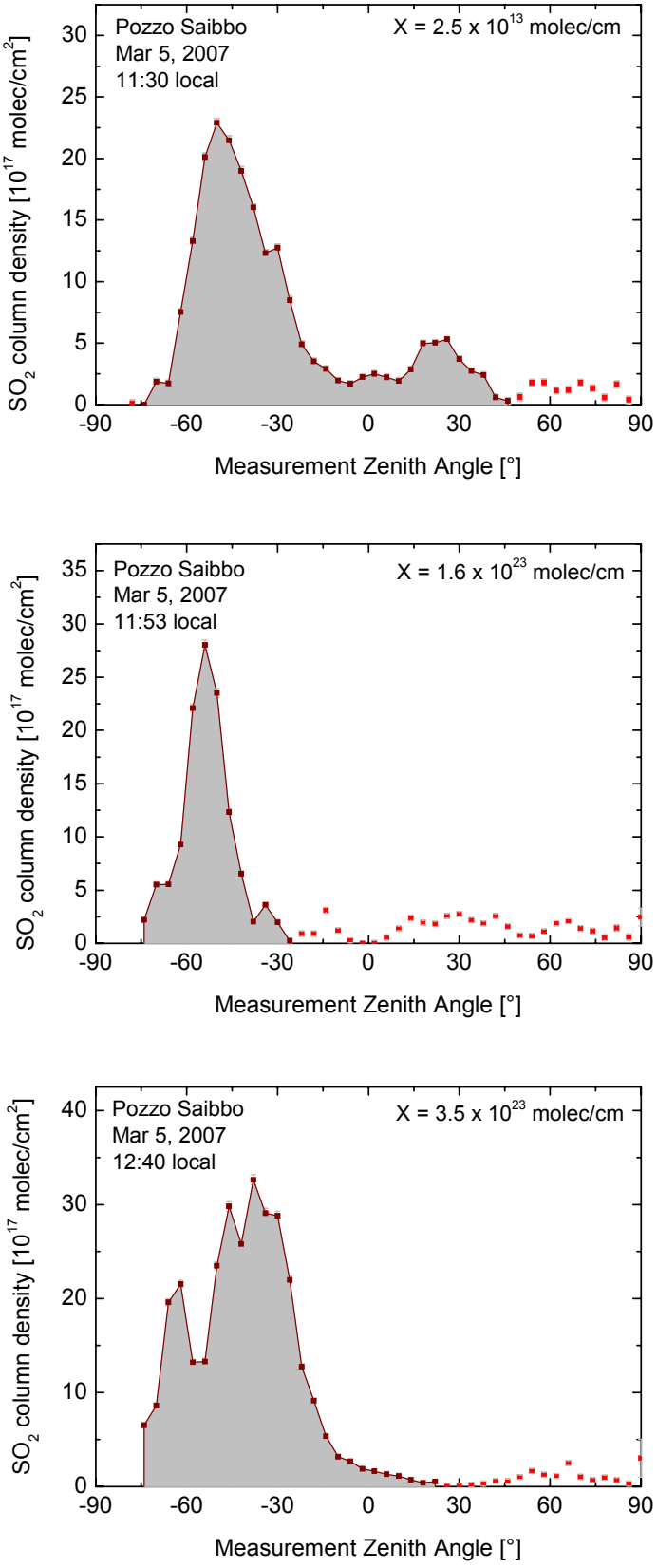

Fig. 5.8 – Three exemplary scans of the plume of Stromboli Volcano (Italy) recorded on March 5, 2007 between 11:30 and 12:40 local time by the NOVAC mark II instrument installed at Pozzo Saibbo. The given integrated SO_2 amount *X* corresponds to the shaded area.

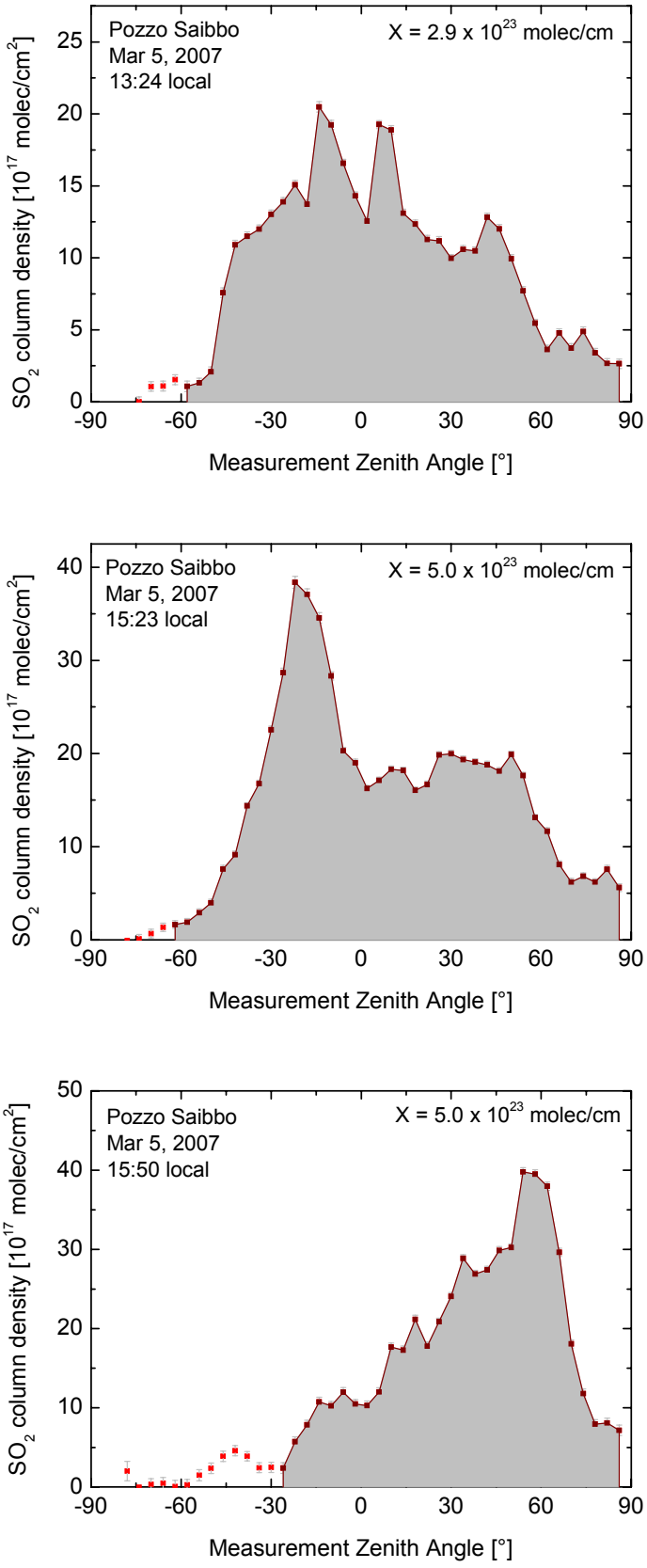

Fig. 5.9 – Three exemplary scans of the volcanic plume of Stromboli Volcano (Italy) recorded on March 5, 2007 between 13:24 and 15:50 local time by the NOVAC mark II instrument installed at Pozzo Saibbo. The given integrated SO_2 amount *X* corresponds to the shaded area.

Aside from the absolute values of the respective peak SO_2 column densities, the shape of the observed SO_2 progressions is also different. The instrument at Pozzo Saibbo detected a sharp peak and a fairly wide shoulder towards the north. The Punta Lena site only observed the sharp peak. This again could be caused by the difference in viewing geometries. In this case, it is likely that the shoulder is not visible from Punta Lena, as it is probably behind the horizon to the north (the scanner can not point beyond +86° MZA due to obstructions in the topography).

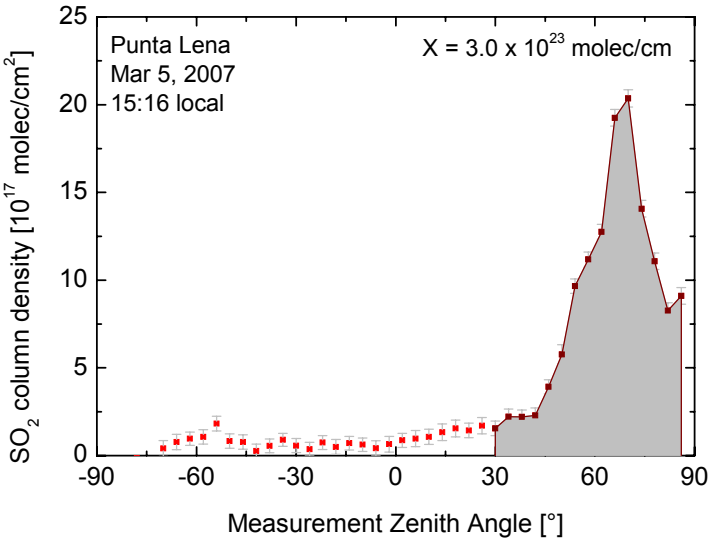

Fig. 5.10 – Example scan through the plume of Stromboli Volcano (Italy) recorded on March 5, 2007 around 15:16 local time by the NOVAC mark II instrument installed at Punta Lena. This scan was recorded almost simultaneously with the scan at 15:23 from Pozzo Saibbo (see Fig. 5.9). Using the two scans, the plume position can be retrieved (also see Fig. 5.11).

Despite the discrepancies, however, it is likely that the sharp peak seen by both instruments was the same feature of the plume. Assuming this is true, simple triangulation can be used to retrieve the plume height, as the two instruments scanned the plume in the same plane.[15] A schematic of the thus retrieved plume geometry is depicted in Fig. 5.11. The Punta Lena instrument detected the plume center at α_{Lena} = +70 MZA, while the plume bearing was α_{Saibbo} = -20 MZA as seen from Pozzo Saibbo. Since the distance z between the instruments is known to be 3.35 km, the plume height can be retrieved by the following set of equations

$$\tan(\alpha_{Lena}) = \frac{z_{Lena}}{h} \qquad \textbf{Eq. 5.1}$$

[15] Even if this is not the case, triangulation can still be applied if the plume height is assumed the same for both instruments. *Johansson 2009a* describe the algorithm implemented to this extent in the NOVAC software (*Johansson 2009b*).

$$\tan(\alpha_{Saibbo}) = -\frac{z_{Saibbo}}{h} \qquad \text{Eq. 5.2}$$

$$z_{Lena} + z_{Saibbo} = z \qquad \text{Eq. 5.3}$$

Solving for h then yields the plume height

$$h = \frac{z}{\tan(\alpha_{Lena}) - \tan(\alpha_{Saibbo})} \qquad \text{Eq. 5.4}$$

For the measurements considered here, a plume height of 1.1 km was calculated. When compared to the summit elevation of Stromboli volcano of 924 m (see Tab. 5.1), this means that the plume was located about 200 m above the emission vent. This is a very reasonable value for light wind conditions (*Burton et al. 2008*), as they were present at Stromboli for the duration of the installations. Wind measurements conducted by INGV Catania on the afternoon of March 5 yielded approximately 5 m/s (*Burton 2007*).[16] In general, winds were light and variable in direction between March 3 and 8, the time period of the installations. Unfortunately, the DOAS instrument was not yet able to conduct wind measurements in the test setup at Stromboli in 2007. Therefore, a wind speed of 5 m/s was assumed for all measurements conducted in the reporting period. The measurements on March 5 described here represent the best recorded measurement of plume height, and a constant plume height of 1.1 km was therefore assumed in the ensuing flux calculations.

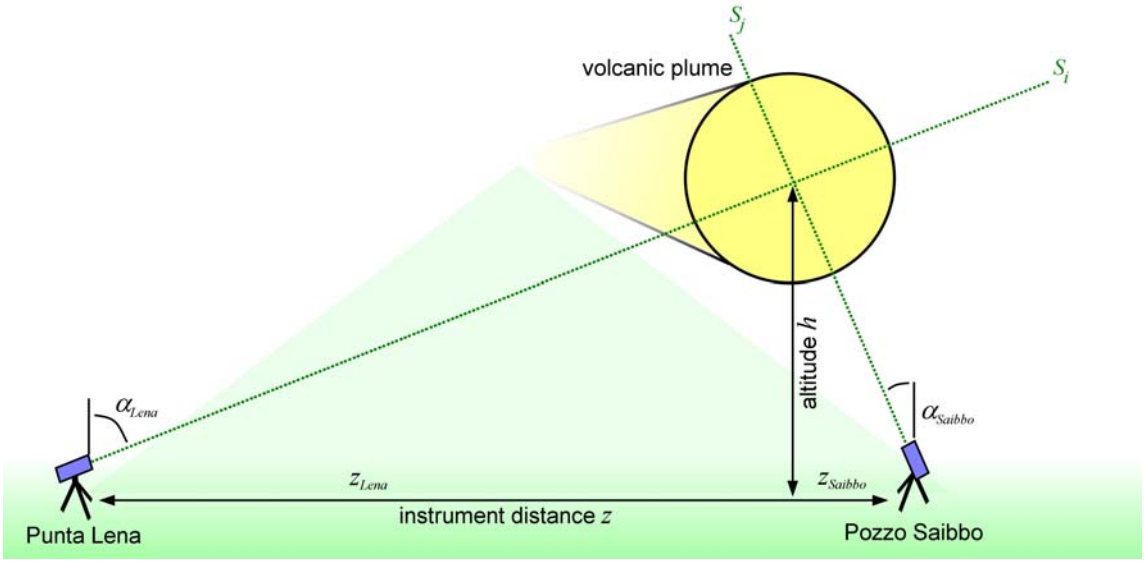

Fig. 5.11 – Measurement geometry of the NOVAC mark II scanning DOAS instruments at Punta Lena and Pozzo Saibbo on the island of Stromboli. When both instruments detect the plume simultaneously, the plume altitude and position can be retrieved. This diagram represents the situation as it was found on March 5, 2007 at 15:20 local time.

[16] Data from *GDAS 2009* indicates lower wind speeds for the time period of the installations. Therefore, the 5 m/s used in the following calculation of SO_2 fluxes can be assumed an upper limit.

In total, the volcanic emissions from Stromboli volcano could be measured on the afternoon of March 4, midday on March 5, and in the morning of March 8. On the other days, the wind direction was such that the plume could not be fully captured (i.e. the plume was either entirely out of sight or near the horizon, and the total SO_2 amount X could not be accurately assessed). Fig. 5.12 shows the measured SO_2 emission flux Φ retrieved from those plume scans that were deemed complete.

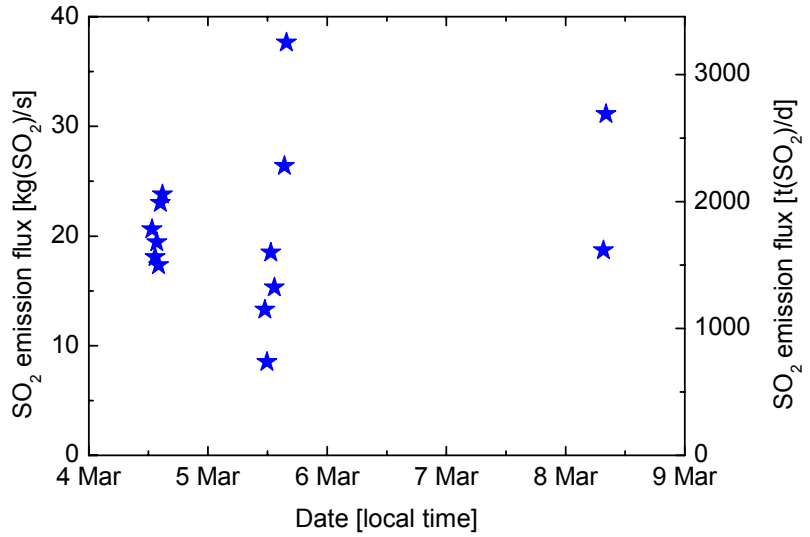

Fig. 5.12- SO_2 emission flux measured at Stromboli volcano on March 4, 5 and 8, 2007. While emissions were fairly constant on March 4, a high amount of variability could be observed on March 5. On March 6 and 7, the plume was blown away from the instruments. Data is only shown for scans in which the plume was entirely captured, with low SO_2 column densities measured on either side.

During the short reporting period, the average retrieved SO_2 flux at Stromboli was about 20 kg(SO_2)/s or approximately 1700 t(SO_2)/d. The values reported here are slightly higher than those reported during the same period by *Burton et al. 2008*, possibly a result of an overestimation in wind speed or a more sensitive retrieval conducted in this study at higher wavelengths (see section 3.4.1 and chapter 8 for details). While fairly constant on March 4, the measured flux was highly variable on March 5 and March 7 (although only 2 complete scans were recorded on the 7th). It is unclear whether this measured variability was caused by true variability in volcanic degassing, or whether the meteorological conditions (wind speed, wind direction, and plume height, turbulence) were the main reason for the fluctuations (see section 3.3.2 and especially Eq. 3.35). Throughout the reporting period, however, the flux was significantly elevated compared to the typical background values of around 150 – 200 t/d of SO_2, a fact that *Burton et al. 2008* attribute to the unusually high lava effusion rate and a

larger volume of ascending, volatile rich magma in the volcanic conduit than is usually the case.

BrO in the plume of Stromboli

Aside from measuring the volcanic SO_2 emission flux, the installed NOVAC mark II instruments can be used for a variety of other tasks (see section 5.1). Among them, the detection of other chemical compounds in volcanic plumes can be of great interest. The quantification of halogen oxides is of special interest, as these can greatly influence air chemistry in and around volcanic plumes, and can at times even be used as a measure for degassing depth (see chapter 2).

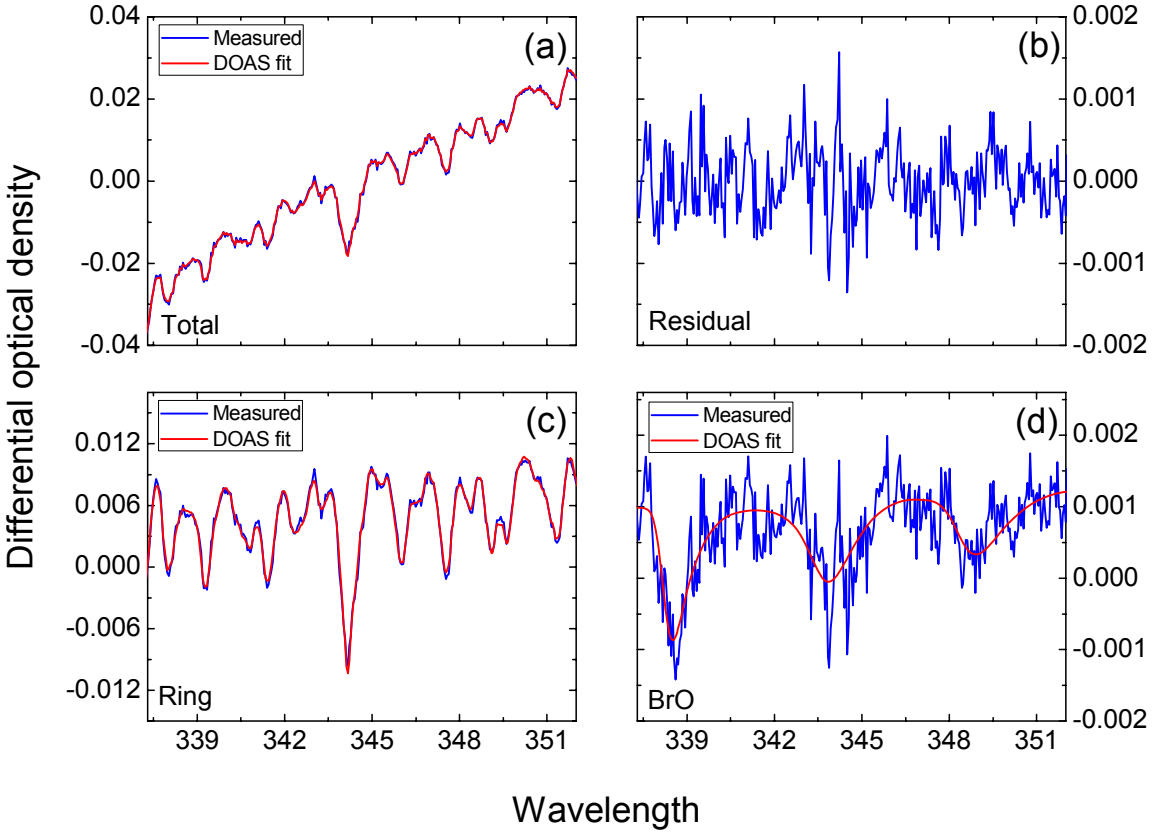

Fig. 5.13 – Example evaluation of BrO measured from Pozzo Saibbo. Inset (a) depicts the total measured optical density (blue) along with the fit result (red). The difference between the two, the fit residual, is shown in inset (b). Inset (c) shows the fit of the Ring spectrum. Here, the DOAS model for the Ring structure (red) is compared to the measured optical density with all contributions by trace gases and the broadband DOAS polynomial subtracted (blue). Finally, the same is shown for the fit of the BrO cross-section in inset (d). Here, a maximum differential optical density of about 1.9×10^{-3} was found, indicating a BrO column density of 1.7×10^{14} molec/cm^2. Not shown are the fits of NO_2, O_3, and the 4th order DOAS polynomial.

The halogen oxide BrO was positively detected in the plume of Stromboli on March 5, 2007, a cloudless day with a high incident solar irradiance. For the BrO retrieval, all spectra recorded between 11:00 and 15:30 at Pozzo Saibbo were sorted according to the respective retrieved SO_2 column density. Next, the 100 spectra (each consisting of 15 exposures) with the least amount of SO_2 were co-added and used as a Fraunhofer reference in the DOAS evaluation. Starting from the highest SO_2 column densities, 50 spectra were co-added and divided by the previously compiled Fraunhofer reference to obtain the optical density. This process was repeated for the next 50 spectra until the measured spectra were all co-added. The co-adding of spectra is a standard practice used to improve the photon statistics of the newly compiled spectra (see chapter 3).

Once the optical density was obtained for all compiled spectra, a DOAS fit specifically aimed at evaluating BrO was applied. In the wavelength range between 337 and 352 nm, the absorption cross-section of BrO was fit to the optical density, along with the cross-sections of NO_2 (*Vandaele et al. 1998*) and O_3 (*Voigt et al. 2001*), a Ring spectrum calculated from the compiled Fraunhofer spectrum, and a 4^{th} order polynomial. An example fit is shown in Fig. 5.13. BrO was positively identified in several of the co-added measurement spectra.

In the next step, the co-added measurement spectra were re-evaluated for SO_2 using the evaluation procedure described in the previous section. In this manner, the molecular ratio of BrO/SO_2 could be obtained by dividing the retrieved BrO column density by that of SO_2. The results of the BrO evaluations are shown in Fig. 5.14 as a function of the SO_2 column density retrieved from the respective spectrum for those data points in which BrO was positively identified above the detection limit. A linear fit to the data (black line in Fig. 5.14) yields a BrO/SO_2 ratio of 6×10^{-5}.

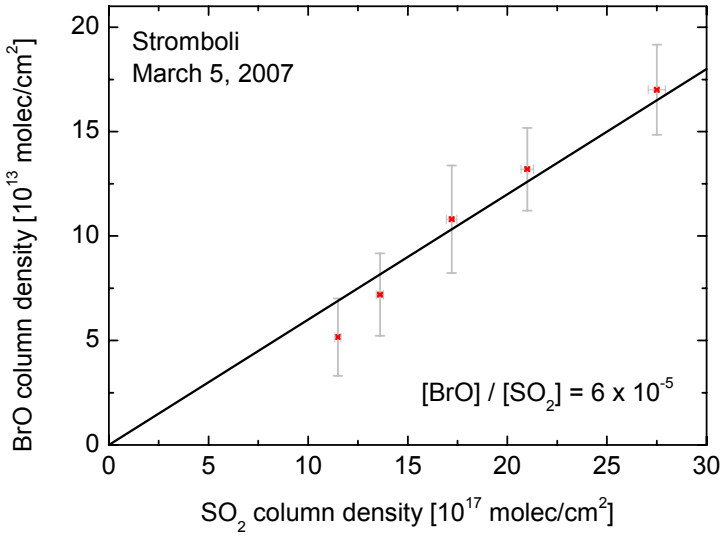

Fig. 5.14 – BrO column density as a function of SO_2 column density measured at Stromboli volcano on March 5, 2007. For this study, all measurements taken between 11:00 and 15:30 local time at Pozzo Saibbo co-added to improve photon statistics.

In previous measurements of BrO at Stromboli on September 27, 2004, *Bobrowski and Platt 2007* reported a BrO/SO_2 molecular ratio of around 2×10^{-4}. The values obtained in this study are clearly below this value. However, it is impossible to draw conclusions as to the reasons for this discrepancy from the two measurements alone. The causes could be either of volcanic or atmospheric origin, or possibly both, and include differences in magma degassing pressure, halogen degassing of a reservoir previously depleted in SO_2, differences in ambient ozone concentration, differences in incident solar radiation, or different plume ages. A more detailed description of the principles governing the BrO/SO_2 ratio in a volcanic plume is given in chapter 2 and chapter 7. Additional, preferably continuous measurements of the BrO/SO_2 ratio along with meteorological parameters are necessary to better constrain the evolution of halogen degassing at Stromboli, and thereby possibly gain insights into degassing processes (also see *Burton et al. 2007a*). However, these measurements do demonstrate that BrO can be retrieved from the standard measurements conducted by the NOVAC mark II instruments installed at Stromboli. Therefore, these could deliver a suitable long-term data set in the near future.

5.3 Popocatepétl (Mexico)

At 5426 m summit elevation, Popocatépetl Volcano is North America's second highest volcano. Located approximately 70 km southeast of Mexico City, it is also one of the most active volcanoes in the world. The glacier-topped stratovolcano contains an approximately 500 m diameter crater. Geological studies show that Popocatépetl has erupted explosively in large Plinian eruptions in the last 15 thousand years. One of these covered a large area currently occupied by Mexico City. More recently, several other Plinian eruptions have occurred, devastating large areas including human settlements on the northeast flank of the mountain, most noticeably in 200 BC and 800 AD (*Delgado Granados et al. 2001*). In the decade of the 1990s, Popocatépetl has emitted record amounts of SO_2 into the free troposphere (*Delgado Granados and Cárdenas González 1997* reported a flux of 2.6×10^6 tons of SO_2 for a 617 day period). More recently, activity has somewhat decreased, but an ongoing eruption of Volcanic Explosivity Index (VEI) 2 still causes intermittent phreatic explosions (*GVP 2009b*).

5.3.1 Instrument installation and configuration

In the scope of the NOVAC project, a network of four scanning DOAS instruments were installed at various locations around the volcano (see Fig. 5.15). As the wind direction at Popocatépetl is highly variable, the instruments were distributed on all sides of the volcano. Tab. 5.2 gives an overview of the geographic locations of the individual installation sites. The instruments at the sites tlamacas-cone, chipiquixtle and colibri are NOVAC mark I scanners.

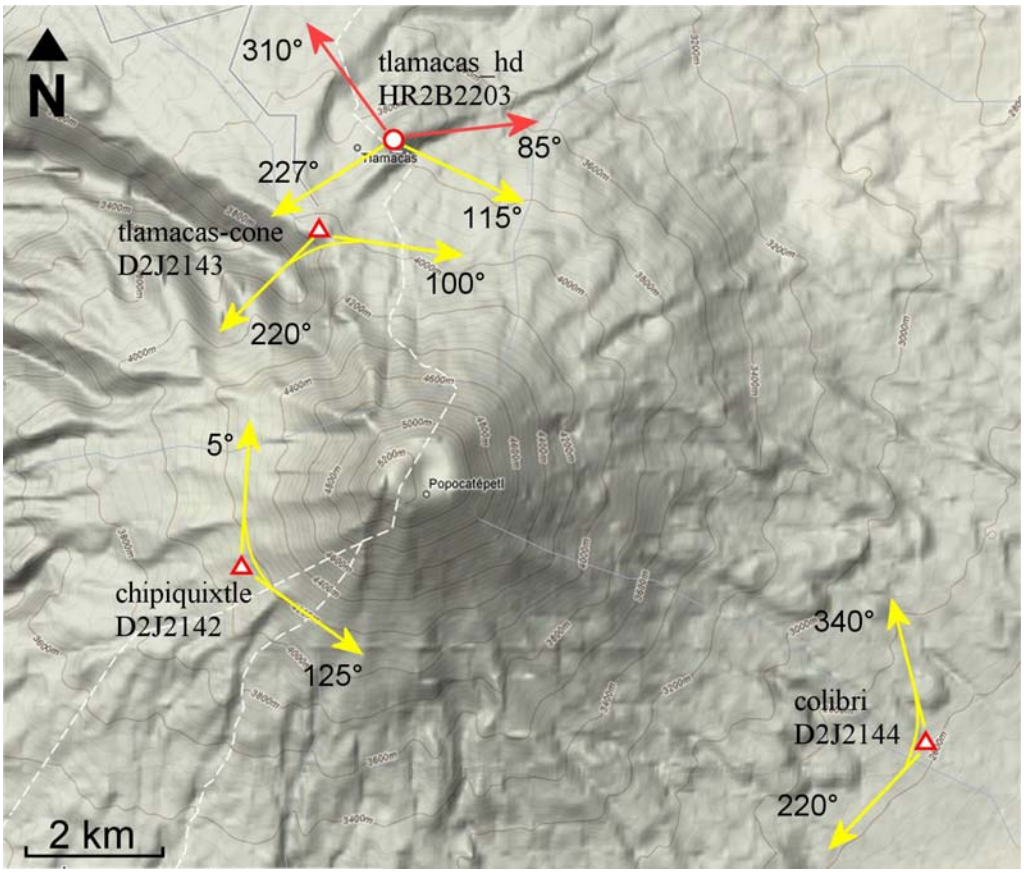

Fig. 5.15 – NOVAC installation geometry at Popocatépetl Volcano (Mexico). Three NOVAC mark I (triangles) and one NOVAC mark II instrument (circle) were installed at four different sites. The NOVAC mark II instrument (tlamacas_hd, spectrometer serial HR2B2203) is configured to scan the plume in a folded plane geometry in the azimuth directions 115° and 227° relative to north. Before and after each scan, tropospheric pollution measurements are conducted in the direction of Puebla (115°) and Mexico City (310°). Here, several spectra are recorded at viewing angles a few degrees below the horizon. The NOVAC mark I instruments all use a conical scan geometry (see *Johansson 2009a* for a detailed description). (Map © 2009 Google & Tele Atlas)

In March of 2008, these were complemented by a NOVAC mark II scanning DOAS (tlamacas_hd) installed on the premises of a Petróleos Mexicanos (PEMEX) radio antenna station at 4030 m elevation and about 5 km north of the volcano's summit. This instrument is associated with the spectrometer serial number HR2B2203. As shown in Fig. 5.16 and Fig. 5.21, the scanning DOAS is mounted on a metal cable shaft. It is connected to a battery, which is in turn charged by a power line kindly provided by PEMEX. The temperature stabilization was set to 20°C, the approximate average daytime temperature at the measurement site. Data is sent via radio modem (*FREEWAVE 2009*) to the Centro Nacional de Prevención de Desastres (CENAPRED), the volcano observatory responsible for the monitoring of Popocatépetl Volcano. Here, it is evaluated in real-time and a rough estimate of the volcanic emission flux is made available to the observatory personal for use in hazard assessment.

The instrument was configured to perform a folded scan in two planes. Before each scan, one spectrum is taken in the zenith (later used as a reference for the evaluation). Also, the dark current and offset are measured with the scanner pointed down towards a baffle. The scan then begins at an azimuth of 115° relative to north, thereby pointing in the direction of the Puebla Valley. Upon reaching the zenith, the instrument rotates and the scan continues at an azimuth angle of 227° relative to north. As with the other installations, 15 exposures are taken in each viewing direction during the scan. During midday, a complete scan from horizon to horizon takes about 30 minutes under clear sky conditions. This geometry enables the measurement of the volcanic emission plume from Popocatépetl for wind directions between about 110 ° and 230°.

Site	Latitude [°N]	Longitude [°E]	Elevation [m]	Instrument Type
tlamacas_hd	19.0667	-98.6287	4030	mark II
tlamacas-cone	19.0565	-98.6374	4045	mark I
chipiquixtle	19.0095	-98.6567	3980	mark I
colibri	18.9869	-98.5577	2670	mark I

Tab. 5.2 – Geographic location of the NOVAC scanning DOAS instruments installed at Popocatéptl Volcano (Mexico).

During DOAS scans of a volcanic plume, the sampling rate of the plume depends on the distance between instrument and plume as well as on the step width between two measurements in the scan (see section 3.3.2). When scanning from a fixed position, the plume is typically closest to the instrument when it is directly above and furthest away when it is near the horizon. It was found that the accuracy of the emission flux retrieval could be improved by decreasing the step width near the horizon, where the plume is especially far from the instrument. This was implemented in the scan geometry used at Popocatépetl. For the spectra taken between 0 and ± 20° measurement zenith angle (MZA), a step width of 5° was used. Between ± 20° and ± 60° MZA, a step width of 4° was used. Between ± 60° and ± 90° MZA, the step width was reduced to 3°. In the direction of Puebla, two spectra were even recorded at 91.5° and 93°, as the implementation of these MZA below the horizon was still possible due to the elevated vantage point of the installation site.

In addition to the scans of the volcanic plume used for SO_2 emission flux determination, the instrument was configured to also point down into the planetary boundary layer (PBL) in two directions. For one, the MZAs 96° and 92° are adjusted at an azimuth of 85° relative to north, thus viewing into the center of the Puebla Valley, a large metropolitan area located at around

2000 m a.s.l. Also, the instrument looks down into the Mexico City Basin (also at around 2000 m a.s.l.) at an azimuth of 310° relative to north and an MZA of 92°. Both these regions are highly polluted urban areas. In addition to monitoring volcanic gases, the goal of these measurements is to quantify NO_2 and possibly SO_2 mixing ratios in the polluted PBL.

Fig. 5.16 – NOVAC mark II instrument installed at the site tlamacas_hd, approximately 5 km north of Popocatépetl Volcano (Mexico). The instrument is located on the premises of a radio-antenna station at 4030 m a.s.l., therefore power is supplied by land line. The rest of the installation (battery, charger, timer, radio modem) are located in a box below the metal cable shaft on which the instrument is mounted, and are connected via the blue cable shown in the image. The instrument is equipped with a sun shield to reduce heating by solar radiation.

Instrumental problems were encountered with this installation in the middle of May, 2008. Water was found to have entered the instrument housing, thus causing the electronics to fail. This phenomenon was attributed to the large temperature fluctuations occurring inside the instrument housing. As the instrument is located at 4000 m a.s.l. the average night-time temperature typically drops to below 10°C. During the day, solar heating of the instrument can cause the temperature inside the housing to reach more than 40°C. Therefore, a temperature difference between night and day of more than 30° is not unusual. As the instrument housing is not airtight, the temperature change is associated with a change in volume of the air inside the instrument housing by approximately 10%. Thus, about 10% of the air inside the instrument housing is exchanged each day, and the total air volume is exchanged about every 2 to 3 weeks. The amount of drying agent placed inside the box must be calculated with this fact in mind.

Three improvements to the instrument were made to avoid the encountered problems. For one, a sun shield was added (see Fig. 5.16) to reduce the solar heating of the instrument during the day. Secondly, a much larger amount of drying agent than originally planned was placed into the housing. Calculations showed that about 500 g of silica gel are necessary to keep the instrument dry for one year. Lastly, the spectrometer insulation was improved by increasing the distance between the hot and cold side of the Peltier cooler using a copper block, thus reducing the thermal power dissipation of the temperature stabilizer. The instrument was reinstalled in November 2008, and has now been running 6 months without failure (see Fig. 5.18).

5.3.2 Measurement examples

Volcanic SO_2 emission flux

The first and foremost objective of the NOVAC installations is the monitoring of SO_2 emission fluxes from Popocatépetl Volcano. As mentioned above, emissions from Popocatépetl are considerable, and continuous monitoring of this very active volcano located close to the Mexico City metropolitan area has a high priority. As described in section 5.3.1, the instrument is configured to perform lateral scans of the volcanic plume when it is blowing in northerly directions. Three example scans recorded on November 17, 2008 are shown in Fig. 5.17. On this day, the plume was blown directly overhead (see Fig. 5.16, the photograph was taken at this time), and the instrument was able to acquire an accurate assessment of the volcanic emission flux. The scans shown in Fig. 5.17 were recorded at 12:24, 14:37 and 16:04 local time. The integrated SO_2 amount X in each scan was retrieved by the NOVAC real-time evaluation software (*Johansson 2009b*) according to the lateral integration method described in section 3.3.2. The SO_2 emission flux was then calculated by multiplying by the wind speed of 10 m/s reported by CENAPRED. The attained SO_2 emission fluxes were 27, 15 and 21 kg(SO_2)/s, respectively.

As mentioned above, the instrument has now been running without failure for the last 6 months. The data is sent by radio link to the CENAPRED volcano observatory in Mexico City. Here, it is evaluated in real-time, and an estimate of the SO_2 emission flux is calculated. The time series of SO_2 emission fluxes measured over the last 6 months is shown in Fig. 5.18. The plume is observable by the instrument a large portion of the time. Peaks in SO_2 flux of over 100 kg(SO_2)/s were observed at the end of November and December, 2008. Since then, the flux has dropped to lower values. Note that this data is the result of a preliminary real-time evaluation. While scans in which the plume was not observable were filtered out, additional studies on the measurement geometries (including data from the other instruments) and meteorological conditions of the individual measurements are necessary to assess the accuracy of the given emission fluxes.

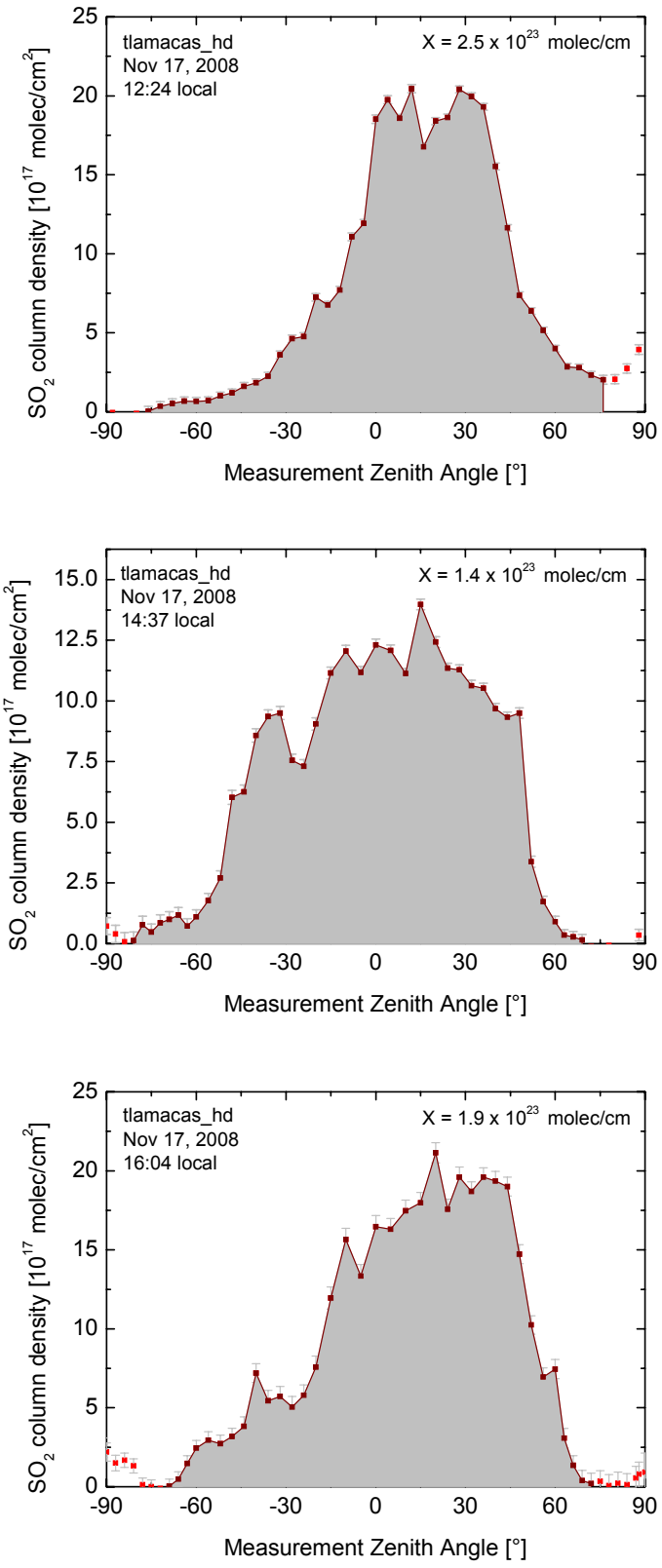

Fig. 5.17 – Three example plume scans recorded by the NOVAC mark II instrument installed at the site tlamacas_hd. In each case, the total SO_2 amount *X* in the plume cross-section is indicated assuming a plume height of 5000 m a.s.l. Multiplying by a wind speed of 10 m/s yields an SO_2 emission flux of 27, 15 and 21 kg(SO_2)/s, respectively.

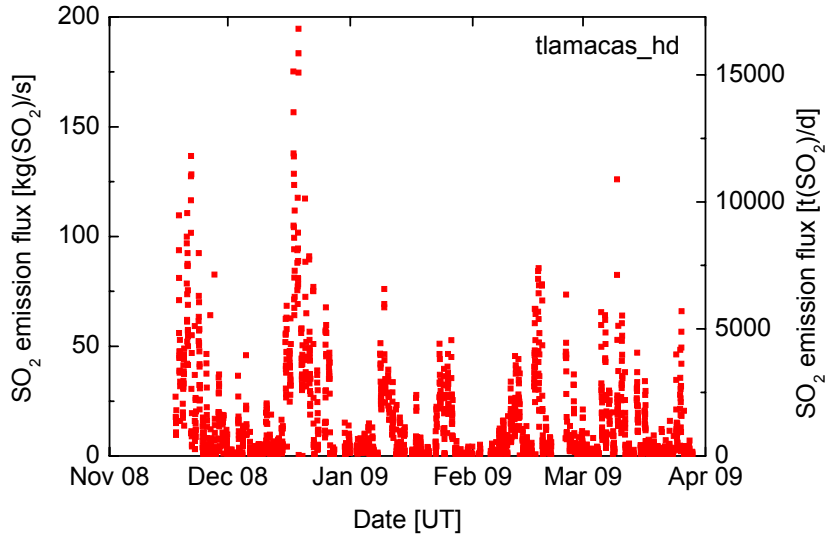

Fig. 5.18 – SO_2 emission flux from Popocatépetl Volcano (Mexico) measured by the NOVAC mark II scanning DOAS instrument tlamacas_hd over the last 6 months. Shown is the raw data retrieved from the NOVAC real-time evaluation routine (see *Johansson 2009a*). Data was downloaded from the NOVAC database[17] and is courtesy of CENAPRED[18] and UNAM.[19]

BrO in the plume of Popocatépetl

One of the additional advantages of the NOVAC mark II instrument when compared to the simpler mark I DOAS scanners is the temperature stability of the optical bench and detector. This allows a more accurate correction of the detector dark current and electronic offset, and enables the co-adding of spectra recorded at different points in time to enhance photon statistics. Co-adding is not possible if temperature changes in the spectrometer cause the instrument calibration and instrument line shape (ILS) to vary between measurements (see section 3.4.5).

This additional functionality is very advantageous when attempting to retrieve trace gases other than SO_2, which typically have much lower optical densities. Here, co-adding of spectra was used to evaluate BrO in the plume of Popocatépetl (the importance of halogen oxides such as BrO for atmospheric chemistry and volcanology are described in chapter 2). For this case study, the 18th of November, 2008 was chosen because of the known meteorological conditions. On this day, the skies over central Mexico were nearly cloudless, thus a high solar irradiance can be assumed in the volcanic plume (this is necessary for the formation of BrO, see section 2.1.4 and chapter 7). The wind direction of 140° relative to north and a wind speed

[17] http://novac.iup.uni-heidelberg.de/

[18] Centro Nacional de Prevención de Desastres

[19] Universidad Nacional Autónoma de México

of 7 m/s (data from CENAPRED) allowed the plume to be observed on the western end of the scan conducted at the tlamacas_hd NOVAC site.

For the evaluation of BrO, all spectra recorded between 11:00 and 15:00 local time (when the incident solar irradiance is highest) were first evaluated for SO_2 and sorted according to their respective SO_2 column densities. In a similar evaluation as performed for the measurements at Stromboli (see section 5.2.2), the 50 spectra (each consisting of 15 individual exposures) with the least SO_2 were co-added to form the Fraunhofer reference spectrum. From this, a Ring spectrum was calculated (see chapter 3) with the DOASIS software (*Kraus 2004*). Next, 25 spectra in order of SO_2 abundance were successively co-added to obtain a co-added measurement spectrum. This step was repeated until all spectra measured during the reporting period had been added to one of the co-added measurement spectra in order of increasing SO_2 amounts. The co-added measurement spectra where then divided by the compiled Fraunhofer reference and a DOAS fit optimized for BrO was performed on the thus obtained optical densities.

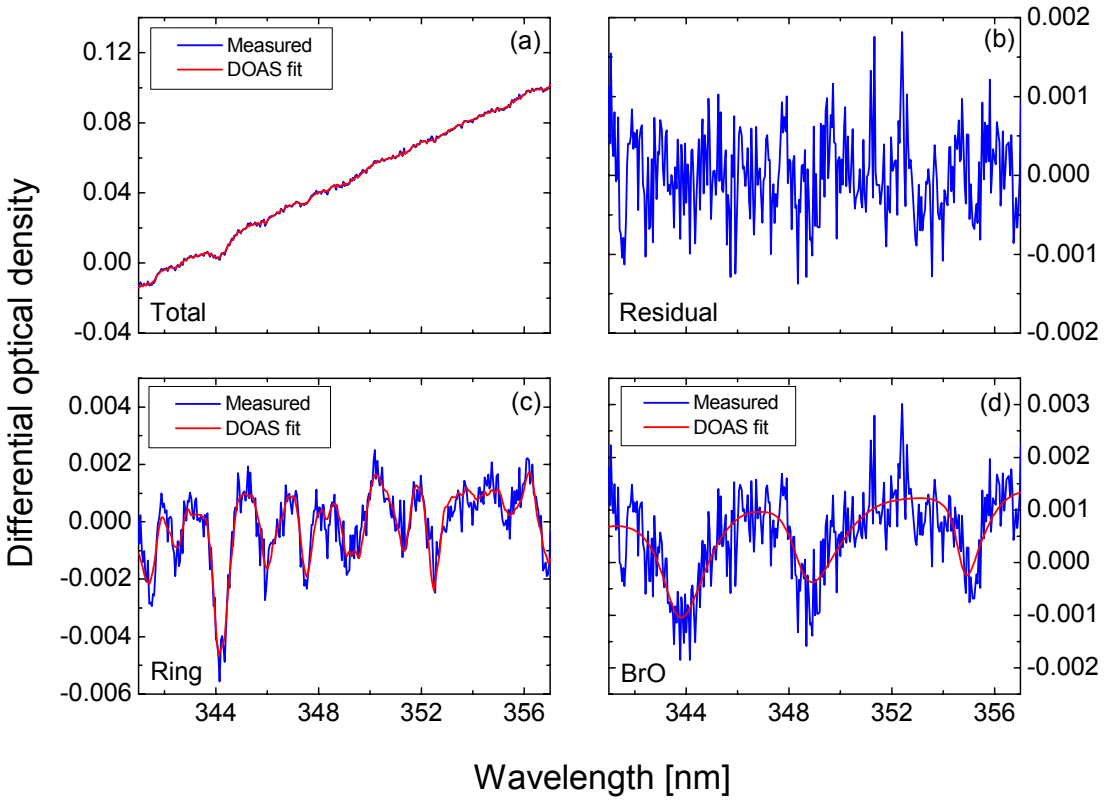

Fig. 5.19 – Fit example of the BrO retrieval conducted for Popocatépetl volcano. Inset (a) depicts the total measured optical density (blue) along with the fit result (red). The difference between the two, the fit residual, is shown in inset (b). Inset (c) shows the fit of the Ring spectrum. Here, the DOAS model for the Ring structure (red) is compared to the measured optical density with all contributions by trace gases and the broadband DOAS polynomial subtracted (blue). Finally, the same is shown for the fit of the BrO cross-section in inset (d). Here, a maximum differential optical density of about 2.1×10^{-3} was found, indicating a BrO column density of 3.1×10^{14} molec/cm^2. Not shown are the fits of NO_2, O_3, and the 4th order DOAS polynomial.

An example fit is shown in Fig. 5.19. The fit was performed in the wavelength range between 341 and 357 nm, a fit window found to be well suited for the evaluation of BrO at this site where large SO_2 column densities are expected in the plume. Aside from the absorption cross-section of BrO (*Wahner et al. 1988*), the cross-sections of O_3 (*Voigt et al. 2001*) and NO_2 (*Vandaele et al. 1998*) were included in the fit, along with a Ring correction spectrum and a 4^{th} order DOAS polynomial to describe broadband structures. A conducted case study showed that it was not necessary to include the SO_2 absorption cross-section in the retrieval at these wavelengths, at least not for the measurements shown here.

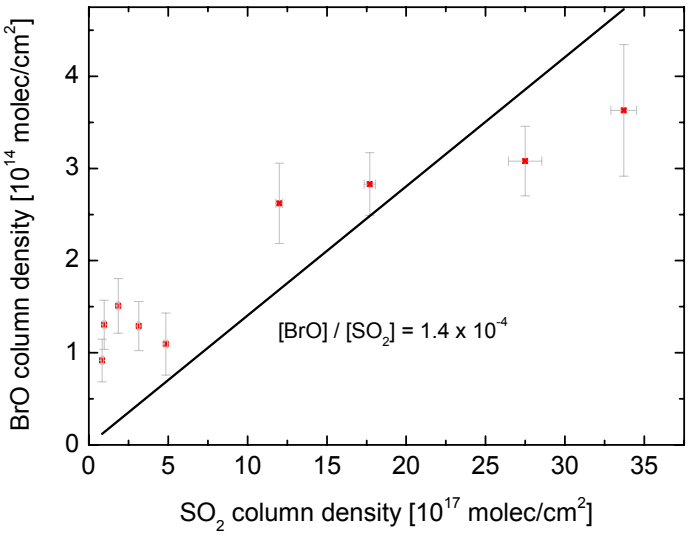

Fig. 5.20 – BrO column densities measured between 11:00 and 15:00 local time on November 18, 2008 at Popocatépetl Volcano (Mexico) as a function of the respective SO_2 column density. Only BrO data above the detection limit is shown. A linear fit of the data yields a BrO/SO_2 molecular ratio of around 1.4×10^{-4}. However, the ratio appears higher for the lower SO_2 column densities, possibly indicating a higher BrO/SO_2 ratio towards the edges of the plume which could be a consequence of ambient ozone mixing into the plume.

BrO was positively identified in many of the co-added measurement spectra. This is the first known detection of BrO in the plume of Popocatépetl Volcano. The results of the BrO evaluation performed for November 18, 2008 are shown in Fig. 5.20. The BrO column density is depicted as a function of the retrieved SO_2 column density in each of the co-added measurement spectra. BrO column densities of up to 3.6×10^{14} molec/cm^2 were retrieved. The black line in Fig. 5.20 represents a linear fit of the data forced to intersect the point of origin. It indicates an average BrO/SO_2 molecular ratio of 1.4×10^{-4}.

However, BrO column densities measured for SO_2 columns below 2×10^{18} molec/cm^2 were found to be enhanced relative to this ratio, the others were below the indicated ratio. This observation could be caused by plume chemistry. The measurements corresponding to the lower SO_2 column densities were likely recorded not in the center but rather towards the edge

of the volcanic plume. As the formation of BrO most likely requires the presence of O_3 in the plume (see section 2.1.4 and chapter 7), it is quite possible that BrO is formed mainly at the edge of a volcanic plume, where ambient air containing O_3 is efficiently mixed with volcanic volatiles. Similar observations have been made using imaging DOAS instruments. *Bobrowski et al. 2007* and *Louban et al. 2009a* report enhanced BrO/SO_2 ratios towards the edge of the plume of Mt. Etna during measurements in May of 2005. In order to back up this theory, however, an in-depth study is required on a longer dataset. Radiative transfer effects should also be taken into account, as the dilution effect (see chapter 8) is stronger at the shorter wavelengths where the SO_2 retrieval is conducted than in the BrO fit region. If left uncorrected, this could cause a plume located at a long distance from the instrument to appear to have an enhanced BrO/SO_2 ratio.

While only covering a single day, this case study proves the presence of BrO in the plume of Popocatépetl. As this is the first known observation of BrO at Popocatépetl, it is significant in and of itself. While time constraints prevented a further evaluation in the scope of this thesis, the availability of 6 months of continuous emissions data at Popocatépetl provides a perfect basis for a follow-up study in which all details will be discussed.

NO_2 in the Mexico City Basin and Puebla Valley

While the NOVAC project is aimed mainly at measuring volcanic gas emissions, times obviously exist in which volcanic emissions at a particular volcano can not be measured by a specific instrument. This may be because the volcano has stopped emitting gas, or because the plume is blown in a direction not observable by the instrument. In such cases, the instruments can be configured to study other atmospheric trace gases. Applications include measuring stratospheric composition (typically at sunup and sunset), background measurements of the free troposphere (in remote sites elevated above the boundary layer), or, as was done here, measuring urban pollution in the boundary layer.

The NOVAC site tlamacas_hd represents a good vantage point for viewing down into both the Mexico City Basin as well as the Puebla Valley. As the Mexico City metropolitan area houses more than 20 million inhabitants, the planetary boundary layer (PBL) in the basin is considerably polluted. While not as populated, the Puebla Valley located 120 km southeast of Mexico City is also an urban area. Both the textile and automobile industry are prominent in the region, and are significant contributors to anthropogenic pollution. Agricultural biomass burning is also considerable source of carbonaceous compounds, NO_x, and aerosols in both regions (see e.g. *Crounse et al. 2009*).

Aside from SO_2 and BrO, the wavelength range of the DOAS spectrometers used in the NOVAC mark II instruments (approximately 295 – 390 nm) is well suited for evaluating NO_2. As described in chapter 2, NO_2 plays an important role in the atmosphere as a precursor for ozone. Its photolysis is held largely responsible for the O_3 production in the troposphere (see R. 2.3, R. 2.4, and Fig. 2.1). In the following, a case study is presented in which spectra from the second half of November and all of December 2008 were evaluated with respect to

NO_2 abundance in the Puebla Valley. For this study, the spectra recorded at a measurement zenith angle (MZA) of 96° (six degrees below the horizon) and at an azimuth of 85° relative to north (the direction of the Puebla Valley) were selected (see Fig. 5.15). This viewing direction is depicted in Fig. 5.21. Here, the polluted PBL is clearly distinguishable as a layer of brown haze.

For each day in the reporting period, all spectra recorded in the above mentioned viewing direction between 11:00 and 14:00 local time were co-added to obtain a tropospheric measurement spectrum. In the same time period, all zenith spectra were also co-added and used as a Fraunhofer reference in the DOAS retrieval. As NO_2 is present in the stratosphere as well as the troposphere, care was taken to limit the evaluation to solar zenith angles between 41 and 48° (corresponding to the time between 11:00 to 14:00 local time), thus keeping differences in the stratospheric optical path between the individual spectra below about 13%.

Fig. 5.21 – Viewing direction of the NOVAC mark II instrument during measurements of urban pollution and biomass burning in the Puebla Valley, 130 km southeast of Mexico City. The boundary layer is clearly distinguishable as an area of brown haze.

After both the tropospheric and Fraunhofer spectrum were compiled, the two were divided by one another, and the logarithm was taken to obtain the optical density. In the next step, the absorption cross-sections of NO_2 (*Vandaele et al. 1998*), O_3 (*Voigt et al. 2001*), a Ring correction spectrum as well as a 4^{th} order DOAS polynomial were fit to the obtained optical density. A wavelength region between 356 and 366 nm was chosen for the NO_2 evaluation. While this range is lower than the wavelength region typically used for NO_2 retrievals, this fit window was found well-suited for the evaluations. First attempts at longer wavelengths failed due to insufficient intensity, a result of the UV filter installed in the NOVAC mark II instrument blocking visible radiation (see section 3.5.1).

An example NO_2 fit is shown in Fig. 5.22. Here, NO_2 was positively identified, and a column density of 1.0×10^{16} molec/cm^2 was obtained. Fig. 5.23 shows the noontime differential NO_2 column densities retrieved for the months of November and December, 2008. Only days are shown in which no SO_2 was observed in the spectra, thus indicating the volcanic plume was not present at the time. Measured differential column densities range between 0 and 1.4×10^{16} molec/cm^2. The average detection limit was 6×10^{15} molec/cm^2.

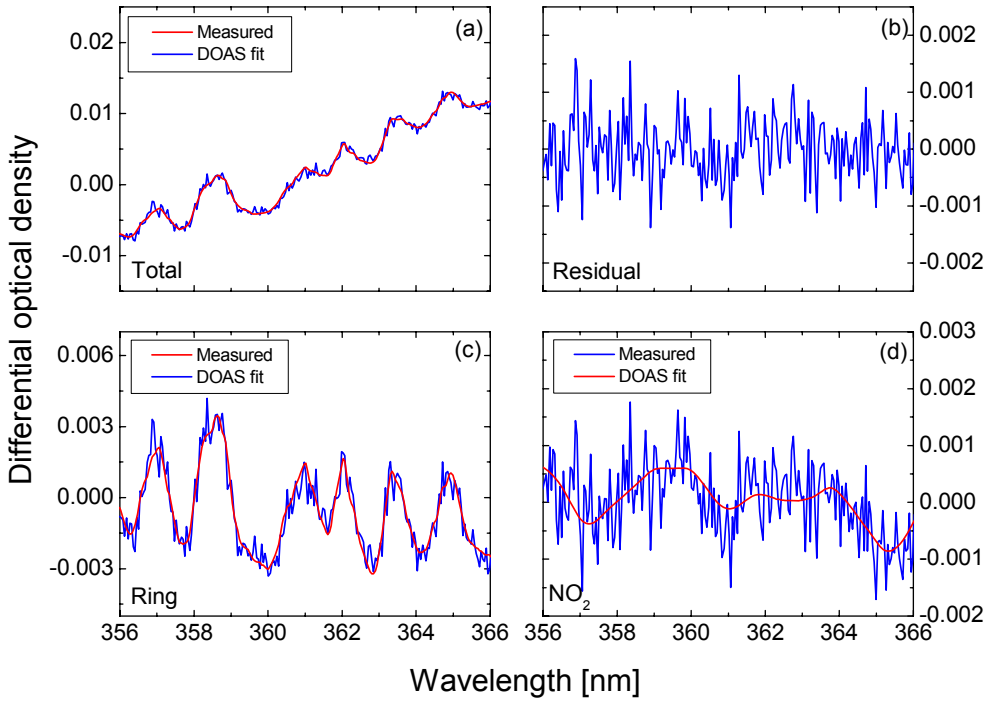

Fig. 5.22 – Example DOAS fit of NO_2 for the urban pollution measurements at the NOVAC site tlamacas_hd. The total DOAS model and the measured optical density spectrum are shown in inset (a). Inset (b) depicts the fit residual (difference between DOAS model and measurement spectrum). Inset (c) shows the contribution of the Ring correction to the DOAS model. The Ring spectrum was clearly identified and the effect was successfully corrected. Inset (d) shows the fit of NO_2. NO_2 was successfully identified in this spectrum, which was compiled from all spectra taken between 11:00 and 14:00 local time in the 96° measurement zenith angle geometry pointing into the Puebla Valley on November 18, 2007. The retrieved NO_2 column density was 1.0×10^{16} molec/cm^2.

The radiative transfer model TRACY-II (*Deutschmann 2008*, also see chapter 8) was used to obtain an estimate for the observed optical path length in the PBL. A model scenario was set up with an instrument located at 4000 m a.s.l. looking 6° down at the ground. The ground level was set to 2000 m a.s.l., the surface albedo was 0.1. In the lowermost 1 km, a well mixed boundary layer containing NO_2 and aerosols was simulated (see *Doran et al. 2005, Baumgardner et al. 2009*). The aerosols featured a single scattering albedo of 0.85 and an asymmetry parameter of 0.6, typical values for an urban aerosol (see e.g. *Kudo et al. 2008,*

Liu et al. 2008). The aerosol extinction coefficient was varied between 0.025 and 0.5, approximately corresponding to visibilities of between 160 km and 8 km in the PBL. Above the 1 km PBL, the air was considered free of aerosols and trace gases with the exception of a stratospheric O_3 layer. The solar zenith angle was fixed at 40°, the solar azimuth was 90° relative to the instrument viewing direction. The model runs were all conducted at 365 nm, approximately where the NO_2 evaluations took place.

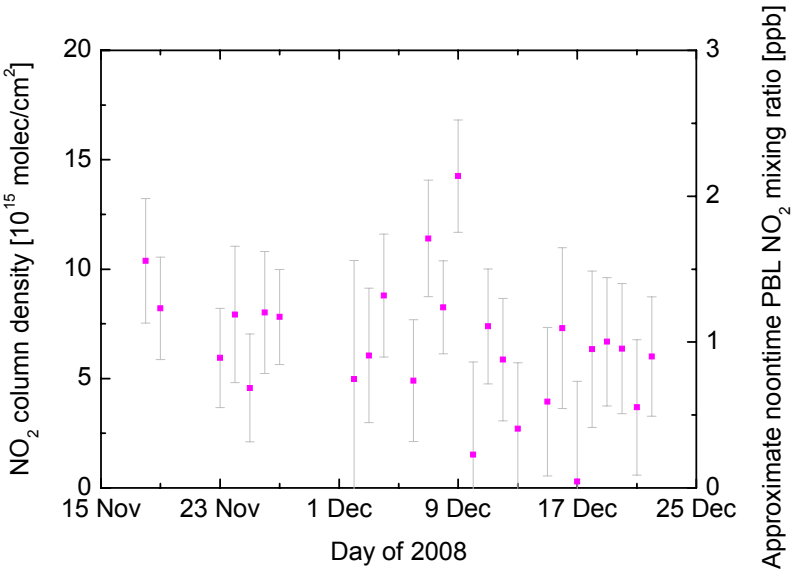

Fig. 5.23 – Time series of the retrieved noontime NO_2 column densities looking into the Puebla Valley. While positively detected, the retrieved column density was often close to the instrument's detection limit, which averaged at 6×10^{15} molec/cm^2. An approximate mixing ratio is given at right assuming a well-mixed, 1 km deep PBL containing NO_2 and aerosols with an extinction coefficient of 0.1 (see Fig. 5.24).

Fig. 5.24 shows the results of the model runs for a number of different aerosol extinction coefficients (AECs). The air mass factor (AMF) plotted in the figure is the ratio of measurement optical path in the PBL divided by the PBL height, in this case 1 km. Optical path lengths in the PBL ranged between 2.2 km for an AEC of 0.5 and 4.4 km for an AEC of 0.025. This diagram shows that the retrieval of NO_2 mixing ratios in the PBL is strongly dependent on the aerosol conditions in this layer. An accurate assessment of NO_2 concentration requires additional information on the geometry of the PBL as well as on the aerosol conditions. A number of techniques could be used to gain such information (e.g. measuring O_4 column densities, relative azimuth intensities or by analyzing the Ring effect, see *Wagner et al. 2004, Friess et al. 2006*), but such studies could not yet be conducted within the scope of this thesis.

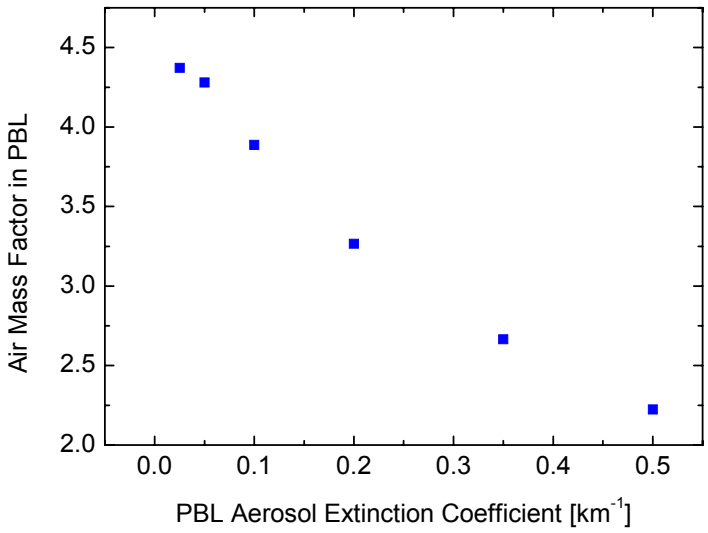

Fig. 5.24 – Sensitivity of the tlamacas_hd NOVAC instrument at 365 nm to a planetary boundary layer (PBL) of 1 km depth assuming a measurement zenith angle of -96°. This geometry is used for NO_2 measurements in the Puebla Valley. As the AMF in the PBL is strongly dependent on the aerosol extinction coefficient, a quantitative measurement will require information on the aerosol conditions in the PBL.

The approximate noontime NO_2 mixing ratio in the PBL shown on the right side of Fig. 5.23 is an estimate obtained assuming an air mass factor of 3.8, which was obtained from the model scenario using an AEC of 0.1 (approximately 40 km visibility in the PBL). The thus obtained values are surprisingly low. In urban areas, NO_2 mixing ratios can easily reach several 10 ppb. While photolysis typically causes a dip in average NO_2 concentrations around noon, this effect is not likely responsible for the low measurement values.

Instead, the most likely explanation for the low mixing ratios appears to be an inhomogeneous PBL. The DOAS instrument is located more than 40 km from the city of Puebla. At 360 nm, the mean free photon path due to Rayleigh scattering is around 15 km. Aerosol scattering decreases this further. Therefore, the radiation measured by the DOAS instrument mostly does not pass the city of Puebla. NO_2 emitted by the city can only be measured if it is transported laterally to a position closer to the instrument. The measurements indicate that transport in this direction is not very efficient, and that the NO_2 concentration in the PBL in the vicinity of the volcano is not typical of an urban environment.

In a second study, the spectra recorded during the reporting period in the direction of the Mexico City Basin (310° azimuth relative to north, 2° below the horizon) were evaluated in the same manner. Although the maximum NO_2 column densities of around 2×10^{16} molec/cm^2. were slightly higher than for the Puebla Valley, the results indicate that measurement conditions here are similar, and that the instrument sensitivity to the truly polluted area of the boundary layer is small.

5.4 Mt. Etna (Italy)

Towering the city of Catania, Sicily's second largest city, Mt. Etna has a summit elevation of approximately 3330 m. Historical lava flows of basaltic composition cover much of the surface of this massive volcano, whose edifice is the highest and most voluminous in Italy (*GVP 2009a*). Lava flows extend to the foot of the volcano on all sides and have reached the sea over a broad area on the southeast flank. At the volcano's summit, three prominent craters dominate the landscape, The Northeast Crater, the Southeast Crater, and the Central Crater. The latter consists of three individual vents called Voragine, Bocca Nova 1, and Bocca Nova 2 (see Fig. 7.15). Persistent explosive eruptions, sometimes with minor lava emissions, often occur at one or more of the summit craters.

Higher lava effusion rates typically originate from flank eruptions. While less frequently active, flank vents originate from fissures that open progressively downward from near the summit. Activity at these vents is commonly accompanied by strombolian eruptions at the upper end of the fissures. Large cinder cones are often constructed over the active vents, especially those of lower-flank lava flows. Historical cones can be observed on all sides of the volcano and up to many kilometers from the summit (see Fig. 5.25).

5.4.1 Instrument installation and configuration

At Mt. Etna, four NOVAC scanning DOAS sites were installed in July of 2008. Fig. 5.25 shows the location of the measurement sites. Two sites are equipped with advanced NOVAC mark II instruments. One mark II instrument is co-located with a simple mark I scanner on a rooftop in the town of Milo (milo_tommaso_house_uhei and milo_tommaso_house_got). At 800 m a.s.l., this site is located at a distance of 10.5 km from the summit directly downwind of the volcano under the predominant wind direction. It is mounted on a tripod and powered by a land line (see Fig. 5.26). An 80 Ah car battery was used as a buffer in case the power is interrupted. This battery is always kept charged by a standard battery charger. The temperature regulator of the instrument was set to 20°C.

The data link for this site was established via WLAN. A directional WLAN antenna sends data in a westerly direction to a repeater site installed by INGV Catania on the southern edge of the horseshoe shaped Valle del Bove. From here, data is relayed to the observatory in Catania, where it is evaluated and displayed in real time. The IP address assigned to the instrument is 10.201.6.41. The co-located NOVAC mark I instrument uses the same power supply and data link, but a different IP address.

The second mark II instrument was installed on the back porch of the Polizia Municipale building in the town of Giarre. It is therefore also located in the predominant wind direction, but is only 70 m a.s.l. and at a distance of 17 km from the summit vents (see Tab. 5.3 for exact location). Here, the instrument was mounted on a concrete wall adjacent to a west-facing, second story porch. A second box was placed at the base of this wall and contains a

car battery for buffering the power supply, a battery charger constantly charging the battery, and a timer that switches the instrument off at night. Again, the spectrometer temperature was kept at a constant 20°C. Unfortunately, the data link between this site and the INGV observatory in Catania could not be established yet, and data must be retrieved manually with a laptop computer.

The Istituto Nazionale di Geofisica e Vulcanologia (INGV) Catania is responsible for measuring SO_2 emissions at Mt. Etna. To this extent, INGV already installed a system of scanning DOAS instruments at Mt. Etna in 2003, the so-called Flux Automatic Measurement Network (FLAME). This network consists of an additional 5 scanning UV-DOAS systems for measuring volcanic SO_2 flux (see e.g. *Salerno et al. 2006, Wright et al. 2008*). In order to allow a direct comparison of the measurements recorded by the new NOVAC instruments with those taken by the FLAME scanners, the NOVAC mark II instruments were configured to perform simple, flat scan geometries similar to those of the FLAME scanners. Both NOVAC mark II instruments begin their scans at an azimuth of 190° relative to north and scan from horizon to horizon in a single plane. As is the case for Popocatépetl (see section 5.3.1), the step width is varied during the scan, with smaller steps taken near the horizon and larger steps performed close to the zenith direction.

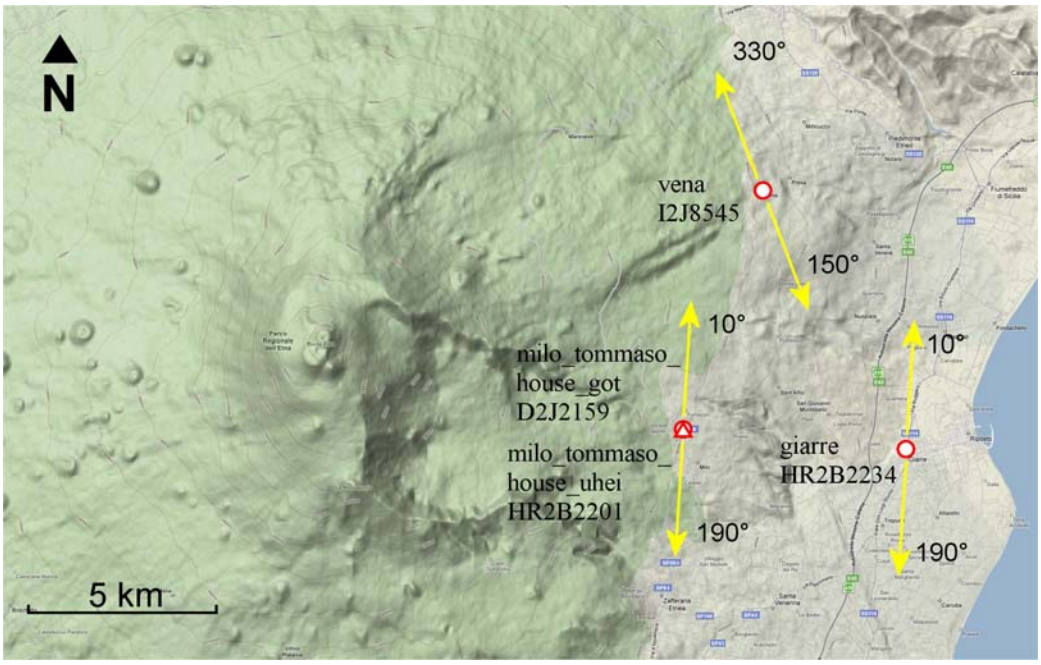

Fig. 5.25 – Geographical location of the four NOVAC instruments installed at Mt. Etna (Italy). NOVAC mark II scanners are installed on a rooftop in the town of Milo (HR2B2201) and on the balcony of a police station in Giarre (HR2B2234). In Milo, a NOVAC mark I instrument is co-located with the mark II scanner for data comparison. A second mark I instrument is installed on the roof of a civic center in the town of Vena. The NOVAC mark II instruments are configured to perform simple, flat scans in order allow direct data comparison to the FLAME[20] network already installed and maintained at Mt. Etna by INGV Catania. (Map © 2009 Google & 2009 Tele Atlas)

[20] Flux Automatic Measurement Network

Site	Latitude [°N]	Longitude [°E]	Elevation [m]	Instrument Type
milo_tommaso_house_uhei	37.7312	15.1130	800	mark II
milo_tommaso_house_got	37.7312	15.1130	800	mark I
giarre	37.7300	15.1839	70	mark II
vena	37.7905	15.1388	730	mark I

Tab. 5.3 - Geographic location of the NOVAC scanning DOAS instruments installed at Mt. Etna (Italy). Here, one instrument was installed downwind of the others to allow plume evolution studies and characterize radiative transfer effects.

Fig. 5.26 – NOVAC mark II DOAS instrument at the site milo_tommaso_house_uhei. The instrument power is supplied by land line and buffered by an 80 Ah car battery. Data is transmitted via WLAN antenna (not shown) to a repeater site on the southern edge of the horseshoe shaped Valle del Bove (see Fig. 5.25). The volcanic plume is clearly visible in the sky over the instrument.

Fig. 5.27 – NOVAC mark II instrument installed at the Polizia Municipale in Giarre. Here, the instrument is mounted on a concrete wall at the base of which a second box contains an 80 Ah car battery, a charger and a timer. Again, the battery is charged by land line. The cable shown hanging out the side of the instrument is used to communicate with the temperature controller and is disconnected after successful configuration.

Mt. Etna has been the subject of a number of studies conducted within the scope of this thesis, thus additional measurement examples are not given here. In the conducted study on radiative transfer effects in and around volcanic plumes described in chapter 8, a comprehensive measurement which included data from the NOVAC scanning instruments is presented. Also, active Long Path DOAS measurements were conducted in the vicinity of the crater. These are described in sections 7.4 and 7.5. In addition, the SO_2-camera described in chapter 4 was tested here. Example measurements are shown in section 4.6. Finally, a comprehensive campaign aimed at quantifying the BrO/SO_2 ratio in the plume of Mt. Etna at different distances from the vent (i.e. plume ages) was carried out in July of 2008. First results from this campaign were presented by *Vogel et al. 2008* and will be subject of an upcoming publication by *Vogel et al. 2009*.

5.5 Tungurahua (Ecuador)

Located 30 km southeast of the city of Ambato on the eastern edge of the Ecuadorian Andes, Tungurahua is a steep-sided stratovolcano with a summit elevation of 5023 m (see Fig. 5.29). Towering more than 3 km above its northern base, it is one of Ecuador's most active volcanoes. The current cone was built on the collapsed remains of two prior volcanic edifices, the second of which collapsed only 3000 years ago producing a large horseshoe shaped caldera open to the west (*GVP 2009a*). Since then, all historical eruptions have originated

from the new summit crater. Strong explosions, pyroclastic flows and lava flows have accompanied these eruptions, the last of which began in 1999 and can be considered ongoing (*GVP 2009c*). In 1999, it caused a temporary evacuation of the 22,000 inhabitants of the town of Baños.

5.5.1 Instrument installation and configuration

The first scanning DOAS spectrometers were installed at Tungurahua volcano by *Arellano et al. 2008b* in 2004. These instruments were replicas of the instruments developed by *Edmonds et al. 2003a* for use at Soufrière Hills Volcano (Montserrat). In the scope of the NOVAC project, four additional DOAS instruments were installed, including one NOVAC mark II scanner. The NOVAC instruments were positioned at three sites on the western side of the volcano, so as to best cover the predominant plume direction (see Fig. 5.28). Two NOVAC mark I instruments with conical scanning geometries (see *Johansson 2009a*) were installed at the sites huayrapata and bayushig. In between the two, a mark I instrument with a flat scanner was installed at pillate. A NOVAC mark II instrument (HR2B2202) with a folded scan geometry was co-located at huayrapata for testing purposes. Tab. 5.4 gives an overview of the geographical locations of the NOVAC instruments.

The NOVAC mark II instrument at huayrapata is installed on the roof of a small concrete structure, which serves as a radio antenna relay station. At this site, a total of three scanning DOAS instruments are running: two NOVAC instruments and an older Montserrat replica (all shown in Fig. 5.30). The mark II instrument is mounted on a tripod and powered by a land line. Two large batteries serve as a buffer in case of short term power failures. A timer turns the instrument off at night and reboots the system every morning. The temperature stabilization of the spectrometer was set to a steady 20°, the approximate daytime average temperature at the measurement site.

The instrument was configured to perform a folded scan in two planes. Before each scan, one spectrum is taken in the zenith (later used as a reference for the evaluation). Afterwards, the dark current and offset are measured by looking downward, where a baffle blocks the scanner. The scan then begins at an azimuth of 90° relative to north, thereby pointing directly along the Pastaza River Valley. Once the zenith is reached, the instrument rotates and the scan continues in an azimuth direction of 200°, thus pointing along the Chambo River Valley. 15 exposures are taken in each viewing direction. This geometry enables the instrument to measure the plume during wind directions between about 80° and 190°. The time for one scan is about 30 minutes but varies depending on the time of day and cloud conditions.

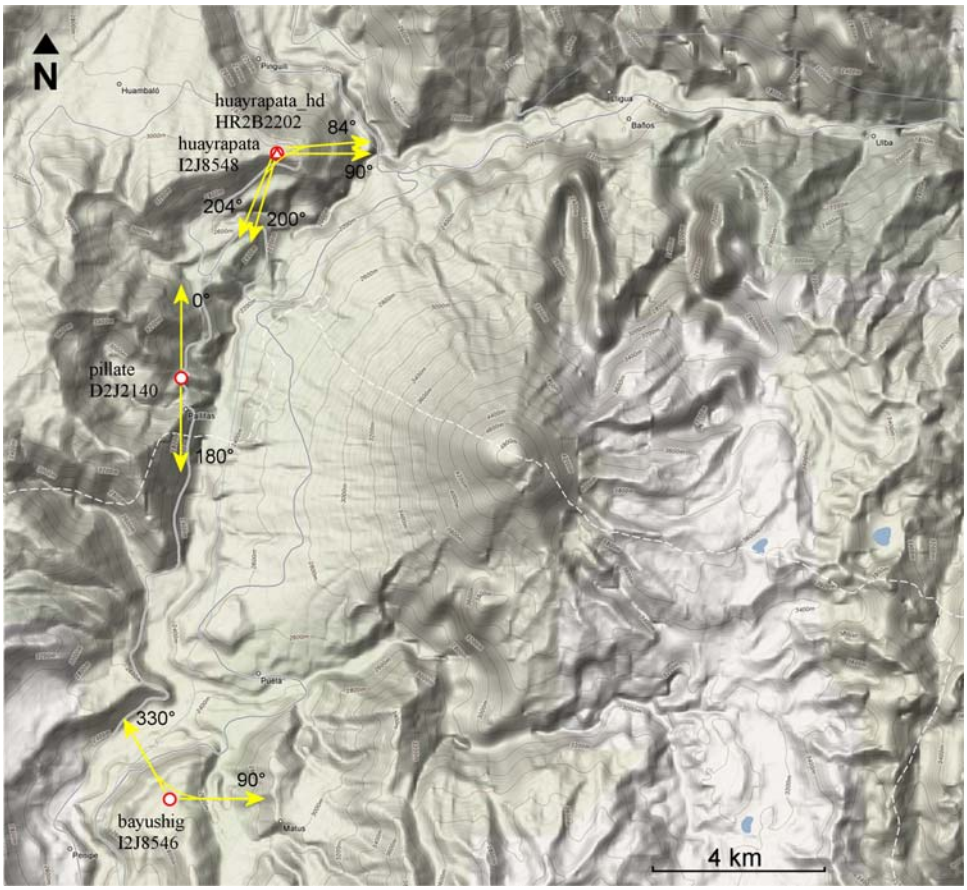

Fig. 5.28 – Geographical location of the NOVAC installations at Tungurahua Volcano (Ecuador). The NOVAC mark II instrument is currently co-located with a simple mark I scanner at the huayarapata measurement site. (Map © 2009 Google, LeadDog Consulting, Europa Technologies)

Site	Latitude [°N]	Longitude [°E]	Elevation [m]	Instrument Type
huayrapata_hd	-1.4047	-78.4948	2910	mark II
huayrapata	-1.4047	-78.4948	2910	mark I
pillate	-1.4536	-78.5131	2610	mark I
bayushig	-1.5435	-78.5171	2780	mark I

Tab. 5.4 - Geographic location of the NOVAC scanning DOAS instruments installed at Tungurahua Volcano (Ecuador).

Fig. 5.29 – Tungurahua Volcano (Ecuador) as seen from the IGEPN Tungurahua Observatory approximately 15 km to the north. The NOVAC site huayrapata is located on the top of the ridge the base of which is shown in the front right of the image.

Fig. 5.30 – Photograph of the NOVAC site huayrapata, about 9 km northwest of the summit of Tungurahua Volcano. Here, three scanning DOAS instruments are installed on the roof of a small concrete structure. The NOVAC mark II instrument is mounted on a tripod between the other two scanners. In the foreground, the NOVAC mark I instrument is seen. It is installed in a large wooden box with the scanner protruding on the right side. In the back, a replica of the DOAS system applied on Soufrière Hills Volcano, Montserrat (*Edmonds et al. 2003a*) is set up. All instruments are powered by a land line buffered by two large car batteries located in the back right box. This housing also contains the radio modems used to send the spectral data to the Tungurahua Observatory located about 8km to the north.

5.5.2 Example measurements

Volcanic SO_2 emission flux

The meteorological conditions at Tungurahua Volcano are dominated by frontal systems moving in from the Amazon River Basin in the east. Therefore, it rains very often and densely overcast skies are typical. These conditions make remote sensing measurements very difficult and at time impossible. During the installation campaign in November of 2008, the huayrapata site was constantly in the clouds, as is shown in Fig. 5.30. SO_2 flux measurements were not possible in these conditions.

Even if measurements had been possible during the installation period, it is likely that gas emission from Tungurahua would have been below the detection limit. Data from previous weeks from the NOVAC mark I instruments indicated emissions were negligible, and that the eruption at Tungurahua that had been ongoing since 1999 had more or less stopped (also see e.g. *SI/USGS 2008*).

However, in the middle of December of 2008, the NOVAC instruments registered a sudden increase in SO_2 emissions. Three example scans recorded on December 15 at the NOVAC site huayrapata_hd are shown in Fig. 5.31. For each scan, the total SO_2 amount X was integrated using the NOVAC data evaluation and display software (*Johansson 2009b*) according to the lateral integration technique described in section 3.3.2. The obtained values for X are shown in the top right corner of the individual diagrams. Multiplication of the integrated SO_2 amount with the wind speed of 1.5 m/s (*GDAS 2009*) yields a volcanic SO_2 emission flux of around 600 t(SO_2)/d. While much higher SO_2 fluxes had been observed in past years, this value is considerably above the background values obtained in previous weeks.

The resumption of volcanic activity was not limited to gas emissions alone. The Instituto Geofísico of the Escuela Politécnica Nacional (IGEPN) reported increased seismicity, ash emissions and the ejection of incandescent blocks during the same time period. A few hours later in the night of December 15, ash plume were observed to rise to 7 km a.s.l.(*SI/USGS 2009*). This example again shows how valuable gas emissions data can be in volcanic risk assessment, as it provides volcano observatories with an additional, independent parameter strongly linked to volcanic activity in general.

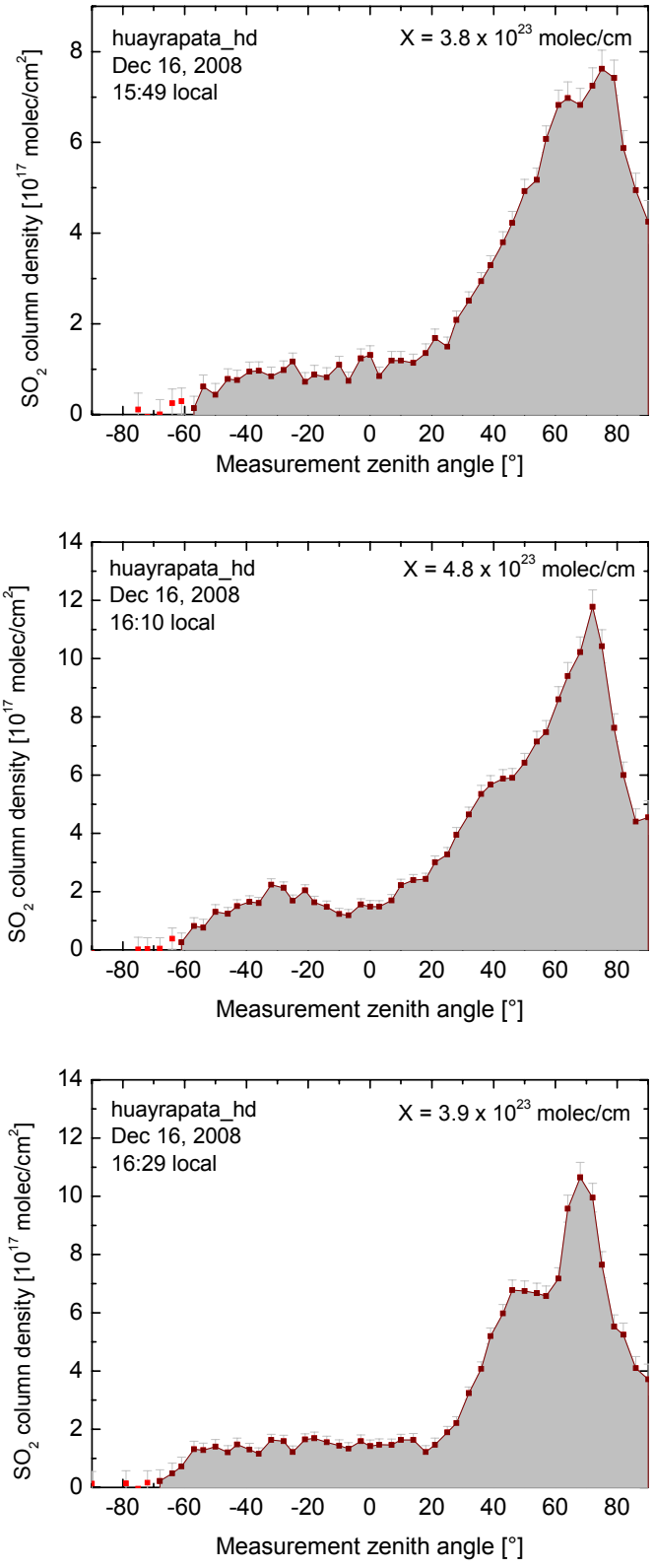

Fig. 5.31 – Three example scans of the emission plume of Tungurahua Volcano (Ecuador) recorded on December 16, 2008 at the NOVAC site huayrapata_hd. After weeks of dormancy, gas emissions from Tungurahua picked up suddenly in the middle of December, 2008. When multiplied by a wind speed of 1.5 m/s (*GDAS 2009*), the depicted scans represent volcanic emission fluxes of 6.8, 7.6 and 6.4 kg(SO_2)/s or around 600 t(SO_2)/d.

6 Investigating volcanic unrest at Kilauea Volcano (Hawaii)

6.1 Background

Kilauea Volcano (Hawaii) is part of a larger volcanic complex forming the islands of Hawaii as the oceanic crust was pushed over a spatially fixed hot spot in the earth's mantle. In the last 100,000 years, Kilauea grew to approximately 1,200 m a.s.l., but the volcano rises more than 6,000 m above the ocean floor. Kilauea is currently one of the world's most active volcanoes, and about 90 % of the basaltic shield volcano's surface is less than 1,100 years old. Approximately 4 km in diameter, the volcano's caldera was formed in several stages about 1,500 years ago and in the 18th century. Historically, eruptions have also originated from the lengthy East and South West Rift Zones, which extend to the sea on both sides of the volcano (*GVP 2009a*).

The volcanic gases H_2O, CO_2, CO, SO_2, H_2S, HCl, and HF have all been measured at Kilauea volcano in the past (see e.g. *Le Guern et al. 1982, Gerlach and Graeber 1985, Sutton et al. 2001, Sutton et al. 2005, Edmonds et al. 2008*). This study is limited to the species SO_2 and BrO, which can be measured with the passive DOAS technique.

In recent years, the largest portion of the emitted SO_2 originated from the Pu'u 'O'o crater along the East Rift Zone. From 2003 to 2007, the total SO_2 emissions from Halema'uma'u crater on the summit of Kilauea have typically been only approximately 100 - 200 t(SO_2)/d, the average emission flux being 140 t(SO_2)/d. Towards the end of December 2007, however, emissions increased to nearly 300 t(SO_2)/d and by mid-February 2008, up to 1,000 t(SO_2)/d were observed (*USGS 2008b*).

This increased activity together with the opening of an actively degassing vent on the western side of Halema'uma'u crater in the second half of February and unusually high SO_2 emissions

from the summit crater in general was motivation for a short measurement campaign at Kilauea Volcano between February 29 and March 2. Although time was short, the goal of the campaign was to quantify SO_2 emissions at various positions on the volcano and determine whether or not BrO was detectable in the emission plumes, a possible indication of magma rising and degassing at shallow depth (see section 2.2.2). The results of the measurements will be described in the following sections.

6.2 Instrumentation and data retrieval

6.2.1 Instrument hardware

The measurements at Kilauea volcano were performed with two different instruments. The traverse measurements were conducted using an open Ocean Optics© HR2000 spectrometer connected by a 200 μm quartz fiber to a zenith looking telescope. The wavelength range of the spectrometer was 295 to 390 nm. The aperture of the telescope was 0.35°, and the field of view was circular. Unfortunately, real time GPS tracking was not available during the campaign, so GPS positions were measured at the start and end of each traverse, and the time was noted. The instrument integration time was kept constant at approximately 5 seconds during the individual traverses, but was adapted to the respective illumination conditions between traverses. The GPS position of each measurement was calculated using a linear interpolation of the vehicle track as well as traverse start and end times (used to calculate average speed). The spectrometer was read out by a laptop computer. Power was supplied by the battery of the vehicle.

For the scanning DOAS measurements conducted at Kilauea, a NOVAC mark II instrument was used. It was placed on a tripod at different measurement positions and configured to scan in a single measurement plane (flat scan). Inside the instrument, an Ocean Optics HR2000 spectrometer identical to the one used for the traverses was employed. The temperature of the spectrometer was regulated to 20°C for all measurements. Power was supplied by a car battery. The recorded spectra were stored on the internal flash memory and downloaded to a laptop PC at the end of each measurement.

6.2.2 Data retrieval techniques

SO_2 data retrieval

SO_2 was evaluated according to the "weak absorption" technique described in section 3.4.1. For each measurement spectrum, several fit windows were chosen, and a separate evaluation was performed in each of these. The final measurement result was obtained by choosing the fit window with the shortest wavelength that met the "weak absorption" criteria i.e. the SO_2 optical density was below 5 %. This criterion ensures that the optical path of the measured

scattered radiation is largely independent of wavelength (except at large distances from the plume, see section 8), and that the standard DOAS approach is applicable for retrieving the SO_2 slant column density.

In addition to the SO_2 absorption cross-section (*Bogumil et al. 2003*, 293 K), the cross-section of O_3 (*Voigt et al. 2001*) as well as a Ring spectrum and the logarithm of a Fraunhofer reference spectrum recorded outside the plume were fit to each measurement spectrum A shift of ±1 channel as well as a squeeze of ±5 % were allowed to compensate for a possible drift in the temperature of the optical bench of the spectrometer. All references were first aligned to the same spectral calibration using a measurement in which all substances were easily identifiable. Afterwards, the shift and squeeze was no longer applied to the individual references, but rather only applied to all references in the same manner.

BrO data retrieval

BrO was evaluated in the wavelength region between 332 and 353 nm. After a first evaluation did not reveal BrO, the signal-to-noise ratio of the scanning DOAS measurements was improved by co-adding the 50 spectra with the highest SO_2 optical densities to an average plume spectrum. Also, the 50 spectra with the lowest SO_2 optical density were summed up and used as the Fraunhofer reference. As each spectrum already contained 15 individual exposures, a total of 750 exposures were used in each case. The logarithm of the Fraunhofer reference, the absorption cross-sections of SO_2 (*Bogumil et al. 2003*), O_3 (*Voigt et al. 2001*), and BrO (*Wahner et al. 1988*), as well as a Ring spectrum and a 5^{th} order polynomial were then fitted to the average plume spectrum. A shift of ±1 channel as well as a squeeze of ±5 % were allowed to compensate for a possible drift in the temperature of the optical bench of the spectrometer. Again, the references were aligned using a spectrum, in which all species were identifiable (except BrO, which was never seen). From that point on, a possible shift and squeeze was performed on all references together. BrO was kept separate, and a larger shift was allowed (± 5 channels), as no alignment could be performed.

Although the signal-to-noise ratio was greatly improved, BrO was still not positively identified at any of the measurement positions. Therefore, the BrO detection limit was calculated at each site. To this extent, the BrO absorption cross-section was removed from the DOAS fit. The residual of the DOAS fit without BrO was then analyzed. An upper limit for the BrO column density of a particular measurement could be approximated by comparing the optical density of the noise in the fit residual with the calculated optical densities of a various amounts of BrO until the maximum optical density that could possibly be superimposed on the fit residual without being identified by the fit was determined. Examples for the determination of BrO upper limits are given in section 6.3.2.

6.3 Measurement results

6.3.1 SO_2 emission fluxes from Pu'u 'O'o and Halema'uma'u craters

Vehicle traverse measurements

On February 29, 2008, an estimate of SO_2 emissions originating from Pu'u 'O'o crater was obtained by means of a DOAS vehicle traverse along Trail of Craters Road. The plume was encountered at ground level (reduced visibility and acrid smell) in the vicinity of the 1969-1974 lava flows (see Fig. 6.1). *GDAS 2009* report a wind speed of 3.5 m/s and a wind direction of 30° azimuth. However, the position at which the center of the plume was found along Trail of Craters Road suggests a wind direction of approximately, 50°. The discrepancy is likely caused by uncertainties in the GDAS model data. As local topography is not included in the wind field model, wind data close to the ground can be inaccurate. A wind direction of 50° was therefore used for calculation of the plume integrated SO_2 amount X (see Fig. 6.2), and 4.77×10^{23} molec/cm were obtained using the traverse integration method described in section 3.3.3. Multiplication with the 3.5 m/s wind speed yields an SO_2 emission flux Φ of 18 kg(SO_2)/s or about 1500 t(SO_2)/d, which is in fair agreement with the range of fluxes measured by the USGS.

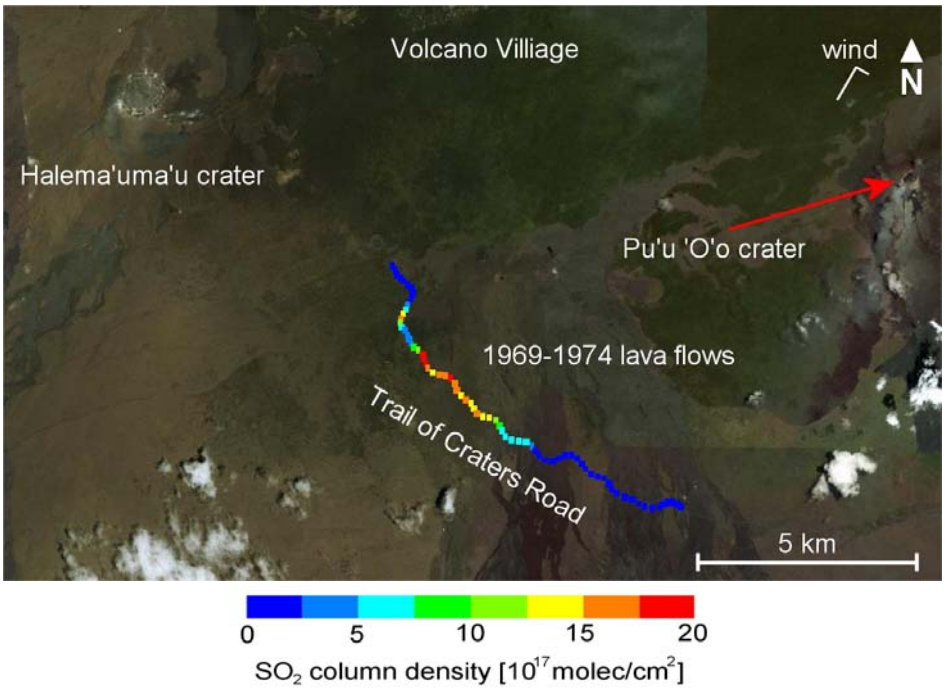

Fig. 6.1 – Results of the vehicle based DOAS traverse conducted on February 29, 2008 between 10:17 and 10:27 local time. The Pu'u 'o'O plume was intercepted in the vicinity of the 1969-1974 lava flows. Integration along the vehicle path and multiplication by the wind speed yields an SO_2 emission flux of 18 kg(SO_2)/s or 1500 t(SO_2)/d. Note that the plume was blown in a more westerly direction than shown on the satellite image. Imagery © 2009 DigitalGlobe & Google

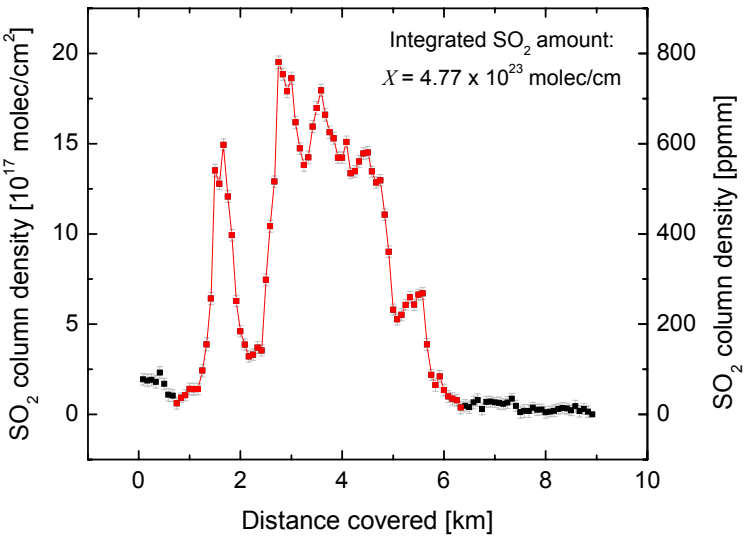

Fig. 6.2 – SO_2 column density measured along Trail of Craters Road on a traverse of the Pu'u 'O'o plume conducted March 2, 2008. The points used for integration of the plume SO_2 amount are highlighted in red, and integration yields $X = 4.77 \times 10^{23}$ molec/cm in the plume. By considering a wind speed of 3.5 m/s, the instantaneous SO_2 emission flux amounts to 18 kg(SO_2)/s or 1500 t(SO_2)/d.

On March 2, 2008, two mobile DOAS traverse measurements were conducted at Halema'uma'u crater. An active volcanic vent had opened on the western side of Halema'uma'u crater only days before (see Fig. 6.3), and the goal of the traverse measurements was to quantify the SO_2 emissions from the Kilauea summit area and in particular from this vent.

Fig. 6.3 – New volcanic vent on the western edge of Halema'uma'u Crater formed in February 2008, as seen from the south on March 2, 2008. This vent was responsible for a large portion of the measured SO_2 emissions originating in the Kilauea summit area between February 29 and March 2. Gas was also emitted along the northeastern crater rim.

Fig. 6.4 – Central part of Halema'uma'u Crater. Some degassing vents can be observed in the center of the crater area, but no degassing is seen on the eastern rim. This changed significantly when a new vent was formed on the lower eastern wall of the crater on March 12, 2008 doubling previous SO_2 emissions (*USGS 2008b*).

Fig. 6.5 shows a two dimensional plot of the measured SO_2 column densities along the path of the first plume traverse. The traverse began at the USGS Hawaiian Volcano Observatory / Jaggar Museum parking lot. Crater Rim Drive was followed into the Kilauea caldera, after which a northerly course was chosen to a position west of Halema'uma'u Crater (marked Scan Site 4 in Fig. 6.5) suitable for scanning DOAS measurements of the main vent emissions (see discussion below). The zenith-looking DOAS instrument measured peak SO_2 column densities west of the vent position, with values reaching 7.5×10^{18} molec/cm^2 or 3000 ppmm.

From the traverse measurements, the plume-integrated SO_2 amount X was calculated as described in section 3.3.3. The profile of the measured SO_2 columns along the traverse path is shown in Fig. 6.6. Elevated SO_2 column densities were encountered along a distance of about 2.5 km. The measured SO_2 column density did not drop to null upon arrival at the end of the traverse, indicating a steady background SO_2 load in the vicinity of the crater. This is likely a result of fumarolic activity in and around the summit region (compare Fig. 6.3 and Fig. 6.4). Integration over the points marked in red in Fig. 6.6 yields a total of plume-integrated SO_2 amount of $X = 3.39\times10^{23}$ molec/cm. Multiplication with the wind speed of 4 m/s (taken from *GDAS 2009*) then yields an instantaneous SO_2 emission flux of 14 kg(SO_2)/s or about 1200 t(SO_2)/d.

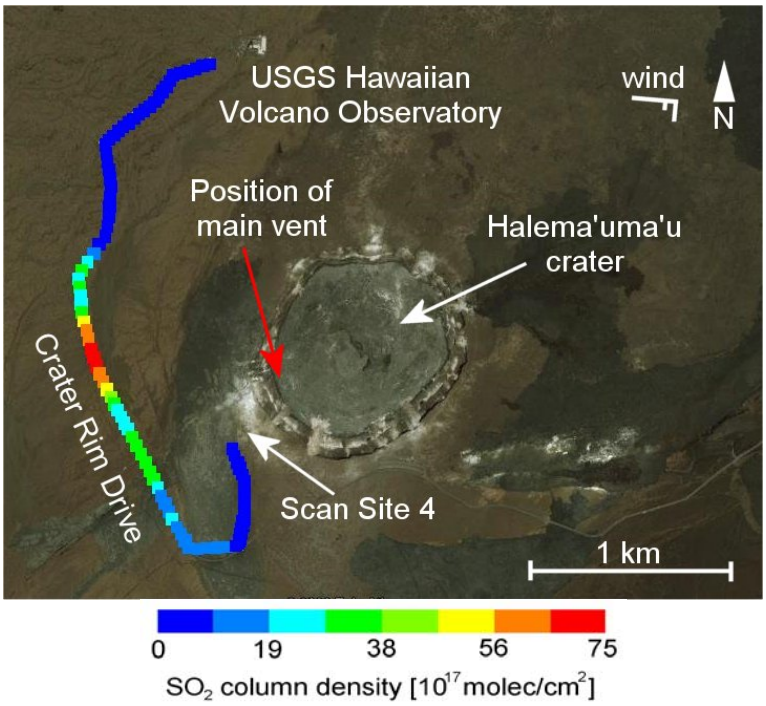

Fig. 6.5 – Results of the first Crater Rim Drive traverse conducted on March 2, 2008 between 11:20 and 11:30 local time. The wind direction was 100° at 4 m/s (*GDAS 2009*), pushing the emissions from the main vent to the west. The calculated SO_2 emission flux was 1200 t(SO_2)/d. Satellite imagery © 2009 DigitalGlobe & 2008 Google

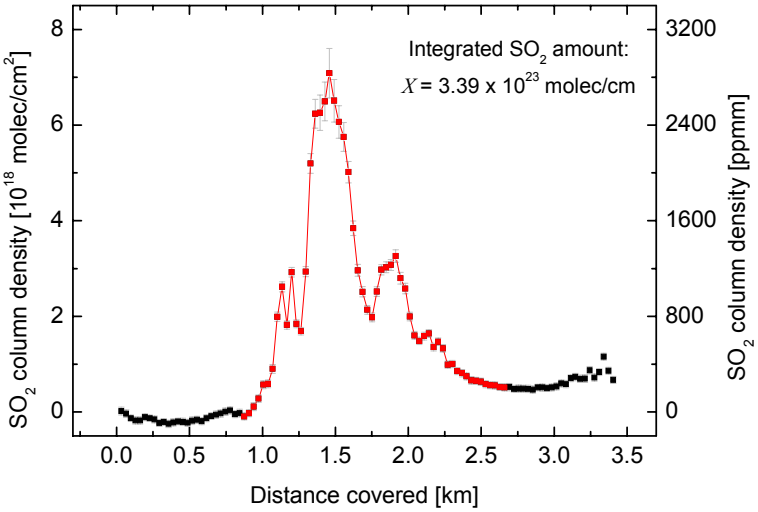

Fig. 6.6 – SO_2 column density measured along the first Crater Rim Driver traverse conducted March 2, 2008 from 11:20 to 11:30 local time. The points used for integration of the plume SO_2 amount are highlighted in red, and integration yields $X = 3.39\times10^{23}$ molec/cm in the plume. By considering the wind speed, the SO_2 emissions were calculated to have been 14 kg(SO_2)/s or 1200 t(SO_2)/d. Satellite imagery © 2009 DigitalGlobe & 2008 Google

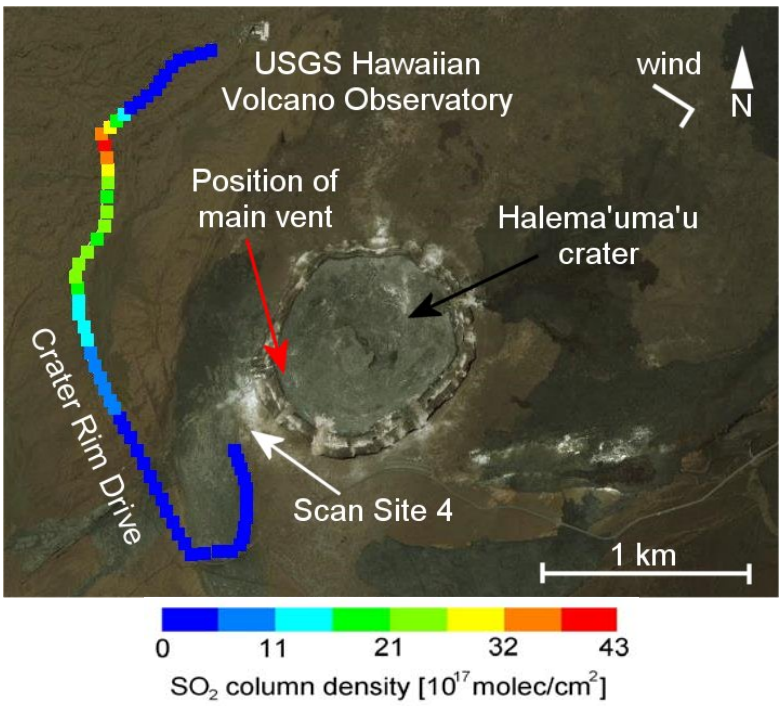

Fig. 6.7 – Results of the second Crater Rim Drive traverse conducted on March 2, 2008 between 13:27 and 13:36 local time. The wind direction shifted slightly to the south and was 120° at 4 m/s during the measurement (*GDAS 2009*). The calculated SO_2 emission flux was 11 kg(SO_2)/s. Satellite imagery © 2009 DigitalGlobe & 2008 Google

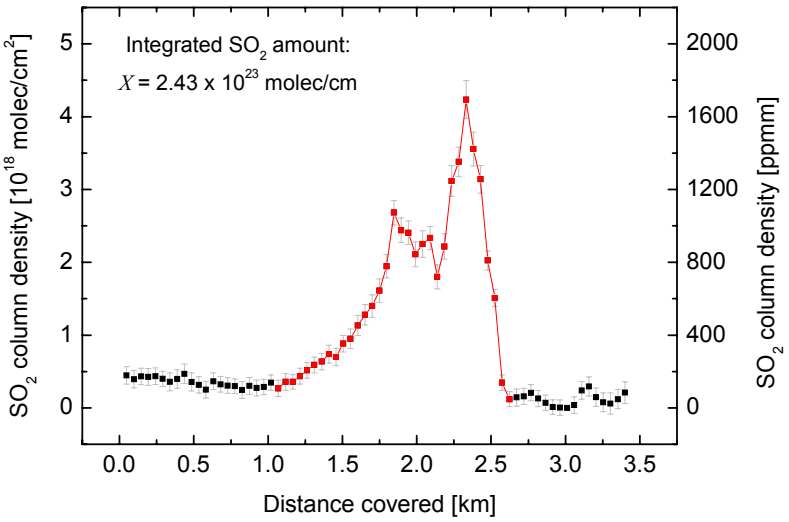

Fig. 6.8 - SO_2 column density measured along the second Crater Rim Driver traverse conducted March 2, 2008 from 13:27 to 13:36 local time. The points used for integration of the plume SO_2 amount are highlighted in red, and integration yields $X = 2.43 \times 10^{23}$ molec/cm in the plume. By considering the wind speed, the SO_2 emissions were calculated to have been 11 kg(SO_2)/s or about 950 t(SO_2)/d.

Fig. 6.7 displays the results of the second traverse of the Kilauea summit plume conducted on March 2, 2008 between 13:27 and 13:36 local time. At this time, the wind direction had shifted from 100° to 120°. The maximum column density was only about half of what was found during the previous traverses and was located farther north than before, in line with the shift in wind direction. Integration of the plume SO_2 amount X, as depicted in Fig. 6.8, yields 2.43×10^{23} molec/cm^2. By multiplying this with the wind speed, an SO_2 emission flux of 11 kg(SO_2)/s or about 950 t(SO_2)/d is obtained.

Both SO_2 flux measurements are slightly higher than the USGS observations mentioned in section 6.1. The reason for this discrepancy could be an inaccurate wind speed or wind direction. *GDAS 2009* model wind data does not take topography into account and therefore tends to be less accurate than measured wind conditions for low altitudes. Variability in the emission strength and turbulence in the atmosphere causing inhomogeneous plume dispersion may also play have played a role. Finally, the utilized weak absorption DOAS retrieval technique yields higher SO_2 column densities than when strong SO_2 absorption bands are evaluated without considering a possible wavelength dependency of the optical path (see section 3.4.1).

Scanning DOAS measurements

Next to the conducted DOAS vehicle traverses, a scanning DOAS instrument (see section 3.5.1 for a technical description) was set up at 5 different measurement locations between February 29 and March 2, 2008. The instrument was configured to subsequently measure the in various directions in a single plane between one horizon and the other. The step width was typically 4°, but certain viewing directions were omitted at times due to topography blocking the line of sight or in directions where no volcanic gas was present and which were used only for referencing purposes. The location and instrument orientation of the individual measurements is shown in Fig. 6.9 and summarized in Tab. 6.1.

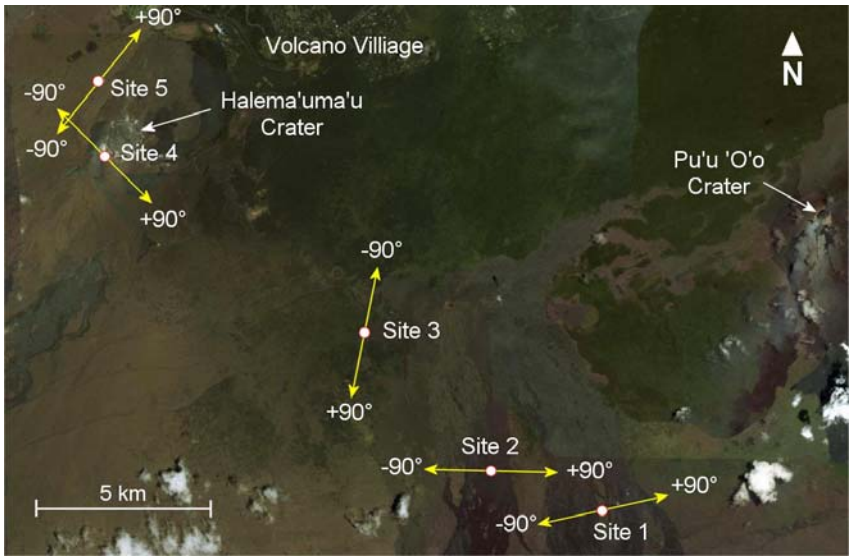

Fig. 6.9 – Positions of the scanning DOAS measurements conducted February 29 – March 2, 2008. The scanning zenith angles +90 and -90 indicate the orientation of the scanning DOAS instrument and correspond to the angles given in the abscissas of Fig. 6.10, Fig. 6.12, and Fig. 6.14. At sites 1-3, the Pu'u 'O'o plume was measured, while sites 4 and 5 aimed at quantifying emissions from Halema'um'u Crater. Satellite Imagery © 2009 DigitalGlobe & 2008 Google

Scan Site	Latitude [° North]	Longitude [° East]	Instr. Azimuth [-90° / +90°]	Measurement Date
Site 1	19.3174	-155.1626	260 / 80	Feb 29, 2008
Site 2	19.3273	-155.1912	273 / 93	Feb 29, 2008
Site 3	19.3606	-155.2232	10 / 190	Mar 1, 2008
Site 4	19.4027	-155.2885	13 / 193	Mar 2, 2008
Site 5	19.4200	-155.2895	312 / 132	Mar 2, 2008

Tab. 6.1 – Overview of scanning DOAS measurement locations. The measurement orientation is given by the instrument azimuth angle. The two values given refer to -90° and +90° scan zenith angle, which is referred to in Fig. 6.10, Fig. 6.12, and Fig. 6.14.

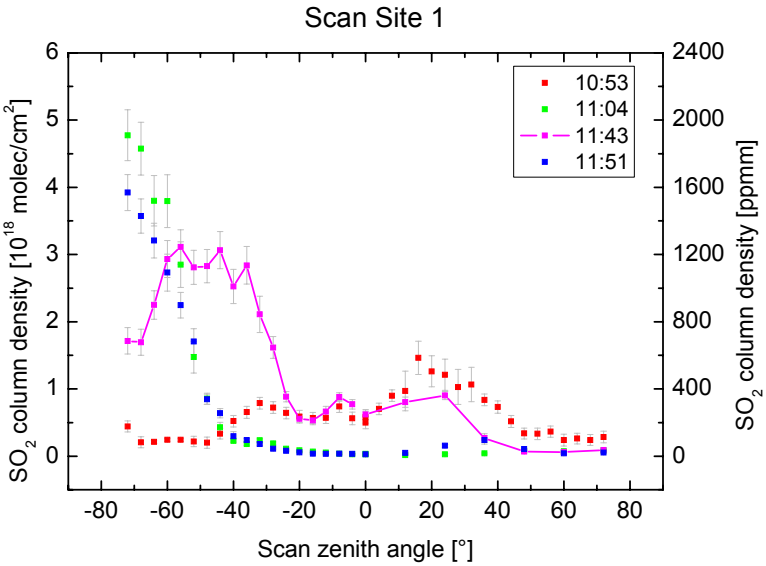

Fig. 6.10 – SO_2 column densities measured at scan site 1 on February 29, 2008. The scan conducted at 11:43 local time was integrated between -90° and 20°, yielding a plume-integrated SO_2 amount *X* of 3.4×10^{23} molec/cm, and an approximate emission flux of 16 kg(SO_2)/s or 1400 t(SO_2)/d from Pu'u 'O'o crater.

Fig. 6.10 shows the results of the scanning DOAS measurement of the Pu'u 'O'o plume conducted on February 29, 2008 at scan site 1 (see Fig. 6.9). Unfortunately, the topography at the site did not allow measurements at an angle more perpendicular to the plume. Therefore, the plume was located more than 5 km from the instrument (compare to Fig. 6.1) and was typically measured at angles very close to the horizon. A very rough estimate of SO_2 emission flux could be calculated from the scan collected at 11:43 local time (shown in magenta in Fig. 6.10), as the plume was blown somewhat closer to the instrument at this time, and the peak SO_2 values were measured approximately 40° above the horizon. If the plume center is assumed to have been 5 km from the instrument at this time, and the scanning plane intercepts the plume at an angle of $\gamma = 20°$, integration between -90° and -20° measurement zenith angle according to the radial integration method described in 3.3.2 yields a plume-integrated SO_2 amount X of about 3.4×10^{23} molec/cm. Multiplication with a wind speed of 4.5 m/s (*GDAS 2009*) yields an approximate emission flux of 16 kg(SO_2)/s or 1400 t(SO_2)/d. While in fair agreement with the DOAS traverse measurement conducted the same day (see Fig. 6.1 and Fig. 6.2), it should be noted that the flux value is very sensitive to the distance between instrument and plume, the uncertainty of which is considerable in this case.

The measurements conducted at scan site 2 could not be evaluated for SO_2 emission flux, as the plume was located too close to the horizon and was only a part of the plume cross-section was measured by the DOAS instrument. At site 3, a different situation was encountered on March 1, 2008. The instrument was set up downwind of the active Pu'u 'O'o vent. A photograph of the NOVAC scanning DOAS as well as a Hoffmann Messtechnik© Mini-DOAS instrument used for data comparison is shown in Fig. 6.11. The instrument orientation

was such that -90° scan zenith angle approximately correspond to the viewing direction of the photograph. At the horizon, a white, slightly condensing plume can be seen extending from the ground to several hundred meters altitude.

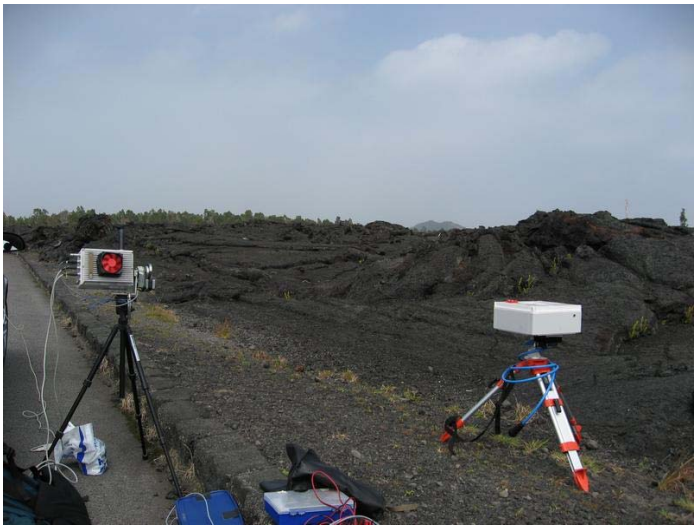

Fig. 6.11 - Scanning DOAS instruments set up at scan site 3 on March 1, 2008. The NOVAC instrument (right side) is set up next to a Mini-DOAS instrument from Hoffmann Messtechnik.© The orientation of the instruments was such that the -90° scan zenith angle pointed along the road in a northerly direction (10° azimuth), as is shown on the photograph. A white plume can be seen between the ground and the first several hundred meters altitude. Measurements revealed, however, that the plume must have extended past the instruments to the south as well.

In the measurements, however, a clear signal from a single plume near the horizon was not detected. Instead, SO_2 could be detected in all viewing directions, and while the maximum column densities were detected near the northern horizon, a positive signal was also detected facing south (see Fig. 6.12). A U-shaped progression was seen, with elevated SO_2 column densities at both horizons and a minimum around 20° scan zenith angle. Similar, albeit symmetric, shapes are typical for Multi-Axis-DOAS measurements of absorbers homogeneously distributed in the lower troposphere (see e.g. *Hönninger et al. 2004a*). Here, the asymmetric progression indicates a laterally inhomogeneous concentration of SO_2, as would be expected in the case of a propagating SO_2 plume. The 9 scans collected between 11:18 and 13:07 local time (shown in Fig. 6.12) all exhibit the same angular dependency, indicating that the geometry of the plume was fairly stable during the measurement time period.

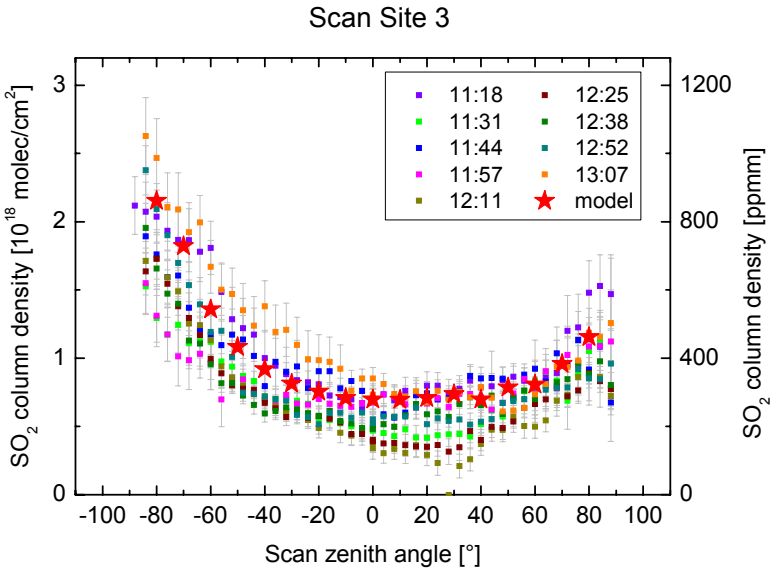

Fig. 6.12 – SO_2 column densities measured at scan site 3 on March 1, 2008. Also shown are the results of a model run with the radiative transfer model TRACY-II (red stars). While the measurements alone do not allow the calculation of an emission flux, the model results indicate an SO_2 emission flux of about 900 t(SO_2)/d.

While this single measurement alone cannot constrain the plume geometry very well, an exemplary model scenario can be set up to describe the measured SO_2 column density progression. The radiative transfer model TRACY-II (see section 8) was used to simulate a measurement under the conditions though to be responsible for the U-shaped measurement result. The model calculations were conducted at 330 nm, where the SO_2 optical density can be considered weak i.e. the optical path of radiation in the plume is not decisively determined by SO_2 absorption. Fig. 6.13 shows the model geometry. An infinitely long volcanic plume was assumed to be propagating along the ground and extend 500 m in height. At ground level, the plume was assumed to be 3.4 km wide, a value typical for Pu'u'O'o plumes at 12 km distance from the vent (compare satellite image in Fig. 6.9). The width was decreased by 200 m on each side for every 100 m altitude, a constraint chosen to match the grid size of the model. Inside the plume, an SO_2 concentration of 1.25×10^{13} molec/cm^3 was chosen, corresponding to an SO_2 mixing ratio of 500 ppb. A scattering aerosol (SSA = 1, g = 0.8) was assumed in line with the white appearance of the plume. The aerosol extinction coefficient was set to 0.5 km^{-1}, corresponding to an approximate visibility inside the plume of 8 km^{-1}. In the ambient atmosphere, the absorption of a typical O_3 and NO_2 profile were considered. The solar zenith angle was set to 30°, the approximate average solar zenith angle during the measurements. The solar azimuth angle was 170°. Further details of the radiative transfer model TRACY-II and additional parameters are described in chapter 8.

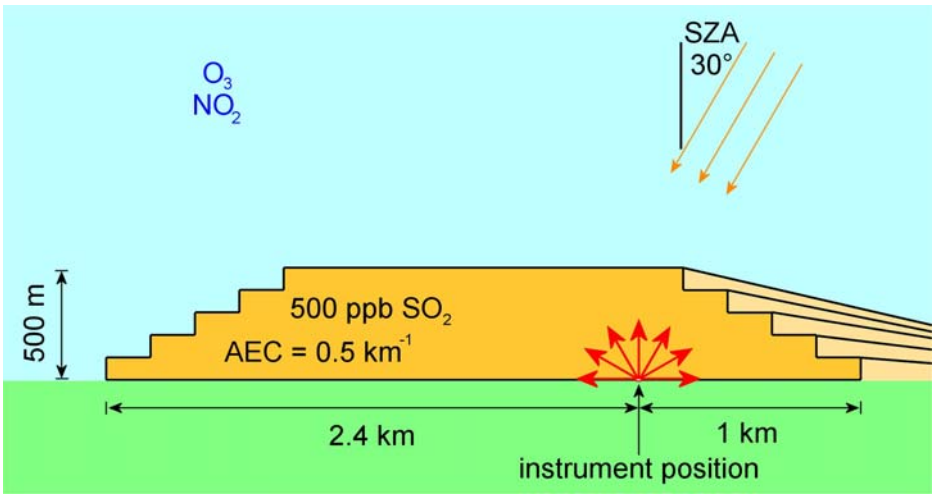

Fig. 6.13 – Model geometry used for simulating the site 3 scanning measurement. The scanning DOAS instrument is positioned inside a grounded plume 12 km east of Pu'u 'O'o. An SO_2 mixing ratio of 500 ppb and an aerosol extinction coefficient (AEC) of 0.5 km^{-1} were assumed. The simulated measurement results are plotted as red stars in Fig. 6.12.

In the described model scenario, an instrument was placed 1 km from the right edge of the plume (see Fig. 6.13). The slant column densities were simulated for various measurement angles between +90 and -90° scan zenith angle, and can be directly compared to the measurement results. The model results are shown as red stars in Fig. 6.12. They match the average of the measurement results well, indicating that the measurement geometry assumed in the model would in reality produce the same results that were obtained in the measurement. It should be noted, however, that the solution is not unique. A smaller plume highly concentrated in SO_2 could produce similar results. Because the emission flux results scale with the SO_2 concentration and with the cross-sectional area of the plume, they scale linearly with the plume height here. The 500 m assumed in this case are only an estimate, and an additional instrument viewing the plume from a position outside the SO_2 cloud would be necessary to better constrain the height.

While not directly possible from the measurement results, integrating the total SO_2 amount becomes a simple task for the simulated volcanic plume. The plume concentration of 1.25×10^{13} molec/cm^3 needs only be multiplied by the plume cross-sectional area of 1.3 km^2 yielding a total SO_2 amount of 1.6×10^{23} molec/cm. Furthermore taking into account the wind data (wind speed 6 m/s from 100° (*GDAS 2009*)) gives an SO_2 emissions estimate of 10 kg(SO_2)/s or about 900 t(SO_2)/d. This value corresponds to the average measured SO_2 emission flux between 11:18 and 13:07. Sensitivity studies showed that measured range corresponds to between 8 and 12 kg(SO_2)/s, or approximately 700 – 1000 t(SO_2)/d.

After the two described scanning measurements of the Pu'u'O'o SO_2 emission flux, a similar measurement was conducted at Halema'uma'u crater on March 2, 2008. The instrument was located at the site marked 4 in Fig. 6.9 and was aimed towards the emissions from the new active vent in the crater's western wall (-90° zenith). The results of the measurement are

shown in Fig. 6.14. The vent emissions are clearly visible on the horizon (-90° scan zenith angle), with SO_2 column densities reaching up to 2.5×10^{19} molec/cm^2. SO_2 levels above and to the south of the instrument (0-90° scan zenith angle) are variable, and only the first measurement conducted at 11:48 local time shows a steady baseline of close to zero. The observed variability is likely due to swirling emissions from fumaroles in and around Halema'uma'u crater and in close proximity to the instrument's position (see Fig. 6.3 and Fig. 6.4).

The emissions from the main vent were estimated by integrating the column densities measured during the scan conducted at 10:48 between -90° and -35° scan zenith angle. The total SO_2 amount X was 3.6×10^{23} molec/cm of plume, assuming the scanning plane intercepted the plume at $\gamma = 45°$ (see section 3.3.2 and compare Fig. 6.5 and Fig. 6.9) and that the distance between instrument and plume was about 500 m. Multiplication by a wind speed of 7 m/s (*GDAS 2009*) yields an SO_2 emission flux of 27 kg(SO_2)/s or 2300 t(SO_2)/d, a sizable amount considering the plume was originating from a fairly small vent. In fact, the SO_2 column densities measured at this vent were the highest ever measured in the course of this thesis. The plume diameter can be estimated to about 400 m, so the average SO_2 mixing ratio inside the plume was larger than 10 ppm, an order of magnitude above the health limit for momentary exposure given by the German Research Foundation (*DFG 2007*).

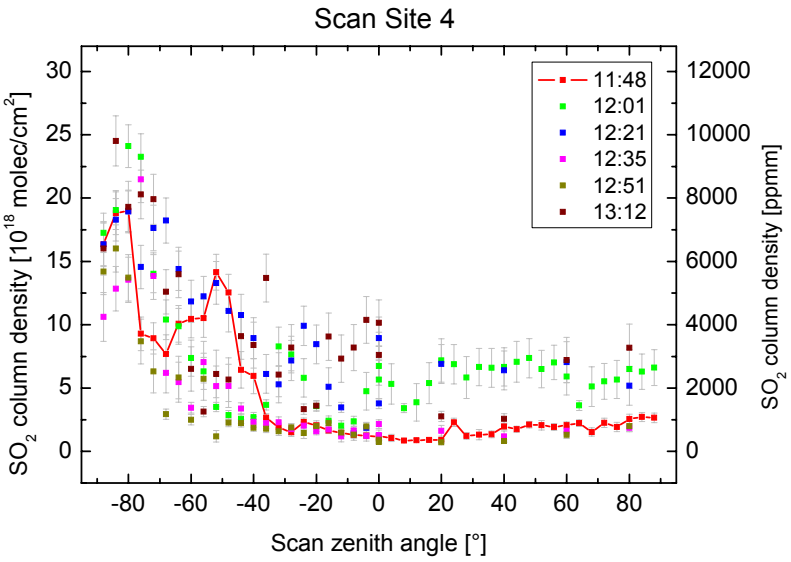

Fig. 6.14 – SO_2 column densities measured at scan site 4 on March 2, 2008. The measurement conducted at 11:48 almost exclusively captures the plume originating from the vent in the western wall of Halema'uma'u Crater (also see Fig. 6.7). The maximum measured SO_2 column density was see on the north-western horizon, with values exceeding 2×10^{19} molec/cm^2 or 8000 ppmm being the largest column densities ever measured in this thesis. Integration between -90 and -35° yields 3.6×10^{23} molec/cm inside the plume.

6.3.2 Attempted retrieval of BrO

Since its first detection in the plume of Soufrière Hills Volcano (Montserrat) by *Bobrowski et al. 2003*, BrO has been detected in volcanic emissions all over the world (see *Bobrowski and Platt 2007* and *von Glasow et al. 2008* for a summary). BrO is an oxidation product of HBr which, along with HCl and HF, is a primary volcanic emission species. Due to the higher solubility of halogens in magma as compared to sulfur, the halogen / sulfur ratio can sometimes be used as an indicator for the pressure (and therefore depth) of volcanic degassing. These and other aspects of interpreting halogen emissions are described in detail in chapter 2.

Next to measuring SO_2 emission fluxes, an attempt was made during the short measurement campaign in February/March 2008 to detect BrO in the plumes of Halema'uma'u and Pu'u'O'o. For both active vents, however, BrO could not be positively identified in the gas emissions. The BrO column densities were below the detection limit of the scanning DOAS instruments at all times. Therefore, upper limits were determined for the individual measurement positions.

BrO upper limit retrieval procedure

The strongest BrO absorption bands are located between 332 and 341 nm (*Wahner et al. 1988*). Therefore, this wavelength range was chosen for the attempt at detecting BrO. Also included in the DOAS fit window were wavelengths up to 353nm, where two additional BrO absorption bands are located. To increase the signal-to-noise ratio of the measurement, the Fraunhofer reference was compiled by co-adding the 50 spectra with the least amount of SO_2 measured at each location. Likewise, the so-called plume average spectrum was compiled by summing up the 50 spectra with the highest amount of SO_2 measured at each position. As each measurement spectrum was composed of 15 individual exposures, a total of 750 exposures were used in both cases. While no longer indicative of the viewing direction, the spectrum attained in this manner is characteristic of conditions inside the volcanic plume.

In the retrieval, the absorption cross-sections of SO_2 (*Bogumil et al. 2003*, 293 K) and O_3 (*Voigt et al. 2001*, 293 K) as well as the logarithm of the Fraunhofer reference, a Ring spectrum and a 5^{th} order polynomial were fit to the logarithm of the plume average spectrum (see section 6.2.2 for details the DOAS fitting process). While the cross-section of BrO (*Wahner et al. 1988*) was also included at first, it was later omitted because a positive identification of this species was not achieved. Instead, the fit residual of the fit without BrO was used as a measure of the maximum possible BrO optical density in the respective measurement. This technique is described in detail in section 3.1.6.

Measured BrO detection limits

As mentioned above, BrO was not detected at any of the measurement sites. However, the detection limit was determined for all five scanning DOAS measurement positions, and therefore an upper limit for the molecular ratio of BrO/SO_2 can be given for each site. Fig. 6.15 shows the results of the DOAS retrieval at measurement site 1, southwest of Pu'u 'O'o.

Because of the high signal to noise ratio, the DOAS model matches the measured optical density very well, and the two are indistinguishable in inset (a). The difference of the two is called the fit residual and shown in inset (d). Inset (b) depicts the fit of SO_2, which in this case is below detection limit in the given wavelength interval. The SO_2 evaluation of this spectrum took place between 319 and 327 nm according to the methods described in section 6.2.2, where the differential absorption of SO_2 is much stronger than above 330 nm. An SO_2 column density of 1.8×10^{18} was found. The Ring spectrum, shown in inset (c), matches the measured optical density well, indicating a successful correction of the Ring effect.

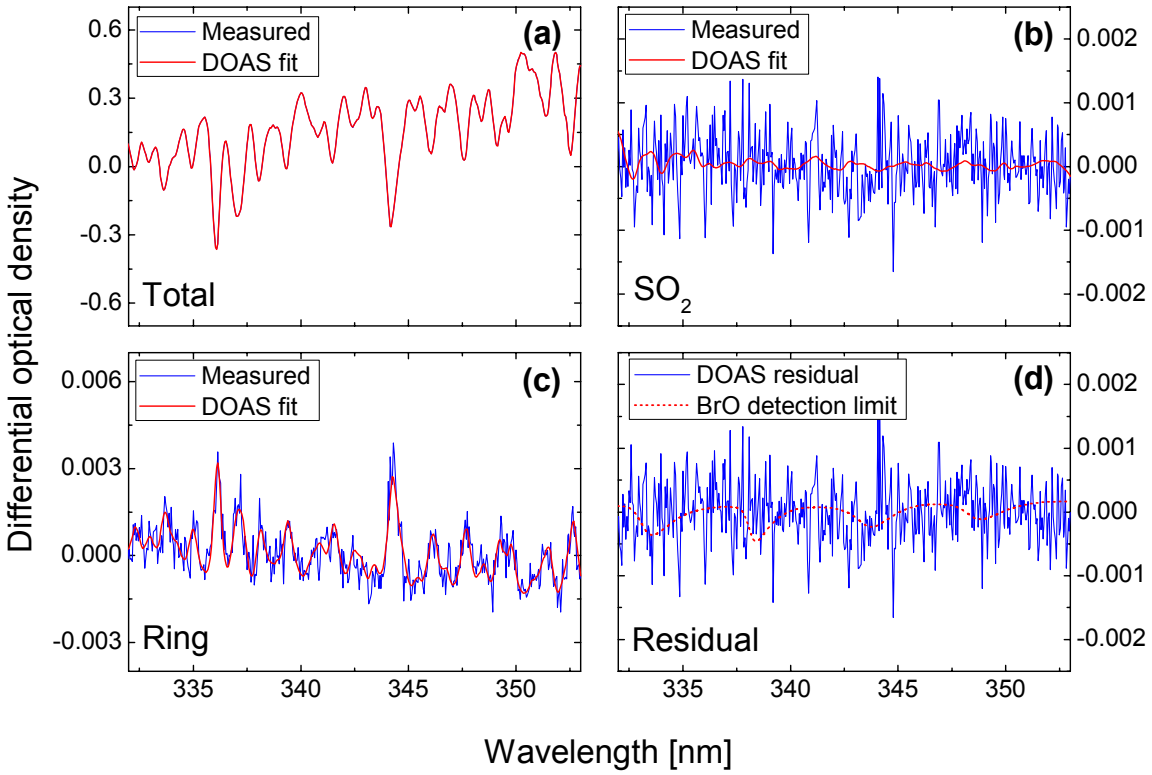

Fig. 6.15 - Retrieval of the BrO detection limit for Scan Site 1. The DOAS model and the measured optical density spectrum are indistinguishable (inset (a)). Inset (b) depicts the fit of SO_2, which in this case could not be identified in the BrO evaluation wavelength range between 332 and 353 nm. Inset (c) shows the contribution of the Ring correction to the DOAS model. The Ring spectrum was clearly identified and the effect was successfully corrected. In inset (d), the fit residual (difference between DOAS model and measurement spectrum) is shown. Also depicted (dotted red line) is the optical density of BrO assuming a column density of 5.4×10^{13} molec/cm^2. This value is deemed the detection limit, as larger optical densities would be clearly visible above the noise level in the fit residual.

The residual of the DOAS fit (shown in inset (d) of Fig. 6.15) is of a relatively high frequency nature, and is likely composed of pure noise and a slightly imperfect correction of the dark current. If BrO was present in the sampled air mass, differential absorption structures of the

species would be visible in the residual. Such structures could be superimposed with the noise of the measurement, but only up to a certain optical density. In this case, the BrO absorption structures were simulated for a fictitious BrO column density of 5.4×10^{13} molec/cm^2. They are shown as a dotted red line in Fig. 6.15, inset (d). It is deemed possible that differential absorption structures of this optical density are superimposed on the fit residual, but larger structures would surely be detected, and BrO could be identified. Therefore, 5.4×10^{13} molec/cm^2 is considered the detection limit of BrO for this measurement. As an SO_2 column density of 1.8×10^{18} molec/cm^2 was found (evaluated in the SO_2 retrieval range), an upper limit for the BrO/SO_2 ratio of 3×10^{-5} can be given.

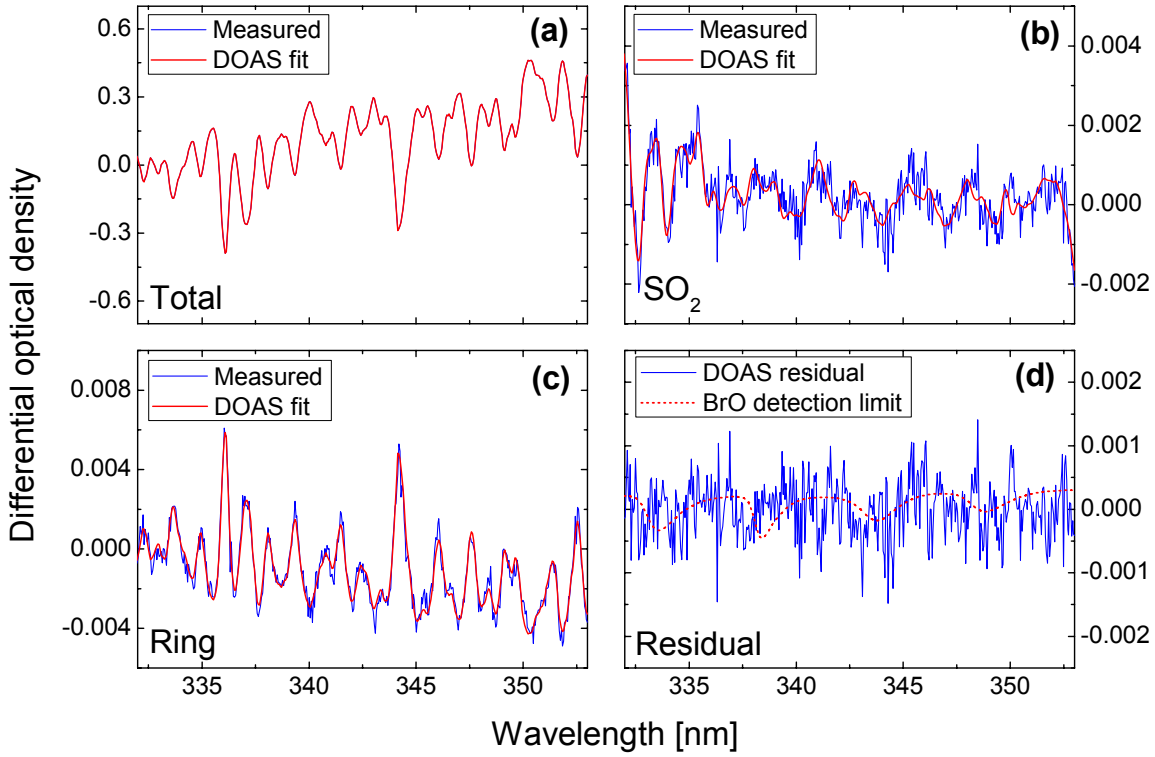

Fig. 6.16 – Retrieval of BrO detection limit for Scan Site 4. The DOAS model and the measured optical density spectrum are again indistinguishable (inset (a)). Inset (b) depicts the fit of SO2, the absorption of which is so strong in this case, that it can clearly be identified in the BrO evaluation range even though the absorption bands are more than an order of magnitude weaker than below 327 nm (*Bogumil et al. 2003*). Inset (c) shows the contribution of the Ring correction to the DOAS model. The Ring spectrum was clearly identified and the effect was successfully corrected. In inset (d), the fit residual (difference between DOAS model and measurement spectrum) is shown. Also depicted (dotted red line) is the optical density of BrO assuming a column density of 6.5×1013 molec/cm^2. This value is deemed the detection limit, as larger optical densities would be clearly visible above the noise level in the fit residual.

Fig. 6.16 depicts the analogous retrieval of the BrO detection limit at scan site 4, only 500 m from the main vent in Halema'uma'u Crater. In this case, the SO_2 column density was so high (also see section 6.3.1) that the differential absorption structures of SO_2 can clearly be seen in the BrO evaluation range (see Fig. 6.16, inset (b)), even though the SO_2 absorption bands are more than an order of magnitude weaker here than below 327 nm. The final SO_2 evaluation conducted between 325 and 332 nm according to the method described in section 6.2.2 yielded an SO_2 column density of 1.3×10^{19} molec/cm^2. The Ring effect was successfully corrected, as shown in inset (c). Note the optical density of the Ring structures is rather large in this case, probably a result of considerably different contributions of Rayleigh (and therefore Raman) and aerosol scattering between the Fraunhofer and plume spectra. Condensation in the plume (see Fig. 6.3) likely increased the relative contribution of aerosol scattering in the average plume spectrum. Inset (d) again shows the fit residual superimposed with a fictitious BrO absorption spectrum. In this case, a BrO column density of 6.5×10^{13} molec/cm^2 was simulated. Higher column densities would result in stronger absorption structures, which would be clearly visible above the measurement noise level. Therefore, 6.5×10^{13} molec/cm^2 is the BrO detection limit of the measurement. When compared to the SO_2 column density of the same measurement (1.3×10^{19} molec/cm^2), an upper limit for the BrO/SO_2 ratio of 5×10^{-6} is obtained.

In Tab. 6.2, the BrO detection limits are given for all 5 sites at which measurements were conducted between February 29 and March 2, 2008. Also given is the respective upper limit of the BrO/SO_2 molecular ratio for each site.

Date	Scan Site	Volcanic Vent	BrO Det. Lim. [molec/cm^2]	Max. BrO/SO_2 Molec. Ratio
Feb 29, 2008	1	Pu'u 'O'o	5.4×10^{13}	3×10^{-5}
Feb 29, 2008	2	Pu'u 'O'o	1.0×10^{14}	8×10^{-5}
Mar 1, 2008	3	Pu'u 'O'o	1.0×10^{14}	7×10^{-5}
Mar 2, 2008	4	Halema'uma'u	6.5×10^{13}	5×10^{-6}
Mar 2, 2008	5	Halema'uma'u	1.0×10^{14}	5×10^{-5}

Tab. 6.2 – Overview of BrO detection limits achieved with the scanning DOAS instrument and resulting upper limits for the BrO/SO_2 molecular ratio at the individual locations.

6.4 Conclusions

After the measurement campaign, activity at Kilauea continued to pick up. 1,500 t(SO_2)/d of SO_2 were determined to be emitted from Halema'uma'u on March 12, and by March 16, emission rates had reached 2,500 t(SO_2)/d, the highest seen since 1979. At 2:58 local time on March 19, an explosion occurred at Halema'uma'u crater, the first since 1924. Debris was scattered over an area of approximately 75 acres. A portion of Crater Rim Drive was covered, and Halema'uma'u overlook, located south of the crater, was damaged (see Fig. 6.17). No lava was erupted, but the largest ejected block was about 1 cubic meter in size and was likely propelled from the vent more than 70 m below the crater rim (*USGS 2008c*). While the measurements described above only represent a snapshot of SO_2 emission fluxes at a single point in time, the history of events leading to the explosion clearly shows how valuable the measurement of SO_2 emissions can be for risk assessment and eruption prediction at volcanoes. Due to their ability to measure the progression of SO_2 emissions over a long period of time, the USGS was well aware that the activity at Kilauea was exceptional and was prepared for an upcoming eruption.

Fig. 6.17 – Damage done to Halema'uma'u Overlook during the March 19, 2008 explosion at the summit of Kilauea Volcano (Hawaii). Impact craters of 30 cm blocks were abundant in the area, and the largest ejected block was 1 cubic meter in size. No fresh lava was erupted, and the erupted blocks are thought to have originated from the walls of Halema'uma'u Crater (*USGS 2008b*). (Photograph © *USGS 2008a*)

The SO_2 emissions measured at the Kilauea volcanic complex between February 29 and March 2, 2008 are in good agreement with those reported by *USGS 2008b*. While SO_2 emission fluxes measured at the Pu'u 'O'o vent were between 900 and 1500 t(SO_2)/d (fairly typical for this vent), the fluxes measured at Halema'uma'u (950 – 2300 t(SO_2)/d) were significantly elevated compared to typical values before December 2007 (150 – 200 t(SO_2)/d) (*USGS 2008b*). Tab. 6.3 gives an overview of all emissions measurements at the two volcanic

vents. Also given is the measurement method used to obtain the respective emission flux value.

BrO could not be detected either at Pu'u 'O'o or Halema'uma'u crater. Instead, only upper limits for the molecular ratio of BrO/SO_2 could be obtained. Tab. 6.4 gives an overview of the upper limits for this ratio, along with measurement time, distance between measurement position and plume, wind speed, and the atmospheric residence time of the plume at the point of measurement.

Date	Time [local]	Volcanic Vent	Measurement Type	SO_2 Emission Flux [$t(SO_2)/d$]
Feb 29, 2008	10:25	Pu'u 'O'o	Traverse	1500
Feb 29, 2008	11:43	Pu'u 'O'o	Scan	1400
Mar 1, 2008	11:18 – 13:07 (average)	Pu'u 'O'o	Scan + Model	900
Mar 2, 2008	11:25	Halema'uma'u	Traverse	1200
Mar 2, 2008	11:48	Halema'uma'u	Scan	2300
Mar 2, 2008	13:31	Halema'uma'u	Traverse	950

Tab. 6.3 – Summary of SO_2 emission fluxes measured during the measurement campaign from February 29 to March 2, 2008. Between 900 and 1500 and $t(SO_2)/d$ were observed at Pu'u 'O'o, and between 950 and 2300 $t(SO_2)/d$ were seen at Halema'uma'u. Both traverses as well as scanning measurements were conducted, and in one case radiative transfer modeling was performed to asses the emission flux.

Kern et al. 2008b showed that the BrO concentrations at Masaya volcano were strongly dependent on incident solar radiation, as BrO is photochemically formed from precursors (see chapter 7). While all scanning DOAS measurements were conducted close to local noon time, when incident solar radiation was highest, the meteorological conditions were not always ideal. While the mornings of February 29 and March 1st were more or less cloud-free, dark clouds and even some rain dominated the afternoons of March 1st and 2nd. Therefore, several of the measurements could be influenced by a lack of incident solar radiation necessary for the effective formation of BrO. Especially the measurements at Halema'uma'u Crater (all conducted March 2nd) are likely affected.

Date & Time [local]	Volcanic Vent	Distance to Vent [km]	Wind Speed [m/s]	Atmos. Res. Time [min]	Max. BrO/SO_2 Molec. Ratio
Feb 29, 2008 9:48 – 11:54	Pu'u 'O'o	9.9	4.5	37	3×10^{-5}
Feb 29, 2008 13:35 – 16:38	Pu'u 'O'o	11.2	5	37	8×10^{-5}
Mar 1, 2008 11:12 – 13:10	Pu'u 'O'o	12.6	6	35	7×10^{-5}
Mar 2, 2008 11:42 – 13:20	Halema'uma'u	0.5	4	2	5×10^{-6}
Mar 2, 2008 14:21 – 15:26	Halema'uma'u	1.5	3	8.3	5×10^{-5}

Tab. 6.4 – Overview of upper limits for the molecular ratio of BrO/SO_2 measured between February 29 and March 2, 2008. Also shown is the distance between the measurement point and the respective volcanic vent, the wind speed, and the resulting atmospheric residence time of the plume at the point of measurement.

BrO is not thought to be directly emitted from volcanoes in significant quantity, as was shown by *Kern et al. 2008b* and is described in section 7. Instead, it is likely a product of an autocatalytic reaction cycle converting HBr in the aerosol phase to gaseous BrO (see section 7). Aside from incident solar radiation, the mixing of atmospheric O_3 into the volcanic plume is also necessary for an effective conversion. *Bobrowski et al. 2007* compared measurements conducted at Mt. Etna in 2004 and 2005 with the results of the MISTRA chemistry model (see *von Glasow et al. 2002b, von Glasow et al. 2002a, von Glasow and Crutzen 2004*) which was set up to model the "bromine explosion" occurring in the volcanic plume. While the range of measurements was somewhat higher than the model could explain, an increase in BrO/SO_2 ratio with time was found both in the measurements and in the model results.

To put the upper limits for the BrO/SO_2 ratios measured at Kilauea in context, they are plotted in Fig. 6.18 together with the Mt. Etna measurements and model results. The upper limits retrieved at Pu'u 'O'o are clearly below the range of measurements seen at Mt. Etna. However, they are still consistent with the range of BrO/SO_2 ratios predicted by the MISTRA model for different initial conditions in the "effective source region" of the volcanic vent (see *Bobrowski et al. 2007*). Therefore, while it is unlikely that Pu'u 'O'o is as strong a source of halogen oxides as Mt. Etna, further measurements conducted at high atmospheric residence times and high incident solar radiation levels might still reveal BrO in the emission plume.

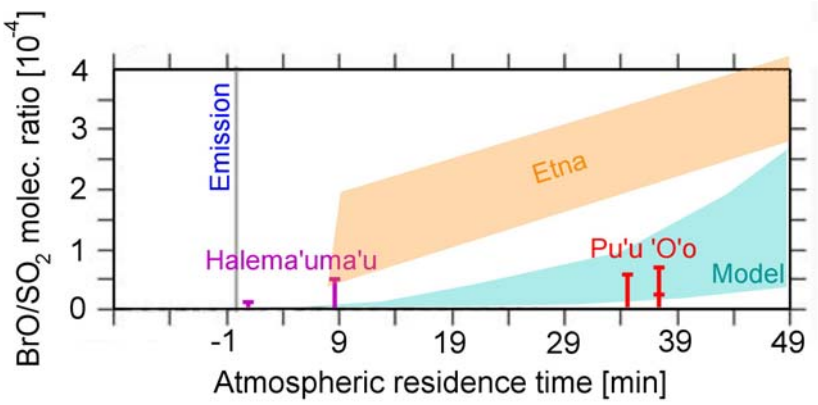

Fig. 6.18 – Comparison of the measured upper limits for the BrO/SO_2 ratio at Kilauea with previous measurements at Mt. Etna as well as results of the MISTRA chemistry model (both from *Bobrowski et al. 2007*). The upper limits measured at Kilauea fall below BrO/SO_2 ratios measured at Mt. Etna 2004 – 2005, but are still consistent with the range of model results obtained for different initial conditions in the "effective source region" of the volcanic vent. See *Bobrowski et al. 2007* for details.

For Halema'uma'u, the situation is not well constrained. The conducted measurements were both performed at relatively close proximity to the emission vent, therefore possibly not allowing enough time for the conversion of HBr into detectable amounts of BrO. In addition, an increasingly dark cloud cover is likely to have significantly reduced the incident solar irradiance in the afternoon of March 2nd. Therefore, further measurements are also necessary at this vent to gain insight into halogen chemistry in the emitted gas.

7 New insights into halogen chemistry in volcanic plumes

7.1 Introduction

In recent years, the chemistry of volcanic plumes has gained in importance. From the standpoint of volcanology, a detailed understanding of the speciation of gases emitted from a volcano at a given time allows insight into the processes responsible for the degassing of volatile species. By creating a comprehensive model of the volcanic degassing processes and using the measured gas composition as an input parameter, much can be learned about the activity taking place kilometres below the Earth's surface in volcanic plumbing systems (*Burton et al. 2007a*, see chapter 2.2). In addition, volcanic emissions measurements today can provide an independent parameter for volcanic risk assessment and eruption prediction (*Aiuppa et al. 2007b*). On the other hand, continuous degassing from volcanoes also has significant atmospheric impacts. Large amounts of SO_2 are emitted into the atmosphere from volcanoes, providing a significant source for atmospheric acidity in some parts of the world (see section 2.1 and e.g. *Arndt et al. 1997*, *Graf et al. 1998*, *Halmer et al. 2002*).

Recently, increasing attention has been paid to the chemistry of halogen species in volcanic plumes, thanks to the rapid development of ground-based techniques such as DOAS. Whilst the emission speciation of halogen compounds can be used to gain insight into volcanic systems, halogens are also of special interest from an atmospheric standpoint, as they are involved in many reaction cycles that can influence the oxidative capacity of the atmosphere by impacting upon the main oxidants O_3 and the OH radical, as well as the O_3 precursors NO and NO_2 (e.g. *Platt and Hönninger 2003*). In 2002, *Bobrowski et al. 2003* for the first time detected bromine monoxide (BrO) in a volcanic plume at Soufrière Hills volcano (Montserrat). Since then, it has been measured at many volcanoes worldwide and the emission of the reactive halogen species BrO, ClO and OClO has been widely discussed (*Gerlach*

2004, Martin et al. 2006, Oppenheimer et al. 2006b, Bobrowski and Platt 2007, Bobrowski et al. 2007).

Whilst these studies have considerably advanced our knowledge of the origin and fate of halogens in volcanic plumes, several important questions remain unanswered. It has been suspected for some time that BrO is not a primary product emitted from volcanoes, but rather that it is mainly formed by the reaction of magmatic gases with atmospheric components mixed into the plume (*Bobrowski et al. 2003, Gerlach 2004, Martin et al. 2006, Oppenheimer et al. 2006b*). Here the oxidation of HBr in the plume, which in turn leads to enhanced levels of reactive Br radicals as well as the photochemically active precursors Br_2 and BrCl seems to play a prominent role. Recent model results (*Bobrowski et al. 2007*) suggest that the peak in the BrO/SO_2 ratio may occur 2 to 3 hours after emission from the crater. Also, the role of the chlorine oxides ClO and OClO in volcanic plume chemistry is not well understood to date. While recent passive DOAS measurements have detected ClO and OClO at various volcanoes (*Bobrowski 2005, Lee et al. 2005, Bobrowski et al. 2007*), model predictions by *Bobrowski et al. 2007* could not reproduce these measurements.

The active Long Path DOAS (LP-DOAS) technique has led to the discovery and investigation of tropospheric halogen oxides in many different settings. Past deployment sites include the marine boundary layer (e.g. *Alicke et al. 1999, Allan et al. 2001, Saiz-Lopez and Plane 2004, Saiz-Lopez et al. 2004*), the vicinity of salt lakes (e.g. *Hebestreit et al. 1999, Stutz et al. 2002*), and polar areas (e.g. *Hausmann and Platt 1994, Tuckermann et al. 1997, Hönninger et al. 2004b, Saiz-Lopez et al. 2007*). Application of LP-DOAS to volcanic plume measurements has the potential to help resolving some of the open questions in the halogen chemistry in these environments. In particular, the extended wavelength range of the LP-DOAS system allows determination of ClO at much lower concentration levels than previously achieved. Night-time LP-DOAS measurements are also permitted, and can be used to investigate BrO formation in volcanic plumes in the absence of solar radiation and therefore without the influence of photochemical reactions. The LP-DOAS measurement principle is described in detail in section 3.1.

This study represents the first successful deployment of LP-DOAS at a volcanic site. To make this possible, a rugged, lightweight instrument was specifically designed for use in remote areas. Measurement concepts for the application of LP-DOAS instruments to volcanic gas emissions are discussed in section 3.2, and technical details of the LP-DOAS instrument designed specifically for this application and used in this study are given in section 3.5.2. Due to the relatively easy accessibility of the crater area, Masaya volcano was chosen as the first study site. Later, measurements with a completely mobile, LED-driven LP-DOAS instrument were conducted on Mt. Etna. The results of both studies are described in this chapter.

7.2 Masaya volcano (Nicaragua) - Experimental methods and study area

7.2.1 Experimental setup

In this first study, the Differential Optical Absorption Spectroscopy (DOAS) technique (*Platt 1994, Platt and Stutz 2008*) was applied to quantify several species in the plume of Masaya volcano. While the main emphasis of this study lies on the measurement of halogens in the early plume using active Long Path DOAS (LP-DOAS), passive Scanning DOAS measurements were conducted simultaneously to characterize the volcanic emission flux during the measurement time period.

Active Long Path DOAS instrument

An LP-DOAS instrument was used to measure the plume composition at Masaya volcano, Nicaragua during an intensive field campaign taking place from April 14 to April 26, 2007. The LP-DOAS instrument uses an artificial light source, in this case a 450 W xenon arc lamp, to measure the characteristic absorption features of gaseous species inside the volcanic plume. Radiation from the light source is coupled into a quartz fibre, the other end of which is positioned in the focal point of a telescope (f = 60cm, d = 20 cm) which then emits a nearly parallel beam of light. This beam passes the volcanic plume and is reflected back to the instrument by a 30 cm diameter array of 10 retro reflector prisms positioned on the opposite side of the plume. The returning light, which has now passed through the plume twice, is collected by the same telescope and spectrally analysed. In this study, an Ocean Optics QE65000 spectrometer with a wavelength range of 275 – 360 nm and a spectral resolution of 0.4 nm was employed. The spectrometer optical bench temperature was stabilized to 15°C with a thermoelectric (Peltier) temperature controller in order to minimize fluctuations in the optical alignment during the measurements. Details of the measurement setup are given in section 3.5.2.

Advantages of active DOAS measurements

Unlike passive DOAS instruments, active LP-DOAS measurements yield the column densities of the different absorbers along a fixed light path, and therefore it is not easily possible to determine a cross-section of the plume. Therefore, such instruments are not well suited for quantifying volcanic fluxes, as can be done with passive DOAS instruments. However active instruments do have a number of advantages. The most obvious benefit is the ability to measure at night. As halogen chemistry in volcanic plumes is thought to greatly depend on photolytic reactions, night-time measurements can give insight into the conditions in the absence of solar radiation, and interesting results were achieved in this regard (see sections 3.3. and 4).

Another advantage is that one is not limited to the spectral wavelengths available in the solar spectrum. Instead, wavelengths in the deeper UV below 300 nm can also be used. In the past,

this has allowed the spectroscopic measurement of H_2S (*O'Dwyer et al. 2003*), and in this case enables a much higher sensitivity for ClO than is attainable with passive instruments. The strongest structures in the ClO differential absorption cross-section are found below 290 nm, in a wavelength range in which no solar radiation reaches the earth's surface (see Fig. 7.6). The strongest absorption band above 300 nm which can barely be detected with a passive instrument is about 6 times weaker than the structures below 287 nm. The next ClO band at 308 nm, also used in the above studies, is more than an order of magnitude weaker. Also, the strongest structures in the SO_2 absorption cross-section, which have a similar shape and frequency as the ClO absorption structures, are also located around 300 nm and therefore can easily interfere with ClO evaluations. In the wavelength range below 285 nm used in this study, the SO_2 absorption bands are a factor of 3 weaker than at 300 nm (also shown in Fig. 7.6).

A third advantage of the active technique is that the light path is clearly defined, and therefore is exactly identical for all wavelengths. This can be of importance when studying different species with absorption structures in different wavelength ranges. Recently, *Mori et al. 2006* observed the effect of UV scattering on the SO_2 column densities measured by passive DOAS instruments and found a strong dependency on the distance of the instrument to the plume as well as on the wavelength chosen for the DOAS evaluation. Passive instruments positioned far from the plume may substantially underestimate the SO_2 column density at low wavelengths due to light entering the instrument's field of view between the instrument and the plume. This light has not passed through the plume. Therefore the fraction of the measured signal originating from such light paths does not contain the absorption structures of species found in the plume and effectively "dilutes" the retrieved trace gas column density. Due to the inherently well defined and known light path of the active instrument used in this study, the dilution effect will not influence the results presented here, but may well have influenced the results of earlier passive measurements used for comparison, especially when SO_2 was evaluated at wavelengths below 310 nm.

Passive Scanning DOAS instruments

Masaya is incorporated in the Network for Observation of Volcanic and Atmospheric Change (see section 5.1 and *NOVAC 2005*). The NOVAC project encompasses a global network of stations to monitor volcanic gas emissions using passive multi-axis scanning DOAS instruments. Scanning DOAS has become a standard measurement technique for the monitoring of volcanic emissions (e.g. *McGonigle et al. 2002, Edmonds et al. 2003a, Galle et al. 2003, Bobrowski 2005*). During the intensive LP-DOAS field campaign, passive DOAS instruments were used to determine the SO_2 emission flux. Two scanning DOAS instruments were permanently installed in the caldera of Masaya, 1.7 km west and 1.3 km southwest of the active Santiago crater (see Fig. 7.1). These positions are downwind of the volcano under the predominant wind direction and chosen such that both instruments can see the plume during most of the time. The NOVAC instruments automatically scan a field of view of 180° in 51 steps of 3.6° each, collecting scattered UV light by means of a small telescope. The light is then transferred into an Ocean Optics S2000 spectrometer with wavelength range of 275 –

430 nm and optical resolution ~0.6 nm for spectral analysis. An image of the NOVAC site Caracol is shown in Fig. 7.2. For more details about the employed instruments and spectral evaluation, see section 3.5.1 and *Galle et al. 2009, Johansson 2009a, Johansson et al. 2009b*.

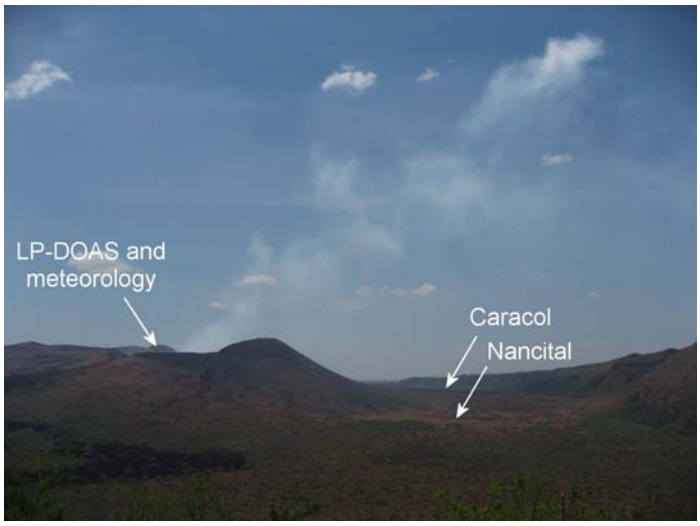

Fig. 7.1 – Relative positions of the Active LP-DOAS and NOVAC instruments (marked Caracol and Nancital) at Masaya volcano (Nicaragua). While the LP-DOAS measurements were conducted at the crater rim, the scanning DOAS instruments were permanently installed in the greater caldera, southwest and typically downwind of the active Santiago crater.

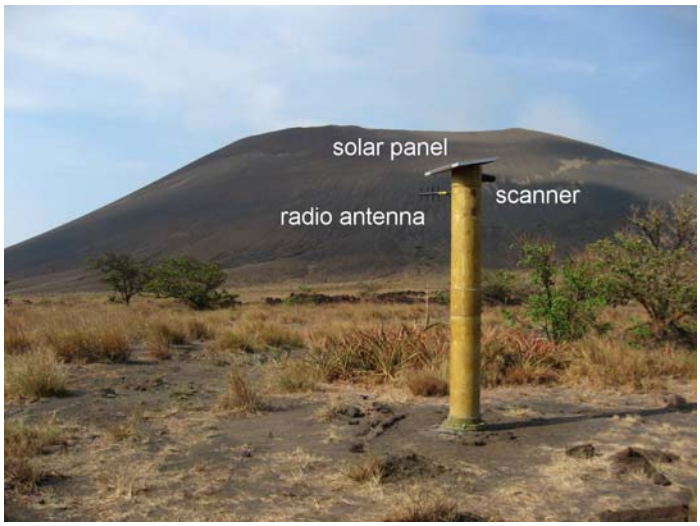

Fig. 7.2 – Image of the NOVAC scanning DOAS site Caracol (11.9766N, 86.1781W). The passive DOAS instrument is permanently installed inside the large, brown post made of synthetic resin to withstand corrosive volcanic gases. The scanner protrudes from the right side of the post. The instrument is powered by a solar panel, and an antenna is used to sends the data to the INETER[21] observatory in Managua via radio modem (see section 3.5.1 for details).

[21] Instituto Nicaragüense de Estudios Territoriales

7.2.2 Measurement location

Masaya volcano is situated in western Nicaragua, about 20 km south of the capital city of Managua. It is one of the most active volcanoes in Nicaragua, steadily degassing hundreds of tons of SO_2 every day (e.g. *Rymer et al. 1998, Delmelle et al. 1999*). Masaya is a large basaltic shield volcano, composed of a nested set of calderas and craters (*Rymer et al. 1998*). Masaya caldera, approximately 6×11 km in size, was formed 2500 years ago by an 8 km^3 basaltic ignimbrite eruption (*Williams 1983*). Inside the caldera, several cones have grown and now host the pit craters of Masaya, Nindiri, Santiago and San Pedro (see Fig. 7.3). The currently active Santiago pit crater was formed in 1858-1859 (*McBirney 1956*).

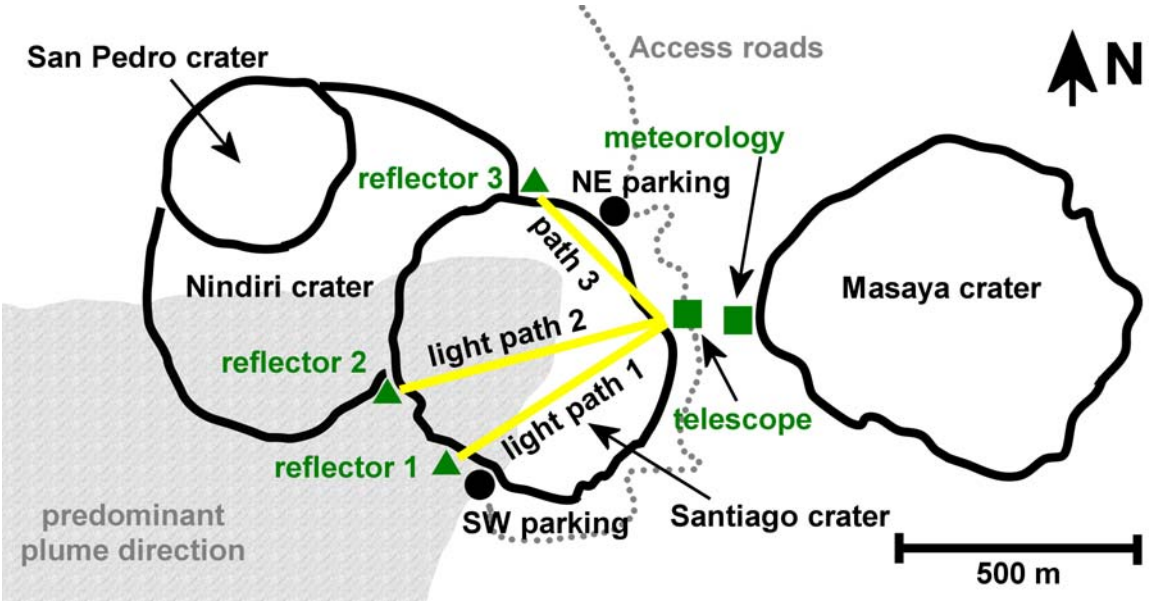

Fig. 7.3 – Measurement setup used for the active Long Path DOAS measurements at Masaya volcano, Nicaragua in April 2007. Retro reflector positions are marked by triangles. The total light paths (i.e. twice the distance between reflector and telescope) were 1120, 1100, and 808 m, respectively. A meteorological station was set up approximately 100 m east of the telescope, on the rim of Masaya crater. The predominant wind direction was east, so the plume was usually blown towards the west, away from the telescope.

The LP-DOAS measurements described here were conducted from April 14 to April 26, 2007 at the active Santiago crater of Masaya volcano. During the measurements, the telescope was always stationed at a small hut on the eastern side of the crater called “wind’s lookout” (see Fig. 7.4). However, three separate light paths were used, as shown in Fig. 7.3. The distances between the telescope and the reflectors were 560, 550, and 404 m, respectively, resulting in total optical path lengths of 1120, 1100 and 808 m. One retro reflector was placed just west of the south-west parking lot, the second one was located on the edge of Nindiri crater, while the third reflector was situated west of the north-east parking lot.

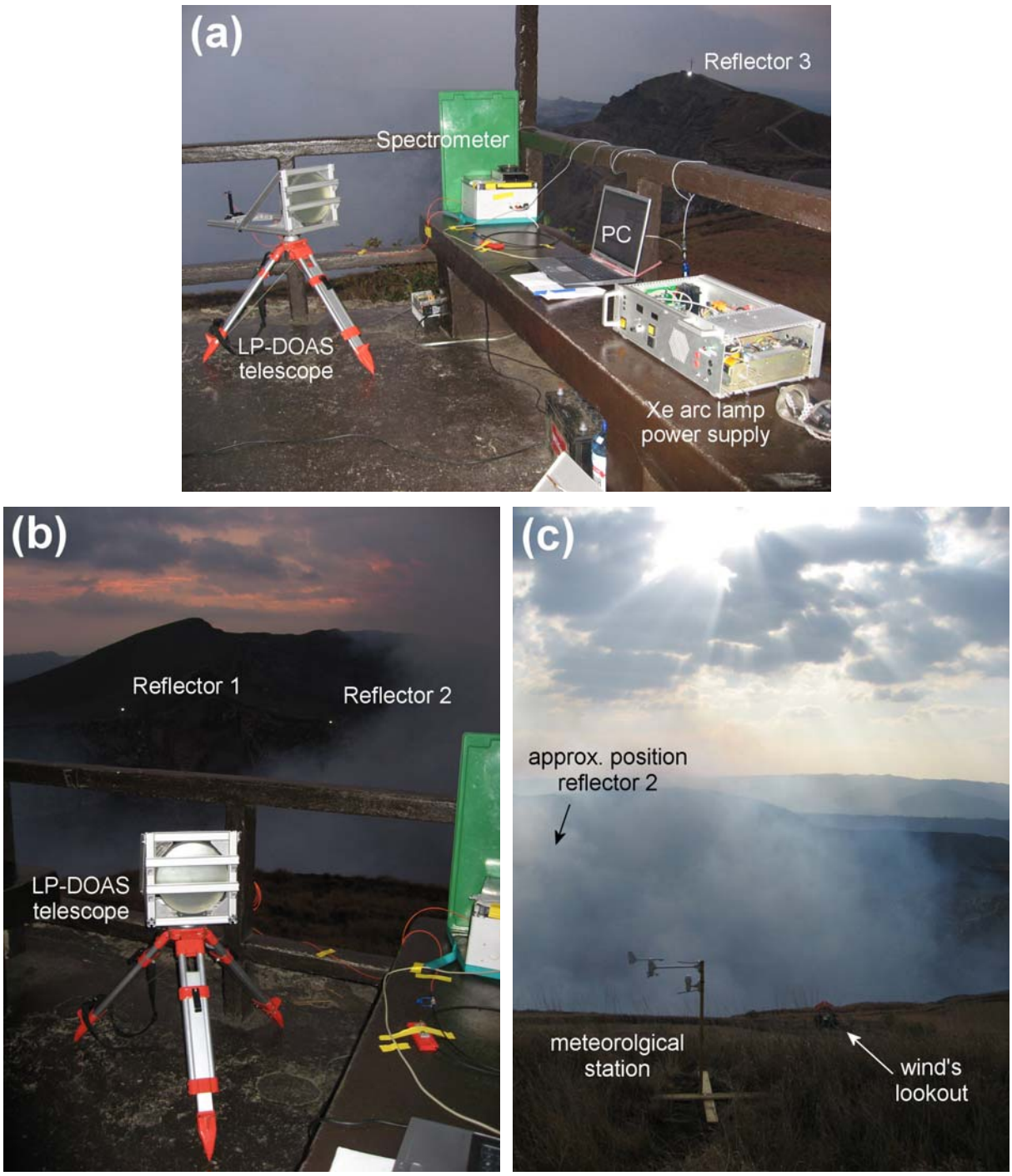

Fig. 7.4 – Images of the LP-DOAS measurement setup at Masaya volcano in April, 2007. The LP-DOAS telescope was located in a small hut called "wind's lookout", located on the rim of the actively degassing Santiago crater (see inset (c)). Inset (a) shows the LP-DOAS setup. A xenon arc lamp (not shown) is coupled into the telescope using a fiber bundle. Here, the telescope is aimed at reflector 1 (shown in inset (b)). The spectrometer was located in the temperature-stabilized housing shown in front of the green sunshield. A laptop PC was used to control the measurement and record data. The power supply for the xenon arc lamp was opened for better ventilation. As images (a) and (b) were taken by flash photography, the retro reflector arrays are visible in the background.

During the measurement time period, a mobile meteorological station was installed on the rim of Masaya crater, the highest point in the proximity of the telescope (see Fig. 7.4 (c)). As is shown in Fig. 7.5, the predominant wind direction was from the east, with wind speeds ranging from 0 to 15 m/s. Therefore, the plume was usually blown towards the west, away from the sensitive telescope and spectrometric instrumentation.

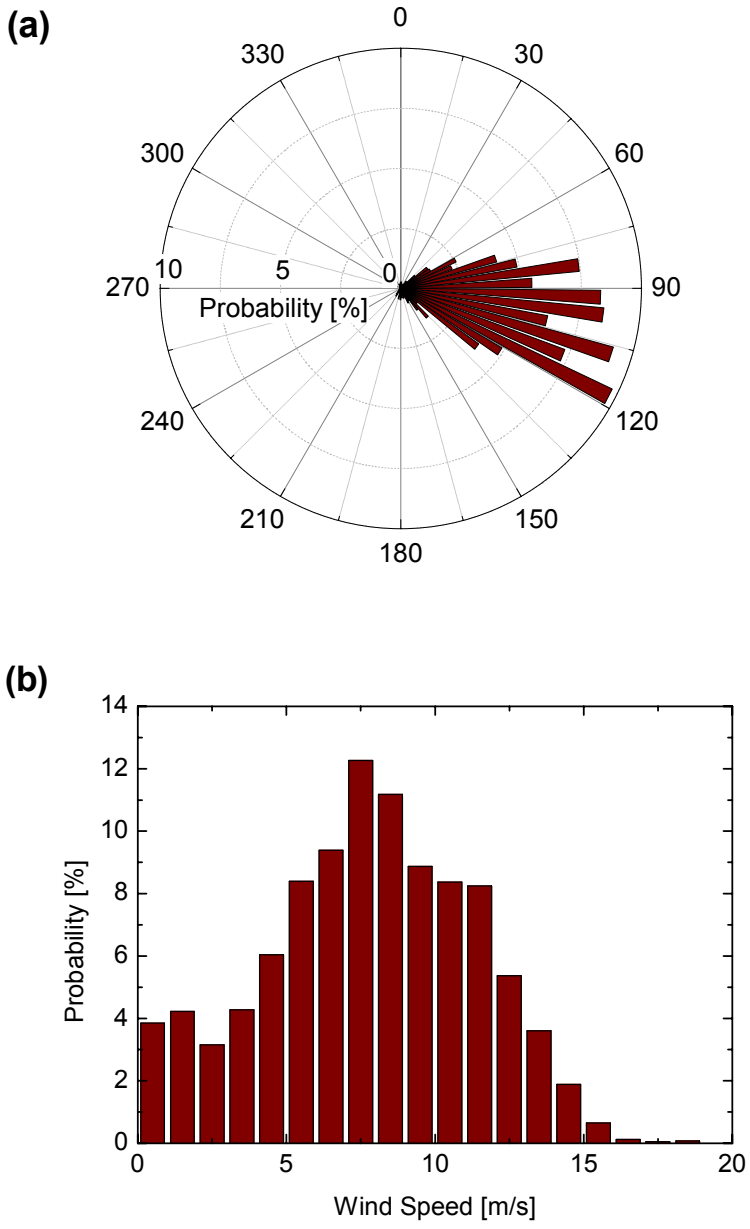

Fig. 7.5 – Average wind direction (a) and wind speed (b) measured by the mobile meteorological station on the rim of the Masaya crater between April 17 and April 26, 2007.

Using this measurement geometry, it was at most times possible to align a light path passing through the centre of the plume, or to choose one running through only the edge of the plume. This was very useful, as it was often not possible to penetrate the centre of the plume due to

high particle load from condensation of water vapour and strong SO_2 absorption, and most measurements were performed on light path 1, typically on the side of the plume. Light path 3 was often outside the plume and was mainly used for background O_3 measurements. (see section 7.3.2.)

7.2.3 Data evaluation

The recorded spectra were all analysed using the same general procedure, which is generally described in chapter 3. First, each spectrum was corrected for electronic offset and dark current signal. The logarithm was then taken of each measurement spectrum to obtain the optical density. Depending on the trace gas of interest, one of four wavelength regions (see below) was then chosen in which a DOAS fit was performed. All relevant trace gases absorbing in the selected wavelength region were included in the DOAS fit along with a polynomial used to compensate any broadband extinction structures caused by Rayleigh and Mie scattering. During the fit, a slight shift and squeeze of the absorption cross-sections was allowed to compensate for any small optical misalignments and shift in the spectral calibration of the spectrometer (*Stutz and Platt 1996*).

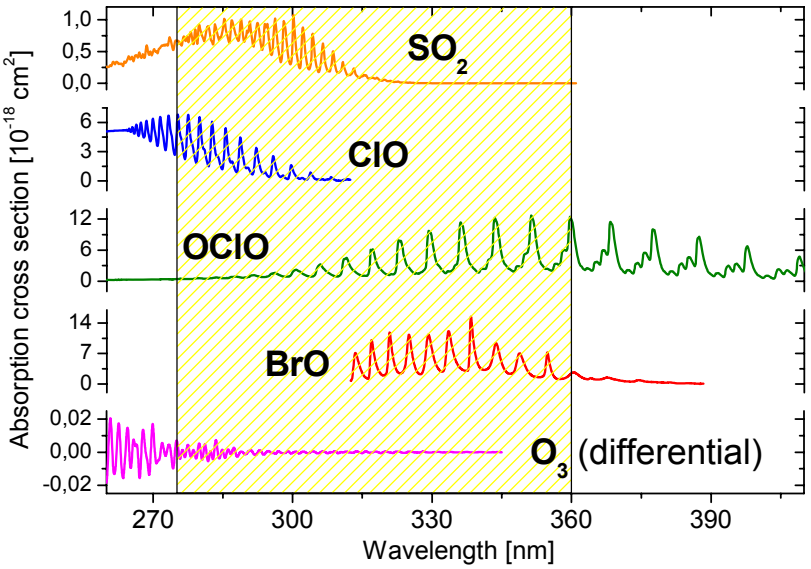

Fig. 7.6 – Absorption cross-sections of SO_2, O_3, and the halogen oxides measured in this study (*Wahner et al. 1987, Wahner et al. 1988, Simon et al. 1990, Voigt et al. 2001, Bogumil et al. 2003*). The O_3 cross-section was filtered to remove broadband absorption and emphasize the differential absorption structures used in the DOAS retrieval. The spectrometer's wavelength range is shaded.

All DOAS retrievals presented here were performed using version 3.2.27324 of the DOASIS software (*Kraus 2004*). In this platform, the absorption cross-sections of SO_2, O_3, BrO, ClO and OClO were fit to the measured optical densities using a non-linear, least-squares fit

according to Levenberg and Marquardt (*Levenberg 1944, Marquardt 1963*). The absorption cross-sections are shown in Fig. 7.6. The fit parameters were optimised for each individual trace gas species (or set of species in the case of BrO and OClO), so a separate evaluation of each was conducted. In each case, a light source reference spectrum was compiled by co-adding several spectra recorded on the individual light paths at times when the wind direction was such that the plume was not intersected by the light beam. Care was taken that no absorption by the volcanic plume was present in any of the compiled references. This referencing method was chosen in order to directly include ambient O_3 and NO_2 absorption in the reference spectrum and therefore minimize later interferences by these species in the plume trace gas evaluations. The four employed fit regions were selected as follows.

1) The wavelength range of 310 to 326 nm was found to be best suited for the SO_2 evaluations. In addition to SO_2 (*Bogumil et al. 2003*), the O_3 absorption cross-section (*Voigt et al. 2001*) was included in the spectral fit to remove structures caused by changes in ambient O_3 between the time of measurement and when the reference spectrum was recorded. Also, a 3^{rd} order polynomial was used to remove the broadband extinction.

2) As background O_3 concentrations can play an important role in the oxidative capacity of the ambient air, a separate study was conducted to retrieve the ambient O_3 concentration. Here, the above mentioned referencing method was replaced by an absolute reference consisting of a directly measured spectrum of the light source. By then considering the O_3 cross-section (*Voigt et al. 2001*) in the fit region between 276 and 288 nm, the O_3 column density was retrieved. The absorption of SO_2 (*Bogumil et al. 2003*) and a 5^{th} order polynomial were also included in the fit.

3) BrO and OClO were both evaluated in the same wavelength range from 331 to 357 nm (*Wahner et al. 1987, Wahner et al. 1988*). This range includes 5 BrO absorption bands as well as 3 OClO absorption bands, and is separated far enough from the strong SO_2 absorption range around 300 nm to reduce interferences in the fit. However, it was still necessary to take the SO_2 absorption into account during the fit (*Bogumil et al. 2003*), as well as that of O_3 (*Voigt et al. 2001*) and a 5^{th} order polynomial. Lastly, as this retrieval took place in a region in which the solar spectrum is prominent, a Fraunhofer reference spectrum was included to remove structures induced by sunlight scattered into the instrument's field of view during the measurement.

An example BrO evaluation is shown in Fig. 7.7. Two measurement spectra are shown in Fig. 7.7 (a). The spectrum plotted in blue was recorded when the plume was blown out of the light path. It contains no absorption structures caused by volcanic emissions, and can therefore be used as a reference spectrum for the DOAS fit. The magenta spectrum was recorded when the light path penetrated a large section of the plume. Very strong SO_2 absorption can easily be seen between 300 and 320 nm, and the SO_2 fit revealed a column density of 6.5×10^{18} molecules/cm^2 in this spectrum. The optical density can be compiled by dividing the reference spectrum by the plume spectrum and taking the logarithm. After removing any broadband structures by fitting a polynomial, the differential optical density is obtained, to which the

absorption cross-sections of the trace gases can be fit. The differential optical density obtained from the two spectra in Fig. 7.7 (a) is shown in Fig. 7.7 (b), zoomed in to the BrO evaluation range of 331 to 357 nm. The measured BrO absorption structure (orange) is clearly visible, and the DOAS fit of BrO (green) matches the measurements well. Here, a column density of 2.3×10^{14} molecules/cm^2 was obtained.

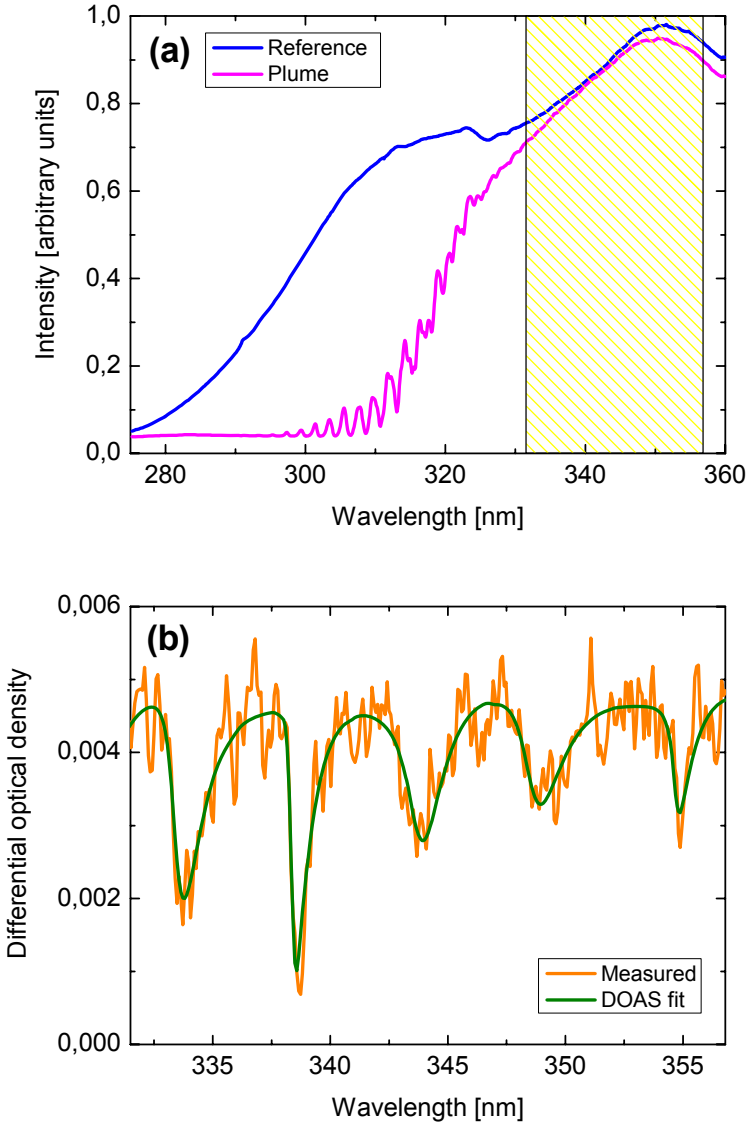

Fig. 7.7 – Example evaluation of BrO. (a) shows two measurement spectra. The spectrum plotted in blue was recorded when the plume was blown out of the light path, while the magenta spectrum was recorded in the plume and clearly shows SO_2 absorption between 300 and 320 nm. The BrO evaluation range was between 331 and 357 nm (shaded area), and (b) shows the measured differential optical density in this wavelength range (orange line). The green line represents the result of the DOAS fit for BrO. A BrO column density of 2.3×10^{14} molecules/cm^2 was obtained in this particular case.

4) For ClO, the wavelength range of 277 to 285 nm was selected, which includes 3 ClO absorption bands (*Simon et al. 1990*). This range was chosen for several reasons. The selected absorption bands are the strongest ClO bands in the spectrometer's wavelength range. Also, the low intensity of solar radiation below 300 nm made it unnecessary to remove background structures originating from solar radiation scattered into the light path. Most importantly, the SO_2 differential absorption cross-section, whose structures are most pronounced at 300 nm, is a factor of 3 less prominent below 285 nm, and therefore interferences with the ClO retrieval were avoided. In addition to ClO, SO_2, O_3 and a 3rd order polynomial were included in the fit. CS_2 and CH_2O were omitted after sensitivity studies failed to detect these species and indicated that the fit was not improved by including them. During the attempted ClO measurements, the exposure time was chosen so that the saturation of the detector was kept constant at about 75% of the well depth for the pixels in the selected wavelength range. Therefore, pixels at higher wavelengths were oversaturated, and in this case, SO_2 had to be evaluated in the same wavelength range (277 to 285 nm) for the determination of ClO/SO_2 ratios.

In a second study, the ClO detection limit was retrieved by omitting the ClO absorption cross-section from the fit and evaluating the fit residual in the above mentioned wavelength region. However, the window from 282.1 – 283.7 nm had to be excluded here, as systematic structures were found in this range, which were attributed to an inaccuracy in the SO_2 absorption cross-section.

7.3 Masaya volcano (Nicaragua) – Results and Discussion

7.3.1 SO_2 measurements

During the intensive field campaign from April 14 to 26, volcanic activity at Masaya was fairly constant. The NOVAC instruments were operational during the second half of the LP-DOAS measurement campaign (from 22 April), and showed an average of about 1500 tons/day of SO_2, as shown in Fig. 7.8. On short time scales, the flux fluctuated by several hundred tons/day, but the average value remained constant throughout the measurement period and showed no long term trends towards lower or higher fluxes.

In the active DOAS measurements, SO_2 was by far the strongest absorber in the analysed wavelength range of 310 to 326 nm (see Fig. 7.7). However, while the general plume direction was fairly stable during the measurements, the plume's shape was dominated by turbulent processes on a smaller scale. Therefore, the time series of SO_2 column densities showed large variations. Measured values ranged between 0 and about 7×10^{18} molecules/cm^2, but the top end of this range was not limited by the SO_2 concentrations themselves, but rather the inability of the light beam to penetrate the plume at higher column densities. This was in part due to the very strong SO_2 absorption below 310 nm, but mainly because of the high

opacity of the plume caused by the condensation of water vapour in the presence of such elevated column densities.

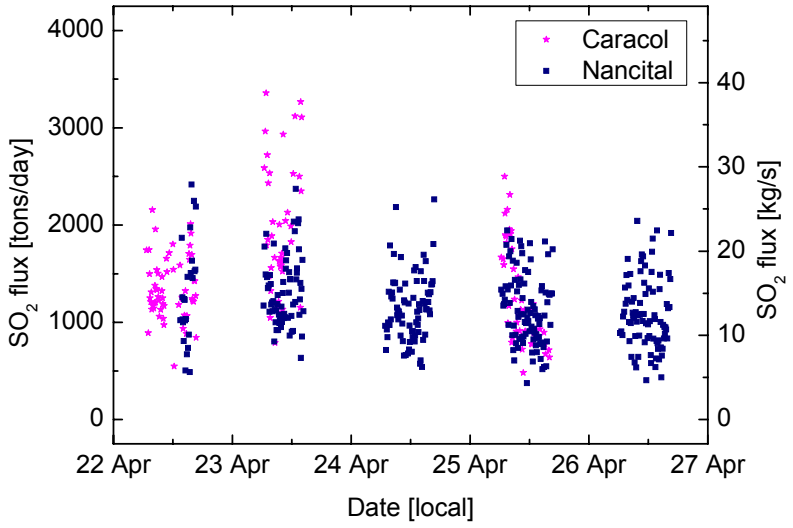

Fig. 7.8 – SO_2 flux measured by passive scanning DOAS instruments at the Caracol (11.97663N, 86.17813W, magenta stars) and Nancital (11.986175N, 86.184433W, blue squares) NOVAC sites located downwind of the Masaya crater in the greater caldera. (NOVAC data provided by Claudia Rivera, personal communication)

Because of the high temporal variability of the measured SO_2 column density and the inability to register SO_2 values above approximately 7×10^{18} molecules/cm^2, the SO_2 measurements are not indicative of the total SO_2 flux over time. Scanning or traverse measurements with passive instruments are much better suited for such surveys. *McGonigle et al. 2004* showed that the depletion of SO_2 via further oxidation by OH radicals and/or wet and dry deposition in particles is slow in the plume at Masaya volcano within the first 25 minutes after emission, and that the condensation of water vapour has little or no effect on the SO_2 concentration within the plume. Therefore, the SO_2 column is used in this study as a measure for the amount of volcanic gas located in the well defined measurement light path during a particular measurement. The other examined species can then be related to the SO_2 column, thus eliminating variations caused by spatial and temporal plume inhomogeneities.

7.3.2 Ozone measurements

O_3 could be evaluated in the measured data by substituting the relative measurement reference with an absolute reference and including O_3 in the fit between 276 and 288 nm (see section 2.3). Due to interferences in the DOAS retrieval, it was not possible to obtain dependable O_3 values at SO_2 column densities above 2×10^{18} molecules/cm^2. Therefore, spectra with these extreme SO_2 absorption values were omitted in the O_3 retrieval. Fig. 7.9 shows the average O_3 mixing ratio along the light path for the time periods in which the night-time measurements

took place (April 17 – 20, 2007 and April 23 – 27, 2007). The ambient O_3 mixing ratios varied between 20 and 40 ppb, with the higher values typically occurring during daylight hours.

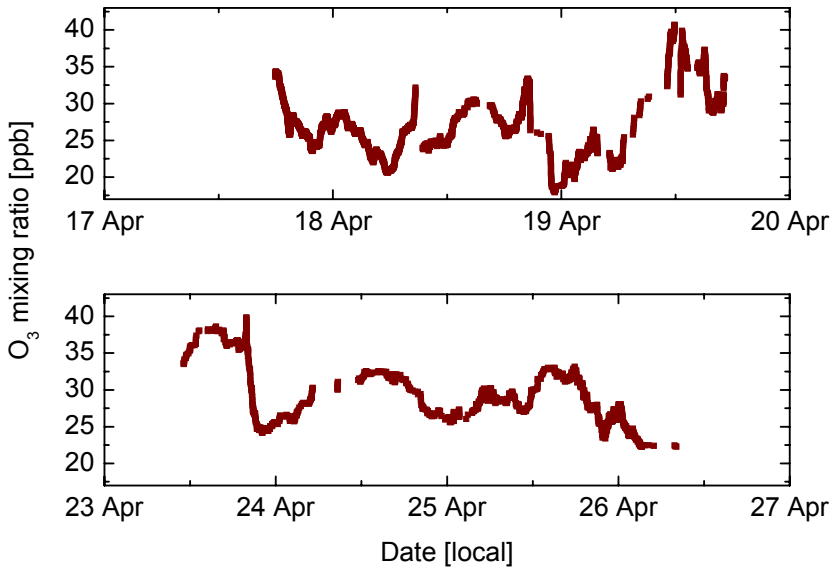

Fig. 7.9 – Average O_3 mixing ratio along the measurement light path for the two time periods in which the night-time measurements took place (April 17 – 20, 2007 and April 23 – 27, 2007). Tick marks indicate midnight (0:00) local time. The mixing ratio is calculated from the column density using the average pressure in the time period (942 hPa).

A comparison of the O_3 and SO_2 column densities revealed no apparent dependency between the two. One might anticipate an anticorrelation of the two measurements, as the volcanic plume is quite likely depleted in O_3 as compared to the background concentration due to autocatalytic O_3 destruction (see section 4), and the SO_2 column density is a tracer for the amount of plume the light path passes through at a given time. Two reasons were held responsible for the absence of this finding: Firstly, the largest portion of the light path was always outside the plume, and the retrieved O_3 column is therefore mainly representative of the O_3 abundance outside the plume, especially since measurements with high SO_2 column densities could not be evaluated for O_3. Also, considerable turbulence was observed in the plume at all times and it is very likely that ambient air was already fairly well mixed with the plume at the point of measurement. This is also suggested by the BrO measurements and their implications described in section 7.6.

7.3.3 BrO measurements

The main goal of the conducted study was the detection and quantification of halogen oxides in the plume of Masaya. BrO was positively detected in many of the LP-DOAS spectra (see e.g. Fig. 7.7 (b)) collected during the daytime. For all measurements taken between 10:00 and 16:00 local time, the average BrO/SO_2 ratio was 3×10^{-5}, as shown in Fig. 7.10.

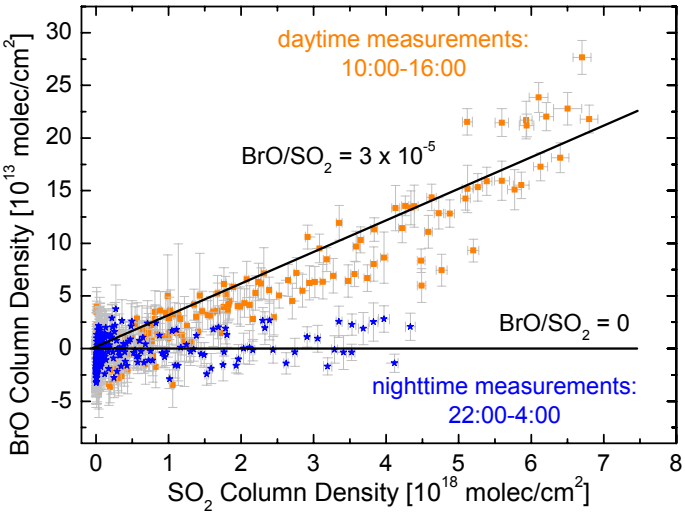

Fig. 7.10 – Retrieved BrO column density as a function of SO_2 column density retrieved from the same measurement spectrum. During the day, a BrO/SO_2 ratio of approximately 3×10^{-5} was typically observed (black line). During the night-time hours of 22:00 to 4:00 local time, all measured BrO values are consistent with 0 within 2σ standard deviation of the measurement error. The BrO detection limit divided by the highest measured SO_2 column density gives an upper limit for the night-time BrO/SO_2 ratio of about 1×10^{-5}.

However, using the active LP-DOAS, BrO measurements could also be conducted at night for the first time. These measurements failed to detect BrO in the light path during the night-time hours from 22:00 to 4:00 local time (black stars in Fig. 7.10) while SO_2 column densities of up to 4.4×10^{18} molecules/cm^2 were registered. All measured BrO values were consistent with 0 within 2σ standard deviation of the measurement error, and therefore below the detection limit of about 4×10^{13} molecules/cm^2. The BrO detection limit divided by the highest measured SO_2 column density results in an upper limit for the night-time BrO/SO_2 ratio of about 1×10^{-5}. The decrease in maximum SO_2 column at night was not caused by a decrease in the SO_2 concentrations themselves but rather by an increase in water vapour condensation as ambient temperature dropped and relative humidity increased at night (see Fig. 7.11). Therefore, the plume opacity was higher and the light path penetration was reduced. A similar diurnal cycle in water vapour condensation in the plume of Masaya volcano was previously reported by *Burton et al. 2001*.

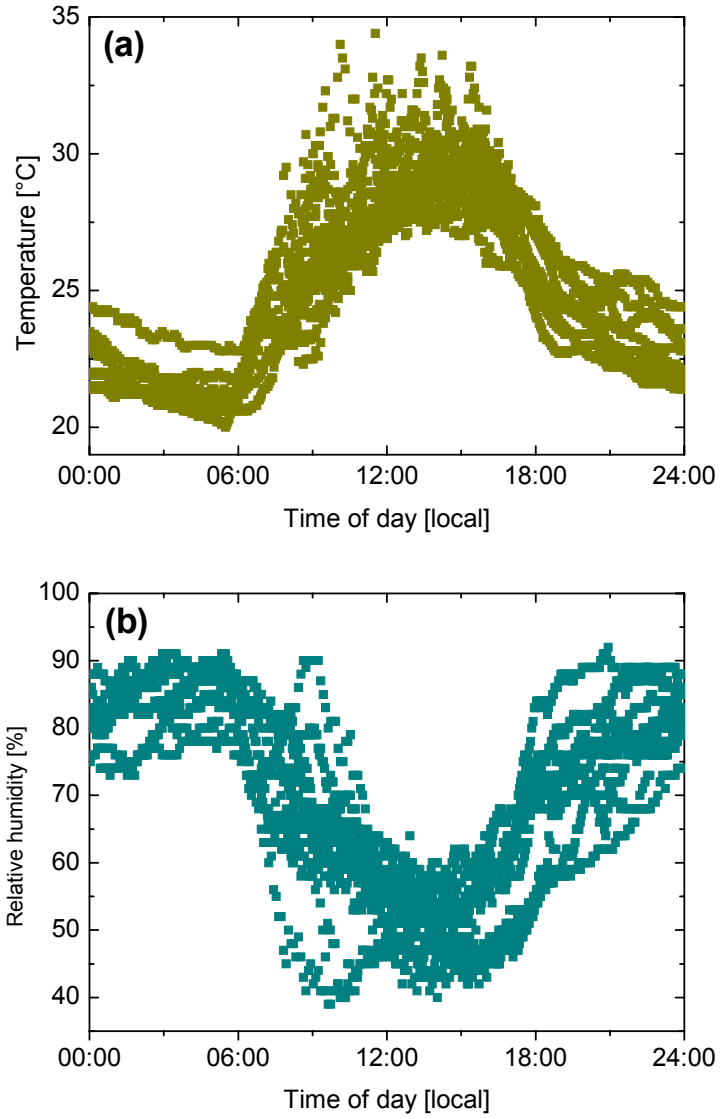

Fig. 7.11 – Diurnal temperature (a) and relative humidity (b) measured by the meteorological station from April 17 to 26, 2007. The relative humidity was always above 70% during night-time hours, causing increased condensation inside the plume.

Fig. 7.12 shows the diurnal variation of the measured BrO/SO_2 ratio compiled from the entire measurement timeframe. Due to the numerical instability of the BrO/SO_2 ratio for low SO_2 columns, only measurements featuring an SO_2 column density at or above 3×10^{18} molecules/cm^2 were selected for this study. The shortage of data points in the early morning hours is again caused by the inability to penetrate the plume due to elevated condensation of water vapour during this time when the relative humidity was highest (Fig. 7.11). During the day, BrO/SO_2 ratios of up to 6.4×10^{-5} were observed, which is consistent with the measurements by *Bobrowski and Platt 2007*, who found an average BrO/SO2 ratio of 8×10^{-5} at Masaya in 2003. The extraterrestrial global irradiance was additionally calculated for

Masaya on April 20, 2007 (solid line in Fig. 7.12), and a clear correlation to the measured maximum BrO/SO_2 ratios can be observed. Lower values were also sometimes observed during the day, but these are likely the result of a reduced actinic flux in the plume due to cloud cover or haze. As mentioned above, all individual BrO/SO_2 ratios measured at night are consistent with 0 within the 2σ standard deviation of the measurement error, and the average over all values between 18:00 and 6:00 local time is 6×10^{-7}.

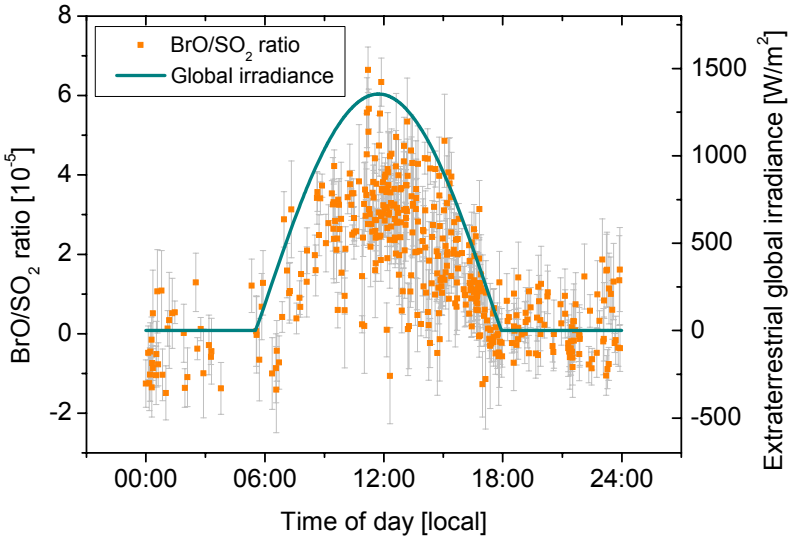

Fig. 7.12 – Diurnal variation of the BrO/SO_2 ratio compiled from the entire measurement timeframe (orange points) and extraterrestrial global irradiance calculated for Masaya volcano on April 20, 2007 (blue line). The maximum BrO/SO_2 ratios coincide with the maximum in solar irradiance at noon. At night, all measured ratios are consistent with 0 within 2σ standard deviation (error bars denote 1σ standard deviation).

7.3.4 ClO measurements

Aside from being able to measure at night, the second large advantage of the active LP-DOAS instrument when compared to passive DOAS measurements is the improved sensitivity and detection limit for ClO (see sections 3.1.6 and 7.2.1). As passive DOAS measurements had showed ClO at Masaya in the past (*Bobrowski 2005*), the detection of ClO with the LP-DOAS was expected. However, while the first DOAS evaluation for ClO yielded a high correlation of the ClO fit coefficient with the SO_2 column density, it was quickly established that this was an artifact.

Even though interferences in the retrieval between SO_2 and ClO were minimized by moving the evaluation range to well below 300 nm (see section 7.2.3), a clear correlation of the fit results of the two species was still observed. It was established that the reference SO_2 absorption cross-section (*Bogumil et al. 2003*) was not precise enough to cleanly remove all

SO_2-structures at high column densities. Therefore, the DOAS fit residual was found to be dependent on the measured SO_2 values. Because of the similarities of the ClO and SO_2 absorption cross-sections, the structures remaining in the fit residual limited the ClO detection capability of the instrument at high SO_2 levels.

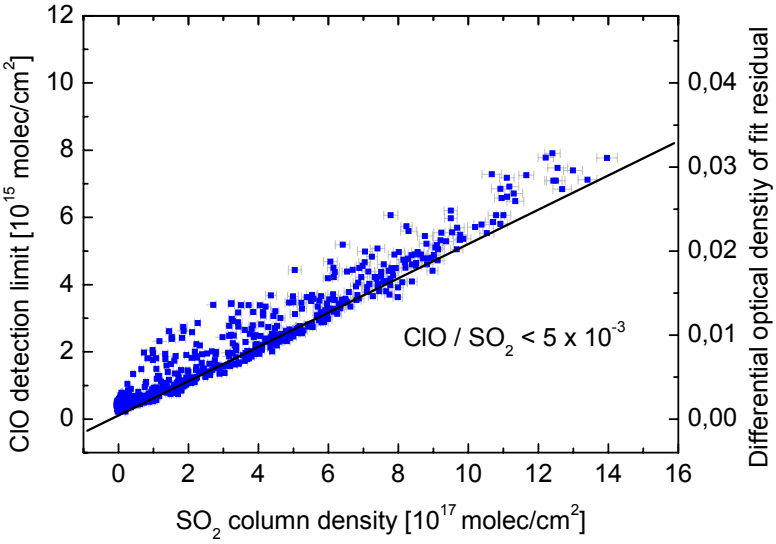

Fig. 7.13 – Detection limit of ClO as a function of the measured SO_2 column density. Also shown is the differential optical density of the DOAS fit residual, which was used to determine the ClO detection limit. As an imperfect SO_2 fit causes differential structures in the fit residual, the detection limit is dependent on the measured SO_2 column. The solid line represents the obtained detection limit of the ClO/SO_2 ratio of 5×10^{-3}.

No ClO absorption structures were observed during the campaign, but the detection limit of the instrument for ClO was determined. This was done by repeating the DOAS evaluation but this time not taking ClO into account. Any ClO absorption structures could easily be detected by the measurement if their differential optical density were larger than that of the remaining structures in the residual. Therefore, the differential optical density of the fit residual is a measure for the ClO detection limit. Because the magnitude of the residual structures depends on the SO_2 column density, the ClO detection limit calculated in this way also depends on the respective SO_2 values. This is not a measurement of ClO, but rather an upper limit for the ClO column density in the plume. The ClO detection limit obtained in this study is shown in Fig. 7.13. Because the structures in the fit residual are caused by an imperfect fit of SO_2, the fit residual and therefore detection limit for ClO is linearly dependent on the measured SO_2 column density. The solid line represents a ClO/SO_2 molecular ratio of 5×10^{-3}. While the DOAS fit was worse at times, the ClO detection limit is on or below this value for the majority of the measurements. Therefore, this value can be regarded as the maximum possible ClO/SO_2 ratio during the measurement period.

7.3.5 OClO measurements

As was the case for ClO, the LP-DOAS measurements at Masaya volcano did not reveal OClO in the volcanic plume, either at day or during night-time hours. Because the OClO evaluation wavelength range is not in the range of strong SO_2 absorption (and due to the higher differential absorption cross-section of OClO), the instrument's detection limit for OClO was almost 3 orders of magnitude better than for ClO, and independent of the measured SO_2 column density (see Fig. 7.14). Here, the detection limit was defined as twice the calculated measurement error (*Stutz and Platt 1996*) and represents a 95% detection confidence. However, the retrieved OClO values remained below the detection limit for all measured SO_2 column densities. Since the measurements were conducted for SO_2 columns of up to 7×10^{18} molecules/cm^2, the constantly obtained OClO detection limit of 5×10^{13} molecules/cm^2 corresponds to a maximum $OClO/SO_2$ molecular ratio compatible with our measurements of approximately 7×10^{-6}. Aside from giving an upper limit for OClO in the plume, this value also has implications for the amount of ClO thought to be present, as will be discussed in section 4.

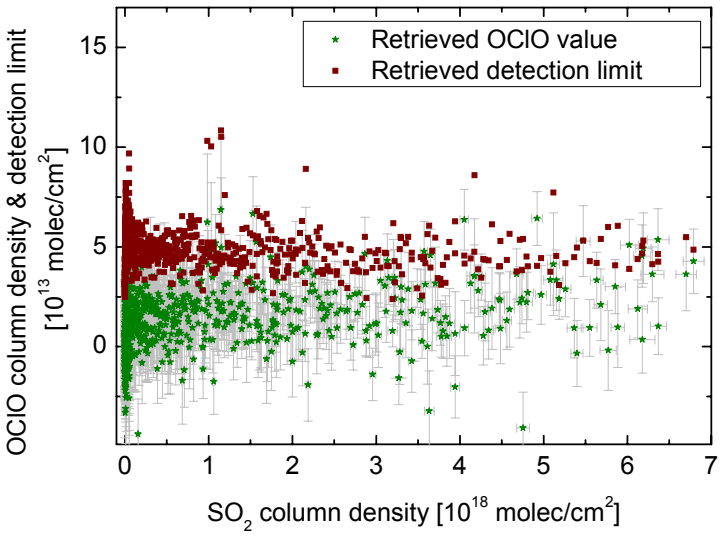

Fig. 7.14 – Retrieved OClO values (green) and OClO detection limit (red) as a function of the measured SO_2 column density. OClO could not be positively detected during the day or at night. It remained below the detection limit for all SO_2 column densities.

7.4 Mt. Etna (Italy) – Experimental Methods and Study Area

Aside from the LP-DOAS campaign carried out at Masaya volcano, several active LP-DOAS measurements were also conducted at Mt. Etna (Italy). Again, the emphasis of the measurements was on quantifying halogen oxides (especially ClO, as the LP-DOAS is much more sensitive than passive measurements to this species, see section 7.2.1) in the young

plume. The measurements were carried out in the scope of NOVAC installation campaigns (also see section 5.4) in August of 2007 and July of 2008. A total of 7 measurements were attempted, 5 of which were successful. One measurement, conducted on July 3, 2008 at the North East (NE) crater of the mountain, had to be aborted during the adjustment of the system. Low wind speeds and variable wind directions caused the plume to swirl in all directions. The LP-DOAS instrument was exposed to extreme SO_2 mixing ratios (estimated at ppm), and the main mirror of the telescope was destroyed. During another measurement on July 8, wind speeds were too low to allow a sampling of the plume at a downwind position. However, successful LP-DOAS measurements were conducted on August 24 of 2007 at 2 different sites) and on July 9, 10 and 15 of 2008 at 3 different sites.

7.4.1 Experimental setup

The setup of the LP-DOAS instrument used for the halogen measurements at Mt. Etna was almost identical to the setup used at Masaya volcano (see section 7.2.1). However, there was one major difference. In contrast to the measurements at Masaya, where both LEDs and xenon arc lamps were utilized as light sources, only LEDs could be applied in the measurements conducted at Mt. Etna, as all measurements were conducted at locations only accessible on foot. Therefore, only the fully mobile LP-DOAS system described in section 3.5.2 could be applied. In 2007, only a single Sensor Electronic Technology© UVTOP 280 nm LED was used. In 2008, the multi LED light source described in section 3.5.2 was applied, thus allowing an expansion of the wavelength range. In addition to the 280 nm LED, one 320 nm and one 340 nm LED were utilized. Again, an Ocean Optics© QE65000 spectrometer with a wavelength range of 275 – 360 nm was used to record the LP-DOAS spectra at an optical resolution of 0.4 nm. An example spectrum is shown in Fig. 3.45, along with the absorption cross-sections of the sought after halogen species. The system was typically split into 3 backpacks for transportation. Carried by a fourth person, a 60 Ah car battery supplied the necessary power. Examples of the instrument setup are shown in Fig. 3.8, Fig. 3.46, Fig. 7.16, and Fig. 7.17.

7.4.2 Measurement locations

As stated above, five successful LP-DOAS measurements were carried out at Mt. Etna in 2007 and 2008, each at a different site. Fig. 7.15 gives an overview of the locations and optical paths of the five measurements. For each site, both the telescope position T and position of the retro reflector array R is marked. The optical path lengths ranged from 40 m to 880 m, as indicated in Tab. 7.1. Sites 1, 2 and 5 were in located the summit area, sites 3 and 4 were approximately 2 km downwind. At site 1, the plume of Voragine crater was measured. The measurements at site 2 and site 5 were aimed at characterizing the plume of the NE crater. Site 3 was chosen to measure emissions from the NE crater, but could also be influenced by emissions from an actively degassing fumarole in the eastern flank of the SE crater (formed in August of 2007, position indicated in Fig. 7.15). At site 4, the optical path

likely crossed a mixture of the plumes from Voragine, the NE crater, and also emissions from the mentioned fumarole.

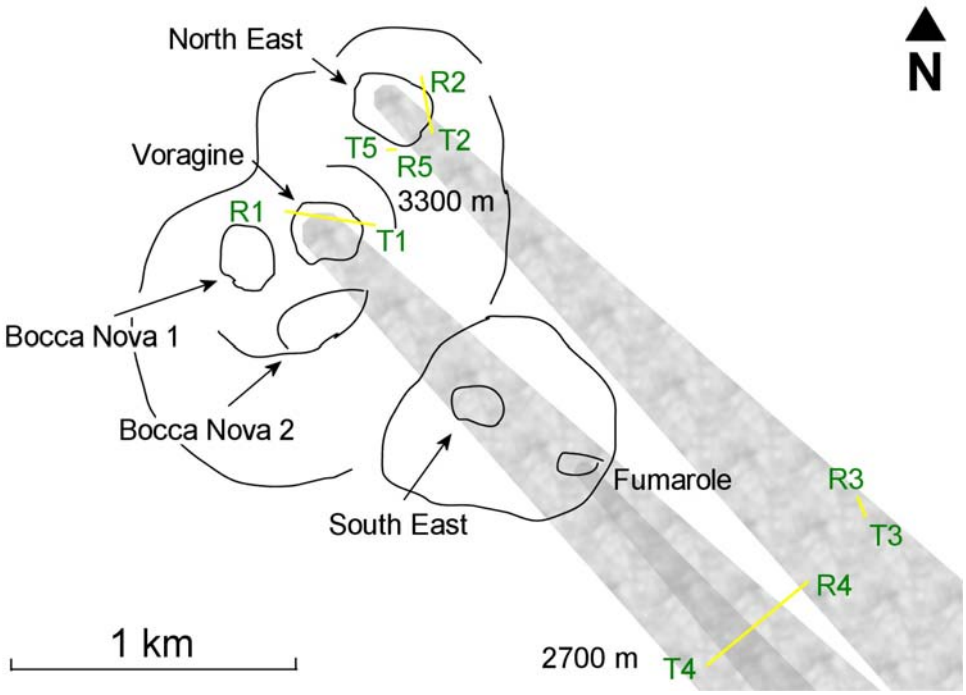

Fig. 7.15 – LP-DOAS light paths for the 5 measurements conducted at Mt. Etna in 2007 and 2008. T1 – T5 mark the telescope positions, R1 – R5 depict the retro reflector sites. The typical wind direction is indicated by the grey plumes. Three measurements were conducted in the crater area and 2 approximately 2 km downwind of the active vents. An actively degassing fumarole opened on the eastern flank of the SE crater in August of 2007. The downwind measurements (especially site 4) were influenced by emissions from this vent.

Site	Measurement Date	Measurement Time [local]	Tel. Latitude [° North]	Tel. Longitude [° East}	Optical path length [m]
1	Aug 24, 2007	12:16 – 13:02	37.7519	14.9965	610
2	Aug 24, 2007	14:11 – 14:53	37.7541	14.9982	460
3	July 9, 2008	13:57 – 14:08	37.7440	15.0145	150
4	July 10, 2008	12:30 – 14:51	37.7401	15.0077	880
5	July 15, 2008	10:24 – 10:50	37.7536	14.9969	40

Tab. 7.1 – Exact locations of the five LP-DOAS sites at Mt. Etna. Also given is the respective optical path length used at each site.

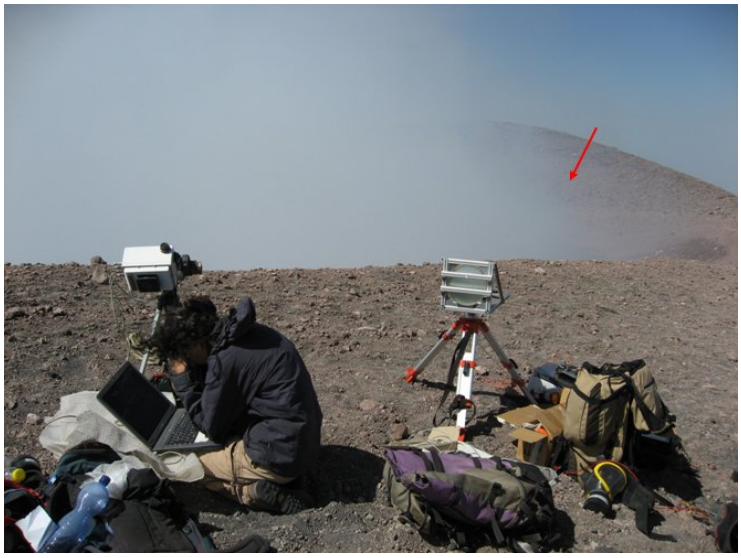

Fig. 7.16 – Image of the LP-DOAS measurements (right) conducted at the NE crater of Mt. Etna (site 2 in Fig. 7.15). The red arrow indicates the position of the retro reflector array. Supplementary MAX-DOAS measurements (left) were conducted simultaneously by Nicole Bobrowski.

Fig. 7.17 – LP-DOAS setup at site 4, about 2 km downwind of the summit craters (see Fig. 7.15) on July 10, 2008. The red arrow again indicates the reflector position. Extreme wind speeds of approximately 20 m/s pushed the volcanic plume down along the eastern flank of the mountain, thus making downwind measurements with the LP-DOAS possible. The instrument was placed as close as possible to a solid rock ledge to shield the telescope from dust and rocks picked up by the strong winds. The explosion seen in the background originates from a newly formed vent. Explosions of increasing intensity at this vent forced the measurements conducted the previous day at site 3 to be aborted and scientists to be rapidly evacuated.

7.4.3 Data evaluation

As the UV-LED light source was used in these measurements, the evaluation of the LP-DOAS spectra was slightly different than for the measurements conducted at Masaya. Evaluations were conducted for SO_2, ClO, and BrO. In all cases, the measured spectra were first corrected for detector dark current and electronic offset. Then the logarithm was taken, and the DOAS fit conceived for the evaluation of the respective species was applied to this spectrum. The individual fits are described below.

1) SO_2 was again by far the most dominant absorber at all sites. In 2007, only a single LED emitting at 280 nm was applied in the measurements. Therefore, the evaluation of SO_2 was conducted between 277 and 285 nm. However, the SO_2 optical densities at the two measurement sites (marked 1 and 2 in Fig. 7.15) were so high that the noise level in many of the spectra was considerable due to a lack of radiation intensity returning from the retro reflector array. In 2008, the SO_2 evaluation was therefore conducted in the wavelength range between 314.5 and 322.5 nm, where the SO_2 absorption cross-section is considerably weaker (both differential and absolute, see e.g. Fig. 7.6).

In both retrievals, a literature SO_2 reference spectrum (*Bogumil et al. 2003*) convoluted by the instrument line shape (ILS) was used to retrieve the SO_2 column density. In addition to a shortcut spectrum of the LED light source (recorded by moving a sand-blasted aluminum plate in front of the fiber bundle, see section 3.5.2), the absorption cross-section of O_3 (*Voigt et al. 2001*) was included. Also, a 4^{th} order polynomial was used to account for broadband structures in the spectrum. A slight shift ($< \pm 0.5$ nm) and stretch/squeeze ($< \pm 5$ %) was allowed to account for temperature fluctuations (see section 3.4.5).

One difficulty in the evaluation of spectra at wavelengths above 300 nm was the influence of scattered solar radiation. Due to the fact that the volcanic plume was typically highly opaque and white in color, a considerable amount of solar radiation was scattered into the light path of the instrument on aerosols and water droplets. In fact, the intensity of the scattered radiation was at times in the same order of magnitude as incident light from the LED light source. Therefore, the background correction was crucial. Background spectra were recorded with the LED light source switched off. Unfortunately, however, an automatic measurement of shortcut and background spectra was not available during the field measurements due to a malfunction in the electronics controlling the shortcut/background system (see section 3.5.1). Therefore, these references had to be recorded manually.

However, the time scale on which plume inhomogeneities move through the optical path of the LP-DOAS system thus changing the scattering conditions is on the order of seconds. A straightforward background correction in which the background spectrum is simply subtracted from the measurement spectrum therefore requires the recording of background spectra on the same time scale. This requires an automatic recording mechanism functioning on the time scale of seconds. Future LP-DOAS measurements conducted at volcanoes should be sure to include such a mechanism.

For these measurements, a more complex background correction was necessary. The logarithm of a high resolution solar spectrum (*Kurucz et al. 1984*) convoluted with the ILS was fit to each individual measurement spectrum to account for the contribution of solar radiation. As scattering conditions changed, the contribution of inelastic Raman scattering also varied. Therefore, the Ring effect also had to be accounted for (see section 3.1). To this extent, a Ring spectrum was calculated from the convoluted solar spectrum and included in the fit. An example SO_2 evaluation is shown in Fig. 7.18.

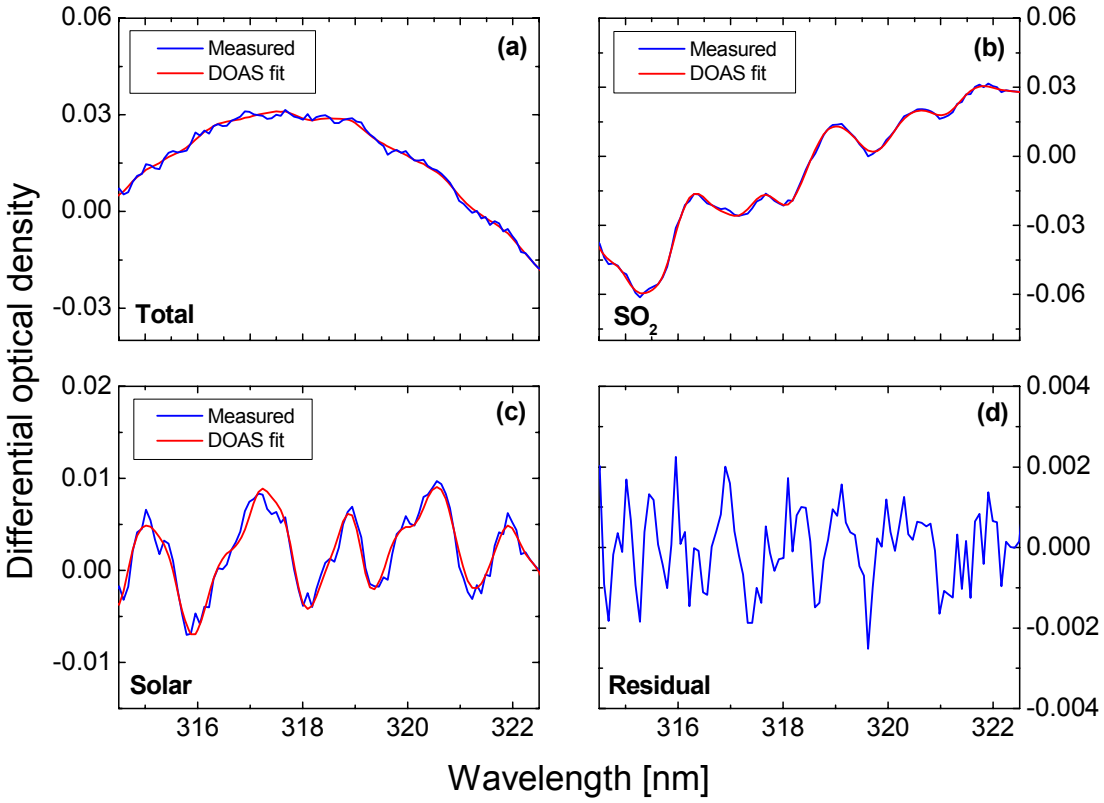

Fig. 7.18 – Example LP-DOAS evaluation of SO_2 in the wavelength range between 314.5 and 322.5 nm. The SO_2 absorption features were clearly found (inset (b)). However, it was necessary to include a solar spectrum (inset (c)) in the fit to correct for solar radiation scattered into the light path of the LP-DOAS system. The O_3 absorption cross-section, the Ring spectrum, the shortcut spectrum and the 4th order DOAS polynomial are not shown. Spectrum recorded on July 15 of 2008 at 10:27 local time at the NE crater of Mt. Etna (site 5).

2) The retrieval of ClO was conducted between 274 and 287 nm, where no solar radiation arrives at the Earth's surface. Therefore, a background correction was not necessary. However, due to the strong SO_2 absorption in the fit region, the residual was typically dominated by structures induced by an imperfect fit of SO_2. Discrepancies in the SO_2 fit could e.g. be induced by different temperatures of the volcanic gas (see section 3.4.5), a non-commutative convolution (see section 3.4.2), or errors in the reference absorption cross-

section (see Fig. 3.37). To reduce the influence of these errors, five different SO_2 absorption cross-sections convoluted in intensity space (details in section 3.4.2) for column densities between 0 and 5×10^{18} molec/cm^2 were included in the fit.[22] A 5th order polynomial was used to account for broadband spectral structures.

The ClO absorption cross-section (*Simon et al. 1990*) included in the DOAS fit featured five absorption bands in the retrieval wavelength. However, ClO could not be positively identified for any of the LP-DOAS measurements. Therefore, the detection limit of the instrument in regard to ClO was determined by using the same fit routine but omitting the ClO absorption cross-section. The peak-to-peak differential optical density of the fit residual obtained in this manner was divided by the differential absorption cross-section of ClO (4×10^{-18} cm^2) to estimate the ClO detection limit (see section 3.1.6, Eq. 3.26). An example of the ClO detection limit determination is shown in Fig. 7.19.

3) For the measurements conducted in 2008 with the extended wavelength range, a BrO retrieval was attempted on the peak of the 340 nm LED. Between 337 and 353 nm, three absorption bands of BrO were fit to the measured optical density. At these wavelengths, solar radiation scattered into the instrument's optical path was very prominent and required additional corrections. Aside from the Ring and Kurucz spectra also used in the SO_2 retrieval, the logarithm of a measured background spectrum along with a respective Ring spectrum were included in the fit. A 5th order polynomial was used to account for broadband spectral features.

To further improve the retrieval, a shortcut spectrum was compiled from spectra recorded over the light path at times when the plume was not in the optical path of the instrument, as established by the SO_2 retrieval. In this way, residual structures originating from the fact that the shortcut was recorded in a different measurement setup (i.e. using an aluminum diffuser plate) than the measurement spectra could be avoided.

Unfortunately, the inability to measure the background caused by scattered solar radiation at high time resolution led to a considerable increase in the detection limit of the instrument towards BrO. While column densities in the order of 10^{13} molec/cm^2 could be measured using the xenon arc lamp at Masaya volcano, the detection limit achieved with the LEDs during the day at Mt. Etna was about an order of magnitude worse. BrO could therefore not be positively identified. Instead, the detection limit of the instrument was retrieved, as was done for ClO.

[22] For future measurements, it could be advantageous to record an own SO_2 reference by positioning a calibration cell into the light path. Although it may again be necessary to take multiple references at different column densities in order to account for the non-linear convolution effect described in section 3.4.2, the ability to remove the strong SO_2 absorption structures in the spectra could well be improved.

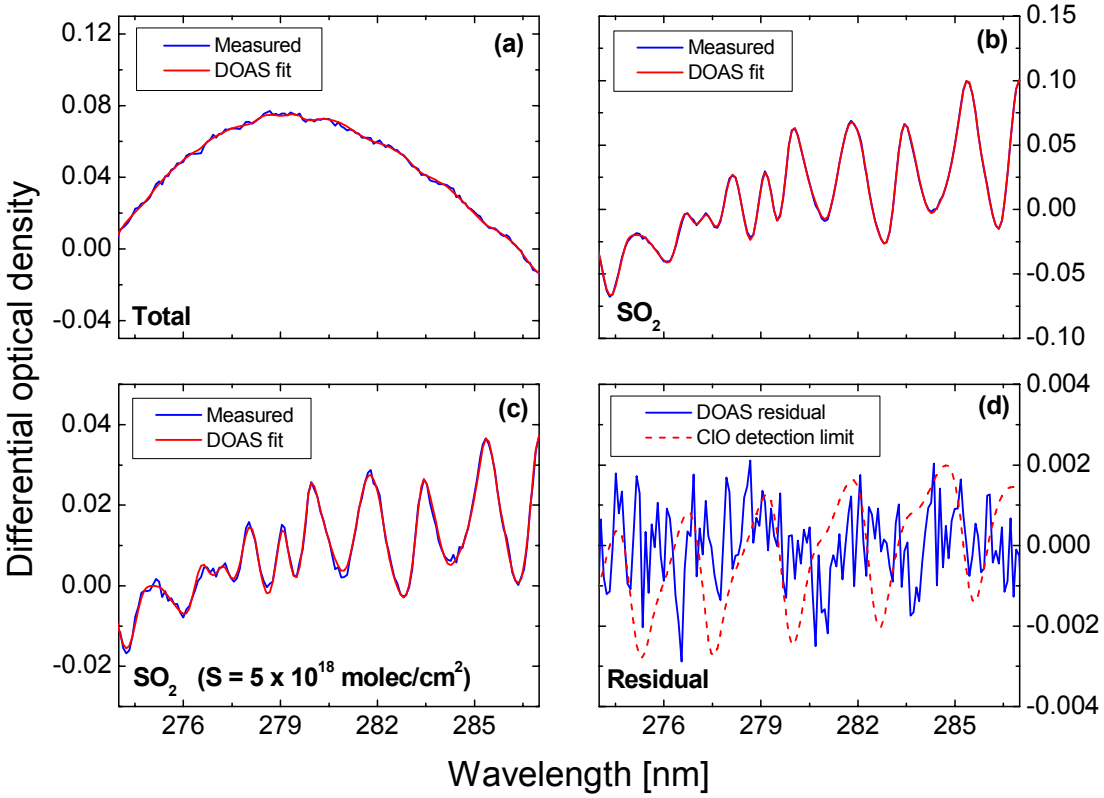

Fig. 7.19 – Example ClO detection limit determination from an LP-DOAS spectrum recorded on July 15, 2008 at 10:26 local time at the NE crater of Mt. Etna (site 5). In the ClO retrieval, five SO_2 absorption cross-sections were fit to the measured spectrum, each convoluted with the ILS in intensity space assuming a different SO_2 column density (see section 3.4.2 for details). Here, the SO_2 cross-sections convoluted for 0 and 5×10^{18} molec/cm^2 are shown (insets (b) and (c)). The fit residual is then used as a measure for the maximum possible ClO optical density. The dotted line in inset (d) represents a ClO column density of 1×10^{15} molec/cm^2, which is considered the detection limit of this measurement.

7.5 Mt. Etna (Italy) – Results and Discussion

7.5.1 ClO measurements

The main goal of the LP-DOAS measurements conducted at Mt. Etna was to quantify ClO emissions using the active DOAS setup. As mentioned in section 7.2.1, the LP-DOAS system's sensitivity regarding ClO is about one order of magnitude better than that of a passive DOAS instrument, a consequence of the expanded UV wavelength range available in from the UV-LED light source. Because of the previous detection of ClO column densities in

the order of several 10^{16} molec/cm^2 in the plume of Mt. Etna by passive DOAS (*Bobrowski 2005, Bobrowski et al. 2007*), a detection by active DOAS was expected. However, ClO remained below the improved LP-DOAS detection limit for all measurements. As the magnitude of the fit residual was largely determined by the optical density of SO_2 in the measured spectra, the ClO detection limit was again dependent on the SO_2 column density present in a particular measurement (compare section 7.3.4 and Fig. 7.13).

Fig. 7.20 shows the ClO detection limit as a function of the SO_2 column density for the measurements conducted at Voragine crater on August 24, 2007 (site 1 in Fig. 7.15). The black line represents a ClO/SO_2 molecular ratio of 9×10^{-3} molec/cm^2. The achieved detection limits of the individual spectra indicate that the ClO/SO_2 ratio was below this value in the sampled air mass.

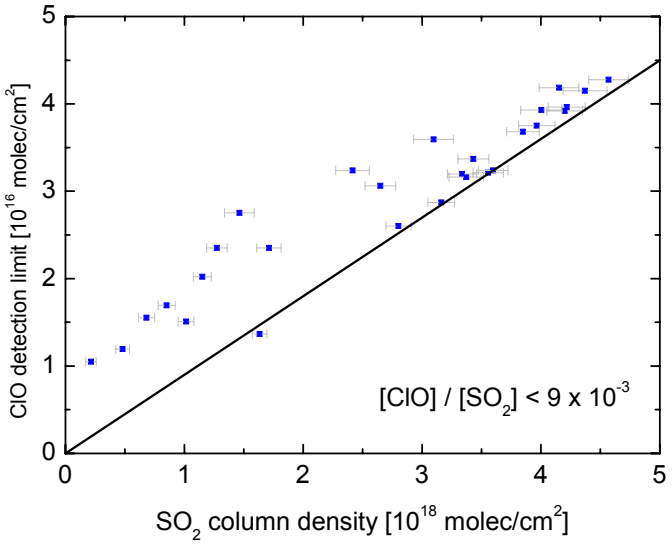

Fig. 7.20 – Detection limit of ClO achieved during LP-DOAS measurements at Voragine crater, Mt. Etna on August 24, 2007 (site 1). ClO was below detection limit for all measurements, but a ClO/SO_2 molecular ratio of more than 9×10^{-3} can be ruled out.

On the same day, the mobile LP-DOAS instrument was also set up at the NE crater (site 2 in Fig. 7.15). Due to the high opacity of the plume at this crater, the light path was not established across the center of the crater, but rather along the eastern side of the vent. The SO_2 column densities measured along this optical path were somewhat smaller than in the previous setup. However, an upper limit for the ClO/SO_2 molecular ratio of 6×10^{-3} was found for some of the spectra, as shown in Fig. 7.21. Others exhibited somewhat larger fit residuals, and therefore larger detection limits.

One possible explanation for the failed detection of ClO during the measurements in 2007 was thought to be the close proximity to the degassing vents. If ClO is not directly emitted from the vent but rather takes some time to form in the plume (as discussed in 7.6), detection

may only be possible after the plume has aged to some degree and mixed with ambient air. Therefore, measurements in 2008 were expanded to include setups located at a larger distance (in this case approximately 2 km) from the active vent. Unfortunately, such measurements rely on very specific meteorological conditions. In low-wind situations, the plume of Mt. Etna, which is emitted from the summit craters at 3300 m a.s.l., typically stays at this altitude as it moves slowly away from the summit area. For moderate to strong wind speeds (> ~15 m/s), the plume is often blown down the slope of the mountain for several hundred meters. The altitude at which the plume leaves the mountain and is blown into the atmosphere depends on the wind speed and direction. For very strong westerly winds (~ 25 m/s), the plume can propagate along the Valle del Bove all the way to altitudes around 2000 m before separating from the ground (observed for several days in July of 2008). As the optical path of the LP-DOAS system is limited to configurations in which both ends are located on the ground, such conditions are necessary to measure the plume composition at a distance from the summit.

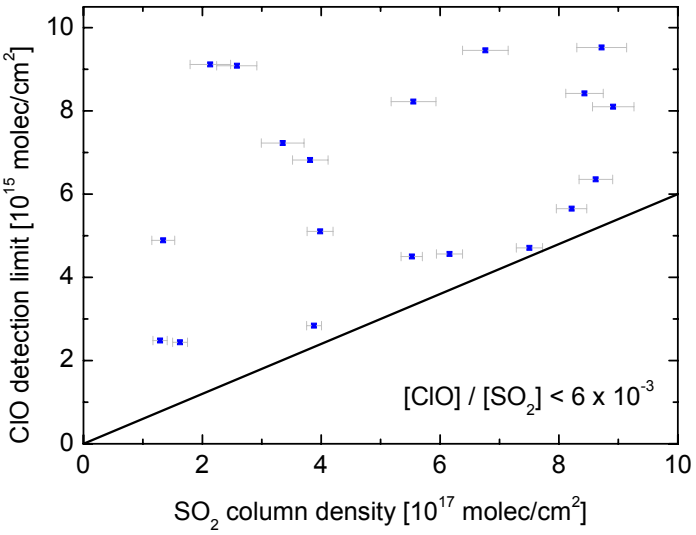

Fig. 7.21 – Detection limit of ClO achieved during LP-DOAS measurements at the NE Crater of Mt. Etna on August 24, 2007 (site 2). ClO was below detection limit for all measurements, but a ClO/SO_2 molecular ratio of more than 9×10^{-3} can be ruled out.

On July 9, 2008, the plume of the summit craters was encountered at site 3, located approximately 2700 m a.s.l. on the eastern flank of the mountain (see Fig. 7.15). In general, the center of the plume from the NE crater seemed to be passing north of the instrument position. However, the instrument could not be set up farther north, as several active vents with ongoing explosions blocked the passage. In fact, the rapidly increasing frequency and magnitude of violent explosions and associated rock falls at the closest vent to the measurement position (located approximately 300 m north of the instrument) cut the measurements short and led to a rapid evacuation from the measurement position.

The sampled gas volume at site 3 is likely to have contained emissions from the NE crater, but was also influenced by emissions from a nearby fumarole. Located on the eastern flank of the SE crater, an active fumarole that was formed during the measurement campaign in August of 2007 remained active during the measurements in 2008, and likely contributed to SO_2 column densities observed at site 3 and especially at site 4. The extreme wind speeds of around 20 m/s in the summit area of the mountain on July 9 and 10, 2008 indicate atmospheric residence times in the order of 2 minutes for gas emitted at the summit vents. While still not very long, this order of magnitude represents the maximum possible residence time achievable for LP-DOAS measurements.

ClO was below the instrument detection limit for both downwind measurements conducted July 9 and 10, 2008 (sites 3 and 4 in Fig. 7.15). In the measurement on July 9, in which emissions from the NE crater likely dominated the measured SO_2 column density, the ClO/SO_2 ratio was below 1.5×10^{-3} molec/cm^2 for a large portion of the measurements (shown in Fig. 7.22). On July 10, the measured volcanic gases were to a large portion emitted from the above mentioned fumarole. Here, a detection limit for the ClO/SO_2 molecular ratio of about 1.9×10^{-3} was achieved (see Fig. 7.23).

In the final LP-DOAS measurement conducted in 2008, the instrument was once again carried all the way to the summit area of Mt. Etna. Due to the high opacity of the plume emitted from the NE crater on July 15, the day of the measurement, a very short optical light path of only 40 m total length was chosen. Despite the short path, SO_2 column densities of up to 3×10^{18} molec/cm^2 were detected, indicating intermittent SO_2 mixing ratios of up to about 45 ppm, more than an order of magnitude above the health limit for momentary exposure given by the German Research Foundation (*DFG 2007*). The detection limits achieved during the measurements indicate that the ClO/SO_2 ratio was below about 1.3×10^{-3} at the carter rim, as is shown in Fig. 7.24.

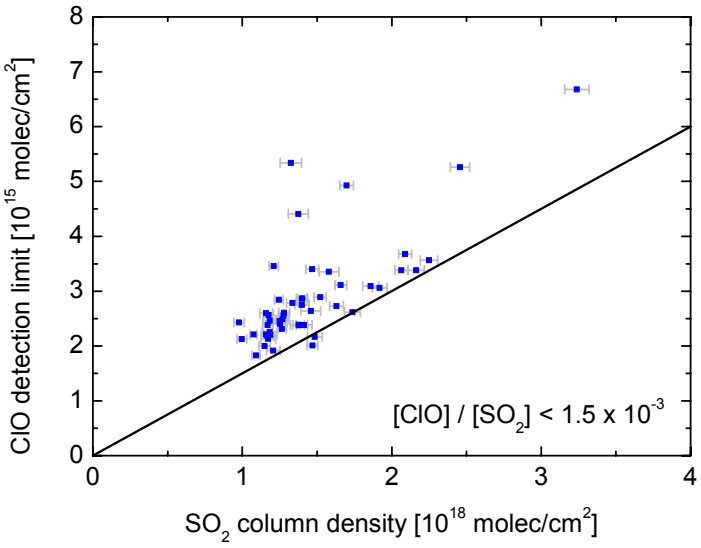

Fig. 7.22 – ClO detection limit achieved during the LP-DOAS measurements on July 09, 2008 downwind of the NE crater on the eastern flank of Mt. Etna (site 3). ClO was below detection limit for all measurements. An upper limit for the ClO/SO_2 molecular ratio of 1.5×10^{-3} was retrieved.

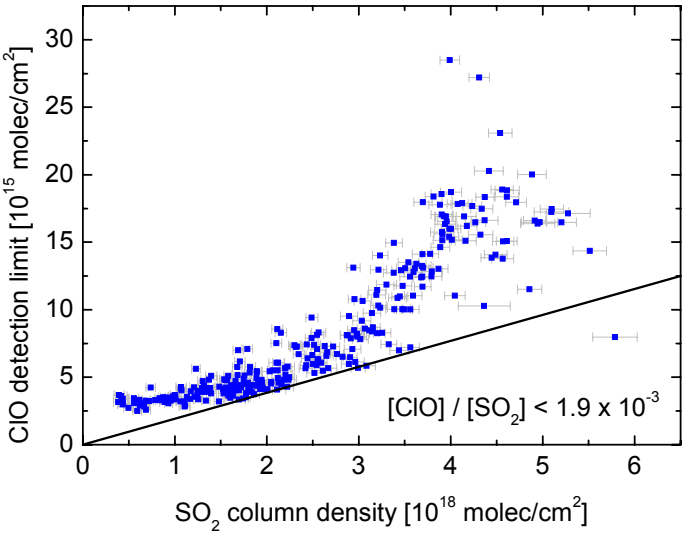

Fig. 7.23 – Detection limit of ClO achieved during LP-DOAS measurements at the NE Crater of Mt. Etna on July 10, 2008 (site 4). ClO was below detection limit for all measurements, but a ClO/SO_2 molecular ratio of more than 1.9×10^{-3} can be ruled out.

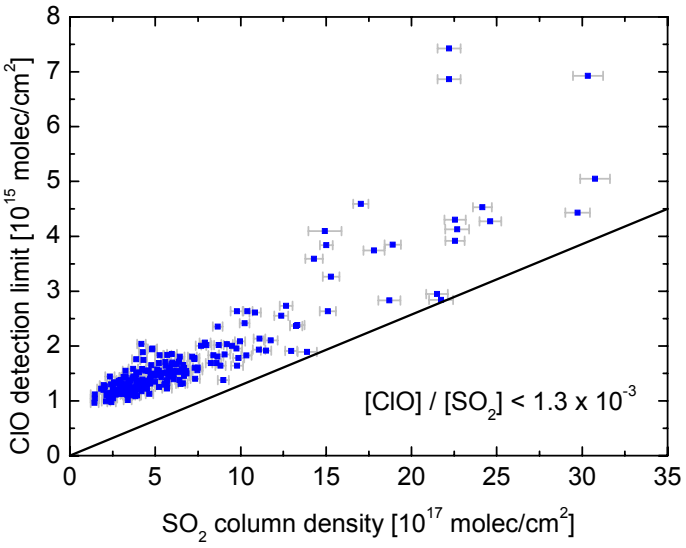

Fig. 7.24 – ClO detection limit achieved during LP-DOAS measurements on July 15, 2008 at the rim of the NE crater of Mt. Etna (site 5). ClO was not detected during the measurement, but a ClO/SO_2 ratio of more than 1.3×10^{-3} could be ruled out.

7.5.2 BrO measurements

The multi-LED light source used in the measurements in 2008 allowed the retrieval of BrO in addition to the ClO/SO_2 measurements described above. Unfortunately, an imperfect correction of the solar radiation scattered in to the optical path of the LP-DOAS instrument led to a degradation of data quality (see section 7.4.3) when compared to the BrO measurements conducted at Masaya volcano (described in section 7.3.3). However, the same approach taken to retrieve ClO detection limits could be used to calculate the instrument detection limit in regard to BrO for each of the three 2008 measurement locations (sites 3, 4 and 5).

While the SO_2 absorption cross-section is no longer very prominent in the BrO evaluation range (337-353 nm), the retrieved BrO detection limit was still found to depend on the SO_2 column density of a particular measurement. Here, the dependency was not caused by an imperfect removal of the SO_2 absorption structures, as was the case for ClO. However, a high SO_2 column density indicates a large amount of volcanic gas in the instrument's optical path. As the volcanic plume contained condensed water droplets and aerosols, an increase in the amount of volcanic gas in the optical path had two effects. For one, light from the LED light source was scattered out of the optical path, thus reducing the measured signal. At the same time, a larger amount of solar radiation was scattered into the light path. In combination, the two effects greatly increased the contribution of scattered solar radiation in the measurement

spectra. Errors in the correction of this solar radiation degraded the detection limit for high SO_2 column densities.

The retrieved BrO detection limits at sites 3, 4 and 5 are depicted in Fig. 7.25, Fig. 7.26, and Fig. 7.27. In each case, the above described dependency on the SO_2 column density can be observed. The calculated detection limits indicate upper limits for the BrO/SO_2 molecular ratio of between 2 and 3×10^{-4} (the detection limit at Masaya was more than an order of magnitude lower, see section 7.3.3). Previous reports of BrO/SO_2 ratios at Mt. Etna (e.g. *Bobrowski and Platt 2007, Bobrowski et al. 2007*) indicate typical values of between 1×10^{-4} and 4×10^{-4}. The upper limits obtained in the LP-DOAS measurements described above exclude the upper end of this range. They indicate that the BrO/SO_2 ratio was in the lower half of the previously reported range at the LP-DOAS measurement sites. This finding is in agreement with the increase in BrO/SO_2 ratio with plume age reported by *Bobrowski et al. 2007* (also see discussion in section 7.6). An improved system for recording background measurements of solar radiation scattered into the optical path of the LP-DOAS is necessary to further reduce the detection limit for BrO, and therefore make a positive identification and quantification of the species possible with the mobile, LED-powered LP-DOAS instrument. A summary of all ClO and BrO upper limits attained in the LP-DOAS measurements at Mt. Etna is given in Tab. 7.2.

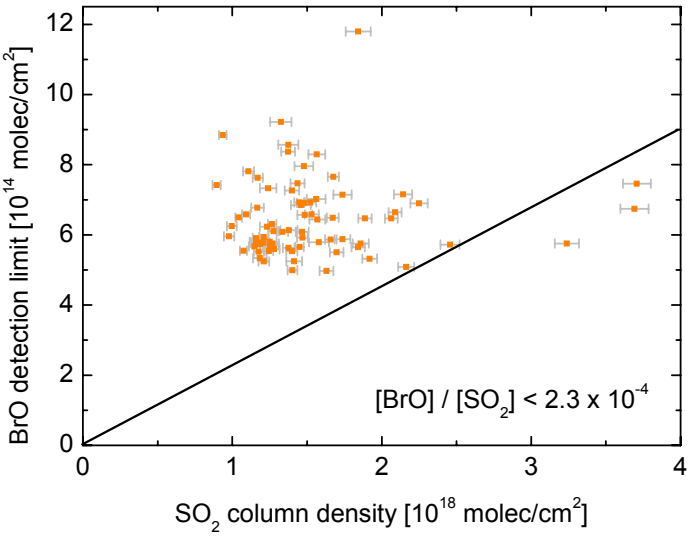

Fig. 7.25 - BrO detection limit achieved during the LP-DOAS measurements on July 09, 2008 downwind of the NE crater on the eastern flank of Mt. Etna (site 3). BrO was below detection limit for all measurements. An upper limit for the BrO/SO_2 molecular ratio of 2.3×10^{-4} was retrieved.

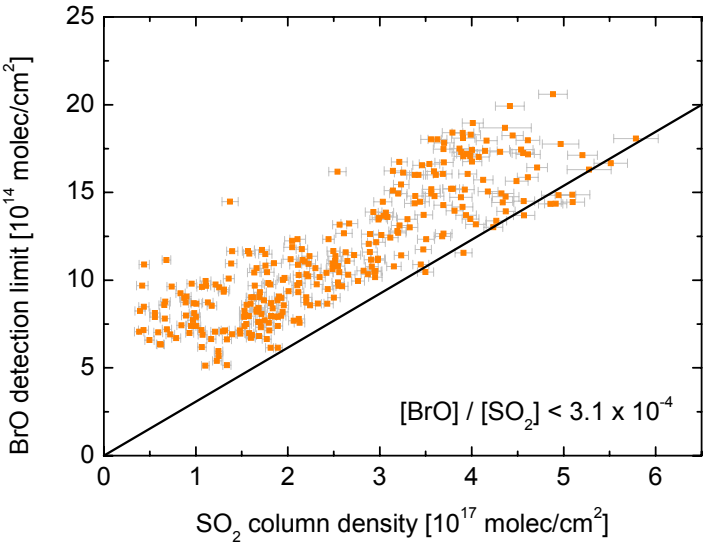

Fig. 7.26 – BrO detection limit achieved during the LP-DOAS measurements on July 10, 2008 downwind of the degassing vent on the eastern flank of the SE crater of Mt. Etna (site 4). BrO was below detection limit for all measurements. An upper limit for the BrO/SO_2 molecular ratio of 3.1×10^{-4} was retrieved.

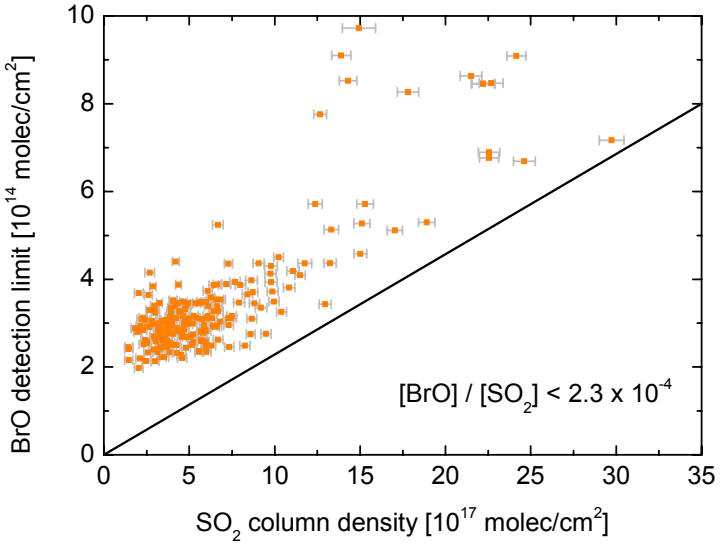

Fig. 7.27 – BrO detection limit achieved during LP-DOAS measurements on July 15, 2008 at the rim of the NE crater of Mt. Etna (site 5). BrO was not detected during the measurement, but a BrO/SO_2 ratio of more than 2.3×10^{-4} could be ruled out.

Site	Measurement Date	Measurement Location	Plume Sampled	Upper Limit ClO/SO_2	Upper Limit BrO/SO_2
1	Aug 24, 2007	Summit	Voragine	9×10^{-3}	–
2	Aug 24, 2007	Summit	North East	6×10^{-3}	–
3	July 9, 2008	Downwind	North East, Fumarole	1.5×10^{-3}	2.3×10^{-4}
4	July 10, 2008	Downwind	Fumarole, NE, Voragine	1.9×10^{-3}	3.1×10^{-4}
5	July 15, 2008	Summit	North East	1.3×10^{-3}	2.3×10^{-4}

Tab. 7.2 – Summary of the upper limits for the molecular ratios of ClO/SO_2 and BrO/SO_2 obtained during LP-DOAS measurements at Mt. Etna in 2007 and 2008.

7.6 Conclusions and Implications

In this chapter, the measurements of halogen oxides in volcanic plumes using an active Long Path DOAS instrument are presented. As this instrument uses its own light source, it was possible for the first time to study the BrO/SO_2 ratio in the plume of Masaya volcano at night. While not entirely unexpected, the results allow new conclusions about BrO formation to be drawn. During the daytime, the BrO/SO_2 ratio was similar to that measured previously at the crater of Masaya volcano with passive DOAS instruments (*Bobrowski and Platt 2007*). However, BrO was below the detection limit during night-time hours, a strong indication that the measured BrO is not directly emitted from Masaya volcano but is instead the product of photodissociation of precursors, e.g. Br_2, which requires solar radiation. It supports the theory that BrO is mainly produced in autocatalytic radical reactions requiring photochemistry. The "bromine explosion" mechanism (R. 7.1 - R. 7.4) is a reaction cycle often postulated to this extent (*Platt and Lehrer 1997, Wennberg 1999, Platt and Hönninger 2003, Bobrowski et al. 2007, Kaleschke et al. 2007, Simpson et al. 2007, von Glasow and Crutzen 2007*). HOBr can effectively convert one bromine atom into two by oxidizing bromide at particle surfaces (R. 7.1). The resulting gas phase Br_2 is photolyzed very rapidly during the day (timescales on the order of minutes), and can then quickly react with O_3 to form BrO (R. 7.2, R. 7.3). This can in turn react with HO_2, which is either formed photochemically during daytime hours or possibly through in situ high temperature reactions in the early plume (R. 7.4). The resulting HOBr starts the cycle anew.

$$HOBr_{(gas)} + Br^-_{(aq)} + H^+_{(aq)} \rightarrow Br_{2\,(gas)} + H_2O \qquad \textbf{R. 7.1}$$

$$Br_2 + h\nu \rightarrow 2\,Br \qquad \textbf{R. 7.2}$$

$$2\,Br + 2\,O_3 \rightarrow 2\,BrO + 2\,O_2 \qquad \textbf{R. 7.3}$$

$$2\,BrO + 2\,HO_2 \rightarrow 2\,HOBr + 2\,O_2 \qquad \textbf{R. 7.4}$$

According to this theory, BrO is a product of reactions requiring the mixing of ambient air into the plume as well as incident solar radiation. Therefore, it should be noted that BrO measurements performed at volcanoes are likely always highly dependent on the degree of plume mixing (as determined by turbulence and the distance from the emission source) as well as on the solar radiation intensity (as given by time of day, latitude, elevation and cloud/aerosol conditions). These parameters therefore need to be taken into account when comparing BrO/SO_2 ratios from different measurements performed at different geographic locations at different times. An insufficient plume age and mixing with ambient air is likely also the reason why the BrO/SO_2 ratio was in the lower range of previous reports at the LP-DOAS sites at Mt. Etna.

The fact that no ClO or OClO was detected at Masaya or Etna volcanoes is surprising, as measurements in 2003 with passive DOAS instruments showed ClO column densities exceeding 5×10^{17} molecules/cm^2 and a ClO/SO_2 ratio of more than 8% at times (*Bobrowski 2005*), which is more than one order of magnitude above the detection limit achieved here. In fact, the following rough calculation indicates that the ClO concentration may well be even lower than our direct measurements show:

The OClO column density detection limit obtained in the LP-DOAS measurements at Masaya was 5×10^{13} molecules/cm^2. Assuming an evenly distributed concentration along 100 meters of the total light path (a conservative estimate), this would correspond to a concentration detection limit of $[OClO]_{lim} = 5\times10^9$ molecules/cm^3. Considering that the SO_2 column density often reached values in excess of 5×10^{18} molecules/cm^2 during the measurements, and that the average daytime BrO/SO_2 ratio was 3×10^{-5}, typical plume concentrations of BrO are estimated to be around 1.5×10^{10} molecules/cm^3. The main reaction believed to be responsible for the formation of OClO is the combination of BrO and ClO:

$$BrO + ClO \rightarrow OClO + Br \qquad \textbf{R. 7.5}$$

The reaction rate coefficient of R. 7.5 is $k_5 = 6\times10^{-12}$ cm^3 molecule^{-1} s^{-1} at room temperature (*Friedl and Sander 1989*). The direct oxidation of ClO by O_3 is not relevant, as it is several orders of magnitude slower (*Birks et al. 1977*). The destruction of OClO by O_3 oxidation is also slow (*Wongdontri-Stuper et al. 1979*). The dominating daytime sink of OClO is its photodissociation:

$$OClO + h\nu \rightarrow ClO + O \qquad \textbf{R. 7.6}$$

The photolysis frequency for reaction R. 7.6 of $J_{OClO} = 7.6\times10^{-2}$ s^{-1} implies a half-life for OClO of only 9 seconds in the atmosphere during the daytime (*Birks et al. 1977*). Due to the speed of reactions R. 7.5 and R. 7.6, it is reasonable to assume a steady state between the two:

$$[BrO]\cdot[ClO]\cdot k_5 - [OClO]\cdot J_{OClO} = 0 \qquad \textbf{Eq. 7.1}$$

Considering the OClO concentration detection limit of $[OClO]_{lim} = 5\times10^9$ molecules/cm^3, this leads to an upper limit for the ClO concentration:

$$[ClO] < \frac{J_{OClO}}{[BrO]\cdot k_5}\cdot[OClO]_{lim} = 4\cdot10^9 \frac{molec}{cm^3} \qquad \textbf{Eq. 7.2}$$

Assuming a 100 m light path in the plume, this corresponds to a column density of 4×10^{13} molecules/cm^2 and a ClO/SO_2 ratio of 8×10^{-6}. This value is more than 2 orders of magnitude below the ClO detection limit achieved in the measurements at Masaya. While only a rough estimate, this calculation points out that the ratio of ClO/OClO should be in the order of unity under the described conditions. Since the sensitivity of active DOAS instruments is about 2 orders of magnitude higher for OClO than for ClO (typically 3 orders of magnitude for passive instruments), this calculation suggests that OClO should always be detectable in volcanic plumes in which ClO is found. When applied to this study, it suggests an upper limit for the ClO/SO_2 ratio of around 10^{-5}, more than 2 orders of magnitude below the actual detection limit of the LP-DOAS instrument (about 5×10^{-3}), and more than 3 orders of magnitude below the detection limit of a passive DOAS.

This, of course, stands in contrast to past measurements of ClO with passive DOAS instruments. Aside from the measurements at Masaya (*Bobrowski 2005*), *Lee et al. 2005* reported ClO column densities of up to 5.9×10^{16} molecules/cm^2 and an average ClO/SO_2 molecular ratio of 4.9% in the plume of Sakurajima volcano in Japan. *Bobrowski et al. 2007* also detected ClO and OClO in the plume of Mt. Etna, Italy. Here, peak ClO column densities of 2.1×10^{17} molecules/cm^2 were measured along with an average ClO/SO_2 molecular ratio of about 5%. OClO was said to be approximately 850 times less abundant than ClO, with columns reaching 2.45×10^{14} molecules/cm^2 and an average $OClO/SO_2$ ratio of 5.7×10^{-5}.

There are several possible explanations for the discrepancy of the results of this study compared to past measurements. For one, the halogen composition of volcanic plumes is known to depend on several factors that can change over time such as the volcanic activity (*Aiuppa et al. 2004b*) and the depth of degassing (*Burton et al. 2007b*) at basaltic volcanoes. On the other hand, the total SO_2 flux emitted from Masaya volcano was similar during the two measurement periods. *McGonigle et al. 2004* found an average SO_2 flux of approximately 11 kg(SO_2)/s (950 t(SO_2)/d) during measurements in 2003, which is comparable to the values measured by the NOVAC scanning DOAS instruments during the measurement campaign. Also, *Horrocks et al. 1999* showed that the halogen plume composition was remarkably stable

at Masaya volcano in 1998/99, with very little variation on the scale of days, months, and even between two measurements one year apart.

A more important difference may be that LP-DOAS measurements are limited to measurement geometries in which the plume passes between the telescope and retro reflectors. The measurements conducted here were therefore sampling an area of the plume much closer to the active vent than is typical for passive DOAS measurements. The above mentioned ClO measurements at Etna and Sakurajima volcanoes were both conducted several kilometres away from the crater where the plume has aged more. In both cases, the respective BrO/SO_2 ratios measured by passive DOAS of 1×10^{-3} and 2.1×10^{-4} were considerably higher than in this study, quite possibly a consequence of a more advanced state of the bromine explosion process. Assuming that chlorine oxides are not directly emitted from the volcano but formed in the plume as is the case for BrO, and that the formation of chlorine oxides is slower than that of BrO (*Bobrowski et al. 2007*) as the process is not autocatalytic and only begins after the aerosol phase is considerably depleted in HBr, this could well explain the absence of ClO and OClO close to the vent. A recent model study by *Roberts et al. 2008* supports this theory.

OClO was detected for the first time at Mt. Etna, Italy. *Bobrowski et al. 2007* observed column densities of up to 2×10^{14} molecules/cm^2 and an average $OClO/SO_2$ molecular ratio of 5.7×10^{-5} at a location 3 km downwind of the crater. At the same time, the ClO/SO_2 ratio was approximately 5×10^{-2}. The discrepancy between these two values stands in contrast to the chemical mechanism presented above (R. 7.5, R. 7.6, Eq. 7.1, Eq. 7.2) which suggests fairly equal amounts of ClO and OClO. It is therefore conceivable that previous measurements of ClO are not entirely reliable due to the difficulties involved in measuring this species with the passive DOAS technique, as mentioned in section 7.2.1 and by the authors themselves (*Bobrowski 2005, Bobrowski et al. 2007*). Another indication for this finding is that attempts at modelling plume chemistry conducted by *Bobrowski et al. 2007* could not reproduce their measured ClO concentrations. The model indicates that, in contrast to bromine, chlorine is not quickly taken up by aerosols but rather remains largely in the gas phase in its less reactive form of HCl, and an efficient recycling mechanism converting HCl to reactive chlorine is missing.

It is however also possible that the chemistry leading to ClO formation is not yet completely understood, and that the mechanism presented in this study as well as that used in past modelling studies is incomplete. To conclusively clarify the magnitude and formation mechanisms of ClO in volcanic plumes, active LP-DOAS measurements at other actively degassing volcanoes are needed, especially at those where high halogen emissions have been observed in the past.

8 Quantifying and correcting for radiative transfer effects in and around volcanic plumes

8.1 Introduction

Remote sensing techniques have become a widespread tool for measuring volcanic emissions. Their area of deployment ranges from volcanic monitoring and risk assessment to specific scientific studies of volcanic activity and plume chemistry. Two types of remote sensing techniques employing absorption spectroscopy can be distinguished. Active remote sensing instruments use artificial light sources while passive instruments use natural sources such as the sun, moon or stars.

All passive and most active remote sensing techniques do not measure the concentration c of a substance, but rather the slant column density S. The column density S is the integral of the concentration of the absorber over the path that radiation takes on its way from the light source to the instrument (see section 3.1). Active instruments have the advantage that their light path is well-defined. Radiation leaves the artificial source, may be redirected by some optical system, passes through the volcanic plume, and is then collected by the receiving optics and analyzed by the instrument. Thereby, the optical density τ of characteristic trace gas absorption lines is measured, which is proportional to the column density S defined as

$$S = \int_L c(l) \cdot dl \qquad \text{Eq. 8.1}$$

Since the optical path length L is known, the average concentration along the path can then easily be calculated according to Eq. 1 as $c_{avg} = S/L$. Examples for such remote sensing setups include active Long-Path Differential Optical Absorption Spectroscopy (LP-DOAS) (see

chapter 7 and *Kern et al. 2008a*) and active Fourier Transform Infrared (FTIR) systems (e.g. *Oppenheimer et al. 1998a*).

Some passive remote sensing instruments, such as solar occultation FTIR (*Francis et al. 1998*) or direct sun DOAS (*Sommer 2008*) measure direct light from a natural light source. For these setups, the optical path is also well-defined. However, the plume must be between the light source (e.g. the sun) and the instrument for the measurements to be performed. Therefore, the instruments must either be mobile and able to adapt to different sun and plume positions, or can only be used under suitable conditions, thus considerably reducing the acquisition efficiency. The presence of clouds in the ambient atmosphere or a high amount of aerosols and condensed water droplets in the plume can also disrupt the well-defined optical path by greatly enhancing scattering processes. Additional details of the solar occultation geometry are given in section 3.3.1.

The alternative light source for passive instruments is sunlight scattered in the atmosphere (see section 3.3.2). The advantage of this source is that it is always present during daylight hours, so stationary instruments can measure the volcanic emissions whenever the plume is in sight of the instrument. Scattered sunlight has been used for techniques such as correlation spectroscopy (COSPEC) (*Moffat and Millán 1971, Stoiber and Jepsen 1973, Stoiber et al. 1983*), passive DOAS in scanning and mobile modes (*Galle et al. 2003, Bobrowski 2005, Elias et al. 2006*), imaging DOAS (*Bobrowski et al. 2006, Louban et al. 2009a*), and the novel SO_2 camera (*Mori and Burton 2006, Bluth et al. 2007, Kick 2008*). For scattered light measurements, however, the light path from the sun to the instrument is variable. While this has been known for some time (*Millán 1980*), the issue of how to correct for errors caused by variations in photon paths was unresolved to date. The focus of this study is to quantify the effects of radiative transfer on results obtained by passive remote sensing measurements using scattered sunlight. We also present the first method for quantitative correction of the measurement errors caused by radiative transfer.

To this end, the concept of the "air mass factor" (AMF) is employed. Typically, the AMF is defined as the ratio between the measured slant column density S of a trace gas and its vertical column density V along a vertical path passing through the entire atmosphere (see e.g. *Solomon et al. 1987, Perliski and Solomon 1993, Marquard et al. 2000, Sinreich et al. 2005, Wagner et al. 2007*). In this study, a slight modification of the concept will be used. Here, the AMF A_T is defined as the ratio between the measured column density $S_{measured}$ and the theoretical column density $S_{straight}$ on a straight line through the volcanic plume along the instrument's viewing direction.

$$AMF = \frac{S_{measured}}{S_{straight}} \qquad \textbf{Eq. 8.2}$$

The two definitions are identical for an instrument looking straight towards the zenith through a volcanic plume directly overhead. However, in the case of a diagonal viewing geometry (see

Fig. 8.8), the straight column density along the diagonal viewing direction will be used in the denominator of the AMF definition, not the vertical column density V.

We use a numerical forward model to gain insight into the radiative transfer processes taking place in and around volcanic plumes. As SO_2 is the volcanic emission species most frequently measured by passive remote sensing techniques, we limit this study to the wavelength range between 300 and 325 nm in which the differential absorption of SO_2 is prominent. The model's output parameter is the AMF, which is calculated from the sum of the column densities along all individual simulated photon paths weighted by the respective path probability. The concentration of SO_2 is assumed to be constant throughout the plume in the model scenarios shown here. Therefore, the resulting AMFs yield the average optical path in the volcanic plume according to Eq. 1. Since each photon takes a different path from the sun to the instrument, the column density seen by an individual photon is theoretically described by the integral of the concentration c over its optical path. However, the measured slant column density represents the average over all photon paths. The AMF therefore describes the average path length inside the plume. An AMF of 1 would mean that the average photon path is equal to the length of the straight line through the plume. Values larger than unity indicate extended photon paths e.g. caused by multiple scattering events inside the plume. However, AMFs below 1 are also possible and imply a shortened average path in the plume e.g. caused by a part of the measured photons missing the plume entirely (see section 8.2.2). These phenomena are described in the following case studies.

8.2 Case studies

As mentioned above, the optical path from the sun to the instrument is different for each individual measured photon in scattered light applications. While it is impossible to know the optical path of a specific photon, this is not necessary because the signal recorded by the instrument is already the average of many statistically independent measurements. Therefore, knowledge of the intensity weighted average optical path is sufficient for calculating average trace gas concentrations from the retrieved column density according to Eq. 8.1. In the following, three different radiative transfer cases will be defined which all contribute to the average optical path of a ground-based remote sensing measurement. In section 8.3, these scenarios will then be quantitatively discussed.

8.2.1 Idealized light path

When conducting remote sensing measurements of volcanic plumes using scattered light in the past, the idealized light path was usually assumed to be the average optical path. In this case, photons are only scattered towards the instrument in the atmosphere behind the plume. They then pass the plume in a straight line and are detected by the instrument. The idealized light path is shown in green in Fig. 8.1. However, even under ideal measurement conditions in

the absence of ambient clouds and aerosols and in the case of a transparent plume, not all photons follow the idealized optical path. The question is rather: what is the contribution of other paths to the measured signal? A method for quantifying these contributions is discussed in section 8.5.

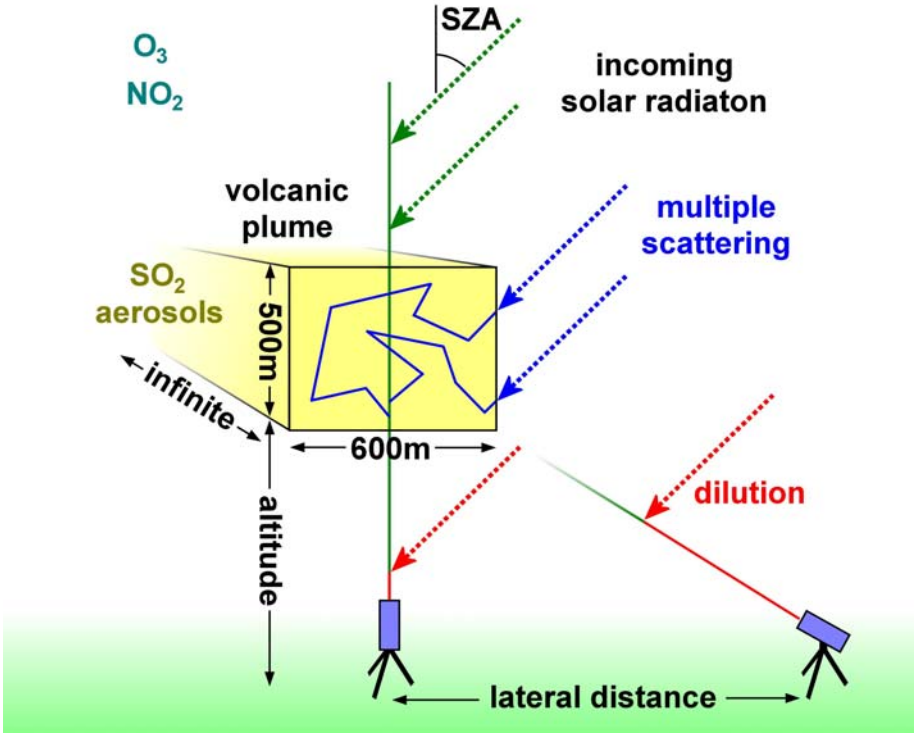

Fig. 8.1 – Schematic of the simulated measurement geometry. The investigated volcanic plume extended 500 m in vertical direction, 600 m in horizontal direction, was infinitely long and was located at different altitudes above the instruments. Inside the plume, variable SO_2 and aerosol concentrations were assumed. Outside the plume, the absorption of O_3 and NO_2 was considered. The solar zenith angle (SZA) was 30° for all scenarios. Also, different possible photon paths from the sun to a remote sensing instrument are shown. The green path shows the idealized photon path: light is scattered above the volcanic plume and passes through the plume in a straight line. The red path represents the dilution effect. Light is scattered between the plume and the instrument and effectively dilutes the measured column density. The blue path depicts the case of multiple scattering occurring inside the plume causing an extension of the light path and therefore an enhancement of the measured column density.

8.2.2 The 'light dilution' effect

In the atmosphere, sunlight is scattered on air molecules (Rayleigh and Raman scattering) and on aerosol particles and condensed water droplets e.g. in clouds (particle scattering). Remote

sensing instruments use this scattered light as a light source to measure the composition of volcanic plumes from a safe distance to a possibly active crater. However, besides the photons scattered behind the plume, some photons will also be scattered in the direction of the instrument between the instrument and the plume (red path in Fig. 8.1). These photons have not passed through the plume and therefore this contribution does not contain spectral absorption structures originating from plume constituents. In effect, light scattered between the instrument and the plume effectively dilutes the measured column density. The so-called 'light dilution' effect was recently quantitatively measured by *Mori et al. 2006* using DOAS instruments.

8.2.3 Multiple scattering

Volcanic plumes often contain a large amount of water vapor. While in gaseous form at high temperatures, this water vapor can condensate as it cools after being emitted into the atmosphere. Therefore, volcanic plumes are often not transparent, but rather more or less opaque. This, along with the presence of solid particles such as ash, can cause an increase in particle scattering as compared to transparent plumes. Therefore, photons can be scattered multiple times inside the volcanic plume and the path length inside the plume may be considerably longer than the straight line (blue path in Fig. 8.1). *Pfeilsticker et al. 1998* and *Veitel et al. 1998* have shown that photon paths in clouds can be enhanced by many tens of kilometers in large, optically thick stratus clouds (also see *Erle et al. 1995, Wagner et al. 1998*). Depending on the size and opacity of a specific volcanic plume, this may occur here as well. However, in the case of very strong absorption inside the plume (either from trace gases or absorbing aerosols), the average photon path in the plume can also be decreased by the presence of water droplets and aerosols, as these constituents can increase the probability of photons reaching the instrument which have only penetrated the outer parts of a plume. In the following, the multiple scattering and light dilution effects are quantitatively described.

8.3 Radiative transfer modeling

When modeling radiative transfer, a measurement is simulated by supplying the model with all information relevant to the measurement and subsequently calculating what the virtual instrument would detect. The advantage of a modeling study over a true measurement is that it allows the implementation of user-defined atmospheric conditions. This provides a perfect platform for sensitivity studies, as all relevant parameters for a simulated measurement can be varied individually while keeping the others constant.

8.3.1 Model description

In this study, the radiative transfer model TRACY-II[23] (*Deutschmann 2008*) was applied to several volcanic scenarios. TRACY-II is a backward Monte Carlo model which generates a representative ensemble of individual photon path trajectories through the simulated atmosphere, each representing a solution of the monochromatic radiative transfer equation. The 3 dimensional model was written at the Institute of Environmental Physics, University of Heidelberg and validated with other radiative transfer models (*Wagner et al. 2007*) and measurements (*Deutschmann 2008*). The advantage of the Monte Carlo approach is that the model is close to the underlying physical processes and therefore the model results are most realistic.

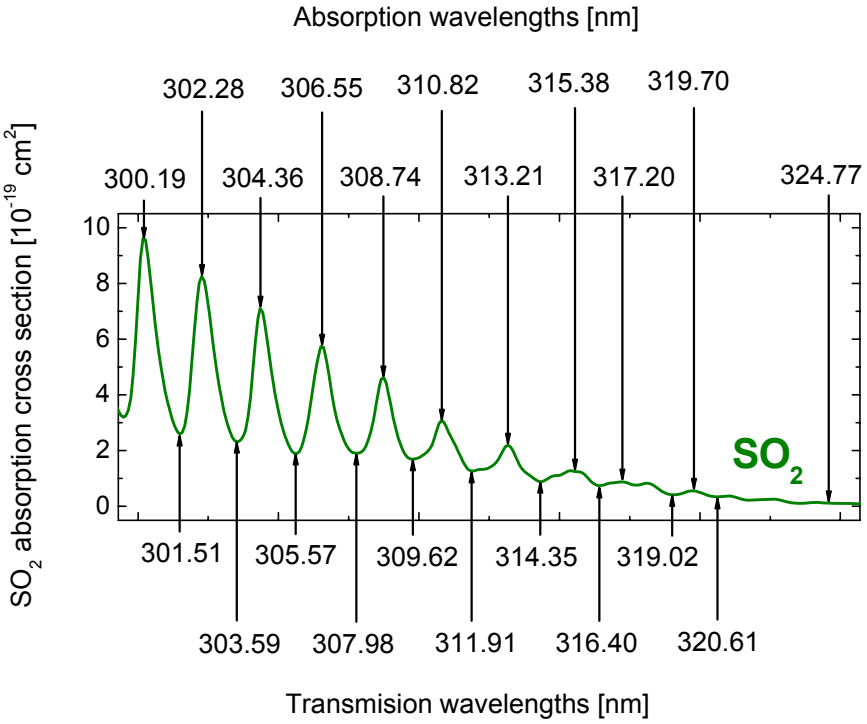

Fig. 8.2 – SO_2 absorption cross-section (green line) according to *Bogumil et al. 2003*. The modeled wavelengths are indicated with arrows. Note that absorption also occurs on the transmission wavelengths near 300 nm.

Because of the importance of SO_2 as a tracer for volcanic activity in general, the radiative transfer model runs were conducted for wavelengths between 300 nm and 325 nm, the spectral range in which SO_2 absorption of scattered sunlight is most prominent. TRACY-II is a monochromatic model, thus only one wavelength could be modeled at a time. This process was repeated for 21 wavelengths between 300 and 325 nm to quantify the wavelength dependence of radiative transfer. As shown in Fig. 8.2, wavelengths were chosen on and

[23] **T**race Gas **RA**diative Transfer Monte **C**arlo (**Y**)Implementation

between the SO_2 absorption lines to allow a description of what each individual absorption band would look like in a measurement from the ground. For the sake of clarity, however, only the wavelengths corresponding to peak absorption of the SO_2 absorption bands are discussed in the following results section. The transmission wavelengths in between the absorption lines were only used to obtain a higher accuracy when simulating true measurement spectra as described in section 8.5, as the effect of absorption occurring on the transmission wavelengths cannot be neglected for strong SO_2 absorption (see Fig. 8.2).

For each scenario, TRACY-II simulates a measured column density S, the definition of which is given in Eq. 8.1. For the calculation, the atmosphere is divided into a discrete three-dimensional grid of voxels. An instrument is placed at some position in this simulated atmosphere, and a representative number N of possible trajectories between the instrument and the sun is calculated according to the physical processes governing radiative transfer in the atmosphere. Next, the radiation intensity I reaching the instrument is computed from the sum of the individual contributions w_i arriving along each trajectory i.

$$I = \frac{1}{N}\sum_i w_i \qquad \textbf{Eq. 8.3}$$

As the attenuation of the individual trajectory intensities w_i by absorption can be expressed according to the Beer-Lambert Law (see Eq. 3.1), the derivative of the total intensity I with respect to the absorption coefficient α_v in each voxel v (defined as the product of the absorption cross-section σ and the absorber concentration c_v) yields

$$\frac{d}{d\alpha_v} I = -\frac{1}{N}\sum_i w_i L_{i,v} \qquad \textbf{Eq. 8.4}$$

Here, $L_{i,v}$ is the light path length of trajectory i in the voxel v. The intensity weighted expectation value of the light path length in the voxel v can be determined by calculating the negative derivative of the logarithm of the intensity I.

$$-\frac{d}{d\alpha_v}\ln(I) = \frac{\sum_i w_i L_{i,v}}{\sum_i w_i} = \langle L_v \rangle \qquad \textbf{Eq. 8.5}$$

The simulated slant column density S is then easily obtained by summing the intensity weighted column densities from each individual voxel.

$$S = \sum_v c_v \cdot \langle L_v \rangle \qquad \textbf{Eq. 8.6}$$

For a more detailed description of the functionality of TRACY-II, see *Deutschmann 2008*.

8.3.2 Scenario description and results

The TRACY-II model was used to implement a simplified 3-dimensional volcanic plume in a simulated atmosphere. Different scenarios were investigated, but in all scenarios the plume was assumed to have a rectangular cross-section with a vertical extent of 500 m, a width of 600 m, and extend indefinitely on either side, as shown in Fig. 8.1. Inside the plume, various amounts of SO_2 and aerosols were simulated. The ambient atmosphere outside the plume was considered to be free of trace gases and clouds or aerosols, except in the last scenario where an ambient aerosol layer was added. However, the absorption of stratospheric ozone and NO_2 were considered by using typical concentration profiles to account for their influence on radiative transfer in the upper atmosphere. An overview of the chosen parameters for the individual scenarios is given by Tab. 8.1. The solar zenith angle was fixed at 30° and the solar azimuth relative to the instrument's viewing direction was kept at 180°, so the sun was always located behind the instrument. A sensitivity study showed that both the solar zenith and azimuth angle play a secondary role, except in the case of ambient aerosols (see AA scenario below). In all presented cases, the instrument field of view was circular with an aperture angle of 0.3°, a typical value for scanning DOAS instruments. Furthermore, a generic planar ground topography with a relatively low surface albedo of 0.03 (compare e.g. *Frederick and Abrams 1981*) was assumed in all scenarios.

Transparent plume, Vertical geometry (TV)

In this first, simple scenario, the plume was assumed to pass directly over the instrument at different altitudes, a geometry typical for a traverse-type DOAS measurement. The SO_2 concentration inside the plume was fixed at 1×10^{12} molecules/cm^3 which corresponds to a vertical column density of 5×10^{16} molecules/cm^2 in the 500 m thick plume, or about 20 ppmm.[24] This is a relatively low SO_2 load for a volcanic plume, but the objective of this scenario was to investigate the dependence of the simulated measurement results on plume altitude. Aerosols were neither considered to be present inside the plume nor in the ambient atmosphere.

The dilution effect described in section 8.2.2 can clearly be seen in the model results of this scenario shown in Fig. 8.3. The higher the plume is above the instrument, the lower the AMF. This decrease in AMF is caused by a relative increase in photons being scattered into the instrument's viewing direction between the plume and the instrument. Because these photons do not display the plume's absorption signal, the measured column density decreases. Interestingly, the wavelength dependency of the dilution effect appears to be almost negligible in this scenario. This appears to contradict the results of *Mori et al. 2006*, who measured a strong wavelength dependency of the dilution effect and recommended using this dependency on wavelength to estimate the magnitude of the effect. Therefore, the lack of wavelength dependence of the simulated AMF is puzzling at first glance. However, while the Rayleigh

[24] The units molecules/cm^2 where converted to ppmm assuming standard pressure and a temperature of 20°C throughout the text: 1 ppmm = 2.5×10^{15} molecules/cm^2

cross-section for scattering on air molecules is proportional to λ^{-4} and changes by 27% between 300 and 325 nm, an increase in scattering towards lower wavelengths both below and above the plume occurs. These increases almost compensate each other and the relative contributions remain almost the same. Only when the distance between instrument and plume approaches the mean free photon path length in the atmosphere (which is approximately 7 km at 300 nm) does the wavelength dependency of the Rayleigh scattering cross-section play a role (see scenario TD). As the results of other scenarios show (see scenarios SV and AV), the influence of SO_2 and aerosol load in the plume is typically far greater.

Scenario	Plume altitude	Instrument lateral distance	SO_2 straight column density	Plume aerosol load	Boundary layer aerosol load
Transparent plume, vertical geometry (**TV**)	*variable*	0 km	20 ppmm	None	none
Transparent plume, diagonal geometry (**TD**)	500 m	*variable*	~ 20 ppmm	None	none
Variable SO_2, vertical geometry (**SV**)	1 km	0 km	*variable*	None	none
Variable aerosol, vertical geometry (**AV**)	1 km	0 km	1000 ppmm	*Variable*	none
Ambient aerosol, diagonal geometry (**AA**)	1 km	3 km	1000 ppmm	8 km^{-1} AEC 500 m visib.	*variable*

Tab. 8.1 – Overview of the investigated radiative transfer scenarios. In each scenario, only a single parameter was varied to determine the sensitivity of the radiative transfer in regard to this quantity. Due to the rectangular cross-section of the plume, the straight column density of the TD scenario varied slightly with the elevation angle of the viewing direction, but this was taken into account when calculating the respective air mass factors.

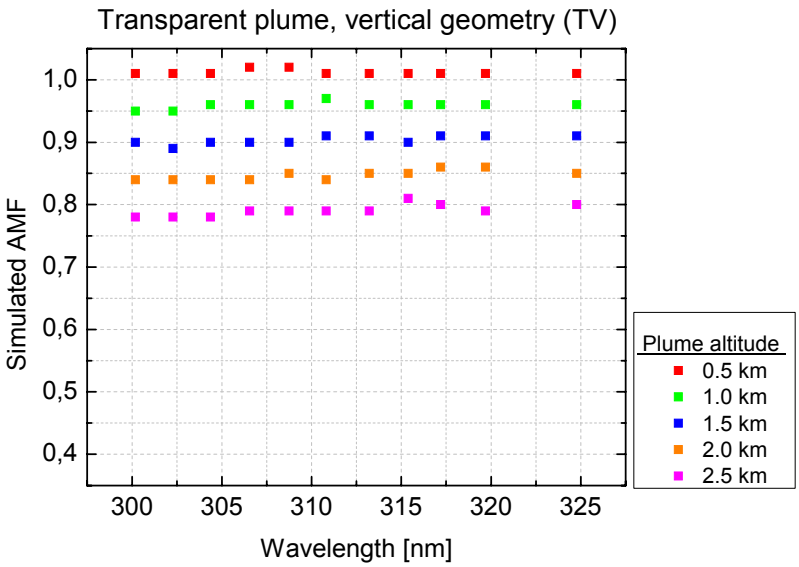

Fig. 8.3 – Results of various model runs for the TV scenario. The dilution effect is clearly visible, as the air mass factors (AMF) decrease with increasing plume altitude. For plumes elevated up to 2.5 km directly above the instrument and low SO_2 column densities, the dilution effect is largely independent of wavelength.

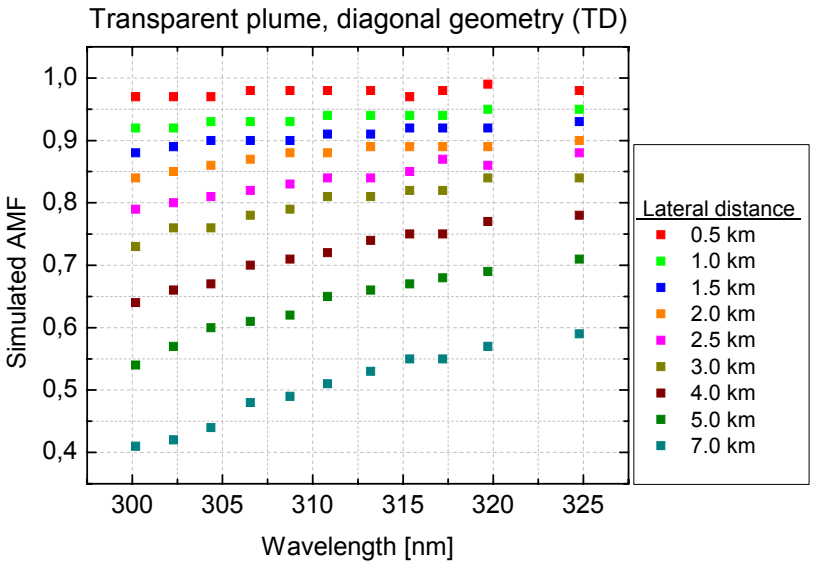

Fig. 8.4 – Results of various model runs for the TD scenario. Individual colors indicate instrument positions at different lateral distances from the plume. The magnitude of the dilution effect is similar to that observed in the TV scenario at equal distances from the plume. For large lateral distances, the dilution effect becomes dependent on wavelength, with shorter wavelengths showing lower AMFs.

Transparent plume, Diagonal geometry (TD)

In this second scenario, the instrument was placed at different lateral distances from the plume, the base of which was fixed at 500 m altitude. Such geometries are typical for stationary scanning DOAS measurements. Otherwise, the conditions remained the same as in the TV scenario, with the SO_2 concentration in the plume again being 1×10^{12} molecules/cm^3 and no aerosols present. The instrument's viewing direction was always chosen to point at the center of the plume by choosing the appropriate instrument elevation angle. Due to the plume's rectangular cross-section, the straight column density varied slightly with the lateral distance and elevation angle, but this variation was accounted for when calculating the respective AMFs.

Fig. 8.4 shows the results of the model runs for the TD scenario. For small lateral distances, the results are comparable to those obtained with the vertical geometry in the TV scenario. As the distance to the plume increases, the dilution continues to grow stronger and the AMFs drop off to values considerably below unity. Also, the AMFs become somewhat dependent on the wavelength at large lateral distances, with smaller AMFs occurring at lower wavelengths. For a lateral distance of 7 km between instrument and plume (approximately the mean free photon path at 300 nm), the AMF at 300 nm is only about 70% of that at 325 nm. Here, the wavelength dependency of the Rayleigh scattering cross-section is influencing the AMF, as the distance to the plume is approaching the mean free photon path length in the atmosphere. Thus, the Rayleigh scattering contributions in front of and behind the plume to the total radiation measured by the instrument are not the same for 300 and 325 nm. However, as the following scenarios show, a far greater AMF dependency on wavelength can be observed for volcanic plumes with higher SO_2 column densities.

Variable SO_2, Vertical geometry (SV)

The goal of this scenario was to analyze to what effect the actual SO_2 concentration inside the plume influences the measured AMF. To this extent, the plume was once again positioned directly over the instrument, this time with a fixed base altitude of 1 km. The SO_2 concentration was varied in the range from 2×10^{12} molecules/cm^3 (40 ppmm) to 1×10^{14} molecules/cm^3 (2000 ppmm). Concentrations within this range are typical for volcanic plumes.

The model results for the SV scenario are shown in Fig. 8.5. The AMF at 325 nm was the same for all SO_2 concentrations. It was slightly below unity, indicating that dilution is again influencing the measurement. However, the AMFs quickly separate towards shorter wavelengths. The higher the SO_2 concentration in the plume, the stronger the AMF decreases towards 300 nm. For a vertical column density of 2000 ppmm, the AMF at 300 nm is less than 50% of its value at 325 nm, even though the plume is only 1 km above the instrument (compare to the TV scenario). This indicates that the average photon paths in the plume are much shorter for wavelengths corresponding to the stronger SO_2 absorption bands, especially at high SO_2 loads.

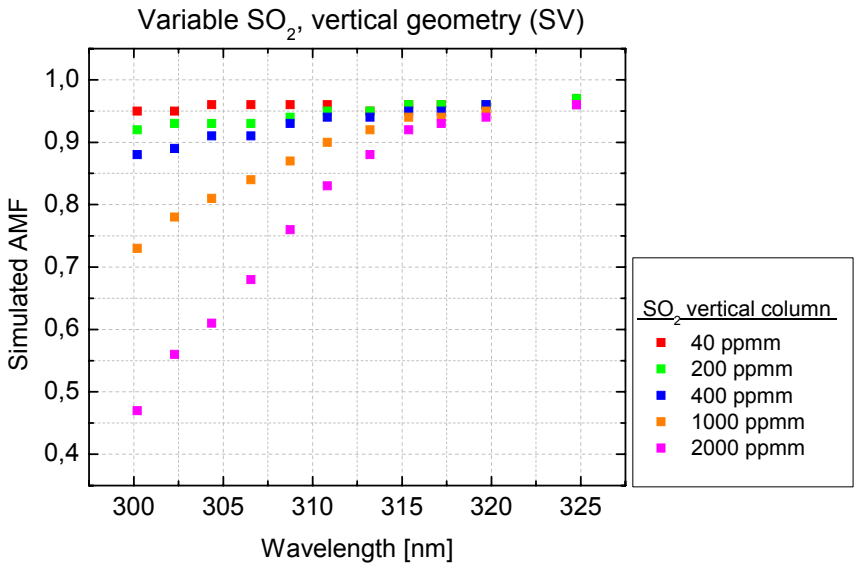

Fig. 8.5 – Results of various model runs for the SV scenario. Individual colors indicate different vertical column densities of SO_2. For high SO_2 loads, the AMF becomes strongly wavelength dependent. The light path in the plume is much shorter for wavelengths on the strong absorption bands near 300 nm than for wavelengths on the weaker bands around 325 nm.

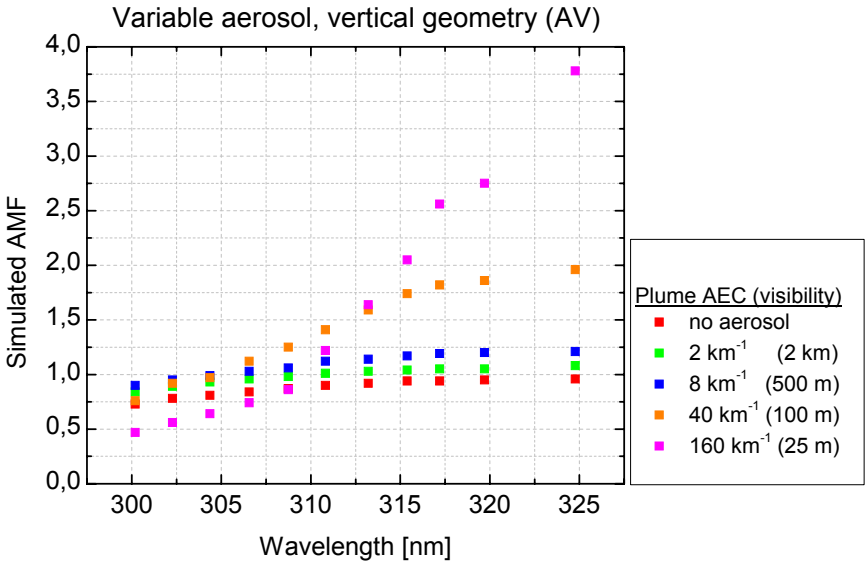

Fig. 8.6 – Results of various model runs for the AV scenario. Individual colors indicate different aerosol extinction coefficients (AEC) inside the plume. The corresponding approximate visibility inside the plume is given in parenthesis. Note the different scale in this diagram. High aerosol loads lead to a strong increase in optical path length inside the plume and therefore AMF at wavelengths around 325 nm, but short optical paths are much more probable for wavelengths on the strong absorption bands near 300 nm.

The reason why the SO_2 concentration influences the dilution effect can be explained by the fact that SO_2 is typically a 'strong absorber' in volcanic plumes, i.e. it absorbs enough radiation to significantly alter the radiative transfer within the plume at certain wavelengths. The dilution effect causes photons to enter the field of view of the instrument without ever having passed through the plume. The relative contribution of these photons to the measurement signal depends not only on the ratio of photons scattered towards the instrument behind as opposed to in front of the plume (analyzed in the previous two scenarios), but also on the probability that radiation of a certain wavelength can penetrate the plume at all. As the SO_2 absorption lines around 300 nm are significantly stronger than those at 320 nm, the probability of a photon passing through the plume on one of these strong absorption lines becomes very small for high SO_2 column densities. In such a case, the relative contribution of the dilution effect is significantly larger than for lower SO_2 loads or higher wavelengths. As the column densities and AMFs are calculated from the logarithm of the measured intensity according to the Beer-Lambert law of absorption, the dilution effect is not linearly proportional to the incident intensity but rather affects strong absorption lines more than weak ones.

Variable Aerosol, Vertical geometry (AV)

This scenario was set up to study the influence of aerosols inside a volcanic plume on radiative transfer. Two types of aerosols can typically be found inside volcanic plumes. Explosive eruptions often produce plumes containing large amounts of ash. Ash plumes are typically dark, a result of a high degree of aerosol absorption i.e. aerosols with a low single scattering albedo (SSA) (see e.g. *Goody and Young 1989*). Light entering plumes of this type is to a large part absorbed by aerosols and cannot easily penetrate the plume. Ash plumes will be the subject of an upcoming independent study. Here, we limit ourselves to plumes from effusively degassing volcanoes which often contain condensing water and typically appear white since water droplets have a high SSA (close to unity). In this case, aerosol scattering outweighs aerosol absorption. Photons entering the plume will usually leave it again, although the average photon path may be considerably extended due to multiple scattering events. This type of plume is usually dominated by sulfate aerosol and condensed water vapor.

In this scenario (AV), a white plume with different aerosol optical densities was considered. As in scenario SV, the plume was located directly over the instrument and spanned the altitude range of 1.0 to 1.5 km. The SO_2 concentration inside the plume was set to 5×10^{13} molecules/cm^2 corresponding to a straight column density of 1000 ppmm, a typical value found at volcanoes. Different amounts of scattering aerosols filled exactly the same volume. Aerosol scattering was approximated by Mie theory and the Henyey-Greenstein phase function (*Henyey and Greenstein 1941*) using an asymmetry parameter of g = 0.8 (see e.g. *Liu et al. 2008*). An SSA of 1 was assumed, indicating a purely scattering aerosol, a good approximation for sulfate aerosol (e.g. *Ogren et al. 1981*). The aerosol extinction coefficient (AEC) inside the plume was varied between 2 km^{-1} and 160 km^{-1} in different model runs. In order to better illustrate the magnitude of the AEC, the approximate visibility inside the plume assuming a homogeneous aerosol distribution can be calculated for each value. The

corresponding approximate visibilities (for a contrast of about 2 %) are given in parenthesis in the legend of Fig. 8.6. The AECs assumed here are higher than most previous studies have assumed (compare e.g. *Spinetti et al. 2003*), the reason for this being that conditions were simulated that are typical of volcanic plumes in close proximity to the emission vent, where plume opacity is high.

The results of the model runs with this scenario are shown in Fig. 8.6. As the aerosol load of the plume is slowly increased, the simulated AMFs initially increase for all wavelengths. This is a result of an extension of the average light path caused by multiple scattering inside the plume. For high aerosol loads and therefore opaque plumes, (AEC > 8 km^{-1}, visibility < 500 m), the photon path enhancement due to multiple scattering becomes dependent on wavelength. For wavelengths around 325 nm, the light paths continue to grow, causing the AMF to increase to values far above unity. For an AEC of 160 km^{-1} (approx. 25 m visibility), the measured column density at 325 nm would overestimate the true straight column by a factor of almost 4 (note the significantly different scale in Fig. 8.6 as opposed to the previous figures). At lower wavelengths, however, the AMFs do not increase as much, and even begin to decrease for high aerosol loads. Strong SO_2 absorption is again responsible for this. Long path lengths inside the plume become increasingly unlikely the stronger the SO_2 absorption is. In fact, an increased aerosol load in the plume will also cause short photon paths to become more probable. Paths in which photons do not penetrate deep into the plume but are rather scattered back out of the plume near the surface become more likely in the presence of scattering aerosols. While these paths are still much less likely than long paths in the case of weak absorption, strong SO_2 absorption around 300 nm eliminates long photon paths, and short paths dominate the measured signal. As a result, the AMF actually decreases for short wavelengths where SO_2 absorption is strong.

Ambient aerosols, diagonal geometry (AA)

Obviously, volcanic plumes are not always surrounded by virtually aerosol free air masses. Depending on the geographic location and emission height, plumes can either be emitted into the planetary boundary layer (PBL) or above it. If emitted into the PBL, aerosol loads in the ambient air will often be considerable, depending on factors such as meteorology, proximity to urban areas, and surrounding terrain type. These factors also determine the optical properties of the aerosols present. Dust and soot, for example, are dark and have a low SSA, while suspended water droplets and sulfate aerosols are white and have SSAs approaching unity (e.g. *Kudo et al. 2008, Liu et al. 2008* and references therein). Above the PBL, aerosol loads will be lower, but the presence of clouds can greatly influence radiative transfer. For remote sensing measurements, not only the aerosol load at the location of the plume is relevant, but also the conditions along the entire light path from the sun to the instrument. Therefore, numerous scenarios can be conceived. In this study, we limit ourselves to a single scenario to demonstrate the importance of ambient aerosols.

In this final scenario, a typical measurement of a condensing plume was simulated. The plume was located between 1 and 1.5 km above and at a lateral distance of 3 km from the instrument. Again, the straight column density was fixed to 1000 ppmm. The plume contained a scattering aerosol (SSA = 1, g = 0.8) with an AEC of 8 km^{-1} (500 m visibility). This plume was emitted into a simulated PBL which extends to 2 km above the ground containing a homogeneously mixed aerosol with different AECs between 0 and 0.5 km^{-1}. The ambient aerosol was assumed to be slightly less reflective than the plume aerosol (SSA = 0.8, g = 0.8).

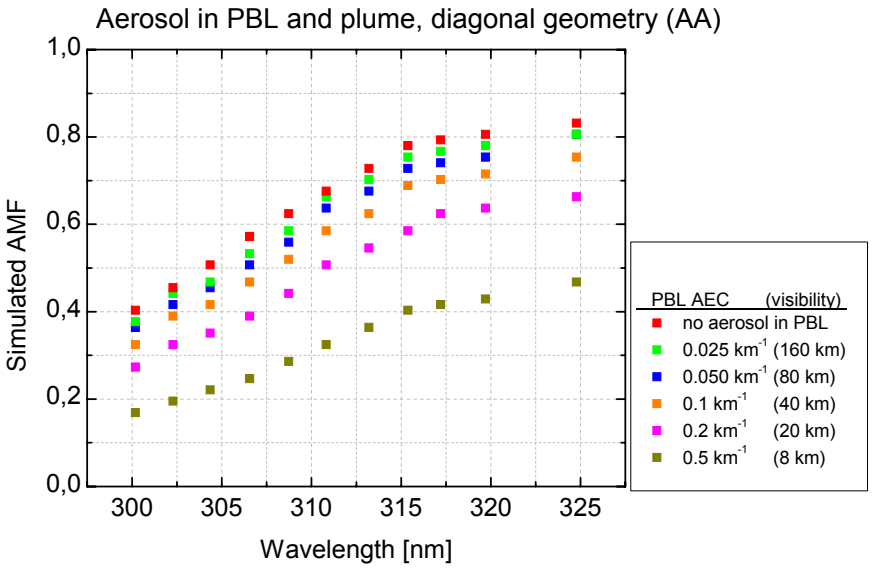

Fig. 8.7 – Results of various model runs for the AA scenario. Individual colors indicate different aerosol extinction coefficients (AEC) in the planetary boundary layer (PBL), which was assumed to be homogeneously mixed and spanning the lowermost 2 km of the atmosphere. The approximate visibility in the PBL is given in parenthesis. Aerosols in the PBL increase the dilution effect, and in this scenario continuously reduce the measured column densities largely independent of wavelength.

Fig. 8.7 shows the results of the ambient aerosol model run (scenario AA). The red points represent a control run in the absence of aerosol in the PBL. The PBL aerosol load is then incrementally increased up to an AEC of 0.5 km^{-1}. Note that this highest considered ambient AEC is still much lower than the plume AEC. The respective approximate visibility in the PBL is again given in parenthesis in the legend. The higher the ambient AEC, the more radiation is scattered on aerosols into the instrument's field of view between the plume and the instrument, thus diluting the absorption signal, but the effect is only weakly wavelength dependent. For AECs below 0.05 km^{-1} (visibility > 80 km), the additional dilution caused by ambient aerosol in the simulated geometry is less than 10 %. However, at higher PBL aerosol loads, the magnitude of additional dilution increases. For an AEC of 0.5 km^{-1} (8 km visibility), the simulated measurement value is additionally reduced by approximately 50 %

due to PBL aerosol dilution. In this case, the simulated measurements greatly underestimate the SO_2 column density, with AMF of between 0.18 and 0.47 depending on the retrieval wavelength. Additional dilution will continue to increase with increasing PBL aerosol load, until the remaining measurement signal is practically lost (e.g. in thick fog).

8.4 Field measurements

In July of 2008, an intensive field study was conducted at Mt. Etna with the goal of characterizing gas emissions using remote sensing instruments. In order to obtain a well constrained overall picture of the position, concentration, and speciation of the volcanic plume, several different instruments were operated at various positions. In the following, simultaneous measurements conducted at 14:30 local time on July 12, 2008 will be discussed.

On this day, 3 different remote sensing instruments were operated. A scanning DOAS instrument (NOVAC mark II instrument described in section 3.5.1) was located on a rooftop in the town of Milo, 10 km east of the active craters at 800 m a.s.l., as shown in Fig. 8.8. From here, it scanned the plume almost vertically in a perpendicular direction (220° azimuth relative to north, see dashed red line in Fig. 8.8), thus measuring plume cross-sections of absorbing gases. At 14:30, the maximum SO_2 absorption was found at 29° elevation above the horizon. The measured vertical plume width was approximately 1 km. A simultaneous automobile-based DOAS traverse measurement (see e.g *McGonigle et al. 2002*) on the A18 roadway 15 km east of the active vents found the center of the plume near the town of Linera (see Fig. 8.8), thus indicating a wind direction at plume height of 306°. The lateral distance between the scanning DOAS instrument and the center of the plume is therefore known to have been 3.8 km, and the plume center was located at 2900 m a.s.l. and 2.1 km above the instrument.

Also located on the rooftop in Milo, an SO_2 camera was set up to image the plume as it was emitted from the vent and blown towards the instrument location. The recently developed SO_2 camera (*Mori and Burton 2006, Bluth et al. 2007, Kick 2008*) uses two UV bandpass filters to alternatively measure the incident solar radiation at 309 ± 4 nm and 325 ± 4 nm. As SO_2 absorption influences the intensity in the first wavelength band and not the second, the logarithm of the obtained intensity ratio is a measure of the SO_2 column density. In this way, 2-dimensional SO_2 distributions can be measured at a high temporal resolution (order of Hz). Both the SO_2-camera measurement technique as well as the technical implementation of the instrument used for the measurements at Mt. Etna are discussed in detail in chapter 4. Fig. 8.9 shows an example measurement recorded with the SO_2 camera. The majority of the plume was emitted from Mt. Etna's northeast crater and was then blown in a south-easterly direction, toward the instrument and to the left in the image. Vertical and horizontal dispersion causes the plume to widen as it is transported.

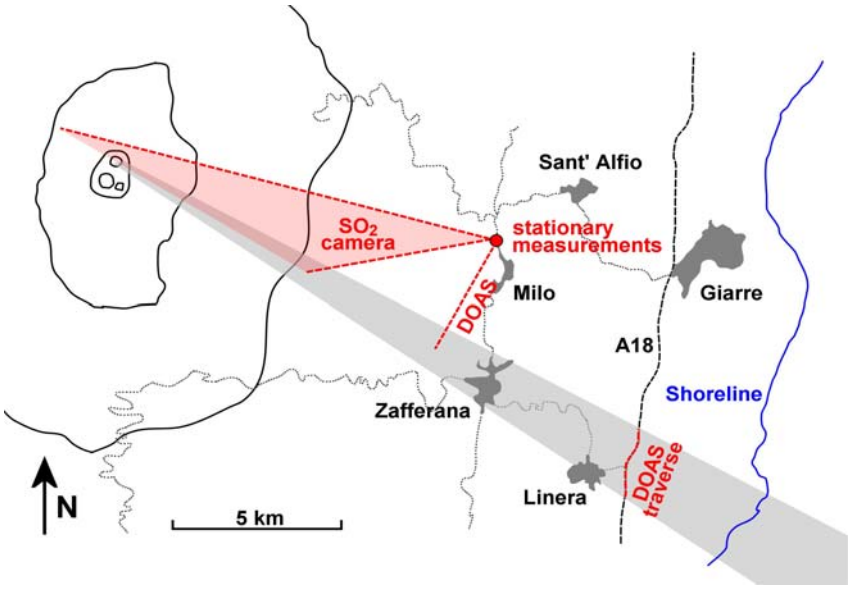

Fig. 8.8 – Schematic geometry of the measurements conducted on July 12, 2008 at Mt. Etna. Stationary measurements were conducted from a rooftop in Milo. Here, an SO_2 camera observed the active vent as well as the emitted plume, and a scanning DOAS measured plume cross-sections at an azimuth angle of 220° relative to north. The maximum SO_2 concentration was found at an elevation angle of 29°. Combined with the wind direction of 306° which was simultaneously measured with a DOAS traverse on highway A18, this yields a plume height of 2900 m a.s.l.

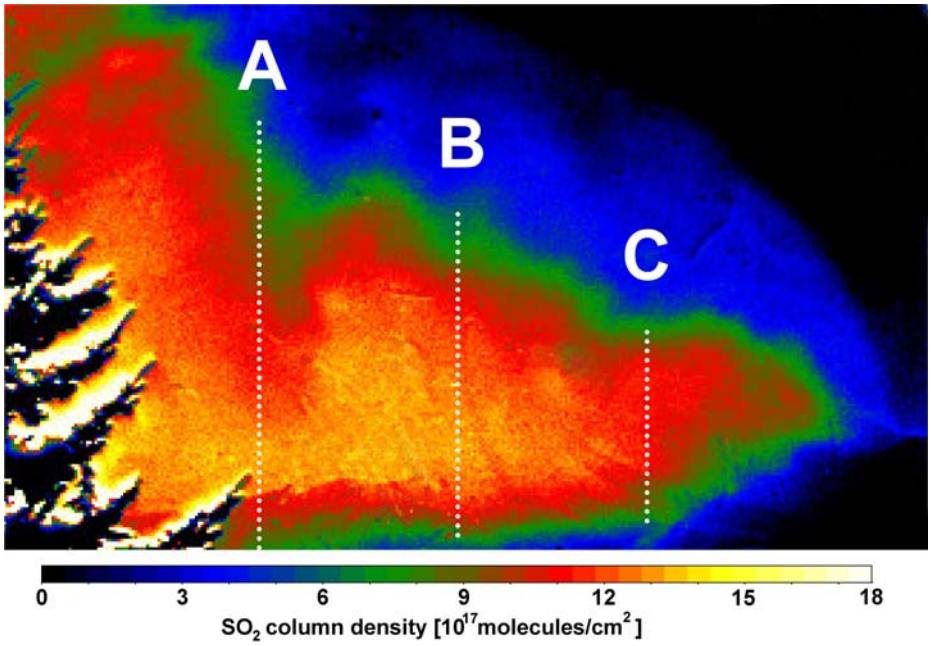

Fig. 8.9 – Example plume measurement recorded by the SO_2 camera on July 12, 2008 at 14:39 local time from a rooftop in Milo. The plume motion was from right to left, but also towards the instrument as shown in Fig. 8.8. The integrated SO_2 amount was determined at three individual positions marked A, B, and C in the image. This image was slightly filtered to remove artifacts caused by dust on the camera's lens. On the left side of the image, a tree obstructed the camera's view of the plume.

From the SO_2-camera image, the total SO_2 amount X in a slice of the volcanic plume was determined at three individual distances 7.1, 7.9 and 8.9 km from the instrument (marked A, B, and C in Fig. 8.9) by integrating the measured column densities along a vertical line. The obtained values were then multiplied by the scalar product of viewing direction and wind direction to correct for non-perpendicular plume intersection (details of this method are given in section 3.3.2.). The corresponding time series of plume-integrated SO_2 amounts X (in molecules/cm) are shown in Fig. 8.10. The variability of volcanic degassing leads to fluctuations in instantaneous SO_2 amount. The values at each individual distance vary by a factor of 2 on a timescale of minutes. The three time series exhibit similar characteristics, with an evident time shift due to the subsequent detection of identical features of the volcanic plume (sequence: A, B, C). This shift can be used to calculate the wind speed v at plume height (see section 3.3.4 and *McGonigle et al. 2005b, Williams-Jones et al. 2006*). For July 12, 14:30, a value of 26 m/s was retrieved, thus allowing the determination of instantaneous emission fluxes $\Phi = X \times v$ for each plume position (displayed at right in Fig. 8.10).

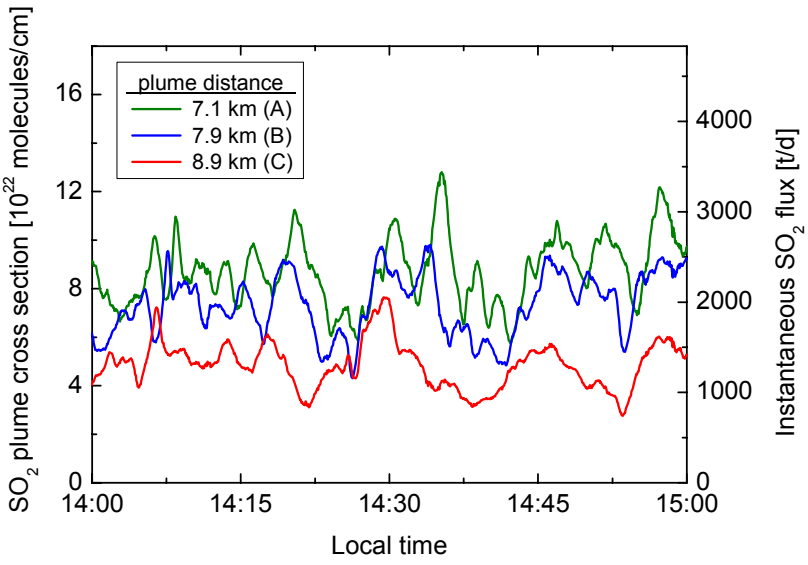

Fig. 8.10 – Time series of integrated SO_2 amounts as measured by the SO_2 camera. The 3 lines indicate the amounts retrieved at positions 7.1, 7.9, and 8.9 km from the instrument (marked A, B and C in Fig. 8.9). The average amounts retrieved between 14:00 and 15:00 were 4.9, 7.3 and 8.7 × 10^{22} molecules/cm, respectively. A wind speed in the plume of 26 m/s was calculated from the correlation of the individual time series. Using this value, the instantaneous SO_2 flux measured at each position can be retrieved and is indicated on the right.

The plume-integrated SO_2 amounts and emission fluxes calculated at different distances from the plume however also exhibit absolute differences. Between 14:00 and 15:00 local time, the integrated SO_2 amount X measured closest to the vent at 8.9 km from the instrument yielded an average 4.9 × 10^{22} molecules/cm, indicating an average emission flux of 1300 t(SO_2)/d. At 7.9 km from the instrument, X averaged 7.3 × 10^{22} molecules/cm yielding a flux of 2000 t(SO_2)/d. As the plume moved even closer to the instrument to a distance of 7.1 km, the SO_2

amount increased yet again, and 8.7×10^{22} molecules/cm were measured on average, corresponding to a flux of 2300 t(SO_2)/d.

These measurements seem to indicate an increase in SO_2 load in the volcanic plume as it is blown away from the vent, but this is highly unlikely. Instead, SO_2 is lost during downwind transport due to processes such as oxidation, dry and wet deposition, absorption and dissolution. Past measurements of the evolution of SO_2 concentrations in volcanic plumes have resulted in loss rates ranging from 10^{-7} to 10^{-3} s^{-1} (e.g. *Martin et al. 1986, Oppenheimer et al. 1998b, McGonigle et al. 2004, Rodríguez et al. 2008*), but never has an increase of SO_2 with plume age been reported.

The measurements conducted here are most likely not caused by an increase in SO_2 with plume evolution, but rather demonstrate how radiative transfer effects can influence remote sensing observations. Because of the considerable distance between plume and instrument, the dilution effect is expected to cause an underestimation in the SO_2 column density (compare Fig. 8.4). Quantifying the exact response of the SO_2 camera to this effect is difficult, as the camera's sensitivity to each individual SO_2 absorption band must be characterized first. However, a qualitative understanding of the measurement can be achieved by realizing the dilution effect increases with distance between instrument and plume. Therefore, the plume-integrated SO_2 amount measured at position A (8.9 km from the instrument) is affected more by dilution than the measurements in which the plume was closer to the instrument. While it is unclear whether the entire discrepancy between the measurement positions can be attributed to the dilution effect alone (note that scenario TD and Fig. 8.4 considered only a very low SO_2 load), the trend is consistent with the model results. Furthermore, all retrieved SO_2 amounts are likely to greatly underestimate the true SO_2 load, as discussed in scenario TD and shown in Fig. 8.4. A quantitative approach to retrieving radiative transfer effects is presented in the next section. However, this requires more spectral information than is available from the SO_2-camera's data.

8.5 Retrieving radiative transfer conditions from DOAS measurements

The radiative transfer effects described above affect all passive remote sensing techniques which use scattered sunlight as a light source. The DOAS technique, however, has a distinct advantage over other methods in that the spectrum of the incident radiation is inherently measured in moderate resolution and is available for further evaluation. In the following, we will discuss how these spectra can be used to retrieve not only the correct SO_2 straight column density or AMF, but also gain information on the radiative transfer conditions of a particular measurement.

As described in section 8.1, DOAS retrievals yield the column density of absorbers in the light path. The column density describes the integrated absorber concentration along the

average photon path. Standard DOAS evaluations assume that the optical path is the same for all wavelengths in the evaluation range. Therefore, the column density is assumed to be independent of wavelength. This presumption is valid for weak absorbers that do not substantially influence the radiative transfer in the atmosphere except for causing the weak differential absorption observed by the DOAS instrument (note that also the wavelength dependence of Rayleigh scattering causes a wavelength dependence of the column density, but this effect is usually negligible over small wavelength intervals). Scenario TV is an example of a weak absorption case (see section 3.4.1 and Fig. 8.3), with total differential optical densities below 4 % resulting in a plume transmittance of larger than 96 % for all wavelengths.

In the case of strong absorption, however, the average optical path from the sun to the instrument is no longer independent of wavelength as is shown in all other model scenarios in this study (Fig. 8.4 - Fig. 8.7, also see section 3.4.1). In such cases, the standard DOAS retrieval can yield incorrect results. An example DOAS measurement of the plume of Mt. Etna also recorded on July 12, 2008, is shown in Fig. 8.11. This measurement was recorded by a DOAS instrument co-located with the SO_2 camera described in section 8.4 as shown in Fig. 8.8. At 14:30 local time, the instrument found the center of the plume at an elevation angle of 29°. The optical density obtained from this measurement is shown in Fig. 8.11 (blue line).

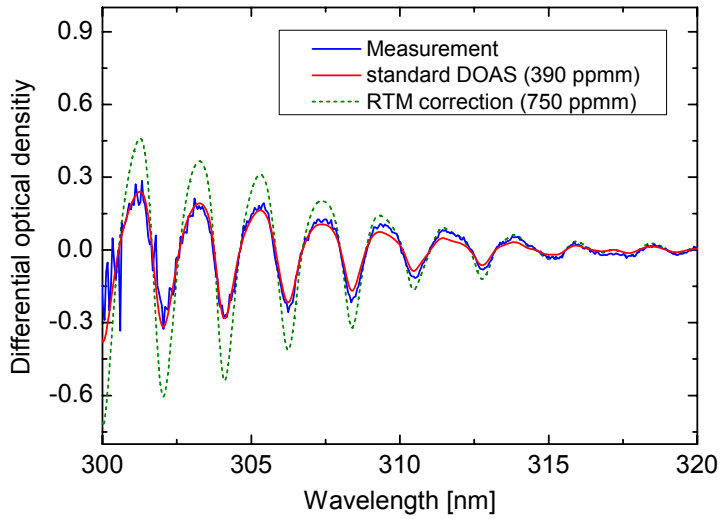

Fig. 8.11 – Standard DOAS retrievals can yield incorrect results if the average photon path is dependent on wavelength, as is the case for strong SO_2 absorption. The blue line shows the differential optical density in the plume of Mt. Etna measured by a scanning DOAS instrument on July 12, 2008. If the SO_2 cross-section is fit to the measurement according to a simple DOAS retrieval algorithm, a value of 390 ppmm is obtained (red line). Radiative transfer calculations, however, show that a more realistic value for the straight column density is 750 ppmm. The dotted line indicates the corresponding optical depth as it would be observed if the optical path was a straight line through the plume.

A simple DOAS retrieval (see e.g. *Platt and Stutz 2008*) was performed on the measurement spectrum. The differential absorption cross-section of SO_2 (*Bogumil et al. 2003*) was fit to the measured differential optical density, along with a 3rd order polynomial used to remove any broadband structures. The fit result, i.e. the SO_2 cross-section multiplied by the retrieved column density, is shown in red. While the SO_2 structures were obviously correctly identified by the fit routine, the absolute depth of the SO_2 absorption structures was not accurately described for all absorption bands. While the simple DOAS fit models the bands around 305 nm fairly well, it seems to overestimate the absorption at shorter wavelengths and underestimate line depth at longer wavelengths.

This effect was first observed by *Mori et al. 2006* (a similar effect was described by *Marquard et al. 2000* for ozone). The model results described above can now explain the phenomenon. It is caused by a wavelength dependency of the average photon path to the instrument. Therefore, a wavelength dependent measurement column density must be assumed in the retrieval. This was implemented by conducting an individual, narrow-band DOAS retrieval on each of the 9 measured SO_2 absorption lines. In this case, only a 1st order polynomial was allowed. Each wavelength window was approximately 2.2 nm wide and encompassed the respective minimum in optical density as well as the two maxima on either side. The results of the wavelength dependent narrow-band DOAS measurements are depicted in blue in Fig. 8.12.

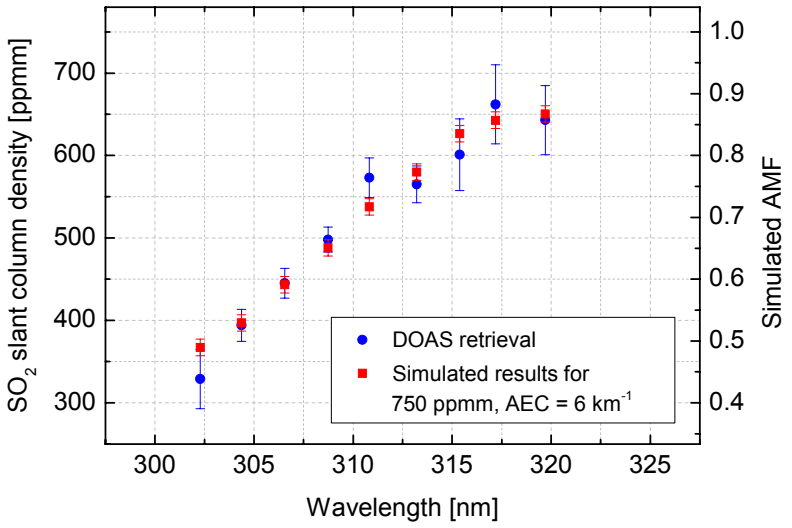

Fig. 8.12 – Example of a retrieval of radiative transfer conditions. Each SO_2 band between 302 and 320 nm was independently evaluated using a narrow-band DOAS retrieval. The results are shown in blue, along with the statistical fit errors. The red values give the results of a TRACYII simulation performed using the actual DOAS measurement geometry, a plume straight column density of 750 ppmm, and a plume AEC of 6 km^{-1}. These final simulation conditions were found by iteratively adjusting the model SO_2 load and AEC until the best match with the measurements was found, and they represent the best estimate for the actual measurement conditions. The given model errors were statistically determined from an ensemble of identical model runs.

A wavelength dependent evaluation yields additional information: not only the column density of SO_2 at a certain wavelength is retrieved, but the dependence of this value on the wavelength is also calculated. By comparing the wavelength dependence of the column density with the results of the radiative transfer model, information on the actual radiative transfer conditions present during the measurement as well as the true straight column density can be retrieved. In other words, the procedure presented in section 8.3 must be inverted: the measured wavelength dependent SO_2 column densities are put into the radiative transfer retrieval along with measurement geometry and meteorological conditions. The model is then used to find the best match of wavelength dependent column densities and returns the corresponding physical conditions, in this case the SO_2 straight column density and the plume AEC.

The radiative transfer model TRACY-II was set up to simulate the actual measurement geometry of the measurement example shown in Fig. 8.12. A plume with 1 km vertical extent was placed 3.8 km away and centered 2.1 km above the instrument in the azimuth direction 220°. The solar zenith and azimuth angles were set to 24° and 235°, respectively in accordance with the actual measurement conditions. The ambient atmosphere was considered free of aerosols, an approximation justified by the observed absence of clouds and visibilities in excess of 50 km during the measurements. The AEC of scattering aerosols (SSA = 1, g = 0.8) inside the plume as well as the plume SO_2 concentration were varied until a match with the measured column density distribution was achieved. The best match was obtained for an SO_2 straight column density of 750 ppmm and an AEC of 0.6 km^{-1}. The AMFs simulated for these values are depicted as red points in Fig. 8.12. The model results match the measurements within the respective errors for all wavelengths. Therefore, the model is thought to reproduce the true measurement conditions well, and the input straight column density and AEC likely match the actual parameters.

The optical density obtained by multiplying the SO_2 differential cross-section with a column density of 750 ppmm is depicted as a dotted line in Fig. 8.11. This line represents the optical density as it would be measured if the average light path were a straight line through the plume for all wavelengths. Obviously, this is not the case for strong SO_2 absorption near 300 nm, as light fails to penetrate the plume effectively on strong absorption bands. For the weak absorption lines near 320 nm, multiple scattering in the plume (expected ~ +15 %, compare to Fig. 8.6) cancels the dilution effect (expected ~ -20 %, compare to Fig. 8.4) to some extent, but even here the measured column density is expected to be 10 % below the actual straight column density (AMF < 0.9).

In summary, this example demonstrates the magnitude of error inherent in remote sensing measurements of volcanic plumes, even under good measurement conditions (clear sky, close proximity to plume). A simple DOAS evaluation conducted between 302 and 320 nm would yield 390 ppmm. A radiative transfer retrieval and subsequent correction yields 750 ppmm, or almost twice the standard DOAS value. Limiting DOAS evaluations to higher wavelengths and therefore weaker SO_2 absorption would increase the accuracy of the results to some

extent in this example, but this is does not always hold true, as can e.g. be seen in the results of the AV scenario for high aerosol loads (Fig. 8.6).

8.6 Conclusions and Outlook

While radiative transfer effects have been a known error source in remote sensing measurements of volcanic plumes for some time, this work for the first time quantitatively discusses the issue (also see *Kern et al. 2009*). The model results presented in section 8.3 provide an information basis for discussing the magnitude of errors encountered. Two radiative transfer effects were identified: the dilution effect and light path extension by multiple scattering in the plume. The parameters governing the magnitude of dilution were identified as being the distance between instrument and plume, the SO_2 load inside the plume, and the aerosol concentration in the ambient air. The parameters influencing light path extension in the plume are aerosol load in the plume as well as the plume SO_2 concentration.

Several examples for the magnitude of radiative transfer effects could be studied under idealized conditions by varying the indicated parameters in model runs with the radiative transfer model TRACY-II. The results showed that radiative transfer is often the dominant source of error in remote sensing measurements. Both, overestimation by several hundred percent as well as underestimation by more than 70 % were obtained in situations that are by all means realistic for volcanic plume measurements, and even higher errors may occur under more extreme conditions.

All model runs were conducted at multiple wavelengths corresponding to the absorption lines of SO_2 between 300 and 325 nm. The radiative transfer effects were found to be dependent on wavelength under most conditions. The information content available in the wavelength dependency was used to propose a retrieval algorithm for DOAS measurements, where moderate resolution spectral information is available in the SO_2 absorption range. The radiative transfer retrieval is based on the concept that the measured column density is dependent on wavelength, a result of strong SO_2 absorption and aerosol scattering influencing the average photon paths from the sun to the instrument. To correctly evaluate the measured spectra, an approach must be used that allows for wavelength dependent column densities. One such approach was described in section 8.5. Here it was demonstrated how additional information gained from the column density wavelength distribution can be used to correct for radiative transfer effects by comparing measurement and model results.

The concept described in this study for the first time allows the correction of radiative transfer effects in passive DOAS measurements, a major step forward considering the magnitude of radiative transfer related errors (see section 8.3). Additionally, information on aerosol parameters inside the plume can be obtained. In this case, the plume AEC was retrieved. With the help of more sophisticated aerosol scattering models, such information could be used to

constrain microphysical aerosol parameters (e.g. size distribution, complex refractive index, particle shape parameters) in the near future.

However, several things remain to be done. For one, the wavelength dependent DOAS retrieval can be improved. Instead of performing multiple, narrow wavelength DOAS retrievals on individual SO_2 absorption bands as described in section 8.5, it would be advantageous to only run a single fit. This can be implemented by multiplying the SO_2 absorption cross-section with a polynomial $P(\lambda)$ during the fit procedure and adding the polynomial coefficients to the fit variables. The polynomial coefficients of the best fit would then describe the wavelength dependency of the measured SO_2 optical density. This would decrease the statistical error inherent in DOAS retrievals in narrow wavelength windows. Alternatively, the SO_2 absorption cross-section could be multiplied by the modeled wavelength dependent AMF of a given scenario before the DOAS fit is applied. In this case, the DOAS retrieval would have to be repeated until the radiative transfer scenario with the best fit is iteratively found, but the advantage would be that the wavelength dependency of the measured column density is taken into account at high resolution.

Next, the inversion of the modeling problem needs to be automated and improved. In the example discussed in section 8.5, the model scenario was modified by hand until it reproduced the measurement results. In this future, this process will be implemented iteratively. However, lookup tables of model results will most likely be necessary, as online computation of radiative transfer scenarios at multiple wavelengths is too time consuming.

Finally, the quantitative determination of ambient aerosol is of great importance and requires further study. In the presented example DOAS measurement, an aerosol-free ambient atmosphere was assumed. This approximation cannot always be applied. In fact, model scenario AA shows that ambient aerosols can considerably influence remote sensing measurements under typical meteorological conditions (see Fig. 8.7). It is unlikely that ambient aerosol conditions can be constrained from the DOAS plume measurement, as is the case for plume aerosols. The information content of a single spectrum is insufficient. However, it has already been shown that multi-axis DOAS measurements can be used to gain ambient aerosol information by e.g. measuring oxygen dimer absorption (*Wagner et al. 2004, Friess et al. 2006*). As the concentration of the oxygen dimer O_4 is known in the atmosphere, variations in absorption strength can give information on optical path lengths. Though sensitivity is limited, this could be used to constrain the plume AMF at the O_4 absorption wavelength if the optical path in a volcanic plume is significantly enhanced. More importantly, however, applying methods such as O_4 absorption, variations in the Ring effect, or intensity ratios at different azimuth angles (see *Wagner et al. 2004, Friess et al. 2006, Irie et al. 2008, Li et al. 2008*) to DOAS measurements conducted outside the plume in close temporal proximity to plume measurements will enable retrievals of ambient aerosol properties in the near future.

9 Summary and Outlook

In this chapter, the most important results obtained in the scope of this thesis will be summarized and a short outlook into future perspectives in the field of UV-spectroscopic volcanic gas emission measurements will be given. The results are divided into four categories: instrumentation and data retrievals, volcanic SO_2 emission fluxes, halogen chemistry in volcanic plumes, and radiative transfer. Each of these is individually presented below.

9.1 Instrumentation and data retrievals

In this thesis, three instruments were developed specifically for volcanic gas emissions measurements. An advanced passive scanning DOAS instrument was designed to meet the requirements of the Network for Observation of Volcanic and Atmospheric Change (NOVAC) project while at the same time featuring enough versatility to allow a number of additional questions to be addressed. The technical design of the so-called NOVAC mark II scanning DOAS instrument is given in section 3.5.1. The most important features of this instrument are the temperature stabilized spectrometer, which is capable of quantifying differential optical densities down to below 1×10^{-3}, thus making the retrieval of weak absorbers (such as BrO) possible, and the dual axis scanner that allows the instrument to look into any direction in the sky (or at the ground). This enables the realization of a wide variety of measurement geometries including volcanic plume scans, wind speed determination, solar occultation measurements, plume composition retrievals as well as tropospheric and stratospheric background measurements (see section 3.3).

Considerable effort was put into the accurate retrieval of SO_2 column densities and volcanic emission fluxes from spectra recorded by the NOVAC mark II instruments, as this was the first and foremost goal of the NOVAC project. Several data retrieval concepts specifically

developed to this extent are described in section 3.4. One of the most important findings was the fact that the optical path through a volcanic plume can be strongly dependent on wavelength. Assuming SO_2 concentrations and geometrical dimensions typical for volcanic plumes, the observed optical density (see Eq. 3.5) can easily reach values of unity or more. Therefore, the species of interest considerably affects the radiative transfer in the plume, and standard DOAS retrievals that do not take this phenomenon into account yield incorrect column densities.

Next to the scanning DOAS instrument, a novel active Long Path DOAS (LP-DOAS) was specifically designed for application in remote volcanic environments. This required reducing the size, weight and power consumption of previous LP-DOAS instruments by at least an order of magnitude each. Two novel technologies enabled this downsizing: the use of a fiber optic bundle to couple light in and out of the LP-DOAS telescope, and the availability of powerful ultra-violet LEDs. The technical description of this instrument is given in section 3.5.2, LP-DOAS measurement concepts are explained in section 3.2.

Finally, a novel SO_2-camera was designed and built in cooperation with *Kick 2008* and *Wöhrbach 2008*. While based on the measurement principle described by *Mori and Burton 2006, Bluth et al. 2007*, several changes to the instrument design were made after conducted model calculations showed that the calibration of the simple SO_2 camera design suggested by the authors depends considerably on the solar zenith angle (SZA), the total O_3 column, the illumination angle of the utilized band-pass filter, and the SO_2 column density itself. By developing a new optical system, the influence of the filter illumination angle was minimized, and model calculations can be used to correct for the other mentioned influences on calibration.

9.2 NOVAC installations and SO_2 emission flux measurements

In the scope of this thesis, 6 NOVAC mark II scanning DOAS instruments were installed at four volcanoes: Stromboli (Italy), Popocatépetl (Mexico), Mt. Etna (Italy) and Tungurahua (Ecuador). The instrument installations and individual measurement configurations are described in detail in chapter 5. At all sites, the instruments are configured to measure SO_2 emission fluxes from the respective volcanoes. The ability to do this was exhibited in a number of example retrievals, which are also described in this chapter. Data continues to be collected at the monitoring sites, and aside from being used by the local observatories for real-time volcanic risk assessment, the collected continuous, high time resolution emission flux datasets will be a valuable resource in furthering our understanding of volcanic processes. By applying the concepts of time series analysis and exploring possible correlations to other geophysical parameters, the measurements may very well help gain new insights into processes occurring at depth, and thereby increase our ability to predict volcanic eruptions. Examples where detected elevated SO_2 emissions helped foresee volcanic crises include the eruption of Santa Ana in October of 2005 (see section 2.2.1) and the reawakening of

Tungurahua in December of 2008 (see section 5.5.2). The data collected by the NOVAC stations will be the topic of future publications by the NOVAC partners associated with each volcano as well as by *Vogel 2010*.

Aside from the stationary scanning measurements conducted by the NOVAC instruments, a short measurement campaign was conducted at Kilauea Volcano (Hawaii) in March of 2008, the results of which are described in chapter 6. During the campaign, the measured SO_2 emission flux at the volcano's summit crater (Halema'uma'u) was found to be significantly elevated compared to background levels. SO_2 emission fluxes between 950 and 2300 t(SO_2)/d were measured on March 2, 2008 whereas *USGS 2008b* reported an average flux of 140 t(SO_2)/d in the time period between 2003 and 2007. On March 19, approximately two weeks after the measurements took place, an explosive eruption occurred at Halema'uma'u Crater, the first since 1924 (*USGS 2008a*). The elevated gas emissions had led to a closure of the southern portion of Crater Rim Drive some weeks before, thus nobody was in danger when Halema'uma'u Overlook was damaged by ejected rocks. This example again shows how gas emissions measurements can assist volcano observatories in risk assessment and eruption prediction.

9.3 Halogen chemistry in volcanic plumes

As mentioned in section 9.1, the NOVAC mark II instruments have the capability to conduct several other measurements aside from the quantification of SO_2 emission flux. With these instruments, BrO was e.g. detected at Stromboli (Italy), where a BrO/SO_2 molecular ratio of 6×10^{-5} was retrieved in an example evaluation (see section 5.2.2). BrO was also detected for the first time ever in the plume of Popocatéptel (Mexico). Here, the average retrieved BrO/SO_2 molecular ratio was 1.4×10^{-4}, although significantly higher values were detected for low SO_2 column densities, likely an indication of an enhanced BrO/SO_2 ratio at the edge of the plume (as described in section 5.3.2). At Mt. Etna, BrO was also detected by the NOVAC mark II scanning DOAS instruments, but these measurements are the topic of a separate upcoming publication by *Vogel et al. 2009*. During the short campaign conducted at Kilauea in March 2008, BrO could not be positively identified. Upper limits for the BrO/SO_2 ratio of between 5×10^{-6} and 8×10^{-5} were retrieved for the individual measurement sites. However, meteorological conditions were not ideal for BrO formation (clouds blocked the sun much of the time thus inhibiting photolysis of precursors), so additional measurements are necessary to accurately characterize the halogen oxide abundances in the plume of Kilauea.

In addition to the passive DOAS BrO measurements, the designed active LP-DOAS instrument was used to quantify the abundances of BrO, ClO and OClO in the plumes of Masaya Volcano (Nicaragua) and Mt. Etna (Italy). The results of these measurements are described in detail in chapter 7. While instrumental issues interfered with the BrO measurements at Mt. Etna and only an upper limit could be retrieved, the measurements at Masaya were groundbreaking. For the first time, the BrO abundance in a volcanic plume

could be measured both at day and at night. The results showed a dramatic diurnal cycle (see Fig. 7.12). At noon, BrO/SO_2 molecular ratios often reached 6×10^{-5}, while the BrO/SO_2 molecular ratios retrieved between sundown and sunup were consistent with null. This finding confirms the hypothesis that BrO is not directly emitted from volcanoes in significant amounts but is instead formed from precursors as a result of photochemical reactions in the volcanic plume. Explained in detail in R. 2.5 to R. 2.12, the so-called bromine explosion cycle is proposed to this extent.

Aside from being able to measure at night, the designed LP-DOAS instrument also has a sensitivity to ClO that is more than an order of magnitude higher than that of passive DOAS instruments (see section 7.2.1). As past reports of ClO detection in volcanic plumes by passive DOAS exist (*Bobrowski 2005, Lee et al. 2005, Bobrowski et al. 2007*, see Tab. 9.1), a detection with the LP-DOAS was expected. However, the ClO/SO_2 ratio remained below the detection limit of about 5×10^{-3} for all measurements at Masaya conducted in April of 2007. For the measurements at Mt. Etna in August of 2007 and July of 2008, ClO was again below the detection limit. In this case, upper limits for the ClO/SO_2 ratio of 9×10^{-3} and 2×10^{-3} can be given for the two different reporting periods.

Volcano	ClO/SO_2	$OClO/SO_2$	Reference
Masaya	8×10^{-2}		*Bobrowski 2005*
Sakurajima	5×10^{-2}		*Lee et al. 2005*
Mt. Etna	5×10^{-2}	6×10^{-5}	*Bobrowski et al. 2007*
Masaya	$< 5\times10^{-3}$ $< 10^{-5}$ from OClO	$< 7\times10^{-6}$	this study
Mt. Etna (2007)	$< 9\times10^{-3}$		this study
Mt. Etna (2008)	$< 2\times10^{-3}$		this study

Tab. 9.1 – Summary of past reported ClO and OClO relative abundances compared to the upper limits calculated from the detection limit of the LP-DOAS instrument used in this study.

The LP-DOAS measurements conducted at Masaya were also sensitive to OClO. However, a similar situation presented itself. OClO could not be detected, and the retrieved detection limits indicated an upper limit for the $OClO/SO_2$ ratio of 7×10^{-6}. This has further implications for the ClO abundance present in the plume at the time. As OClO is formed from the reaction of ClO with BrO, and the dominant sink is the quick photolysis of OClO, a rough calculation (presented in section 7.6) can be applied to determine the steady state concentration of ClO as a function of the OClO concentration. This approximation shows that, in the presence of BrO

(as was the case at Masaya), the ClO concentration should be of the same order of magnitude as the OClO concentration. Therefore, the upper limit for the $OClO/SO_2$ ratio can be regarded as valid for the ClO/SO_2 ratio as well, thus further reducing the possible ClO abundance in the measurement (see Tab. 9.1).

There are several possible explanations for the discrepancy of the results of this study compared to past measurements. For one, the halogen composition of volcanic plumes is known to depend on several factors that can change over time such as the volcanic activity (*Aiuppa et al. 2004b*) and the depth of degassing (*Burton et al. 2007b*) at basaltic volcanoes. A more important difference may be that LP-DOAS measurements are limited to measurement geometries in which the plume passes between the telescope and retro reflectors. The measurements conducted here were therefore sampling an area of the plume much closer to the active vent than is typical for passive DOAS measurements. The above mentioned ClO measurements at Etna and Sakurajima volcanoes were both conducted several kilometers away from the crater where the plume has aged more. In both cases, the respective BrO/SO_2 ratios measured by passive DOAS of 1×10^{-3} and 2.1×10^{-4} were considerably higher than in this study, quite possibly a consequence of a more advanced state of the bromine explosion process. Assuming that chlorine oxides are not directly emitted from the volcano but formed in the plume as is the case for BrO, and that the formation of chlorine oxides is slower than that of BrO (*Bobrowski et al. 2007*) as the process is not autocatalytic and only begins after the aerosol phase is considerably depleted in HBr, this could well explain the absence of ClO and OClO close to the vent. A recent model study by *Roberts et al. 2008* supports this theory.

In August of 2004, OClO was detected for the first time at Mt. Etna. *Bobrowski et al. 2007* observed column densities of up to 2×10^{14} molecules/cm^2 and an average $OClO/SO_2$ molecular ratio of 5.7×10^{-5} at a location 3 km downwind of the crater. At the same time, the ClO/SO_2 ratio was approximately 5×10^{-2}. The discrepancy between these two values stands in contrast to the chemical mechanism presented above (R. 7.5, R. 7.6, Eq. 7.1, Eq. 7.2) which suggests fairly equal amounts of ClO and OClO. It is therefore conceivable that previous measurements of ClO are not entirely reliable due to the difficulties involved in measuring this species with the passive DOAS technique, as mentioned in section 7.2.1 and by the authors themselves (*Bobrowski 2005, Bobrowski et al. 2007*). Another indication for this finding is that attempts at modelling plume chemistry conducted by *Bobrowski et al. 2007* could not reproduce their measured ClO concentrations. The model indicates that, in contrast to bromine, chlorine is not quickly taken up by aerosols but rather remains largely in the gas phase in its less reactive form of HCl, and an efficient recycling mechanism converting HCl to reactive chlorine is missing.

It is however also possible that the chemistry leading to ClO formation is not yet completely understood, and that the mechanism presented in this study as well as that used in past modelling studies is incomplete. To conclusively clarify the magnitude and formation mechanisms of ClO in volcanic plumes, active LP-DOAS measurements at other actively

degassing volcanoes are needed, especially at those where high halogen emissions have been observed in the past.

9.4 Quantifying radiative transfer in and around volcanic plumes

As the NOVAC project progressed, the need for an accurate assessment of measurement errors became more and more prominent. It was soon established that uncertainties in the optical path of radiation between the sun and the instrument is a large, if not the largest source of error in the SO_2 flux measurements. While radiative transfer effects have been a known error source in remote sensing measurements of volcanic plumes for some time (e.g. *Millán 1980*), this work for the first time quantitatively discusses the issue (also see *Kern et al. 2009*). The model results presented in section 8 provide an information basis for discussing the magnitude of errors encountered.

Two main radiative transfer effects which falsify the column density measured by a DOAS instrument were identified: the dilution effect and optical path extension by multiple scattering in the plume. The parameters governing the magnitude of dilution were identified as being the distance between instrument and plume, the SO_2 load inside the plume, and the aerosol concentration in the ambient air. The parameters influencing light path extension in the plume are aerosol load in the plume as well as the plume SO_2 concentration. In model runs, both overestimation by several hundred percent as well as underestimation by more than 70 % were obtained in situations that are typical for volcanic plume measurements, and even higher errors may occur under more extreme conditions.

The radiative transfer effects were found to be dependent on wavelength under most conditions. While at first complicating the situation, the additional information content given by this wavelength dependency was used to propose a radiative transfer retrieval algorithm for DOAS measurements. This retrieval is based on the concept that the measured column density is dependent on wavelength, a result of strong SO_2 absorption and aerosol scattering influencing the average photon paths from the sun to the instrument (also see section 3.4.1). To correctly evaluate the measured spectra, an approach must be used that allows for wavelength dependent column densities. One such approach was described in section 8.5. Here it was demonstrated how additional information gained from the column density wavelength distribution can be used to correct for radiative transfer effects by comparing measurement and model results.

The concept described in this study for the first time allows the correction of radiative transfer effects in passive DOAS measurements, a major step forward considering the magnitude of radiative transfer related errors (see section 8.3). However, the implications of this retrieval go beyond the simple correction of SO_2 column densities. Additional information on aerosol parameters inside the plume can be also obtained, thus opening the door to direct aerosol

measurements with DOAS instruments. Here, only the aerosol extinction coefficient inside the plume was retrieved. With the help of more sophisticated aerosol scattering models, however, such information could possibly be used to constrain microphysical aerosol parameters (e.g. size distribution, complex refractive index, particle shape parameters) in the near future.

However, a number of things remain to be done. For one, the wavelength dependent DOAS retrieval needs to be improved so that it incorporates the information from all SO_2 absorption bands at once instead of evaluating each one separately (see section 8.5). Also, the inversion of the modeling problem needs to be automated and improved. For this, lookup tables of model results will most likely be necessary, as online computation of radiative transfer scenarios at multiple wavelengths is too time-consuming. Computing time would also be reduced if the radiative transfer model TRACY-II is replaced by the newer Monte-Carlo code by *Deutschmann 2009* called McArtim.[25] Finally, the quantitative determination of ambient aerosol is of great importance and requires further study. In the presented example DOAS measurement, an aerosol-free ambient atmosphere was assumed, but it is obvious that this approximation cannot always be applied. Multi-axis DOAS measurements conducted outside the volcanic plume can be used to gain ambient aerosol information by e.g. measuring oxygen dimer absorption, variations in the Ring effect, or intensity ratios at different azimuth angles (see *Wagner et al. 2004, Friess et al. 2006, Irie et al. 2008, Li et al. 2008*).

9.5 Final remarks

It is not surprising that remote sensing techniques have established themselves so quickly in the scientific community dealing with volcanic gas emissions. In addition to the obvious advantage of being able to measure volcanic gases at a safe distance from an often hazardous emission crater, these techniques have greatly improved the accuracy with which total volcanic emission fluxes of certain species (especially SO_2) can be determined. This is owed to the fact that remote sensing instruments inherently integrate the concentration of an absorber along one dimension. The second dimension can then easily be integrated by scanning or traversing the plume, or by using a 2 dimensional detector (as is e.g. the case for the SO_2-camera).

Nevertheless, the remote sensing of volcanic gases is still a relatively young field, and it is constantly evolving. By applying new technology such as the NOVAC mark II scanning DOAS, the LP-DOAS, or the SO_2-camera to volcanic emissions measurements, much can still be learned about the physical and chemical processes occurring in and around volcanic plumes. In the future, different remote sensing techniques will be combined in monitoring

[25] Monte Carlo Atmospheric Radiative Transfer Inversion Model

networks therefore allowing insights into gas composition and evolution at high spatial and temporal resolutions.

This data is immediately valuable for studying the influence of volcanic gas emissions on the atmosphere. However, the key quest in volcanology remains the search for links between the observation of certain phenomena and the volcanic processes occurring at depth that produce these phenomena. In this sense, volcanic gas emission measurements need to be incorporated into multi-parameter geophysical and geochemical monitoring approaches interacting with computer models of volcanic processes in an attempt to understand these. Volcanic gas emissions may be a telegraph from the deep, but the telegraph is encrypted and deciphering it always requires additional information.

10 References

Acker K, Febo A, Trick S, Perrino C, Bruno P, Wiesen P, Möller D, Wieprecht W, Auel R, Giusto M, Geyer A, Platt U, Allegrini I (2006) Nitrous acid in the urban area of Rome. Atmos Environ 40:3123-3133

Aiuppa A, Baker DR, Webster JD (2008) Halogens in volcanic systems. Chem Geol doi:10.1016/j.chemgeo.2008.10.005

Aiuppa A, Bellomo S, D'Alessandro W, Federico C, Ferm C, Valenza M (2004a) Volcanic plume monitoring at Mt. Etna by diffusive (passive) sampling. J Geophys Res 109:D21308

Aiuppa A, Federico C, Franco A, Giudice G, Gurrieri S, Inguaggiato S, Liuzzo M, McGonigle AJS, Valenza M (2005) Emission of bromine and iodine from Mount Etna volcano. Geochem Geophy Geosy 6:doi:10.1029/2005GC000965

Aiuppa A, Federico C, Giudice G, Gurrieri S, Paonita A, Valenza M (2004b) Plume chemistry provides insights into mechanisms of sulfur and halogen degassing in basaltic volcanoes. Earth Planet Sc Lett 222:469-483

Aiuppa A, Franco A, von Glasow R, Allen AG, D'Alessandro W, Mather TA, Pyle DM, Valenza M (2007a) The tropospheric processing of acidic gases and hydrogen sulphide in volcanic gas plumes as inferred from field and model investigations. Atmos Chem Phys 7:1441-1450

Aiuppa A, Moretti R, Federico C, Gaetano G, Gurrieri S, Liuzzo M, Papale P, Shinohara H, Valenza M (2007b) Forecasting Etna eruptions by real-time observation of volcanic gas composition. Geology 35:1115-1118

Albritton DL, Schmeltekopf AL, Zare RN (1976) An introduction to the least-squares fitting of spectroscopic data. In: Narahari RK, Weldon, MW (ed) Molecular Spectroscopy: Modern Research. Academic Press, Orlando, Florida, 1-67

Alicke B, Hebestreit K, Stutz J, Platt U (1999) Iodine oxide in the marine boundary layer. Nature 397:572-573

Allan BJ, Plane JMC, McFiggans G (2001) Observations of OIO in the remote marine boundary layer. Geophys Res Lett 28:1945-1948

Allard P, Burton MR, Muré F (2005) Spectroscopic evidence for a lava fountain driven by previously accumulated gas. Nature 433:407-410

Allen AG, Oppenheimer C, Ferm C, Baxter PJ, Horrocks LA, Galle B, McGonigle AJS, Duffell HJ (2002) Primary sulfate aerosol and associated emissions from Masaya Volcano, Nicaragua. J Geophys Res 107:4682

Allen G, Mather TA, McGonigle AJS, Aiuppa A, Delmelle P, Davison B, Bobrowski N, Oppenheimer C, Pyle DM, Inguaggiato S (2006) Sources, size distribution, and downwind grounding of aerosols from Mt. Etna. J Geophys Res 111:D10302

Andres RJ, Kasgnoc AD (1998) A time-averaged inventory of subaerial volcanic sulfur emissions. J Geophys Res 103:25251-25261

Andres RJ, Rose WI, Stoiber RE, Williams SN, Matías O, Morales R (1993) A summary of sulfur dioxide emission rate measurements from Guatemalan volcanoes. B Volcanol 55:379-388

Annamalai K, Puri IK (2006) Combustion science and engineering. CRC Press, London, pp 1184

Arciniega-Ceballos A, Chouet B, Dawson P, Asch G (2008) Broadband seismic measurements of degassing activity associated with lava effusion at Popocatépetl Volcano, Mexico. J Volcanol Geoth Res 170:12-23

Arellano SR, Hall M, Samaniego P, Le Pennec J-L, Hidalgo S, Galle B (2008a) Degassing patterns of Tungurahua volcano, Ecuador, inferred from high-temporal resolution SO_2 monitoring. IAVCEI General Assembly 2008, Reykjavik, Iceland,

Arellano SR, Hall M, Samaniego P, Le Pennec J-L, Ruiz A, Molina I, Yepes H (2008b) Degassing patterns of Tungurahua volcano (Ecuador) during the 1999-2006 eruptive period, inferred from remote spectroscopic measurements of SO_2 emissions. J Volcanol Geoth Res 176:151-162

Ariya A, Peterson KA (2005) Chemical Transformation of Gaseous Elemental Hg in the Atmosphere. In: Pirrone N, Mahaffey, KR (ed) Dynamics of Mercury Pollution on Regional and Global Scales: Atmospheric Processes and Human Exposures Around the World. Springer US, New York, 261-294

Arndt RL, Carmichael GR, Streets DG, Bhatti N (1997) Sulfur dioxide emissions and sectorial contributions to sulfur deposition in Asia. Atmos Environ 31:1553-1572

Axelsson H, Edner H, Galle B, Ragnarson P, Rudin M (1990a) Differential Optical Absorption Spectroscopy (DOAS) Measurements of Ozone in the 280-290 nm Wavelength Region. Appl Spectrosc 44:1654-1658

Axelsson H, Galle B, Gustavsson K, Regnarsson P, Rudin M (1990b) A transmitting/receiving telescope for DOAS measurements using retro reflector technique. In Optical Remote Sensing of The Atmosphere, vol 4 of 1990 OSA Technical Digest Series, 641-644,

Badalamenti B, Bruno N, Caltabiano T, Di Gangi F, Giammanco S, Salerno G (2004) Continuous soil CO_2 and discrete plume SO_2 measurements at Mt. Etna (Italy) during 1997-2000: a contribution to volcano monitoring. B Volcanol 66:80-89

Bagnato E, Aiuppa A, Parello F, Calabrese S, D'Alessandro W, Mather TA, McGonigle AJS, Pyle DM, Wängberg I (2007) Degassing of gaseous (elemental and reactive) and particulate mercury from Mount Etna volcano (Southern Italy). Atmos Environ 41:7377-7388

Balcone-Boissard H, Villemant B, Boudon G, Michel A (2009) Halogen behaviours during andesitic magma degassing: from magma chamber to volcanic plume. Geophys Res Abstr 11:EGU2009-11985-1

Baumgardner D, Grutter M, Allan J, Ochoa C, Rappenglueck B, Russel LM, Arnott P (2009) Evolution of anthropogenic pollution at the top of the regional mixed layer in the central Mexico plateau. Atmos Chem Phys Discuss 9:3265-3306

Bekker A, Holland HD, Wang P-L, Rumble D, Stein HJ, Hannah JL, Coetzee LL, Beukes NJ (2004) Dating the rise of atmospheric oxygen. Nature 427:117-120

Berner RA (1991) A model for atmospheric CO_2 over Phanerozoic time. Am J Sci 291:339-376

Berresheim H, Wine PH, Davis DD (1995) Sulfur in the Atmosphere. In: Singh HB (ed) Composition, Chemistry and Climate of the Atmosphere. Van Nostrand, Reinhold, New York, 251-307

Bevington PR, Robinson KD (2002) Data reduction and error analysis for the physical sciences. Mcgraw-Hill Higher Education, Columbus, Ohio, USA, pp 336

Birks JW, Showmaker B, Leck TJ, Borders RA, Hart LJ (1977) Studies of reactions of importance in the stratosphere. II. Reactions involving chlorine nitrate and chlorine dioxide. J Chem Phys 66:4591-4599

Blitz MA, Hughes KJ, Pilling MJ (2003) Determination of the High-Pressure Rate Coefficient and the Enthalpy of Reaction for OH + SO_2. Phys Chem A 107:1971-1978

Bluth GJS, Doiron SD, Schnetzler CC, Krueger AJ, Walter LS (1992) Global tracking of the SO_2 clouds from the June 1991 Mount Pinatubo eruptions. Geophys Res Lett 19:151-154

Bluth GJS, Shannon JM, Watson IM, Prata AJ, Realmuto VJ (2007) Development of an ultra-violet digital camera for volcanic SO_2 imaging. J Volcanol Geoth Res 161:47-56

Bobrowski N (2005) Volcanic Gas Studies by MAX-DOAS. PhD Thesis, University of Heidelberg.

Bobrowski N, Hönninger G, Galle B, Platt U (2003) Detection of bromine monoxide in a volcanic plume. Nature 423:273-276

Bobrowski N, Hönninger G, Lohberger F, Platt U (2006) IDOAS: A new monitoring technique to study the 2D distribution of volcanic gas emissions. J Volcanol Geoth Res 150:329-338

Bobrowski N, Platt U (2007) SO_2/BrO ratios studied in five volcanic plumes. J Volcanol Geoth Res 166:147-160

Bobrowski N, von Glasow R, Aiuppa A, Inguaggiato S, Louban I, Ibrahim OW, Platt U (2007) Reactive halogen chemistry in volcanic plumes. J Geophys Res 112:D06311

Bogumil K, Orphal J, Homan T, Voigt S, Spietz P, Fleischmann O, Vogel A, Hartmann M, Bovensmann H, Frerick J, Burrows J (2003) Measurements of molecular absorption spectra with the SCIAMACHY Pre-Flight Model: instrument characterization and reference data for atmospheric remote-sensing in the 230-2380nm region. J Photoch Photobio A: Chemistry 157:167-184

Bösch H (2002) Studies of the Stratospheric Nitrogen and Iodine Chemistry by Balloon-Borne DOAS Measurements and Model Calculations. PhD thesis, University of Heidelberg.

Bösch H, Camy-Peyret C, Chipperfield MP, Fitzenberger R, Harder H, Platt U, Pfeilsticker K (2003) Upper limits of stratospheric IO and OIO inferred from center-to-limb-darkening-corrected balloon-borne solar occultation visible spectra: Implications for total gaseous iodine and stratospheric ozone. J Geophys Res 108:4455

Brasseur GP, Granier C (1992) Mount Pinatubo aerosols, chlorofluorocarbons, and ozone depletion. Science 257:1239

Brasseur GP, Orlando JJ, Tyndall GS (1999) Atmospheric Chemistry and Global Change. Oxford University Press, New York, Oxford, pp 654

Brassington DJ (1981) Sulfur dioxide absorption cross-section measurements from 290 nm to 317 nm. Appl Opt 20:3774-3779

Brocks JJ, Logan GA, Buick R, Summons RE (1999) Archean Molecular Fossils and the Early Rise of Eukaryotes. Science 285:1033-1036

Burton MR (2007) Personal communication. March 5, 2007

Burton MR, Allard P, Murè F, La Spina A (2007a) Magmatic gas composition reveals the source depth of slug-driven Strombolian explosive activity. Science 317:227

Burton MR, Caltabiano T, Muré F, Salerno G, Randazzo D (2008) SO_2 flux from Stromboli during the 2007 eruption: Results from the FLAME network. J Volcanol Geoth Res doi:10.1016/j.jvolgeores.2008.11.025

Burton MR, Mader HM, Polacci M (2007b) The role of gas percolation in quiescent degassing of persistently active basaltic volcanoes. Earth Planet Sc Lett 264:46-60

Burton MR, Oppenheimer C, Horrocks LA, Francis PW (2001) Diurnal changes in volcanic plume chemistry observed by lunar and solar occultation spectroscopy. Geophys Res Lett 28:843-846

Carapezza M-L, Inguaggiato S, Brusca L, Longo M (2004) Geochemical precursors of the activity of an open-conduit volcano: The Stromboli 2002-2003 eruptive events. Geophys Res Lett 31:L07620

Carn S (2006) NASA Earth Observatory: Eruption of Mount Nyamulagira (Nyamuragira). http://earthobservatory.nasa.gov/NaturalHazards/view.php?id=17755

Carn S (2008) NASA Earth Observatory: Sulfur Dioxide Cloud from Aleutians' Kasatochi Volcano. http://earthobservatory.nasa.gov/IOTD/view.php?id=8998

Carn S, Krueger A, Arellano SR, Krotkov NA, Yang K (2008) Daily monitoring of Ecuadorian volcanic degassing from space. J Volcanol Geoth Res 176:141-150

Carn SA, Strow LL, Souza-Machado Sd, Edmonds Y, Hannon S (2005) Quantifying tropospheric emissions with AIRS: The 2002 eruption of Mt. Etna (Italy). Geophys Res Lett 32:L02301

Casadevall T, Rose WI, Gerlach TM, Greenland LP, Ewert J, Wunderman R, Symonds R (1983) Gas Emissions and the Eruptions of Mount St. Helens Through 1982. Science 221:1383-1385

Cashman KV, Cronin SJ (2008) Welcoming a monster to the world: Myths, oral tradition, and modern societal response to volcanic disasters. J Volcanol Geoth Res 176:407-418

Cashman KV, Giordano G (2008) Volcanoes and human history. J Volcanol Geoth Res 176:325-359

Cox IJ (1993) A Review of Statistical Data Association Techniques for Motion Correspondence. Int J Comput Vision 10:53-66

Cox RA, Sheppard D (1980) Reaction of OH radicals with gaseous compounds. Nature 284:330-331

Crounse JD, DeCarlo PF, Blake DR, Emmons LK, Campos TL, Apel EC, Clarke AD, Weinheimer AJ, McCabe DC, Yokelson RJ, Jimenez JL, Wennberg PO (2009) Biomass burning and urban air pollution over the Central Mexican Plateau. Atmos Chem Phys Discuss 9:2699-2734

Crutzen PJ (1996) My life with O_3, NO_x, and other YZO_x compounds (Nobel lecture). Angewandte Chemie Int Ed Engl 35:1759-1776

Delgado Granados H, Alvarez Nieves JM, Rivera Cárdenas C, Cárdenas González L, Guevara E, Galle B, Alonso P, Morquecho C (2008) Observing volcanic plumes of Popocatépetl volcano (Mexico) with a mini-DOAS network: getting closer to forecasting eruptive events. IAVCEI 2008 General Assembly, Reykjavik, Iceland, August 19, 2008

Delgado Granados H, Cárdenas González L (1997) Passive degassing at Volcan Popocatépetl (Mexico): 2.6 x 10^6 tons of SO_2 released in 617 days of activity. Volcanic Activity and the Environment. Abstracts., Puerto Vallarta, p. 49

Delgado Granados H, Cárdenas González L, Piedad Sánchez N (2001) Sulfur dioxide emissions from Popocatépetl volcano (Mexico): case study of a high-emission rate, passively degassing erupting volcano. J Volcanol Geoth Res 108:107-120

Delmelle P (2003) Environmental impacts of tropospheric volcanic gas plumes. In: Oppenheimer C, Pyle, DM, Barclay, J (ed) Volcanic Degassing. Geological Society Special Publication No. 213. 381-399

Delmelle P, Baxter P, Beaulieu A, Burton MR, Francis P, Garcia-Alavarez J, Horrocks L, Navarro M, Oppenheimer C, Rothery D, Rymer H, Amand KS, Stix J, Strauch W, Williams-Jones G (1999) Origin, effects of Masaya volcano's continued unrest probed in Nicaragua. EOS Trans Am Geophys Union 80:575-581

Delmelle P, Stix J, Baxter P, Garcia-Alavarez J, Barquero J (2002) Atmospheric dispersion, environmental effects and potential health hazard associated with the low altitude gas plume of Masaya volcano, Nicaragua. Bull Volcanol 64:423-434

Delmelle P, Stix J, Bourque CPA, Baxter P, Garcia-Alavarez J, Barquero J (2001) Dry deposition and heavy acid loading in the vicinity of Masaya volcano, a major sulfur and chlorine source in Nicaragua. Environ Sci Technol 7:1289-1293

Dessert C, Dupré B, François LM, Schott J, Gaillardet J, Chakrapani G, Bajpai S (2001) Erosion of Deccan Traps determined by river goechemistry: impact on the global climate and the $^{87}Sr/^{86}Sr$ ratio of seawater. Earth Planet Sc Lett 188:459-474

Deutschmann T (2008) Atmospheric radiative transfer modelling with Monte Carlo methods. Diploma thesis, University of Heidelberg.

Deutschmann T (2009) McArtim - Monte Carlo Atmospheric Radiative Transfer Inversion Model. http://joseba.mpch-mainz.mpg.de/matr/tracy_II/documentation/McArtim_Documentation.html

DFG (2007) Deutsche Forschungsgemeinschaft: MAK- und BAT-Werteliste 2007, Senatskommission zur Prüfung gesundheitsschädlicher Arbeitsstoffe, Mitteilung 43: VCh. http://www.grillo.de/uploads/media/Schwefeldioxid.pdf

Doran JC, Abbott S, Archuleta J, Bian X, Chow J, Coulter RL, de Wekker SFJ, Edgerton S, Elliot S, Fernandez A, Fast JD, Hubbe JM, King C, Langley D, Leach J, Lee JT, Martin TJ, Martinez D, Martinez JL, Mercado G, Mora V, Mulhearn M, Pena JL, Petty R, Porch W, Russel C, Salas R, Shannon JD, Shaw WJ, Sosa G, Tellier L, Templeman B, Watson JG, White R, Whiteman CD, Wolfe D (2005) The IMADA-AVER Bouindary Layer Experiment in the Mexico City Area. B Am Meteorol Soc 79:2497-2508

DORSIVA (2005) Development of Optical Remote Sensing Instruments fo Volcanological Applications - Final Scientific Report. In 62 pages, DORSIVA Consortium, September 30, 2005

Edmond JM, Huh Y (2003) Non-steady state carbonate recycling and implications for the evolution of atmospheric P_{CO2}. Earth Planet Sc Lett 216:125-139

Edmonds M, Gerlach TM, Herd RA (2008) Halogen degassing during ascent and eruption of water-poor basaltic magma. Chem Geol published online:

Edmonds M, Herd RA, Galle B, Oppenheimer C (2003a) Automated, high time-resolution measurements of SO_2 flux at Soufrière Hills Volcano, Montserrat. B Volcanol 65:578-586

Edmonds M, Oppenheimer C, Pyle DM, Herd RA (2003b) SO_2 emissions from Soufrière Hills volcano and their relationship to conduit permeability, hydrothermal interaction and degassing regime. J Volcanol Geoth Res 124:22-43

Edmonds M, Pyle DM, Oppenheimer C (2001) A model for degassing at Soufrrère Hills Volcano, Montserrat, West Indies, based on geochemical data. Earth Planet Sc Lett 186:159-173

Edner H, Sunesson A, Svanberg S, Uneus L, Wallin S (1986) Differential optical absorption spectroscopy system used for atmospheric mercury monitoring. Appl Opt 25:403-409

Elias T, Sutton AJ, Oppenheimer C, Horton KA, Garbeil H, Tsanev V, McGonigle AJS, Williams-Jones G (2006) Comparison of COSPEC and two miniature ultraviolet spectrometer systems for SO_2 measurements using scattered sunlight. B Volcanol 68:313-322

Endo ET, Murray T (1991) Real-Time Seismic Amplitude Measurements (RSAM): a volcano monitoring and prediction tool. B Volcanol 53:533-545

Erle F, Pfeilsticker K, Platt U (1995) Onthe influence of tropospheric clouds on zenith-scattered-light measurements of stratospheric species. Geophys Res Lett 22:2725-2728

Fickel M (2008) Measurement of trace gas fluxes from point sources with Multi-Axis Differential Optical Absorption Spectroscopy. University of Heidelberg.

Fiedler F (1982) Atmospheric circulation. In: Jaeschke W, Georgii, HW (ed) Chemistry of the unpolluted and polluted troposphere. Reidel, Dordrecht, 119-154

Fischer TP, Roggensack K, Kyle PR (2002) Open and almost shut case for explosive eruptions: Vent processes determined by SO_2 emission rates at Karymsky volcano, Kamchatka. Geology 30:1059-1062

Francis P, Burton MR, Oppenheimer C (1998) Remote measurements of volcanic gas compositions by solar occultation spectroscopy. Nature 396:567-570

Frankenberg C, Platt U, Wagner T (2005) Iterative maximum a posteriori (IMAP)-DOAS for trace gas retrieval of strong absorbers: Model studies for CH_4 and CO_2 retrieval from near infrared spectra of SCIAMACHY onboard ENVISAT. Atmos Chem Phys 5:9-22

Frederick JE, Abrams RB (1981) The surface albedo of the earth in the near ultraviolet (330-340 nm). Remote Sens Environ 11:337-347

FREEWAVE (2009) Spread Spectrum Wireless Data Transceiver User Manual. http://www.freewave.com/files/Manuals/LUM0002AF%20Rev%20G%20FGR%20User%20Manual.pdf

Friedl RR, Sander SP (1989) Kinetics and product studies of the reaction of ClO + BrO using flash photolysis-ultraviolet absorption. J Phys Chem 93:4764-4771

Friess U, Monks PS, Remedios JJ, Rozanov A, Sinreich R, Wagner T, Platt U (2006) MAX-DOAS O_4 measurements: A new technique to derive information on atmospheric aerosols: 2. Modeling studies. J Geophys Res 111:D14203

Frins E, Bobrowski N, Platt U, Wagner T (2006) Tomographic MAX-DOAS observations of sun illuminated targets: a new technique providing well defined absorption paths in the boundary layer. Appl Opt

Galle B, Bobrowski N, Carn S, Durieux J, Johansson M, Kasereka M, Oppenheimer C, Yalire M, Zhang Y (2005) Gas emissions from Nyiragongo volcano D. R. of Congo, measured by UV mini-DOAS spectroscopy. Geophys Res Abstr 7:332

Galle B, Johansson M, Rivera C, Zhang Y, Kihlman M, Kern C, Lehmann T, Platt U, Arellano S, Hidalgo S (2009) NOVAC - A global network for volcano gas monitoring: network layout and instrument description. submitted to J Geophys Res

Galle B, Oppenheimer C, Geyer A, McGonigle AJS, Edmonds M, Horrocks L (2003) A miniaturized ultraviolet spectrometer for remote sensing of SO_2 fluxes: A new tool for volcano surveillance. J Volcanol Geoth Res 119:241-254

Garrat JR (1994) Incoming shortwave fluxes at the surface - A comparison of GCM results with observations. J Clim 7:72-80

Gasso S (2008) Satellite observations of the impact of weak volcanic activity on marine clouds. J Geophys Res 113:D14S19

Gasso S, Allen J, Riebeek H (2008) NASA Earth Observatory: Low-Level Volcanic Activity Impacts Clouds. http://earthobservatory.nasa.gov/IOTD/view.php?id=8444

GDAS (2009) Archived data from the National Center for Environmental Prediction's (NCEP) Global Data Assimilation System (GDAS). www.ready.noaa.gov/ready/amet.html

Gerlach TM (2004) Volcanic sources of tropospheric ozone-depleting trace gases. Geochem Geophy Geosy 5:Q09007

Gerlach TM, Graeber EJ (1985) Volatile budget of Kilauea volcano. Nature 313:273-277

Gerlach TM, McGee KA, Elias T, Sutton AJ, Doukas MP (2002) Carbon dioxide emission rate of Kilauea Volcano: Implications for primary magma and summit reservior. J Geophys Res 107:2189

Geyer A (2000) The role of the nitrate radical in the boundary layer. PhD thesis, University of Heidelberg.

Geyer A, Alicke B, Ackermann R, Martinez M, Harder H, Brune W, Carlo Pd, Williams E, Jobson T, Hall S, Shetter R, Stutz J (2003a) Direct observations of daytime NO_3: Implications for urban boundary layer chemistry. J Geophys Res 108:4368-4378

Geyer A, Bächmann K, Hofzumahaus A, Holland F, Konrad S, Klüpfel T, Pätz H-W, Perner D, Mihelcic D, Schäfer H-J, Volz-Thomas A, Platt U (2003b) Nighttime formation of peroxy and hydroxyl radicals during the BERLIOZ campaign: Observations and modeling studies. J Geophys Res 108(D4):8249

Gobiet A, Baumgärtner D, Krobath T, Maderbacher R, Putz E (2004) Urban Air Pollution Monitoring with DOAS Considering the Local Meteorologica Situation. Environ Monit Assess 65:119-127

Gonzalez RC, Woods RE (2001) Digital Image Processing. Prentice Hall International, pp 793

Goody RM, Young YL (1989) Atmospheric Radiation (Theoretical Basis). Oxford University Press, Oxford, pp 519

Götz FWP (1931) Zum Strahlungsklima des Spitzbergensommers. Strahlungs- und Ozonmessungen in der Königsbucht 1929. Gerl Beitr Geophys 31:119-154

Götz FWP, Meetham AR, Dobson GMB (1934) The vertical distribution of ozone in the atmosphere. Proc Roy Soc A 145:416-446

Graf H-F, Feichter J, Langmann B (1997) Volcanic sulfur emissions: estimates of source strength and its contribution to the global sulfate distribution. J Geophys Res 102:10727-10738

Graf H-F, Langmann B, Feichter J (1998) The contribution of Earth degassing into the atmospheric sulfur budget. Chem Geol 147:131-145

Greve A, Neckel H (1996) On the consistency of solar limb darkening observations at UV wavelengths (2000 - 3300 Å). Astron Astrophys Suppl Ser 120:35-39

GVP (2009a) Smithsonian Institution's Global Volcanism Program (GVP). http://www.volcano.si.edu/

GVP (2009b) Smithsonian Institution's Global Volcanism Program (GVP). Eruptive History of Popocatépetl Volcano. http://www.volcano.si.edu/world/volcano.cfm?vnum=1401-09=&volpage=erupt

GVP (2009c) Smithsonian Institution's Global Volcanism Program (GVP). Eruptive History of Tungurahua Volcano. http://www.volcano.si.edu/world/volcano.cfm?vnum=1502-08=&volpage=erupt

Halmer MM, Schmincke H-U, Graf H-F (2002) The annual volcanic gas input into the atmosphere, in particular into the stratosphere: a global data set for the past 100 years. J Volcanol Geoth Res 115:511-528

Hansteen TH, Freundt A, Kutterolf S, Galle B (2008) Magma flux rates through the Central American Volcanic Arc (CAVA) estimated from regional SO_2 fluxes at quiescently degassing volcanoes. IAVCEI General Assembly 2008, Reykjavik, Iceland,

Harding D, Miller JM (1982) The influence on rain chemistry of the Hawaiian volcano Kilauea. J Geophys Res 87:1225-1230

Harris AJL, Dehn J, Patrick M, Calvari S, Ripepe M, Lodato L (2005) Lava effusion rates from hand-held thermal infrared imagery: an example from the June 2003 effusive activity at Stromboli. B Volcanol 68:107-117

Hartl A (2007) Tomographic Reconstruction of 2-D Atmospheric Trace Gas Distributions from Active DOAS Measurements. PhD Thesis, University of Heidelberg.

Hartl A, Song BC, Pundt I (2006) 2-D reconstruction of atmospheric concentration peaks from horizontal long path DOAS tomographic measurements: parameterisation and geometry within a discrete approach. Atmos Chem Phys 6:847-861

Hausmann M, Platt U (1994) Spectroscopic measurement of bromine oxide and ozone in the high Arctic during Polar Sunrise Experiment 1992. J Geophys Res 99:25399-25413

Hebestreit K, Stutz J, Rosen D, Matveiv V, Peleg M, Luria M, Platt U (1999) DOAS measurements of tropospheric bromine oxide in mid-latitudes. Science 283:55-57

Heckel A, Richter A, Tarsu T, Wittrock F, Hak C, Pundt I, Junkermann W, Burrows J (2005) MAX-DOAS measurements of formaldehyde in the Po-Valley. Atmos Chem Phys 5:909-918

Henyey L, Greenstein J (1941) Diffuse radiation in the galaxy. Astrophys J 93:70-83

Heue K-P, Wagner T, Broccardo SP, Walter D, Piketh SJ, Ross KE, Beirle S, Platt U (2008) Direct observation of two dimensional trace gas distributions with an airborne Imaging DOAS instrument. Atmos Chem Phys 8:6707-6717

Hobbs PV, Tuell JP, Hegg DA, Radke LF, Eltgroth MW (1982) Particles and gases in the emissions from the 1980-1981 volcanic eruptions of Mt. St. Helens. J Geophys Res 87:11062-11086

Holland HD (1978) The Chemistry of the Atmosphere and Oceans. John Wiley & Sons, New York, Chichester, Brisbane, Toronto, pp 351

Hönninger G, Friedeburg Cv, Platt U (2004a) Multi Axis Differential Optical Absorption Spectroscopy (MAX-DOAS). Atmos Chem Phys 4:231-254

Hönninger G, Leser H, Sebastián O, Platt U (2004b) Ground-based measurements of halogen oxides at the Hudson Bay by active longpath DOAS and passive MAX-DOAS. Geophys Res Lett 31:L04111

Horrocks L, Burton MR, Francis P, Oppenheimer C (1999) Stable gas plume composition measured by OP-FTIR spectroscopy at Masaya Volcano, Nicaragua, 1998 - 1999. Geophys Res Lett 26:3497-3500

Horrocks L, Oppenheimer C, Burton MR, Duffell HJ, Davies NM, Martin NA, Bell W (2001) Open-path Fourier transform infrared spectroscopy of SO_2: An empirical error budget analysis, with implications for volcano monitoring. J Geophys Res 106:27647-27659

Huebert B, Vitousek P, Sutton AJ, Elias T, Heath J, Coeppicus S, Howell S, Blomquist B (1999) Volcano fixes nitrogen into plant-available forms. Biogeochemistry 47:111-118

Hulst HCvd (1957) Light scattering by small particles. Wiley, New York, pp 470

Inguaggiato S, Rizzo A (2004) Dissolved helium isotope ratios in ground-waters: a new technique based on gas-water re-equilibration and its application to Stromboli volcanic system. Appl Geochem 19:665-673

INGV (2007) Istituto Nazional di Geofisica e Vulcanologia, Sezione Catania. Smithsonian Institution / U.S. Geological Survey Weekly Volcanic Activity Reports, February 28 - March 6, 2007. http://www.volcano.si.edu/world/volcano.cfm?vnum=0101-04=&volpage=weekly

IPCC (2007) Intergovernmental panel on climate change: climate change 2007 - the physical science basis. http://www.ipcc.ch/ipccreports/ar4-wg1.htm

Irie H, Kanaya Y, Akimoto H, Iwabuchi H, Shimizu A, Aoki K (2008) First retrieval of tropospheric aerosol profiles using MAX-DOAS and comparison with lidar and sky radiometer measurements. Atmos Chem Phys 8:341-350

Jähne B (2002) Digitale Bildverarbeitung (Digital Image Processing). Springer Verlag, Heidelberg, pp 618

Johansson M (2009a) Application of Passive DOAS for studies of Megacity Air Pollution and Volcanic Gas Emissions. Chalmers University of Technology.

Johansson M (2009b) NOVAC data evaluation and display software. www.novac-project.eu

Johansson M, Galle B, Rivera C, Zhang Y (2005) Tomographic reconstruction of gas plumes using scanning mini-DOAS instruments. Geophys Res Abstr 7:08058

Johansson M, Galle B, Rivera C, Zhang Y (2009a) Tomographic Reconstruction of Gas Plumes Using Scanning DOAS. submitted to B Volcanol

Johansson M, Galle B, Zhang Y, Rivera C, Chen D, Wyser K (2009b) The Dual-Beam mini-DOAS technique - measurements of volcanic gas emission, plume height and plume speed with a single instrument. B Volcanol published online:DOI 10.1007/s00445-008-0260-8

Johansson M, Kihlman M, Norman P, Rivera C, Zhang Y, Galle B (2008) NOVAC Station User Manual.

Johnson JB, Harris AJL, Hoblit RP (2005) Thermal observations of gas pistoning at Kilauea Volcano. J Geophys Res 110:B11201

Junge CE, Chagnon CW, Manson JE (1961) Stratospheric aerosols. J Meteorol 18:81-108

Kajino M, Ueda H, Satsumbayashi H, An J (2004) Impacts of the eruption of Miyakejima Volcano on air quality over far east Asia. J Geophys Res 109:D21204

Kaleschke L, Neff B, Plane JMC, Platt U, Richter A, Roscoe HK, Sander R, Shepson P, Sodeau J, Steffen A, Wagner T, Wolff E (2007) Halogens and their role in polar boundary-layer ozone depletion. Atmos Chem Phys 7:4375-4418

Kantzas EP, McGonigle AJS (2008) Ground Based Ultraviolet Remote Sensing of Volcanic Gas Plumes. Sensors 8:1559-1574

Kaschka T, von Glasow R, Platt U (2009) Modeling of nitrogen chemistry in volcanic plumes. in final preparation

Kazahaya K, Shinohara H, Saito G (1994) Excessive degassing of Izu-Oshima volcano: magma convection in a conduit. B Volcanol 56:207-216

Kazahaya K, Shinohara H, Uto K, Odai M, Nakahori Y, Mori H, Iino H, Miyashita M, Hirabayashi J (2004) Gigantic SO_2 emission from Miyakejima volcano, Japan, caused by caldera collapse. Geology 32:425-428

Kazahaya R, Mori T, Kazahaya K, Hirabayashi J (2008) Computed tomography of SO_2 concentration distribution in the volcanic plume of Miyakejima, Japan, by airborne traverse technique using three UV spectrometers. Geophys Res Lett 35:L13816

Kennett JP, Stott LD (1991) Abrupt deep-sea warming, palaeoceanographic changes and benthic extinctions at the end of the Palaeocene. Nature 353:225-229

Kern C (2004) Applicability of light-emitting diodes as light sources for active long path DOAS measurements: A feasibility study. Diploma thesis, University of Heidelberg.

Kern C (2006) Characterizing Ocean Optics Spectrometers. In internal report, 14 pages, Institute of Environmental Physics, April 12, 2006

Kern C, Deutschmann T, Vogel L, Wöhrbach M, Wagner T, Platt U (2009) Radiative transfer corrections for precise spectroscopic measurements of volcanic emissions. submitted to B Volcanol

Kern C, Sihler H, Vogel L, Rivera C, Herrera M, Platt U (2008a) Halogen oxide measurements at Masaya volcano, Nicaragua using active long path differential optical absorption spectroscopy. B Volcanol DOI 10.1007/s00445-008-0252-8

Kern C, Sihler H, Vogel L, Rivera C, Herrera M, Platt U (2008b) Halogen oxide measurements at Masaya volcano, Nicaragua using active long path differential optical absorption spectroscopy. B Volcanol DOI 10.1007/s00445-008-0252-8:

Kern C, Trick S, Rippel B, Platt U (2006) Applicability of light-emitting diodes as light sources for active differential optical absorption spectroscopy measurements. Appl Opt 45:2077-2088

Kerrick DM (2001) Present and past nonanthropogenic CO_2 degassing from the solid earth. Rev Geophys 39:565-585

Khokhar MF, Frankenberg C, Van Roozendael M, Beirle S, Kühl S, Richter A, Platt U, Wagner T (2005) Satellite Observations of Atmospheric SO_2 from Volcanic Eruptions during the Time-Period of 1996 to 2002. Adv Space Res 36:879-887

Kick F (2008) A UV camera for the measurement of atmospheric trace gas distributions (translated from German). Undergraduate thesis, University of Heidelberg.

Kihlman M (2007) The BECK-IPC based MAX-DOAS system. http://www.kedu.se/novac/NOVACcomputer.doc

Kraus S (2004) DOASIS: DOAS Intelligent System. http://www.iup.uni-heidelberg.de/bugtracker/projects/doasis/

Kudo R, Uchiyama A, Yamazaki A, Kobayashi E, Nishizawa T (2008) Retrieval of aerosol single-scattering properties from diffuse and direct irradiances: Numerical studies. J Geophys Res 113:D09204

Kump LR, Barley ME (2007) Increased subaerial volcanism and the rise of atmospheric oxygen 2.5 billion years ago. Nature 448:1033-1036

Kurucz RL, Furenlid I, Brault J, Testerman L (1984) Solar flux atlas from 296 to 1300 nm. National Solar Observatory, Sunspot, New Mexico, pp 240

Kutterolf S, Freundt A, Pérez W (2008) Pacific offshore record of plinian arc volcanism in Central America: 2. Tephra volumes and erupted masses. Geochem Geophy Geosyst 9:Q02S02

Lautze NC, Harris AJL, Bailey JE, Ripepe M, Calvari S, Dehn J, Rowland SK, Evans-Jones K (2004) Pulsed lava effusion at Mount Etna during 2001. J Volcanol Geoth Res 137:231-246

Le Guern F, Nohl A, Bicocchi P (1982) Field Measurements of Volcanic Gases. Volcano Island (Italy), Kilauea (Hawaii, U.S.A.), Merapi (Java, Indonesia). B Volcanol 45:229-233

Lee C, Kim YK, Tanimoto H, Bobrowski N, Platt U, Mori T, Yamamoto K, Hong CS (2005) High ClO and ozone depletion observed in the plume of Sakurajima Volcano, Japan. Geophys Res Lett 32:L21809

Lehmann T, Kern C, Vogel L, Platt U (2009) Implementing automated wavelength calibration and parameterization of the optical transfer function in DOAS data retrievals. Germany Physical Society (DPG) Annual Meeting 2009, Hamburg, Germany, March 3, 2009

Leigh RJ, Corlett GK, Frieß U, Monks PS (2007) Spatially resolved measurements of nitrogen dioxide in an urban environment using concurrent multi-axis differential optical absorption spectroscopy. Atmos Chem Phys 7:4751-4762

Leser H, Hönninger G, Platt U (2003) MAX-DOAS measurements of BrO and NO_2 in the marine boundary layer. Geophys Res Lett 30:1537

Levenberg K (1944) A method for the solution of certain non-linear problems in least squares. Q Appl Math 2:164-168

Li X, Brauers T, Shao M, Garland RM, Wagner T, Deutschmann T, Wahner A (2008) MAX-DOAS measurements in southern China: 1. automated aerosol profile retrieval using oxygen dimers absorptions. Atmos Chem Phys Discuss 8:17661-17690

Lissberger PH, Wilcock WL (1959) Properties of All-Dielectric Interference Filters. II. Filters in Parallel Beams of Light Incident Obliquely and in Convergent Beams. J Opt Soc Am 49:126-128

Liu H, Pinker RT, Chin M, Holben B, Remer L (2008) Synthesis of information on aerosol optical properties. J Geophys Res 113:D07206

Louban I, Bobrowski N, Rouwet D, Inguaggiato S, Platt U (2009a) Imaging DOAS for volcanological applications. B Volcanol DOI:10.1007/s00445-008-0262-6

Louban I, Píriz G, Platt U, Frins E (2009b) Measurement of SO_2 and NO_2 applying ToTaL-DOAS from a remote site. J Opt A: Pure Appl Opt 10:104017

Lyons TW (2007) Paleoclimate: Oxygen's rise reduced. Nature 448:1005-1006

Malinconico LL (1979) Fluctuations in SO_2 emission during recent eruptions of Etna. Nature 278:43-45

Manatt SL, Lane AL (1993) A compilation of the absorption cross sections of SO_2 from 106 to 403 nm. J Quant Spec and Rad Transf 50:267-276

Mankin WG, Coffey MT, Goldman A (1992) Airborne observations of SO_2, HCl, and O_3 in the stratospheric plume of the Pinatubo Volcano in July 1991. Geophys Res Lett 19:179-182

Marquard LC, Wagner T, Platt U (2000) Improved air mass factor concepts for scattered radiation differential optical absorption spectroscopy of atmospheric species. J Geophys Res 105:1315-1327

Marquardt DW (1963) An algorithm for least squares estimation of non-linear parameters. J Soc Ind Appl Math 11:431-441

Martin D, Ardouin B, Bergametti G, Carbonelle J, Faivre-Pierret R, Lambert G, Le Cloarec MF, Sennequier G (1986) Geochemistry of Sulfur in Mount Etna Plume. J Geophys Res 91:12249-12254

Martin RS, Mather TA, Pyle DM (2006) High-temperature mixtures of magmatic and atmospheric gases. Geochem Geophy Geosy 7:Q04006

Mather TA, Allen AG, Davison BM, Pyle DM, Oppenheimer C, McGonigle AJS (2004) Nitric acid from volcanoes. Earth Planet Sc Lett 218:17-30

McBirney AR (1956) The Nicaraguan volcano Masaya and its Caldera. EOS Trans Am Geophys Union 37:83-96

McCormick MP, Thomason LW, Trepte CR (1995) Atmospheric effects of the Mt Pinatubo eruption. Nature 373:399-404

McGee TJ, Burris J (1987) SO_2 absorption cross sections in the near UV. J Quant Spec and Rad Transf 37:165-182

McGonigle AJS, Aiuppa A, Giudice G, Tamburello G, Hodson AJ, Gurrieri S (2008) Unmanned aerial vehicle measurements of volcanic carbon dioxide fluxes. Geophys Res Lett 35:L06303

McGonigle AJS, Delmelle P, Oppenheimer C, Tsanev VI, Delfosse T, Horton H, Williams-Jones G, Mather TA (2004) SO_2 depletion in tropospheric volcanic plumes. Geophys Res Lett 31:L13201

McGonigle AJS, Hilton DR, Fischer TP, Oppenheimer C (2005a) Plume velocity determination for volcanic SO_2 flux measurements. Geophys Res Lett 32:L11302

McGonigle AJS, Inguaggiato S, Aiuppa A, Hayes AR, Oppenheimer C (2005b) Accurate measurement of volcanic SO_2 flux: Determination of plume transport speed and integrated SO_2 concentration with a single device. Geochem Geophy Geosy 6:Q02003

McGonigle AJS, Oppenheimer C, Galle B, Mather TA, Pyle DM (2002) Walking traverse and scanning DOAS measurements of volcanic gas emsission rates. Geophys Res Lett 29:1985

Mellqvist J, Rosén A, Axelsson H (1992) Temperature dependence of the absorption spectra of nitrogen oxide, nitrogen dioxide and sulfur dioxide in the application of differential optical absorption spectroscopy. Analyst 117:417-418

Merten A (2008) New design of Longpath-DOAS instruments based on fibre optics and applications in the study of the urban atmosphere. PhD thesis, University of Heidelberg.

Merten A, Tschritter J, Platt U (2009) Novel Design of DOAS-Long-path Telescopes based on fiber optics. submitted to Appl Opt

Métrich N, Allard P, Spillaert N, Andronico D, Burton MR (2004) 2001 flank eruption of the alkali and volatile-rich primitive melt responsible for Mount Enta's evolution in the last three decades. Earth Planet Sc Lett 228:1-17

Mettendorf K-U, Hartl A, Pundt I (2006) An indoor test campaign of the tomography long path differential optical absorption spectroscopy technique. J Environ Monit 8:279-287

Meyer W, Neldel H (1937) Z Tech Phys 12:588

Millán MM (1980) Remote sensing of air pollutants. A study of some atmospheric scattering effects. Atmos Environ 14:1241-1253

Moffat AJ, Millán MM (1971) The applications of optical correlation techniques to the remote sensing of SO_2 plumes using sky light. Atmos Environ 5:677-690

Mori T, Burton MR (2006) The SO_2 camera: a simple, fast and cheap method for ground-based imaging of SO_2 in volcanic plumes. Geophys Res Lett 33:L24804

Mori T, Mori T, Kazahaya K, Ohwada M, Hirabayashi J, Yoshikawa S (2006) Effect of UV scattering on SO_2 emission rate measurements. Geophys Res Lett 33:L17315

Murrells TP, Lovejoy ER, Ravishankara AR (1990) Oxidation of CS_2 by Reaction with OH. 1. Equilibrium Constant for the Reaction OH + CS_2 <-> CS_2OH and the Kinetics of the CS_2OH + O_2 Reaction. J Phys Chem 2381-2386

Nadeau PA, Williams-Jones G (2009) Apparent dowinwind depletion of volcanic SO_2 flux - lessons from Masaya Volcano, Nicaragua. B Volcanol 71:389-400

Newhall CG, Self S (1982) The Volcanic Explosivity Index (VEI) An Estimate of Explosive Magnitude of Historical Volcanism. J Geophys Res 87:1231-1238

Niragu J, Becker C (2003) Volcanic emissions of mercury to the atmosphere: global and regional inventories. Sci Total Environ 304:3-12

NOVAC (2005) Network for Observation of Volcanic and Atmospheric Change. http://www.novac-project.eu

NOVAC (2006) Network for Observation of Volcanic and Atmospheric Change. 1st annual report

O'Dwyer M, Padgett MJ, McGonigle AJS, Oppenheimer C, Inguaggiato S (2003) Real-time measurement of volcanic H_2S and SO_2 concentrations by UV spectroscopy. Geophys Res Lett 30:1652

Ogren JA, Charlson RJ, Radke LF, Domonkos SK (1981) Absorption of Visible Radiation by Aerosols in the Volcanic Plume of Mount St. Helens. Science 211:834-836

Oliver-Smith A (1996) Anthropological research on hazards and disasters. Ann Rev Anthropol 25:303-328

Olmos R, Barrancos J, Rivera C, Barahona F, López DL, Henriquez B, Hernández A, Benitez E, Hernández PA, Pérez NM, Galle B (2007) Anamolous Emissions of SO_2 During the Recent Eruption of Santa Ana Volcano, El Salvador, Central America. Pure Appl Geophys 164:2489-2506

Oppenheimer C, Francis P, Burton MR, Maciejewski AJH, Boardman L (1998a) Remote measurement of volcanic gases by Fourier transform infrared spectroscopy. Appl Phys B - Lasers O 67:505-515

Oppenheimer C, Francis P, Stix J (1998b) Depletion Rates of Sulfur Dioxide in Tropospheric Volcanic Plumes. Geophys Res Lett 25:2671-2674

Oppenheimer C, Kyle PR, Tsanev VI, McGonigle AJS, Mather TA, Sweeney D (2005) Mt. Erebus, the largest point source of NO_2 in Antarctica. Atmos Environ 39:6000-6006

Oppenheimer C, Pyle DM, Barclay J (2003) Volcanic Degassing. Geological Society Publishing House, London, pp 420

Oppenheimer C, Tsanev V, Bani P, Crimp R, Cronin S, Calkins J, Charley D, Lardy M (2006a) Colossal sulphur and bromine degassing from Ambrym Volcano, Vanuatu. 3rd international DOAS Workshop, Bremen, Germany, March 21, 2006

Oppenheimer C, Tsanev VI, Braban CF, Cox RA, Adams JW, Aiuppa A, Bobrowski N, Delmelle P, Barclay J, McGonigle AJS (2006b) BrO formation in volcanic plumes. Geochim Cosmochim Ac 70:2935-2941

Ort MH, Elson MD, Anderson KC, Wendell AD, Samples TL (2008) Variable effects of cinder-cone eruptions on prehistoric agrarian human populations in the American southwest. J Volcanol Geoth Res 176:363-376

Parker DE, Wilson H, Jones PD, Christy JR, Folland CK (1996) The impact of Mount Pinatubo on world-wide temperatures. Int J Climatol 16:487-497

Pennisi M, Le Cloarec MF (1998) Variations of Cl, F, and S in Mount Etna's plume, Italy, between 1992 and 1995. J Geophys Res 103:5061-5066

Perliski LM, Solomon S (1993) On the evaluation of air mass factors for atmospheric near-ultraviolet and visible absorption spectroscopy. J Geophys Res 98:10363-10374

Perner D, Platt U (1979) Detection of nitrous acid by differential optical absorption. Geophys Res Lett 6:917 - 920

Peters C, Pechtl S, Stutz J, Hebestreit K, Hönninger G, Heumann KG, Schwarz A, Winterlik J, Platt U (2005) Reactive and organic halogen species in three different European coastal environments. Atmos Chem Phys 5:3357-3375

Pfeilsticker K, Erle F, Funk O, Marquard L, Wagner T, Platt U (1998) Optical path modifications due to tropospheric clouds: implications for zenith sky measurements of stratospheric gases. J Geophys Res 103:25323-25335

Philipona R (2002) Underestimation of solar global and diffuse radiation measured at Earth's surface. J Geophys Res 107:4654

Pikelnaya O, Hurlock SC, Trick S, Stutz J (2007) Intercomparison of multiaxis and long-path differential optical absorption spectroscopy measurements in the marine boundary layer. J Geophys Res 112:D10S01

Pinardi G, Van Roozendael M, Fayt C (2007) The influence of spectrometer temperature variability on the data retrieval of SO_2. In NOVAC second annual activity report, 44-48, NOVAC consortium, September 30, 2007

Platt U (1994) Differential Optical Absorption Spectroscopy (DOAS). In: Sigrist MW (ed) Monitoring by Spectroscopic Techniques. Wiley, New York, 27-84

Platt U (2007) Plume Longitudinal Diffusion, Insititute of Environmental Physics, University of Heidelberg. Personal communication. November 7, 2007

Platt U, Heue K-P, Pöhler D (2008a) Two- and three dimensional observation of trace gas and aerosol distributions. 7th International Symposium for Advanced Environmental Monitoring, Honolulu, Hawaii, USA, February 26, 2008

Platt U, Hönninger G (2003) The Role of Halogen Species in the Troposphere. Chemosphere 52:325-338

Platt U, Lehrer E (1997) Arctic Tropospheric Ozone Chemistry, ARCTOC. In In final report EU-Proj. EV5V-CT93-0318 European Union,

Platt U, Meinen J, Pöhler D, Leisner T (2008b) Broadband Cavity Enhanced Differential Optical Absorption Spectroscopy (CE-DOAS) - Applicability and Corrections. Atmos Meas Tech Discuss 1:481-507

Platt U, Perner D, Harris GW, Winer AM, Pitts JN (1980a) Detection of NO_3 in the polluted troposphere by differential optical absorption. Geophys Res Lett 7:89-92

Platt U, Perner D, Harris GW, Winer AM, Pitts JN (1980b) Observations of nitrous acid in an urban atmosphere by differential optical absorption. Nature 285:312-314

Platt U, Perner D, Pätz HW (1979) Simultaneous measurements of atmospheric CH_2O, O_3, and NO_2 by differential optical absorption. J Geosphys Res 84:6329 - 6335

Platt U, Stutz J (2008) Differential Optical Absorption Spectroscopy - Principles and Applications. Springer, Berlin Heidelberg New York, pp 1-597

Prata AJ, Bluth GJS, Werner C, Realmuto VJ, Carn S, Watson IM (2009) Remote Sensing of Gas Emissions from Volcanoes. In: Dean KG, Dehn, J (ed) Monitoring Volcanoes in the North Pacific. Observations from Space. Springer, New York, Heidelberg,

Pundt I, Mettendorf K-U (2005) Multibeam long-path differential optical absorption spectroscopy instrument: a device for simultaneous measurements along multiple light paths. Appl Opt 44:4985-4994

Pundt I, Mettendorf K-U, Laepple T, Knab V, Xie P, Lösch J, von Friedeburg C, Platt U, Wagner T (2005) Measurements of trace gas distributions by Long-Path DOAS-Tomography during the motorway campaign BAB II: experimental setup and results for NO_2 (BAB II special issue). Atmos Environ 39:967-975

Pyle DM, Mather TA (2003) The importance of volcanic emissions for the global atmospheric mercury cycle. Atmos Environ 37:5115-5124

Pyle DM, Mather TA (2009) Halogens in igneous processes and their fluxes to the atmosphere and oceans from volcanic activity: A review. Chem Geol doi:10.1016/j.chemgeo.2008.11.013

Rappaport TS (2002) Wireless Communications: Principles and Practice. Prentice Hall PTR, Upper Saddle River, New Jersey, USA, pp 736

Raymo ME, Ruddiman WF, Froelich PN (1988) Influence of late Cenozoic mountain building on ocean geochemical cycles. Geology 16:649-653

Richter A (2008) SO_2 vertical column measurements of the August 7, 2008 eruption of Kasatochi Volcano (Alaska) from the GOME2 instrument on board METOP. http://www.iup.uni-bremen.de/doas/images/highlights/gome2_so2_kasatochi_large.gif

Ripepe M, Harris AJL, Carniel R (2002) Thermal, seismic and infrasonic evidences of variable degassing rates at Stromboli volcano. J Volcanol Geoth Res 118:285-297

Roberts TJ, Braban CF, Martin RS, Oppenheimer C, Adams JW, Cox RA, Jones RL, Griffiths PT (2008) Formation of BrO and ClO_x in volcanic plumes and chemical impacts on O_3. Chem Geol doi:10.1016/j.chemgeo.2008.11.012

Robock A (2000) Volcanic eruptions and climate. Rev Geophys 38:191-219

Rodríguez LA, Watson IM, Edmonds M, Ryan G, Hards V, Oppenheimer C, Bluth GJS (2008) SO_2 loss rates in the plume emitted by Soufrière Hills volcano, Montserrat. J Volcanol Geoth Res 173:135-147

Rodríguez LA, Watson IM, Rose WI, Branan YK, Bluth GJS, Chigna G, Matías O, Escobar D, Carn S, Fischer TP (2004) SO_2 emissions to the atmosphere from active volcanoes in Guatemala and El Salvador 1999-2002. J Volcanol Geoth Res 138:325-344

Rose WI, Millard GA, Mather TA, Hunton DE, Andserson B, Oppenheimer C, Thornton BF, Gerlach TM, Viggiano AA, Kondo Y, Miller TM, Ballenthin JO (2006) Atmospheric chemistry of a 33-34 hour old volcanic cloud from Hekla Volcano (Iceland): insights from direct sampling and application of chemical box modeling. J Geophys Res 111:D20206

Rymer H, van Wyk de Vries B, Stix J, Williams-Jones G (1998) Pit crater structure and processes governing persistent activity at Masaya Volcano, Nicaragua. B Volcanol 59:345-355

Saiz-Lopez A, Mahajan AS, Salmon RA, Bauguitte SJ-B, Jones AE, Roscoe HK, Plane JMC (2007) Boundary Layer Halogens in Coastal Antarctica. Science 317:348-351

Saiz-Lopez A, Plane JMC (2004) Novel iodine chemistry in the marine boundary layer. Geophys Res Lett 31:L04112

Saiz-Lopez A, Plane JMC, Shillito JA (2004) Bromine oxide in the mid-latitude marine boundary layer. Geophys Res Lett 31:L03111

Salerno G, Burton MR, Caltabiano T, Bruno N, Condarelli D, Longo V, Muré F (2006) High-term resolution SO_2 flux measurements using an automated UV scanner array: First 16-month results on Mt. Etna (Itlay). Geophys Res Abstr 8:03098

Schroeder WH, Anlauf KG, Barrie LA, Lu JY, Steffen A, Schneeberger DR, Berg T (1998) Arctic springtime depletion of mercury. Nature 394:331-332

Schroeder WH, Munthe J (1998) Atmospheric mercury: an overview. Atmos Environ 32:809-822

Seinfeld JH, Pandis SN (2006) Atmospheric Chemistry and Physics: Air Pollution to Climate Change. John Wiley & Sons, New York, pp 1326

SET (2009) Sensor Electronic Technology, Inc - UVTOP technical datasheet. http://www.s-et.com/datasheet/SET_UVTOP_Catalog.pdf

SI/USGS (2008) Smithsonian Institution / U.S. Geological Survey Weekly Volcanic Activity Report, 5-11 November 2008. http://www.volcano.si.edu/reports/usgs/index.cfm?content=archive

SI/USGS (2009) Smithsonian Institution / U.S. Geological Survey Weekly Volcanic Activity Report, 10-16 December 2008.

Sigurdsson H, Houghton B, McNutt SR, Rymer H, Stix J (2000) Encyclopedia of Volcanoes. Academic Press, San Diego, USA, pp 1417

Sihler H (2007) Light-emitting diodes as light sources in spectroscopic measurements of atmospheric trace gases. Diploma thesis, University of Heidelberg.

Sihler H, Kern C, Poehler D, Platt U (2008) Applying light-emitting diodes with narrow-band emission features in differential optical absorption spectroscopy. in preparation (Appl Opt)

Simon FG, Schneider W, Moortgat GK, Burrows J (1990) A study of the ClO absorption cross-section between 240 and 310 nm and kinetics of the self-reaction at 300K. J Photoch Photobio 55:1-23

Simpson WR, von Glasow R, Riedel K, Anderson P, Ariya P, Bottenheim J, Burrows J, Carpenter L, Frieß U, Goodsite ME, Heard D, Hutterli M, Jacobi H-W, Kaleschke L, Neff B, Plane JMC, Platt U, Richter A, Roscoe HK, Sander R, Shepson P, Sodeau J, Steffen A, Wagner T, Wolff E (2007) Halogens and their role in polar boundary-layer ozone depletion. Atmos Chem Phys 7:4375-4418

Sinreich R, Friess U, Wagner T, Platt U (2005) Multi axis differential optical absorption spectrosocopy (MAXDOAS) of gas and aerosol distributions. Faraday Discuss 130:132-164

Sinreich R, Volkamer R, Filsinger F, Frieß U, Kern C, Platt U, Sebastian O, Wagner T (2007) MAX-DOAS detection of glyoxal during ICARTT 2004. Atmos Chem Phys 7:1293-1303

Solomon S, Schmeltekopf AL, Sanders RW (1987) On the interpretation of zenith sky absorption measurements. J Geophys Res 92:8311-8319

Sommer T (2008) Direct sun light measurements of volcanic plumes using differential optical absorption spectroscopy. Diploma thesis, University of Heidelberg.

SONY (2006) ILX511 - 2048 pixel CCD Linear Image Sensor (B/W). Technical datasheet. http://www.oceanoptics.com/technical/detectorsonyILX511.pdf

Spinetti C, Buongiornio MF, Lombardo V, Merucci L (2003) Aerosol optical thickness of Mt. Etna volcanic plume retrieved by means of the Airborne Multispectral Imaging Spectrometer (MIVIS). Ann Geophys Italy 46:439-449

Staudacher T, Ferrazzini VF, Peltier AP, Kowalski PK, Catherine PC, Boissier PB (2008) Multi-discipline monitoring of eruptions at Piton de la Fournaise, Ile de la Réunion. IAVCEI General Assembly 2008, Reykjavik, Iceland,

Steffen A, Douglas T, Amyot M, Ariya P, Aspmo K, Berg T, Bottenheim J, Brooks S, Cobbett F, Dastoor A, Dommergue A, Ebinghaus R, Ferrari C, Gardfeldt K, Goodsite ME, Lean D, Poulain AJ, Scherz C, Skov H, Sommar J, Temme C (2008) A synthesis of atmospheric mercury depletion event chemistry in the atmosphere and snow. Atmos Chem Phys 8:1445-1482

Stevenson DS, Blake S (1998) Modelling the dynamics and thermodynamics of volcanic degassing. B Volcanol 60:307-317

Stoiber RE, Jepsen A (1973) Sulfur dioxide contributions to the atmosphere by volcanoes. Science 182:577-578

Stoiber RE, Malinconico LL, Williams SN (1983) Use of the correlation spectrometer at volcanoes. In: Tazieff H, Sabroux, JC (ed) Forecasting volcanic events. Elsevier, Amsterdam, 424-444

Storey M, Duncan RA, Swisher CC (2007) Paleocene-Eocene Thermal Maximum and the Opening of the Northeast Atlantic. Science 316:587-589

Stutz J, Ackermann R, Fast JD, Barrie L (2002) Atmospheric reactive chlorine and bromine at the Great Salt Lake, Utah. Geophys Res Lett 29:1380

Stutz J, Platt U (1996) Numerical analysis and error estimation of the statistical error of differential optical absorption spectroscopy measurements with least-squares methods. Appl Opt 35:6041-6053

Sutton AJ, Elias T, Gerlach TM, Stokes JB (2001) Implications for eruptive processes as indicated by sulfur dioxide emissions from Kilauea Volcano, Hawaii, 1979-1997. J Volcanol Geoth Res 108:283-302

Sutton AJ, Herd RA, Elias T, Edmonds M, Horton H, Garbeil H, Teves A (2005) Continuous SO_2 emission rate measurements at Kilauea: Capturing transitory events. AGU Fall Meeting 2005, San Francisco, USA,

Sweeney D, Kyle PR, Oppenheimer C (2008) Sulfur dioxide emissions and degassing behavior of Erebus volcano, Antarctica. J Volcanol Geoth Res 117:725-733

Tabazadeh A, Turco RP (1993) Stratospheric chlorine injection by volcanic eruptions: HCl scavenging and implications for ozone. Science 260:1082-1086

Tazieff H, Sabroux JC (1983) Forecasting Volcanic Events (Developments in Volcanology). Elsevier Science Ltd, London, Amsterdam, New York, pp 660

Textor C, Graf H-F, Herzog M, Oberhuber JM (2003) Injection of gases into the stratosphere by explosive volcanic eruptions. J Geophys Res 108:4606

Textor C, Graf H-F, Timmreck C, Robock A (2004) Emissions from volcanoes. In: Granier C, Artaxo, P, Reeves, C (ed) Emissions of Atmospheric Trace Compounds. Klewer, Dordrecht, Netherlands, 269-303

Theys N, Van Roozendael M, Dils B, Hendrick F, Hao N, De Mazière M (2009) First satellite detection of volcanic bromine monoxide emission after the Kasatochi eruption. Geophys Res Lett 36:L03809

Trick S (2004) Formation of nitrous acid on urban surfaces: A physical-chemical perspective. PhD thesis, University of Heidelberg.

Tschritter J (2007) Design of a third generation DOAS optical system and comparison with conventional systems (translated from German). Diploma thesis, University of Heidelberg.

Tuckermann M, Ackermann R, Gölz C, Lorenzen-Schmidt H, Senne T, Stutz J, Trost B, Unold W, Platt U (1997) DOAS-observation of halogen radical-catalyzed Arctic boundary layer ozone destruction during the ARCTOC-campaigns 1995 and 1996 in Ny-Alesund, Spitsbergen. Tellus 49B:533-555

Twomey S (1974) Pollution and planetary albedo. Atmos Environ 8:1251-1256

USGS (2008a) U.S. Geological Survey, Hawaiian Volcano Observatory, 2007 - 2008 Kilauea Eruption Timeline. http://hvo.wr.usgs.gov/kilauea/timeline/

USGS (2008b) U.S. Geological Survey, Hawaiian Volcano Observatory, Smithsonian Institution / U.S. Geological Survey Weekly Volcanic Activity Reports, March 19, 2008. http://www.volcano.si.edu/reports/usgs/

USGS (2008c) U.S. Geological Survey, Hawaiian Volcano Observatory, Smithsonian Institution / U.S. Geological Survey Weekly Volcanic Activity Reports, March 20, 2008. http://www.volcano.si.edu/reports/usgs/

Van Roozendael M, Pinardi G, Hermans C, Fayt C, Merlaud A (2006) MiniDOAS calibration issues. 2nd NOVAC retrieval workshop, Gothenburg, Sweden, December 19, 2006

Van Roozendael M, Wagner T, Richter A, Pundt I, Arlander DW, Burrows J, Chipperfield MP, Fayt C, Johnston PV, Lambert J-C, Kreher K, Pfeilsticker K, Platt U, -P. PJ, Sinnhuber B-M, Tornkvist KK, Wittrock F (2002) Intercomparison of BrO measurements from ERS-2 GOME, ground-based and balloon platforms. Adv Space Res 29:1661-1666

Vandaele AC, Hermans C, Simon PC, Carleer M, Colins R, Fally S, Mérienne MF, Jenouvrier A, Coquart B (1998) Measurements of the NO_2 absorption cross-sections from 42000 cm^{-1} to 10000 cm^{-1} (238-1000 nm) at 220 K and 294 K. J Quant Spec and Rad Transf 59:171-184

Vandaele AC, Simon PC, Guilmot M, Carleer M, Colin R (1994) SO_2 absorption cross section in the UV using a Fourier transform spectrometer. J Geophys Res 99:25599-25605

Veitel H (2002) Vertical profiles of NO_2 and HONO in the boundary layer. PhD thesis, University of Heidelberg.

Veitel H, Funk O, Kurz C, Platt U, Pfeilsticker K (1998) Geometrical path length probability density functions of the skylight transmitted by midlatitude cloudy skies: Some case studies. Geophys Res Lett 25:3355-3358

Villemant B, Boudon G (1999) H_2O and halogen (F, Cl, Br) behaviour during shallow magma degassing processes. Earth Planet Sc Lett 168:271-286

Villemant B, Hammouya G, Michel A, Semet M, Komorowksi J-C, Boudon G, Cheminée J-L (2005) The memory of volcanic waters: Shallow magma degassing revealed by halogen monitoring in thermal springs of La Soufrière volcano (Guadeloupe, Lesser Antilles). Earth Planet Sc Lett 237:710-728

Viramonte JG, Incer-Barquero J (2008) Masaya, the "Mouth of Hell", Nicaragua: Volcanological interpretation of the myths, legends and anecdotes. J Volcanol Geoth Res 176:419-426

Vogel L (2010) DOAS observations of chemistry in volcanic plumes conducted in the scope of the Network for Observation of Volcanic and Atmospheric Change. PhD thesis, in preparation, University of Heidelberg.

Vogel L, Kern C, Fickel M, Wöhrbach M, Platt U (2008) Halogen oxides in volcanic plumes: Simultaneous measurements at different plume ages. Eos Trans AGU Fall Meeting 2008

Vogel L, Kern C, Fickel M, Wöhrbach M, Platt U (2009) BrO/SO_2 ratios measured for different plume ages at Mt. Etna, Italy. in preparation

Vogt R, Crutzen PJ, Sander R (1996) A mechanism for halogen release from sea-salt aerosol in the remote marine boundary layer. Nature 383:327-330

Voigt S, Orphal J, Bogumil K, Burrows JP (2001) The temperature dependence (203-293K) of the absorption cross sections of O_3 in the 230-850nm region measured by Fourier-transform spectroscopy. J Photoch Photobio 143:1-9

Volk R (2008) Messung von NO_2 und SO_2 Flüssen an anthropogenen Emissionsquellen - Determination of emission fluxes from anthropogenic sources using vehicle based Multi-Axis Differential Optical Absorption Spectroscopy. Diploma thesis, University of Heidelberg.

Volkamer R, Etzkorn T, Geyer A, Platt U (1998) Correction of the Oxygen Interference with UV Spectroscopic (DOAS) Measurements of Monocyclic Aromatic Hydrocarbons in the Atmosphere. Atmos Environ 32:3731-3747

Volkamer R, Molina LT, Molina MJ, Shirley T, Brune WH (2005a) DOAS measurement of Glyoxal as a new marker for fast VOC chemistry in urban air. Geophys Res Lett 32:L08806

Volkamer R, Spietz P, Burrows JP, Platt U (2005b) High-resolution absorption cross-section of Glyoxal in the UV/vis and IR spectral ranges. J Photoch Photobio A: Chemistry 172:35 - 46

von Friedeburg C, Pundt I, Mettendorf K-U, Wagner T, Platt U (2005) Multi-AXis-(MAX) DOAS Measurements of NO_2 during the BAB II Motorway Emission Campaign, (BAB II special issue). Atmos Environ 39:977-985

von Glasow R (2008) Halogen and sulphur chemistry in volcanic plumes. Geophys Res Abstr 10:EGU-2008-A-07959

von Glasow R, Bobrowski N, Kern C (2008) The effects of volcanic eruptions on atmospheric chemistry. Chem Geol doi:10.1016/j.chemgeo.2008.08.020

von Glasow R, Crutzen PJ (2004) Model study of multiphase DMS oxidation with a focus on halogens. Atmos Chem Phys 4:589-608

von Glasow R, Crutzen PJ (2007) Tropospheric halogen chemistry. In: Holland HD, Turekian, KK, Keeling, RF (ed) Treatise on Geochemistry, Vol. 4. Elsevier-Pergamon, Amsterdam, 1-67

von Glasow R, Sander R, Bott A, Crutzen PJ (2002a) Modeling chemistry in the marine boundary layer. 2. Interactions with sulfur and cloud-covered MBL. J Geophys Res 107:4323

von Glasow R, Sander R, Bott A, Crutzen PJ (2002b) Modeling halogen chemistry in the marine boundary layer. 1. Cloud-free MBL. J Geophys Res 107:4341

von Glasow R, von Kuhlmann R, Lawrence MG, Platt U, Crutzen PJ (2004) Impact of reactive bromine chemsitry in the troposphere. Atmos Chem Phys 4:2481-2497

Wagner T, Burrows JP, Deutschmann T, Dix B, von Friedeburg C, Frieß U, Hendrick F, Heue K-P, Irie H, Iwabuchi H, Kanaya Y, Keller J, McLinden CA, Oetjen H, Palazzi E, Petritoli A, Platt U, Postylyakov O, Pukite J, Richter A, van Roozendael M, Rozanov A, Rozanov V, Sinreich R, Sanghavi S, Wittrock F (2007) Comparison of box-air-mass-factors and radiances for Multiple-Axis Differential Optical Absorption Spectroscopy (MAX-DOAS) geometries calculated from different UV/visible radiative transfer models. Atmos Chem Phys 7:1809-1833

Wagner T, Dix B, v. Friedeburg C, Friess U, Sanghavi S, Sinreich R, Platt U (2004) MAX-DOAS O_4 measurements: A new technique to derive information on atmospheric aerosols - Principles and information content. J Geophys Res 109:D22205

Wagner T, Erle F, Marquard L, Otten C, Pfeilsticker K, Senne T, Stutz J, Platt U (1998) Cloudy sky photon path lengths as derived from DOAS observations. J Geophys Res 103:25321

Wahner A, Ravishankara AR, Sander SP, Friedl RR (1988) Absorption cross section of BrO between 312 and 385 nm at 298 and 223 K. Chem Phys Lett 152:507-512

Wahner A, Tyndall G, Ravishankara AR (1987) Absorption cross sections for OClO as a function of temperature in the wavelength range 240-480nm. J Phys Chem 91:2734-2738

Walker JCG, Hays PB, Kasting JF (1981) A negative feedback mechanism for the long-term stabilization of Earth's surface temperature. J Geophys Res 86:9776-9782

Wallace L, Livingston W (1992) The effect of the Pinatubo cloud on hydrogen chloride and hydrogen flouride. Geophys Res Lett 19:1209

Watson IM, Oppenheimer C, Voight B, Francis PW, Clarke A, Stix J, Miller A, Pyle DM, Burton MR, Young SR, Norton G, Loughlin S, Darroux B, MVO-Staff (2000) The relationship between degassing and ground deformation at Soufriere Hills Volcano, Montserrat. J Volcanol Geoth Res 98:117-126

Wennberg P (1999) Bromine explosion. Nature 397:299-300

Werner CA, Hurst T, Scott B, Sherburn S, Christenson BW, Britten K, Cole-Baker J, Mullan B (2008) Variability of passive gas emissions, seismicity, and deformation during crater lake growth at White Island Volcano, New Zealand, 2002-2006. J Geophys Res 113:B01204

White JU (1942) Long optical paths of large aperture. J Opt Soc Am 32:285-288

White JU (1976) Very long optical paths in air. J Opt Soc Am 66:411-416

Widenhorn R, Blouke MM, Weber A, Rest A, Bodegom E (2002) Temperature dependence of dark current in a CCD. SPIE Proceedings: Congress for Sensors and camera systems for scientific, industrial, and digital photography applications III, San Jose, USA, January 21-23, 2002

Wild M, Ohmura A, Gilgen H, Roecker E (1995) Validation of general circulation model radiative fluxes using surface observations. J Clim 8:1309-1324

Williams SN (1983) Geology and eruptive mechanisms of Masaya caldera complex. PhD thesis, Dartmouth College.

Williams-Jones G, Horton KA, Elias T, Garbeil H, Mouginis-Mark PJ, Sutton AJ, Harris AJL (2006) Accurately measuring volcanic plume velocity with multiple UV spectrometers. B Volcanol 68:328-332

Williams-Jones G, Stix J, Heiligmann M, Barquero J, Fernandez E, Gonzalez ED (2001) A model of degassing and seismicity at Arenal Volcano, Costa Rica. J Volcanol Geoth Res 108:121-139

Wittrock F, Oetjen H, Richter A, Fietkau S, Medeke T, Rozanov A, Burrows J (2004) MAX-DOAS measurements of atmospheric trace gases in Ny-Ålesund - Radiative transfer studies and their application. Atmos Chem Phys 4:955-966

WMO (2007) Scientific assessment of ozone depletion: 2006. World Meteorological Organization. Global Ozone Research and Monitoring Project.
http://www.wmo.int/pages/prog/arep/gaw/ozone_2006/ozone_asst_report.html

Wöhrbach M (2008) Further development and testing of a UV-camera for the determination of trace gas distributions (translated from German). University of Heidelberg.

Wongdontri-Stuper W, Jayanty RKM, Simonaitis R, Heicklen J (1979) The Cl_2 photosensitized decomposition of O_3: The reactions of ClO and OClO with O_3. Photochem 10:163

Wright TE, Burton MR, Pyle DM, Caltabiano T (2008) Scanning tomography of SO_2 distribution in a volcanic gas plume. Geophys Res Lett 35:L17811

Zerefos C, Nastos P, Balis D, Papayannis A, Kelepertsis A, Kannelopoulou E, Nikolakis D, Eleftheratos C, Thomas W, Varotsos C (2006) A complex study of Etna's volcanic plume from ground-based, in-situ and space borne observations. Intern J Rem Sens 27:1855-1864

Zhang Y (2005) Wireless sensor network for volcano monitoring. Masters thesis, Chalmers University of Technology.

Zong Y, Brown SW, Johnson BC, Lykke KR, Ohno Y (2006) Simple spectral stray light correction method for array spectroradiometers. Appl Opt 45:1111-1119

11 List of figures

12 Acknowledgements

I would like to thank the following people for their support. The work presented in this thesis would not have been possible without them.

Special thanks to Ulrich Platt for giving me the opportunity to work in this research field. While always there to give advice and countless ingenious ideas (only a small part of which could be realized in this thesis), but at the same time giving me the freedom to choose which directions to emphasize, he was a wonderful advisor and I look forward to a continuing cooperation in the future.

Aside from doing a tremendous job in coordinating the multi-cultural and sometimes chaotic NOVAC community, Bo Galle was also a great mentor to me. His group at Chalmers University in Gothenburg is also an extraordinary bunch, and special thanks to Claudia Rivera, Mattias Johansson, Yan Zhang and Patrik Norman. The meetings we had towards the beginning of the project were key in getting off on the right track, and later fieldwork we did together was great fun.

Perhaps the most gratifying aspect of the NOVAC project was that it enabled me to get to know such a large number of wonderful people. It is impossible to name them all, but special thanks to Nicole Bobrowski, Fabio Vita, Salvo Inguaggiato and the INGV (Palermo) group, Mike Burton, Tomasso Caltabiano, Guiseppe Salerno and the INGV (Catania) group, Wilfried Strauch, Martha Herera and Manuel Alfaro from INETER (Managua), Santiago Arellano, Silvana Hidalgo, Freddy Vásconez and the IG group in Quito, Hugo Delgado and Jose Manuel Alvarez Nieves from UNAM and the CENAPRED group (Mexico City), Jeff Sutton at HVO (Hawaii), Michel Van Roozendael, Caroline Fayt and Gaia Pinardi from BIRA (Brussels), Thor Hansteen from IFM-GEOMAR (Kiel) as well as numerous others!

At the Institute of Environmental Physics I need to thank Leif Vogel first, as his coming on board in the volcano group saved me from almost drowning in work, and fieldwork was so much more fun with him! A number of undergraduate students also put their heads into

remote sensing of volcanoes. Many of the results shown in this thesis were as much their work as they were mine, and I hope I have given them the credit they deserve. In chronological order they are Holger Sihler, Tobias Sommer, Felix Kick, Matthias Fickel, Markus Wöhrbach and Rainer Volk.

Besides the people directly involved with volcanoes, a number of others were a source of inspiration and also helped me out a lot in proofing this thesis. Special thanks to Tim Deutschmann, Marcel Dorf, Lena Kritten, Thomas Lehmann, André Merten, Denis Pöhler, Katja Seitz, Jens Tschritter, and Roland von Glasow. Thomas Wagner was not only helpful in discussing a number of issues concerning radiative transfer, he was also interested enough to referee the thesis! Now that it's finished, I certainly know how much work that will be, and I thank him very much.

Last but not least, my family and friends were ceaseless in their support, and I can't thank them enough. Most of all, Katrin endured my frequent absences and thesis sulkiness without a word of complaint and still wants to marry me now that it's all done. I am deeply grateful, and look forward to taking on the next adventure together!